UNIVERSITÄT BAYREUTH

Developing Atomic Force Microscopy Methods for Soft Matter Characterization

Dissertation

to be awarded the degree
Doctor of Natural Sciences (Dr. rer. nat.)

at the Faculty of Biology, Chemistry and Earth Sciences
University of Bayreuth

submitted by
Nadine Raßmann
born in Villingen-Schwenningen

Bayreuth 2025

The work described in this thesis was carried out at the Chair of Physical Chemistry II: Interfaces and Nanoanalytics at the University of Bayreuth from January 2020 to July 2025 under the supervision of Prof. Dr. Georg Papastavrou.

This is a full reprint of the thesis submitted to obtain the academic degree of Doctor of Natural Sciences (Dr. rer. nat.) and approved by the Faculty of Biology, Chemistry and Geosciences of the University of Bayreuth.

Form of the thesis:	Cumulative thesis
Thesis submitted:	09.07.2025
Admission by the doctoral committee:	16.07.2025
Date of Defense:	24.03.2026
Acting Dean:	Prof. Dr. Janosch Hennig

Doctoral committee:

Prof. Dr. Georg Papastavrou	(Reviewer)
Prof. Dr. Regine von Klitzing	(Reviewer)
Prof. Dr. Johannes Brendel	(Chair)
Prof. Dr. Thomas Scheibel	

(additional reviewer Prof. Dr. André Gröschel)

«Es ist nicht genug, zu wissen,
man muss auch anwenden;
es ist nicht genug zu wollen,
man muss auch tun.»

Johann Wolfgang von Goethe

meinen Eltern

Acknowledgements

Starting my PhD journey, I imagined embarking on a scientific adventure. Little did I know how challenging, turbulent, and rewarding episodes of this journey would be, both scientifically and personally. Having mastered it, I am more than grateful for the experience and am proud of the scientist and person I have grown into throughout the past five years. However, all of this would not have been possible without the brilliant and loving minds surrounding and supporting me along the way. Thank you for your scientific and personal guidance, memorable experiences, shared laughter and tears, long-lasting, deepened and new friendships, and for believing in me when I didn't. This section is devoted to all of you, and I want to express my deepest gratitude.

Foremost, I would like to warmly thank Prof. Georg Papastavrou for guiding me all the way from my very first HiWi as a bachelor student to finishing the biggest scientific adventure so far — submitting this thesis. Thank you for giving me the freedom to explore what I was curious about throughout my PhD, trusting me, and providing a wonderful AFM playground to do fun science. I am thankful for the ongoing support and the opportunity to research "down under" for three months.

I am grateful for financial support from the Fonds of the Chemical Industry (FCI) of the German Chemical Industry Association (VCI), through a Kekulé Fellowship. Moreover, I acknowledge the support by the Elite Network Bavaria in the Framework of the Elite Study Program Macromolecular Science, the University of Bayreuth Graduate School (UBTGS), and the Program CoMento by the Equal Opportunities Department of the University of Bayreuth.

Working with scientists from different labs on interdisciplinary research questions has been a pleasure and a big inspiration. Thanks to all my collaborators and colleagues for engaging in scientific discussions, insights into your work, and developing and realizing ideas together. I owe a big thanks to our collaborators at the Department of Biomaterials (University of Bayreuth), Theoretical Physics VI (University of Bayreuth), Tissue Engineering and Regenerative Medicine (University Hospital Würzburg), and Biocolloids (University Fribourg Switzerland). A special thanks to Bettina for a fun project together. Thank you, Sebastian and Richard, for the interesting insights into the world of theoretical physics. I am very grateful for your patience in explaining simulations to me and the interesting conversations on how the same system looks from

an experimental and a theoretical perspective. Thank you, Katinka, for all your efforts synthesizing microgels!

I am especially grateful for the whole PCII lab; the journey wouldn't have been the same without you. Thank you for the fun time in and beyond the lab, discussing science, life, and much more, for barbecues on our lovely terrace, and crazy friday-afternoon experiments. You have been a great support, especially throughout the tougher phases of my PhD.

A huge thank you, Nico, for always making time to discuss science's big and small challenges and instrumental first-aiding, especially in the early phase of my PhD. I am grateful for your patience, guidance on navigating a PhD's ups and downs, an incredible scientific gut feeling, and reminding me to refocus when diving too deep into something again. Thanks for lending me an „Augentier"from time to time.

I am absolutely thankful for the best office mates — Paul, Leonie, Inka and Roman — I could have wished for. Thank you, Paul, for always being open to discussing the wildest ideas, thinking outside the box, and balancing our office structure-chaos equilibrium. A big thanks to Leonie for always being there, for long talks, and for being a big motivation to not compromise on sports in between the lab work and writing. Thank you, Roman, for countless ideas, and small „I've quickly built something"-tools to ease everyday lab work. And of course, I am beyond grateful for all the effort, time, energy, and precision you dedicated to the EnoCP endeavour. Your perspective on electrochemistry and "everything with a cable" has been invaluable to me.

I greatly thank Steffen for exploring the world of microgels together, long hours at the microscopes, AFMs and discussing data. A big thanks also goes to Agnes and Tamino, who complemented the team microgels. Thank you, Sebastian „Seppl", for all the technical discussions about AFM and crazy ideas that have worked out perfectly. You've been a great companion. Big thank you, Dr. Mandy, Dr. Kandy, and Basti, for all the small tricks and tweaks at the AFM; they have saved me so many times. I am grateful to my students Steffen, Agnes, Roman, Sofie, Henrike, and Jessica. I have learned a lot from you!

Liebe Sieglinde, liebe Sybille herzlichen Dank für Eure Unterstützung in allen organisatorischen Belangen und immer ein offenes Ohr. Mein besonderer Dank gilt auch Nina Volk, Markus Hund und Petra Zippilius für technische Unterstützung in allen Laborlebenslagen.

During the final months of my PhD journey, I had the opportunity to spend a few months researching Australia, an experience that let me grow scientifically but even more personally. A great thanks to Prof. Frank Caruso and the entire CNG at the University of Melbourne. I highly appreciate the warm welcome to the group. Thank you for

introducing me to the world of MPNs and opening up a new perspective on „how to do science“. It’s been a pleasure to work and discuss science with you, Wanjun and Omid. A great shout-out to the CNG wildlife expedition crew, Antonella, Pippa, Soraia, Marco, Mathias, and Yeray, you made my research stay in Melbourne a special experience within and beyond the lab. Moreover, I’d like to send thank you hugs to Hikaru, Jihan, Indira, Rebecca, Ana, Nuria, Ravi, Sam, and Martin, who have been the loveliest surprise I could have ever dreamt of awaiting me down under.

Liebe „Froinde“, Dr. Corinna „Cöörinna“, Dr. Andreas „Andos“, Dr. Sebastian „Sebi“ und Paulina ihr seid die besten Freunde, die man sich nur so wünschen kann. Danke für eine wundervolle Studienzeit, gemeinsame LGS-Chill- und legendäre Kochabende (auf euren Hunger ist Verlass, das lässt mein Kochherz höher schlagen). Danke, dass ihr immer da seid. Auf das wir noch viele tolle Erlebnisse und Lebensabschnitte in gemeinsamen „Publikationen“ festhalten können. Liebe Babsi, was als Schnappsidee auf dem CSG Sommerfest begann, wurde zu einem Abenteuer, an das wir uns noch lange zurückerinnern werden. Vielen Dank für eine wunderschöne Koala-Reise :) Mille Grazie Greta! Thank you for being a wonderful and caring friend, I have learnt so much from you. Vielen lieben Dank an Leonie, Alex, Teresa, Roman, Tamino, Ina, Max und die sportlichen Andis für eine ausgezeichnete Lab-hard Work-out harder Balance.

Ganz besonders möchte ich aber meiner Familie danken. Ohne Euch wäre ich nicht die Person, die ich heute bin. Liebe Mama, lieber Papa, danke für die Neugier, die ihr uns schon als Kindern mitgegeben habt und die Motivation offen zu sein, immer etwas Neues zu lernen. Mama, Danke, dass Du mich durch alle Tiefen und Höhen begleitet und unterstützt hast. Mama und Bernhard, ganz lieben Dank dafür, dass ihr mir den Raum (sinnbildlich ebenso wie wörtlich) gegeben habt, mich voll und ganz der letzten Etappe des Diss-Marathons zu widmen. Liebes Bruderherz, danke Dir, dass du immer da bist aber auch für lange Gespräche über die „wundersame Welt der Wissenschaft“ mindestens so leidenschaftliche wie nerdige Platte vs. Kugel Diskussionen.

Lieber Edu, ein riesiges Dankeschön für Deine Unterstützung, deine unermüdliche Geduld mit meinen Laborlaunen, dass Du immer an mich glaubst, und für mich da bist. Ich weiß nicht, ob ich ohne Dich den Mut und die Energie gehabt hätte, dieses Abenteuer Promotion bis zum Ende durchzustehen. Vielen lieben Dank für wunderschöne (wenn auch viel zu kurze) Wochenenden in Würzburg, die mich immer wieder aus dem Dissdschungel herausgeholt haben. Muchísimas Gracias! Ich freue mich auf das nächste Kapitel mit Dir :)

List of Publications

This thesis is written as a cumulative dissertation. It is based on the following peer-reviewed publications:

[1] Bettina Tran, Samuel Watts, Jules D. P. Valentin, Nadine Raßmann, Madeleine Ramstedt, Georg Papastavrou and Stefan Salentinig:
„pH-responsive Virus-based Colloidal Crystals for Advanced Material Platforms“,
Advanced Functional Materials, **2024**, *34*(37), 202402257.

[2] Nadine Raßmann, Melina Weber, Roman J. E. Glaß, Klaus Kreger, Nicolas Helfricht, Hans-Werner Schmidt and Georg Papastavrou:
„Electrogelation: Controlled Fast Formation of Micrometer-Thick Films from Low-Molecular Weight Hydrogelators“,
Langmuir, **2023**, *39*(48), 17190–17200.

[3] Nadine Raßmann, Roman J. E. Glaß, Nicolas Helfricht and Georg Papastavrou:
„Electrochemical Picobalance: Proof-of-Principle for an Electrochemical Cantilever-based Mass Balance“,
Electrochimica Acta, **2025**, *540*, 146907.

[4] Nadine Raßmann[#], Steffen Trippmacher[#], Agnes Specht, Katinka Theis, Tamino Rößler, Sebastian Wohlrab, Richard Kellnberger, Sahar Salehi, Hendrik Bargel, Nicolas Helfricht, Krystyna Albrecht, Thomas Scheibel, Jürgen Groll, Stephan Gekle and Georg Papastavrou:
„Determining the Elastic Modulus of Microgel Particles by Nanoindentation“,
ACS Applied Nano Materials, **2025**, *8*(11), 5383-5398.
[#] these authors contributed equally.

This thesis does not include results from the following peer-reviewed publications, and manuscripts:

[5] Christoph Sommer, Hendrik Bargel, Nadine Raßmann and Thomas Scheibel: „Microbial repellence properties of engineered spider silk coatings prevent biofilm formation of opportunistic bacterial strains“,
MRS Communications, **2021**, *11*, 356–362.

[6] Agnes Specht, Steffen Trippmacher, Nadine Raßmann, Tamino Rößler, Katinka Theis, Krystyna Albrecht, Nicolas Helfricht, Jürgen Groll, and Georg Papastavrou: „High-Throughput Mechanical Characterization of Single Microgel Particles by Fluidic Force Microscopy“,
Small, **2025**, *21*(38), e05367.

The following conference presentations were part of my PhD:

[1] **Poster presentation:** „Soft Hydrogel Films by Electrogelation“,
FCI Stipendiatentreffen, **2022**, Würzburg.

[2] **Oral presentation:** „Growing Micrometer-Thick Films of Low-Molecular Weight Hydrogelators by Electrogelation“,
19th Zsigmondy Colloquium, **2024**, Düsseldorf.

Summary

This dissertation investigated soft matter by surface analytical tools, primarily based on atomic force microscopy (AFM). Throughout the work, AFM-based techniques were developed and employed to gain an in-depth understanding of soft matter's physico-chemical properties and formation processes. The work covered method developments, ranging from hyphenating existing techniques with electrochemistry to correlating X-ray scattering and AFM, as well as for studying the elasticity of particulate soft matter.

The first project studied the nanostructure of colloidal crystals from bacteriophages. The assembly of the colloidal structures was governed by the interaction of bacteriophages with polyelectrolyte and depended on the chain length of the polycation as well as the assembly pH. Small-angle X-ray scattering (SAXS) proposed a hexagonal structure of the colloidal crystals in suspensions. Establishing an AFM-based imaging approach allowed for the characterization of the nanostructure of the surface-immobilized colloidal crystal in liquid, in real space, for the first time. By complementary use of AFM and SAXS, the hexagonal pattern of the colloids in the assemblies could be verified in real and reciprocal space.

The second project characterized the electrochemical formation of a hydrogel film from a low molecular weight compound by two AFM-based techniques. The low molecular weight hydrogelator (LMWHG) was electrogelated directly at the electrode interface. Electrochemical water splitting at the working electrode induced the required pH shift to trigger interface-mediated hydrogelation of the pH-responsive LMWHG. Implementing the electrochemical cell into the AFM allowed to study the film thickness directly in the swollen state by means of AFM nanoindentation. Additionally, the films were dried, and the thickness was determined at a scratch in the dried films. Combining both AFM-based techniques, the impact of the LMWHG concentration, applied potential, and gelation time on the electrogelation could be demonstrated. Establishing the AFM-based techniques for thickness characterization opened up the possibility of controlling the hydrogel thickness. The electrogelation was studied exemplarily on a benzenetrisamide LMWHG. However, the principle and characterization techniques would work for any pH-responsive hydrogelator.

The third project developed a novel method — the electrochemical picobalance — by integrating cantilever-based mass sensing with electrochemistry. Suitable electrochemical balance probes with an integrated microelectrode were custom-developed and fabricated.

These electrochemical balance probes (EBPs) served a dual purpose: they detected the deposited mass via changes in the cantilever resonance frequency while they acted as microelectrodes simultaneously. The electrochemical standard process of copper deposition was employed to validate the novel method. The copper deposition on the marked not only the first electrodeposition on an AFM cantilever, simultaneously tracked electrochemically and gravimetrically. More importantly, the evaluation of the electrochemical mass via Faraday's law of electrolysis demonstrated the quantitative mass detection at the electrochemical picobalance with a mass resolution of $\lesssim 1$ pg. The here-developed and validated analytical technique enables tracing dynamic electrochemically induced or stimulated processes like electrogelation directly on an AFM cantilever with picogram resolution.

Finally, the fourth project reassessed and enhanced a widely used method, namely AFM-nanoindentation. Albeit the technique of nanoindentation has been used for decades, there is still an ongoing discussion about the role of the indenter geometry and other parameters. Here, a systematic approach to these problems has been pursued. Two different microfluidically fabricated microgels were characterized by AFM nanoindentation, focusing on the impacts of experimental parameters like the geometry of the indenter, contact model, alignment of the indenter with the sample, or ramping velocity. The identical particles were indented with up to six cantilever-based indenters resembling the conical, spherical, and parallel-plate interaction geometries to elucidate the impact of the indenter geometry on the Young's modulus. Combining AFM nanoindentation with finite element simulations of the microgel deformation before and during the indentation and total internal reflection fluorescence (TIRF) microscopy was the key to unraveling previously observed deviations between different indenter geometries. The findings showed that the simplified double contact model (SDC model) describes the indentation more adequately in comparison to the simpler Hertz model. Residual discrepancies between the indenter geometries in the framework of the SDC model originated from the varied contribution of the substrate-particle adhesion, which depends on the indenter size. The project concluded with best-practice advice to improve microgel nanoindentation's cross-study comparability and data accuracy, which is also directly transferable for analyzing single cells.

Zusammenfassung

Diese Dissertation untersuchte weiche Materie mit oberflächenanalytischen Methoden, hauptsächlich basierend auf Rasterkraftmikroskopie. Im Rahmen dieser Arbeit wurden rastermikroskopische Techniken, zur Charakterisierung physikochemischer Eigenschaften und Bildungsprozesse von weicher Materie, entwickelt und angewendet. Die Arbeit umfasste hierbei Methodenentwicklungen von der Verknüpfung existierender Methoden mit Elektrochemie hin zur korrelativen Verwendung von Rasterkraftmikroskopie und Streumethoden, sowie Elastizitätsbestimmung partikulärer weicher Systeme.

Das erste Projekt untersuchte die Nanostruktur von Kolloidkristallen aus Bakteriophagen. Die Bildung der Kolloidkristalle wurde durch die Interaktion der Biokolloide mit Polyelektrolyten abhängig vom pH-Wert der umgebenden Lösung, sowie der Länge des Polykations gesteuert. Ergebnisse von Röntgenstreuexperimenten implizierten eine hexagonale Struktur der Kolloidkristalle in Suspension. Die Entwicklung einer rasterkraftmikroskopischen Technik zur Abbildung der filigranen Nanostukturen in Flüssigkeit, immobilisiert an einer Goldoberfläche, bestätigte die hexagonale Nanostruktur der Biokolloide im Realraum. Die Kombination komplementärer Techniken, Rasterkraftmikroskopie und Röntgenkleinwinkelstreuung ermöglichte den übereinstimmenden Nachweis hexagonaler kolloidaler Strukturen im Real- und reziproken Raum.

Das zweite Projekt charakterisierte die elektrochemische Hydrogelbildung eines niedermolekularen Gelatormoleküls mittels zweier Rasterkraftmikroskopiemethoden. Die niedermolekulare, hydrogelbildende Verbindung wurde elektrochemisch an einer Elektrode geliert, ein Prozess der als Elektrogelierung bezeichnet wird. Die benötigen Protonen, um die Assemblierung der Moleküle zu initiieren, wurden elektrochemisch direkt an der Elektrodenoberfläche durch die Elektrolyse von Wasser generiert. Die Implementierung der Elektroden in eine Flüssigkeitszelle für Rastermikroskopie ermöglichte die Charakterisierung der Filmdicke im gequollenen Zustand mittels Indentationsmessungen. Darüber hinaus wurden die Hydrogelfilme getrocknet und die Schichtdicke aus Rasterkraftmikroskopieaufnahmen an der Kante eines Kratzers bestimmt und die Ergebnisse beider Methoden an denselben Filmen gegenübergestellt. Auf Grundlage beider Methoden konnte der Einfluss des angelegten Potenzials, der Elektrogelierungsdauer und der Gelatorkonzentration auf die Dicke der Hydrogelfilme demonstriert werden. Die rasterkraftmikroskopische Schichtdickenbestimmung legte hierdurch die analytische Grundlage zur Kontrolle der Schichtdicke im Assemblierungsprozess der niedermolekularen Hydrogel Filme. Die Elektrogelierung wurde hier exemplarisch anhand eines

Trisamides untersucht. Sowohl das Prinzip der Elektrogelierung, also auch die Methoden zu Charakterisierung der Filmdicke, sind auf andere pH-responsive Gelatoren übertragbar.

Das dritte Projekt entwickelte eine neue Methode, die elektrochemische Picowaage, durch Fusionierung einer existierenden Cantilever-basierten Picowaage mit einer elektrochemischen Zelle. Hierzu wurden spezielle elektrisch isolierte Rasterkraftmikroskopiesonden, welche eine planare Mikroelektrode beinhalten, entwickelt. Diese fungierten in der elektrochemischen Picowaage gleichermaßen als Arbeitselektrode und Massensensor. Die neue Methode wurde anhand der Kupferabscheidung, einem elektrochemischem Standardprozess, validiert. Hierdurch konnte nicht nur erstmals ein elektrochemischer Depositionsprozess, der mit einer Massenänderung einhergeht, simultan elektrochemisch und gravimetrisch auf einem AFM Cantilever verfolgt werden. Vielmehr wurde mit der Auswertung elektrochemischen Masse, nach Faradays Eletrolysegesetz, die quantitative Massendetektion in der Picowaage mit einer Auflösung von $\lesssim 1$ pg demonstriert. Die erfolg-reiche Validierung und Kalibrierung ermöglicht zukünftig dynamische elektrochemische Prozesse, wie die Elektrodepostion weicher Materie oder elektrische Stimulation biologischer Zellen, direkt an Rasterkraftmikroskopiesonden simultan gravimetrisch und potentiometrisch zu verfolgen.

Das vierte Projekt setzte sich mit den instrumentellen Einflussfaktoren der rasterkraftmikroskopiegestützten Nanoindentation von Mikrogelpartikeln auseinander. Während die Technik zur Charakterisierung von Zellen und Mikrogelen bereits breite Anwendung findet, waren essenzielle Fragen zum Einfluss der Indentergeometrie, weiterer experimenteller Parameter, sowie die Beschreibung der Interaktion durch ein geeignetes Kontaktmodell, bisher nur unzureichend geklärt. Im Rahmen des letzten Projekts wurden diese offenen Fragen systematisch adressiert. Einzelne Mikrogelpartikel wurden mit sechs verschiedenen Indentern (rund, konisch, Kompression zwischen zwei Platten) deformiert und die Elastizitätsmoduln bestimmt. Die Indentationsdaten wurden mit Finite-Elemente-Simulationen und Interner Totalreflexionsfluoreszenzmikroskopie des Kontakts kombiniert. Dabei konnte gezeigt werden, dass das Doppelkontaktmodell die bessere Beschreibung der Interaktion im Vergleich zum einfacheren Hertz Modell bietet und die verbleibende Diskrepanz auf unterschiedlich ausgeprägten Einfluss der Substrat-Partikel Adhäsion für verschiedene Indenter zurückgeführt werden kann. Darüber hinaus wurde die Wichtigkeit akkurater, Rasterkraftmikroskopie-basierter Ausrichtung von Indenter zum Mikrogelpartikel sowie der Einfluss von Indentationsgeschwindigkeit und Indentationstiefe demonstriert. Ausgehend von den umfangreichen experimentellen Untersuchungen verschiedener instrumenteller Einflussfaktoren auf die Elastizitätsmessungen mit den Rasterkraftmikroskop wurden praktische Hinweise für weitere Arbeiten auf ähnlichen Systemen formuliert.

Contents

Part I

Introduction and Fundamentals

1 Introduction

Soft matter science, as the name implies, investigates the formation, characteristics, and functionalities of materials that can easily be deformed.[1–3] Typical examples include (bio)polymers, colloidal dispersions, nanoparticles, proteins, gels, liquid crystals, and surfactants.[1–3] All of these classes of matter fall in terms of their mechanical behaviour between solids and liquids, showing characteristics of either depending on the length and time scales. Furthermore, they are built from subunits on a mesoscopic scale, i.e., larger than the atomic scale but much smaller than the size of the material. The *softness* is created by relatively weak interactions, i.e., *surface forces* with bonding energies comparable to thermal energy, which hold the mesoscopic subunits of soft matter together.[1–3] In turn, minimal external stimuli are sufficient to disturb the system or change its structure. Self-organization or assembly driven by supramolecular interactions is a common phenomenon.[4–9] For instance, surfactant molecules form a micelle in order to avoid contact between their hydrophobic part and the surrounding aqueous phase.[10] Proteins fold induced by interactions between functional groups in different parts of the amino acid sequence.[11] The self-organization, adaptability, and softness open new routes for advanced materials design and custom-tailored functionalities by tuning the physical and chemical properties of the subunits and their interactions to create new functions on a microscopic level.[1–3] This versatility drives research on self-healing [12] and stimuli-responsive materials [13]. Moreover, soft matter is valued for application in nanotechnology [14, 15], in biomaterials, biofabrication and biomedicine [16], in sensing and actuation applications [17, 18], as well as in soft robotics [19].

The advancement in materials science has always been intertwined with the development of new analytical techniques, which enable an ever-enhanced understanding of their assembly, structure, and physicochemical characteristics. The physicochemical properties of soft matter arise from its structure and the associated interaction forces on colloidal scales.[1–3] However, in contrast to classical condensed matter like ionic crystals or metals, the prediction of the material's properties is less straightforward for soft matter systems due to the more degrees of freedom of the subunits compared to atoms in a fixed lattice.[1] Moreover, a different set of advanced strategies and techniques is required to study soft matter, and there is an increasing need for technical innovation and enhancing the existing analytical toolbox. Powerful methods to study soft matter are scattering techniques [20] like small-angle X-ray scattering (SAXS) [21], small-angle

neutron scattering (SANS) [22] or light scattering as well as microscopy techniques [23], ranging from optical [24], via electron [25] to atomic force microscopy (AFM) [26]. In the context of soft matter, AFM is a particularly valuable technique, as it not only allows us to study the topography or nanostructure but also measure surface forces quantitatively.[26, 27]

Atomic force microscopy has evolved into an advanced analytical tool since its invention by Binnig, Quate, and Gerber in the 1980s [28]. AFM is a scanning probe technique using a cantilever that interacts with its surroundings based on nearfield forces.[26–30] Soon after its invention, AFM has been used to study soft structures, i.e., for imaging DNA strands.[31] Beyond investigating the structure of soft and living matter [32, 33], AFM is used to study film thickness [34–37] and access nanomechanical properties [38] of tissue [39, 40], single cells [41–43], polymers [44–46], and hydrogels [47, 48] quantitatively. Understanding the tissue and cell mechanobiology [49] is not only crucial in cancer research [50–53], but elasticity governs the performance of soft biomaterials [54–56]. Beyond investigating static materials properties, AFM has recently become increasingly popular for studying dynamic processes.[57, 58] The advent of high-speed AFM imaging modes [59] supported this direction of method development. Another AFM-based technique to study dynamic processes is the picobalance, which gives quantitative access to cell mass changes in living cells with a resolution in the picogram range.[60]

AFM-based methods have undergone a steep evolution over the past four decades. However, driven by advancements and innovations in materials design and fabrication, there is still an ongoing need for innovation in analytical development. By developing and verifying novel AFM-based techniques, as well as improving existing ones, access is granted to so far inaccessible information on soft matter assembly and properties across different soft matter systems.

1.1 Objective and Structure

The objective of this thesis is *enhancing the AFM toolbox for investigating soft matter assembly and the resulting structure and physicochemical properties*. Four projects cover the entire range of developing AFM-based techniques for different kinds of soft matter. Soft matter in the form of nanoscale assembled biocolloids via hydrogel thin films to particulate hydrogels is the subject of this thesis. Figure 1.1 illustrates how AFM-based techniques are used to investigate the properties of interest, i.e., nanostructure, film thickness, nanomechanical properties, and assembly dynamics.

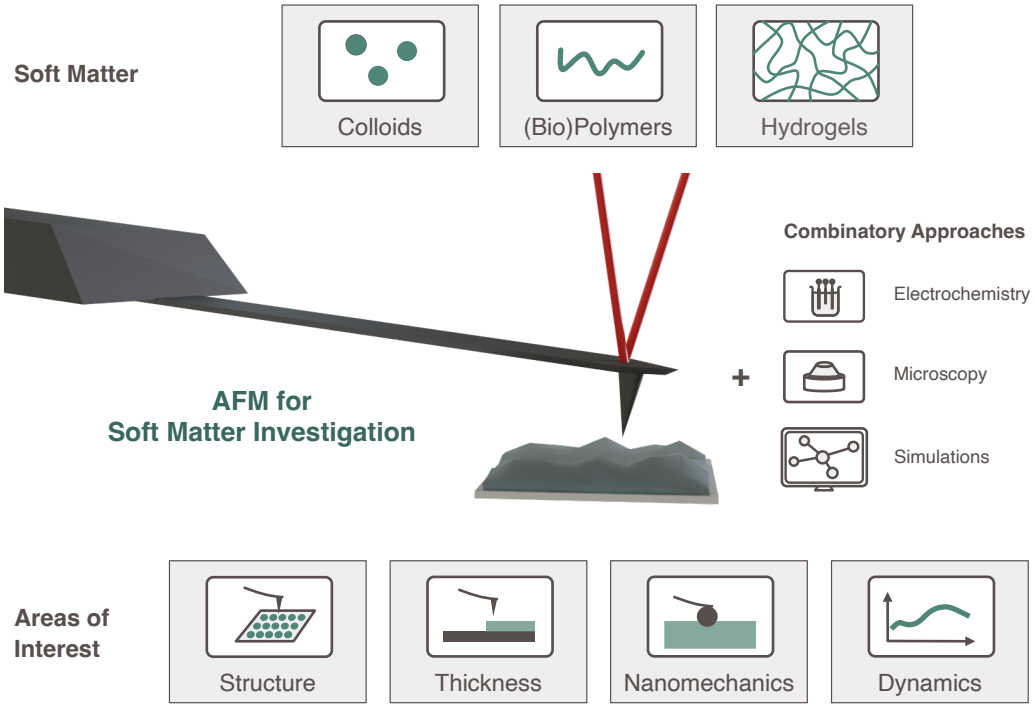

Figure 1.1. AFM for soft matter investigation. Areas of interest include soft matter nanostructure, film thickness, nanomechanical properties, and assembly dynamics.

The first part provides some theoretical fundamentals of atomic force microscopy and the basics of electrochemistry relevant for this thesis. In the second part, the experimental results on AFM method development for soft matter are presented across four subprojects.

The first project assembles nanocolloids and polyelectrolytes to form colloidal crystals in suspension. The hexagonal nanostructure suggested by SAXS is validated in real space by advanced AFM imaging in liquid for the first time. In the second project, smaller low molecular weight compounds are assembled into highly swollen supramolecular hydrogel films by electrogelation. The impact of the gelation parameters, time, potential, and concentration, is revealed by combining electrochemically controlled assembly of hydrogels with two AFM-based techniques to study the film thickness in the swollen and dried state. The third project introduces a new AFM tool by hyphenating the picobalance technique, an AFM-based mass balance, with electrochemistry. Custom-designed microelectrode cantilevers act as mass sensors to dynamically study mass transfer or changes under electric control. Finally, the last project addresses long-discussed questions of the cantilever choice, contact model, and instrumental parameters for AFM-based nanoindentation to study the elasticity of particulate soft matter.

References

(1) Nagel, S. R. *Rev. Mod. Phys.* **2017**, *89*(2), 025002.

(2) Barrat, J.-L.; Del Gado, E.; Egelhaaf, S. U., et al. *J. Phys. Mater.* **2024**, *7*(1), 012501.

(3) Vilanova, N.; Voets, I. K. In *Lecture Notes in Physics: Soft Matter at Aqueous Interfaces*; Springer International Publishing: Cham, 2016, pp 3–27.

(4) Kopeček, J.; Yang, J. *Angew. Chem. Int. Ed.* **2012**, *51*(30), 7396–7417.

(5) De Loos, M.; Feringa, B. L.; van Esch, J. H. *Eur. J. Org. Chem.* **2005**, *2005*(17), 3615–3631.

(6) Huang, Y.; Wu, C.; Chen, J.; Tang, J. *Angew. Chem. Int. Ed.* **2024**, *63*(9), e202313885.

(7) Magri, A.; Petriccione, M.; Cerqueira, M.; Gutiérrez, T. *Adv. Colloid Interface Sci.* **2020**, *285*, 102279.

(8) Mendes, A.; Baran, E.; Reis, R.; Azevedo, H. *Interdiscip. Rev. Nanomed. Nanobiotechnol.* **2013**, *5*(6), 582–612.

(9) Sinha, N.; Langenstein, M.; Pochan, D.; Kloxin, C.; Saven, J. *Chem. Rev.* **2021**, *121*(22), 13915–13935.

(10) Maibaum, L.; Dinner, A. R.; Chandler, D. *J. Phys. Chem. B* **2004**, *108*(21), 6778–6781.

(11) Baldwin, R. *J. Mol. Biol.* **2007**, *371*(2), 283–301.

(12) Wang, S.; Urban, M. W. *Nat. Rev. Mater.* **2020**, *5*(8), 562–583.

(13) Rivera-Tarazona, L.; Campbell, Z.; Ware, T. *Soft Matter* **2021**, *17*(4), 785–809.

(14) Hamley, I. *Angew. Chem. Int. Ed.* **2003**, *42*(15), 1692–1712.

(15) *Soft Matter Nanotechnology*; Chen, X., Fuchs, H., Eds.; Wiley: 2015.

(16) *Soft Matter for Biomedical Applications*; Azevedo, H. S., Mano, J. F., Borges, J., Eds.; The Royal Society of Chemistry: 2021.

(17) Li, M.; Pal, A.; Aghakhani, A.; Pena-Francesch, A.; Sitti, M. *Nat. Rev. Mater.* **2022**, *7*, 235–249.

(18) Apsite, I.; Salehi, S.; Ionov, L. *Chem. Rev.* **2022**, *122*(1), 1349–1415.

(19) Majidi, C. *Adv. Mater. Technol.* **2019**, *4*(2), 1800477.

(20) *Neutrons, X-rays, and Light: Scattering Methods Applied to Soft Condensed Matter*; Lindner, P., Oberdisse, J., Eds.; Elsevier: 2025.

(21) Stribeck, N., *X-Ray Scattering of Soft Matter*; Springer: Berlin, Heidelberg, 2007.

(22) Liu, D.; Song, K.; Chen, W., et al. *Nuclear Anal.* **2022**, *1*(2), 100011.

(23) Mittal, V.; Matsko, N. B., *Analytical Imaging Techniques for Soft Matter Characterization*; Springer: Berlin, Heidelberg, 2012.

(24) Lee, T.; Senyuk, B.; Trivedi, R. P.; Smalyukh, I. I. In *Fluids, Colloids and Soft Materials: An Introduction to Soft Matter Physics*; John Wiley & Sons, Inc: Hoboken, NJ, USA, 2016, pp 165–186.

(25) Franken, L.; Grünewald, K.; Boekema, E.; Stuart, M. *Small* **2020**, *16*(14), e1906198.

(26) Tsukruk, V. V.; Singamaneni, S., *Scanning Probe Microscopy of Soft Matter*; Wiley: Weinheim, 2011.

(27) Butt, H.-J.; Cappella, B.; Kappl, M. *Surf. Sci. Rep.* **2005**, *59*(1-6), 1–152.

(28) Binnig, G.; Quate, C.; Gerber, C. *Phys. Rev. Lett.* **1986**, *56*(9), 930–933.

(29) Voigtländer, B., *Scanning Probe Microscopy*; Springer: Berlin, Heidelberg, 2015.

(30) Bian, K.; Gerber, C.; Heinrich, A. J., et al. *Nat. Rev. Methods Primers* **2021**, *1*(1), 36.

(31) Hansma, H.; Vesenka, J.; Siegerist, C., et al. *Science* **1992**, *256*(5060), 1180–1184.

(32) Dufrêne, Y.; Ando, T.; Garcia, R., et al. *Nat. Nanotechnol.* **2017**, *12*(4), 295–307.

(33) Joshua, A.; Cheng, G.; Lau, E. *Appl. Surf. Sci. Adv.* **2023**, *17*, 100448.

(34) Uzüm, C.; Hellwig, J.; Madaboosi, N.; Volodkin, D.; von Klitzing, R. *Beilstein J. Nanotechnol.* **2012**, *3*, 778–788.

(35) Sommer, C.; Bargel, H.; Raßmann, N.; Scheibel, T. *MRS Commun.* **2021**, *11*(3), 356–362.

(36) Lobo, R. F. M.; Pereira-da-Silva, M. A.; Raposo, M., et al. *Nanotechnology* **1999**, *10*(4), 389–393.

(37) Hong, X.; Gan, Y.; Wang, Y. *Surf. Interface Anal.* **2011**, *43*(10), 1299–1303.

(38) Garcia, R. *Chem. Soc. Rev.* **2020**, *49*(16), 5850–5884.

(39) Wenderott, J.; Flesher, C.; Baker, N., et al. *Sci. Rep.* **2020**, *10*(1), 20423.

(40) Cho, D.; Aguayo, S.; Cartagena-Rivera, A. *Biomaterials* **2023**, *303*, 122389.

(41) Dokukin, M.; Guz, N.; Sokolov, I. *Biophys. J.* **2013**, *104*(10), 2123–2131.

(42) Ding, Y.; Xu, G.; Wang, G. *Sci. Rep.* **2017**, *7*, 45575.

(43) Viljoen, A.; Mathelié-Guinlet, M.; Ray, A., et al. *Nat. Rev. Methods Primers* **2021**, *1*(1), 63.

(44) Miyake, K.; Satomi, N.; Sasaki, S. *Appl. Phys. Lett.* **2006**, *89*(3), 031925–031921.

(45) Mokhtari, A.; Tala-Ighil, N.; Masmoudi, Y. A. *J. Mater. Eng. Perform.* **2022**, *31*(4), 2715–2722.

(46) Domke, J.; Radmacher, M. *Langmuir* **1998**, *14*(12), 3320–3325.

(47) Girardo, S.; Träber, N.; Wagner, K., et al. *J. Mater. Chem. B* **2018**, *6*(39), 6245–6261.

(48) Kim, E.; Lee, H. *J. Pol. Sci.* **2022**, *60*(11), 1670–1699.

(49) Krieg, M.; Fläschner, G.; Alsteens, D., et al. *Nat. Rev. Phys.* **2019**, *1*, 41–57.

(50) Deng, X.; Xiong, F.; Li, X., et al. *J. Nanobiotechnol.* **2018**, *16*(1), 102.

(51) Kwon, S.; Yang, W.; Moon, D.; Kim, K. *J. Cancer* **2020**, *11*(18), 5403–5412.

(52) Radman, B.; Alhameed, A.; Shu, G.; Yin, G.; Wang, M. *J. Mater. Chem. B* **2024**, *12*(22), 5299–5324.

(53) Zemla, J.; Danilkiewicz, J.; Orzechowska, B., et al. *Semin. Cell. Dev. Biol.* **2018**, *73*, 115–124.

(54) Kilpatrick, J.; Revenko, I.; Rodriguez, B. *Adv. Healthc. Mater.* **2015**, *4*(16), 2456–2474.

(55) Variola, F. *Phys. Chem. Chem. Phys.* **2015**, *17*(5), 2950–2959.

(56) Xu, D.; Harvey, T.; Begiristain, E., et al. *J. Mech. Behav. Biomed. Mater.* **2022**, *133*, 105329.

(57) Nievergelt, A.; Banterle, N.; Andany, S.; Gönczy, P.; Fantner, G. *Nat. Nanotechnol.* **2018**, *13*(8), 696–701.

(58) Fukuda, S.; Ando, T. *Rev. Sci. Instrum.* **2021**, *92*(3), 033705.

(59) Ando, T. *Biophys. Rev.* **2018**, *10*(2), 285–292.

(60) Martínez-Martín, D.; Fläschner, G.; Gaub, B., et al. *Nature* **2017**, *550*(7677), 500–505.

Theoretical Background

2

This thesis revolves around developing, implementing, and applying advanced surface analytical techniques, which will be introduced throughout the following sections. The first part focuses on atomic force microscopy (AFM), the central instrumental technique for all projects. AFM-based force spectroscopy, nanoindentation, and mass measurements will be introduced. Finally, electrochemical techniques with relevance for this thesis and with particular attention to combinatory approaches with AFM and quartz crystal microbalance (QCM) are introduced.

2.1 Atomic Force Microscopy

The atomic force microscope belongs to the scanning probe microscopes (SPM) family.[1] Binnig and Rohrer developed the first SPM, the scanning tunneling microscope (STM) [2], in 1981, for which they were awarded the Nobel Prize in Physics in 1986 [3]. The principle of the STM is based on quantum tunneling and enables unprecedented insights into the structure of condensed matter. Recording the tunneling current while lateral scanning of the sample surface creates a topographic image up to atomic resolution.[2, 4] However, measuring a tunneling current requires (semi-)conductive tips and samples, which limits its range of application. In 1986, Binnig, Quate, and Gerber invented another member of the SPM family derived from the STM: the atomic force microscope (AFM).[5] Like in STM, the AFM uses a sharp tip to probe the interaction with the sample surface. However, the previous limitation of conductive tips (and samples) is overcome as the AFM employs a cantilever to sense interaction forces instead of measuring a tunneling current.[1] Thus, the AFM is more widely applicable, including operation in vacuum, air, and liquid, as well as under physiological conditions with environmental control.[6–9] Due to its versatility and capability to precisely sense forces and manipulate objects on the nanoscale, the AFM is valued in an impressive variety of fields ranging from the characterization of defects in battery materials [10], semiconductor industry [11], nanotechnology [12], to the investigation of biomaterials [13] or living cells in life science and biomedicine [14, 15]. Due to its broad applicability and operation under varied conditions, AFM plays a crucial role in soft matter research [16, 17].

2.1.1 Fundamentals of Atomic Force Microscopy

Instrumentally, an AFM setup can be roughly divided into the scan head and stage, forming the operational part, and the AFM controller, responsible for signal control and processing (cf. Figure 2.1). The central piece of any AFM is a microfabricated cantilever, which bends due to the forces acting between the cantilever and the sample. Such forces can, among others, include electrostatic [18, 19], van-der-Waals [20], or steric forces [21]. An AFM senses forces as small as piconewtons, which allows tracking, *e.g.*, the unfolding of proteins [22, 23] and enables atomic resolution [24]. Sample sizes up to 100 µm in x- and y-directions facilitate large-scale investigation of materials or tissues [25]. Recently, combinatory approaches have enabled further extension of the maximal scan area without sacrificing lateral resolution.[26]

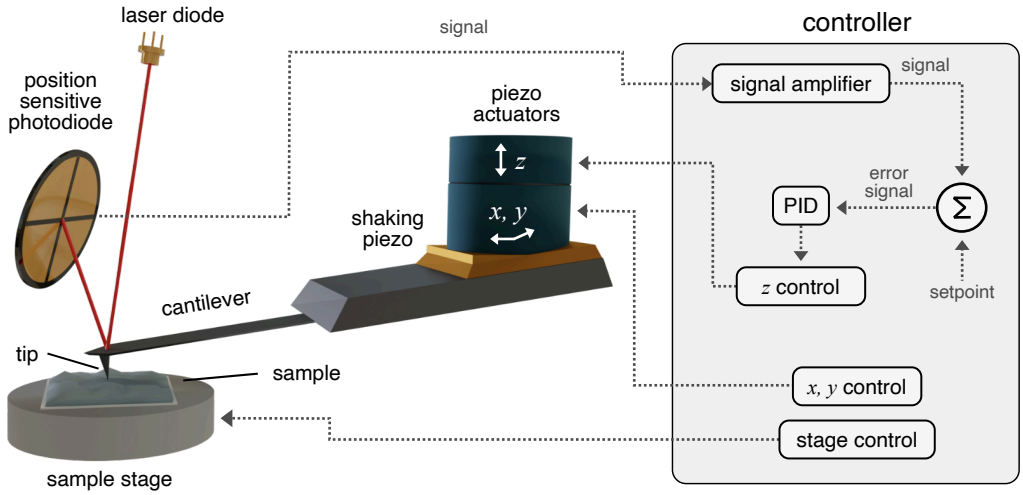

Figure 2.1. Schematic of an AFM setup. A microfabricated cantilever interacts with a sample. A laser is focused on the backside of its free end and reflected to a position-sensitive photodiode. Deflection of the cantilever results in a changed photodiode signal. Piezo actuators facilitate lateral (x, y) and vertical (z) movement of the cantilever. The AFM controller comprises a proportional-integral-differential (PID) feedback loop to control the z-movement based on the signal readout of the photodiode.

The cantilever beam, fixed at one end to a chip, is mounted to the scan head. Its free end, often equipped with a sharp tip, bends upon interaction with the sample. The most common approach to read out the cantilever deflection is the optical lever technique (OLT).[27] For this technique, a laser beam is focused on the backside of the cantilever, and the position-sensitive four-quadrant photodiode then monitors the reflected beam.[9, 27] Piezoelectric actuators move the AFM cantilever laterally (x, y) and vertically (z) with sub-nanometer precision. The sample stage holds the sample and, in some cases, allows for lateral and vertical movement on length scales beyond the

extension limit of the piezoelectric actuators or alignment with optional components like an inverted optical microscope. In sample scanner AFMs, the sample stage contains the x- and y-piezo-scanner rather than the scan head, facilitating tip movement in all three dimensions.[1, 28, 29]

Optical Lever Technique

The most commonly used technique to detect the cantilever deflection in AFM setups is the beam deflection or optical lever technique (OLT), illustrated in Figure 2.2. A laser diode emits a beam which is focused on the free end of the cantilever, where it reflects to a position-sensitive diode (PSD).[27]

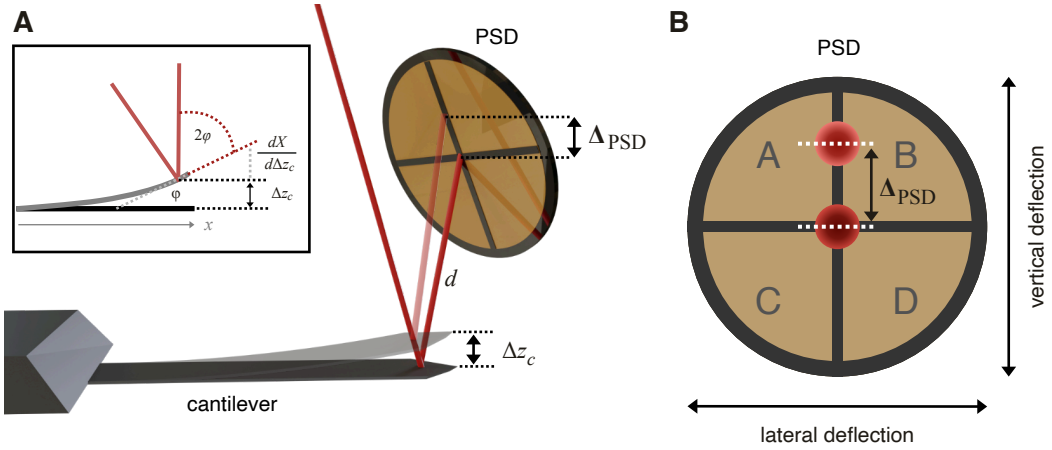

Figure 2.2. The cantilever deflection is monitored by the optical lever technique (OLT). **A** A laser beam is reflected on the backside of the cantilever to a position-sensitive photodiode (PSD). When exposed to a force, the bending cantilever changes the reflection angle, resulting in a position change of the reflected beam on the PSD Δ_{PSD}. The inset illustrates how bending the cantilever by an angle φ changes the reflected laser beam by 2φ. **B** Changes in the position of the beam on the position-sensitive photodiode cause a deflection signal Δ_{PSD} in volts.

The PSD consists of four quadrants (named A-D in Figure 2.2B). When an external force is exerted on the cantilever, its free end is displaced. The bending angle φ is defined by the cantilever slope at its free end by Eq. 2.1.[1, 28]

$$\varphi = \frac{d\Delta z_c}{dX} \tag{2.1}$$

If the cantilever deflects by Δz_c with a bending angle φ, a change in Δ_{PSD} is detected on the PSD due to the angular movement of the reflected laser beam. According to Eq.

2.2 the cantilever deflection is proportional to the deflection signal on the PSD Δ_{PSD} positioned at a distance d from the cantilever.[1, 28]

$$\Delta_{\mathrm{PSD}} = 2 \tan \varphi \cdot d \tag{2.2}$$

The vertical deflection signal Δ_{PSD} is defined by the intensity quotient of the upper half of the PSD and the lower half (Eq. 2.3). In contrast, the intensity ratio of the right and left halves of the PSD yields the lateral deflection (Eq. 2.4).[1, 28]

$$\Delta_{\mathrm{PSD}} = \frac{A+B}{C+D} \tag{2.3}$$

$$\Delta_{\mathrm{PSD}}(\mathrm{lateral}) = \frac{A+C}{B+D} \tag{2.4}$$

Consequently, when the laser beam is centered on the PSD, the lateral and vertical deflection signals equal 0. The deflection signal is typically normalized to the total signal intensity of the photodiode to account for temporal fluctuations in the beam intensity.[1, 28] Apart from the beam deflection technique, other approaches based on interferometry or piezoresistance exist [1] but are less common and were not relevant to this work.

Tip Shape and Colloidal Probes

The heartpiece of the AFM is the microfabricated cantilever, which senses the interaction forces with a sample. The most well-known cantilevers are equipped with a sharp tip at their free end (cf. Figure 2.3A). Sharp tip cantilevers provide a high lateral resolution, which is crucial when studying the topography of a sample by laterally scanning the tip across the sample's surface. The contact area of a sharp tip is defined by its tip radius (typically $r < 5 - 10$ nm). Single-molecule force spectroscopy uses sharp tip cantilevers to probe the interaction of single molecules. Due to the small dimensions of the sharp tip, ideally, only one chain attaches.[22]

Sharp tips are prone to deformation and abrasion when in physical contact with the sample. Thus, their interaction geometry can change throughout AFM experiments. However, precise information on the tip geometry is required for a quantitative relation of the interaction forces measured by AFM to theory.

Butt et al. [30] and Ducker et al. [31] overcame this limitation by attaching µm-sized colloidal microspheres to the free end of AFM cantilevers instead of the sharp tips. A SEM image of a so-called colloidal probe made from a SiO_2 microsphere with a diameter of $d \approx 6.8$ µm is depicted in Figure 2.3B. The spherical shape allows quantifying interaction forces, e.g., using the Derjaguin approximation [32], which relates the interaction energy of two arbitrarily shaped objects to two planar surfaces. In general, larger forces are

sensed due to the increased interaction area with colloidal probes compared to sharp tip cantilevers, which enhances the overall force resolution.[28]

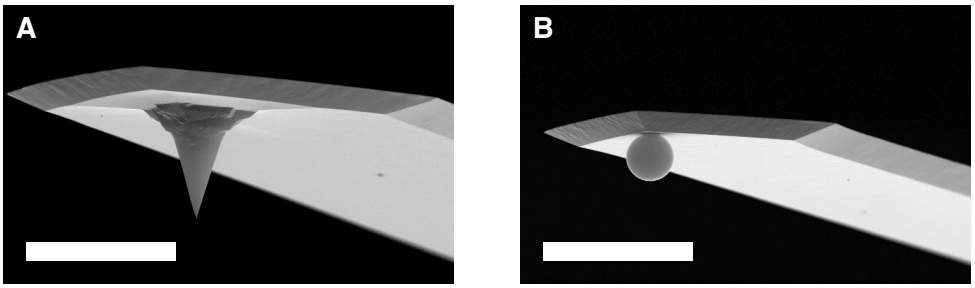

Figure 2.3. Different types of cantilevers used in AFM experiment: SEM images of a **A** sharp tip cantilever and a **B** spherical SiO_2 colloidal probe. The scale bars are 25 µm.

Depending on the desired application, colloids made from various inorganic [30, 31] and polymeric [33] materials and surface modifications [34, 35] can be employed to study the interaction forces with other colloidal objects or surfaces. Later, this approach has been extended beyond spherical inorganic colloids to study fibers [36–38], rod-shaped colloids [39] or soft particles [40–42]. The FluidFM technology [43] increased the flexibility of the colloidal probe technique as reversible aspiration [44] rather than irreversible gluing [30, 31] or sintering [45] allows quick a exchange of the probe upon contamination and studying a statistically relevant number of particles with a single cantilever [19, 44, 46, 47]. However, the classical colloidal probe approach remains the standard technique, and numerous fabrication strategies for colloidal probes used in a wide range of AFM-based force interaction studies exist.[48, 49]

In the context of AFM-based nanoindentation, sharp tips and spherical non-deformable colloidal probes are the primarily used tip shapes.[50] Sharp tips are valued for studying local variations in stiffness on living cells and tissues. Meanwhile, spherical colloidal probes provide a defined geometry on bulk materials. Section 2.1.3 introduces theoretical models for the indentation with sharp tips and spherical colloids, and Chapter 7 corroborates the impact of tip shape on nanoindentation for µm-sized hydrogel particles.

Topographic Imaging

Scanning the AFM tip laterally, i.e., in x- and y-direction across a sample, yields a topographic image. A feedback loop (cf. Figure 2.1) ensures proper tracking of the sample's topography by adjusting the tip position in the z-direction. In the simplest case, in contact mode, the cantilever tip is in permanent contact with the sample.[51] Its deflection is used as the feedback parameter, and the z-piezo position is adjusted to maintain a constant deflection of the cantilever. Permanent mechanical contact of the

cantilever induces static and frictional forces during scanning, which can harm the sample and abrade the tip.[52] To overcome the limitations of the contact mode, intermittent contact imaging modes have been developed. The first step was the introduction of the alternating current (AC) or tapping mode by Zhong et al.[53]. In AC mode, the cantilever is driven to oscillation close to its resonance frequency using a shaking piezo. The oscillation is damped near the surface, resulting in intermittent tip-sample contact. The degree of damping is used as the feedback parameter for tracing the topography. Qualitative contrast in the phase shift between the excitation and the cantilever response can be observed, but there is no direct control or readout of the forces involved. Meanwhile, AC mode enables fast scanning at low lateral forces in air; imaging in liquid surroundings, however, is less straightforward. Stronger damping of the oscillation amplitude, paired with excitation of the surrounding liquid in addition to the cantilever, results in much broader and often unclear resonance peaks.[54] Photothermal excitation [55, 56] or using an entirely different imaging mode altogether, e.g., off-resonant modes [57] or the pulsed force mode [58], are possible alternatives. Nowadays, several commercial modes like PeakForce Tapping [59], Qi [60], or the wave mode [61] are implemented into state-of-the-art AFMs. These modes offer direct control over the acting forces, i.e., by applying an adequate setpoint. Additionally, information about adhesive and electric or elastic properties can be extracted for every pixel of the topographic image.[62–64]

2.1.2 Sensing Forces Using a Cantilever

Cantilevers can be described as springs deflected by external force. They serve as force sensors in an AFM measurement. For the limitation of small deflections, cantilevers follow Hooke's law (Eq. 2.5), which means their deflection Δz_c is proportional to the force F, with the spring constant k_c being the proportionality factor.[28, 29]

$$F = k_c \Delta z_c \tag{2.5}$$

The condition of small deflections is met for typical deflections Δz_c in the nanometer range compared to the cantilever length, ranging from a few tens to a few hundred micrometers. However, the AFM does not directly measure the forces acting on the cantilever. Instead, the cantilever deflection is measured and converted to a force by several conversion and calibration steps introduced in the following paragraphs. [28, 29]

Deflection Sensitivity of the Optical Detection System

Converting the cantilever deflection into a force requires the exact knowledge of the sensitivity of the optical detection system, often stated as its inverse value, InvOLS (inverse optical lever sensitivity), for convenience. Experimentally, the InvOLS is determined by ramping the cantilever against a non-deformable substrate and evaluating the slope in the constant compliance region. On a non-deformable sample, the cantilever deflection and the resulting signal at the PSD are directly proportional to the z-piezo movement. Multiplying the PSD signal with the InvOLS yields the cantilever deflection in metres, which is related to the force by the stiffness of the cantilever spring in Eq. 2.6, its spring constant k_c.[28]

$$F = \Delta_{PSD} \cdot \text{InvOLS} \cdot k_c \tag{2.6}$$

Spring Constants of Cantilevers

Generally, the geometry (thickness t_c, width w_c, and length L_c) and the Young's Modulus of the cantilever material E_c, typically silicon or silicon nitride, define the spring constant k_c of a cantilever (Eq. 2.7).[28]

$$k_c = \frac{F}{\Delta z_c} = \frac{E_c w_c t_c^3}{4 L_c^3} \tag{2.7}$$

However, the theoretical calculation of the spring constant can only provide a rough estimation; deviations of calculated values compared to experimentally calibrated spring constants can be significant.[28, 65, 66] The spring constant depends on the third power of the thickness (Eq. 2.7). Thus, small errors in the cantilever thickness t_c result in significant deviations in k_c. However, the thickness is the least defined dimension during the etching process for cantilever fabrication. Moreover, the theoretical calculation does not account for coatings, such as reflective backside coatings, to increase the sensitivity or a conductive layer surrounding the cantilever.[67] Lastly, the thin-film elasticity of silicon cantilevers has been shown to differ significantly from the bulk properties [68], which results in another potential error source. However, knowing the cantilever's spring constant with high precision is inevitable for quantifying interaction forces. Hence, the spring constant has to be calibrated experimentally for each cantilever [28], and several sources in the literature compared the accuracy and applicability of different calibration techniques [69–71] including an international cross-laboratory round robin [72]. In the following, three well-established techniques [65, 73–75], which are widely used in the literature and throughout this thesis, are introduced.

In general, thermal fluctuations in the environment excite the cantilever and are acquired as a power density spectrum (PDS) (cf. Figure 2.4). The full spectrum comprises several peaks, the fundamental resonance frequency (visible in Figure 2.4), and higher modes of the cantilever oscillation (outside of the depicted frequency window in Figure 2.4), respectively. Depending on the calibration method, the resonance peak's frequency and quality factor, or the peak integral, are extracted from the PDS to calculate the spring constant.[28]

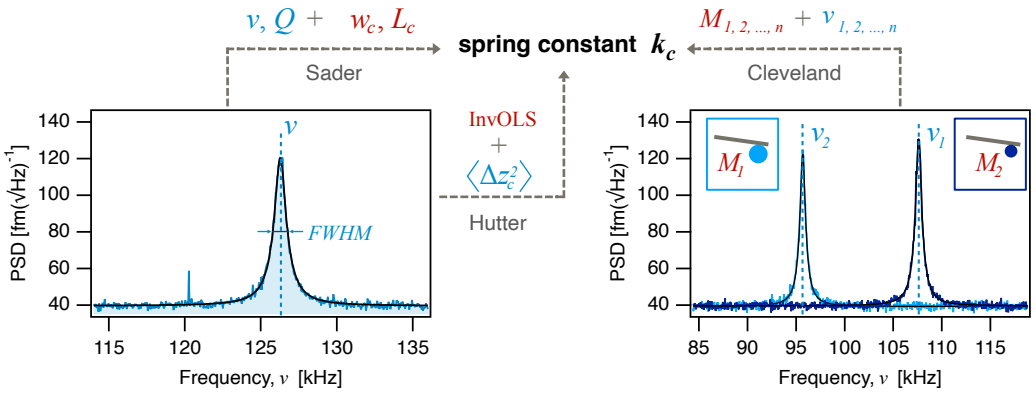

Figure 2.4. Calibration of AFM cantilevers. Power spectral density (PSD) of an NSC35 type cantilever excited by thermal fluctuations (blue), single harmonic oscillator fit of the fundamental resonance frequency ν (black). Different measures of the resonance peak are used to determine the spring constant depending on the chosen method: (i) resonance frequency ν and quality factor Q of the fundamental resonance [65, 73]; (ii) mean square deflection amplitude $\langle \Delta z_c^2 \rangle$ [75]; (iii) fundamental resonance frequencies $\nu_{1,2,\ldots,n}$ with added masses $M_{1,2,\ldots,n}$ [74].

Sader [65, 73] introduced a method that determines the spring constant based on the top-view dimensions of the cantilever and its thermal noise spectrum. The spring constant calculation (Eq. 2.8) takes the quality factor $Q = \frac{FWHM}{\nu}$ ($FWMH$: full width at half maximum), the resonance frequency ν, the density of the surrounding medium ρ, and the imaginary part of the hydrodynamic function $\Gamma_i(Re)$ into account. $\Gamma_i(Re)$ denotes the viscosity of the surrounding medium.

$$k_c = 0.1906 \rho w_c^2 L_c Q \Gamma_i(Re) (2\pi \nu_0)^2 \tag{2.8}$$

Hutter and Bechhoefer [75] modeled the cantilever as a harmonic oscillator, which assigns a kinetic energy of $\frac{1}{2} k_B T$ per vibration mode for the oscillation of the cantilever according to the equipartition theorem. In practice, the mean square deflection amplitude $\langle \Delta z_c^2 \rangle$ is extracted from a Lorentzian fit to the fundamental resonance in the thermal noise spectrum. This approach neglects the contribution of higher oscillation modes,

which is accounted for by a correction factor.[76, 77] The spring constant k_c is calculated according to Eq. 2.10.

$$\frac{1}{2}k_c\langle\Delta z_c^2\rangle = \frac{1}{2}k_B T \tag{2.9}$$

$$k_c = \frac{k_B T}{\langle\Delta z_c^2\rangle} \tag{2.10}$$

The raw detector signal is converted into the power spectral density (PSD) using the InvOLS, the sensitivity of the laser detection system. The InvOLS is calibrated by ramping the cantilever against a non-deformable substrate and fitting the slope in the constant compliance regime of the deflection vs. z-piezo displacement curve.

Cleveland [74] proposed another simple and versatile approach to determine a cantilever's spring constant by attaching an external mass to the free end of the cantilever. The resonance frequency ν of the cantilever

$$\nu = \frac{1}{2\pi}\sqrt{\frac{k_c}{m^*}} \tag{2.11}$$

shifts to a smaller frequency ν_1 when a mass M_1 is attached:

$$\nu_1 = \frac{1}{2\pi}\sqrt{\frac{k_c}{m^* + M_1}}. \tag{2.12}$$

Knowing the attached masses ($M_{1,2,\ldots,n}$), the spring constant k_c can be calculated according to

$$k_c = \frac{4\pi^2(M_1 - M_2)}{\frac{1}{\nu_1^2} - \frac{1}{\nu_2^2}} \tag{2.13}$$

as the effective mass M of the cantilever remains unchanged. In practice, spherical particles with high densities, e.g., tungsten ($\rho_W = 19.25\ \mathrm{g\,m^{-3}}$), are picked up from a glass slide while recording the resulting frequency shift. The diameter of the microspheres is easily accessible by optical microscopy, which allows the calculation of the theoretical microsphere mass using the bulk density of the respective material.

By inverting this technique, colloidal objects can also be 'weighed,' provided the spring constant k_c is known.[78–80] Chapter 6 introduces a new approach to weigh masses in combination with electrodeposition, which uses the inverse added mass technique.

Direct Force Measurements

As the cantilever acts as a force sensor, ramping it perpendicularly to the sample surface yields a distance-dependent force profile.[28] Initially, a z-piezo displacement curve, as schematically depicted in Figure 2.5 is obtained. The deflection is converted to a force according to Eq. 2.6. The distance is given by the z-piezo displacement corrected for the cantilever deflection.

Any force profile comprises at least two segments: the approach of the cantilever towards the surface (red curve and arrows in Figure 2.5) and the retraction of the cantilever from the surface (blue curve and arrows in Figure 2.5). Additional segments, such as hold times or modulations in contact or away from the surface, can be implemented.

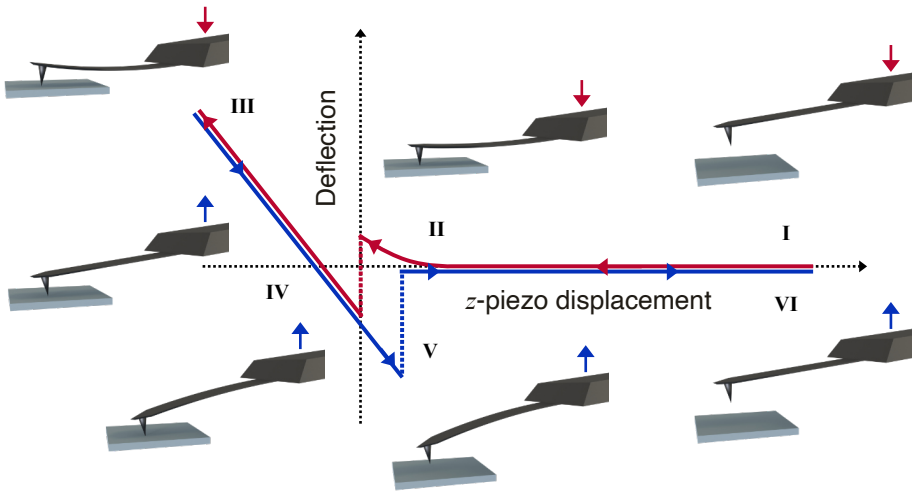

Figure 2.5. Exemplary force vs. z-piezo displacement curve. The approach of the cantilever is depicted in red; retraction from the surface is shown in blue. The insets illustrate the deflection of the cantilever in the respective part of the curve. **I** No forces are sensed if the cantilever is far from the surface. **II** In the vicinity of the surface, long-range forces (here depicted as repulsive) result in the bending of the cantilever away from the surface. The cantilever snaps into contact when the short-range attractive forces overcome the repulsive long-range interactions. **III** The cantilever is further approached until the setpoint value is reached and subsequently retracted. **IV** Upon retraction, the cantilever deflection decreases and inverses at some point. **V** The cantilever adheres to the surface until the bending forces overcome the attractive tip-sample interaction (adhesion) and the cantilever snaps out of contact. **VI** Finally, the cantilever returns to its equilibrium position without any forces acting.

Initially, the cantilever is far away from the surface, and no interaction forces are sensed **I**. Hence, the cantilever remains non-deflected in its equilibrium position. Moving the cantilever towards the sample surface, long-range interactions, such as electrostatic forces, act on the cantilever. In the depicted case of a repulsive interaction **II** the cantilever deflects away from the surface. Likewise, attractive interactions are possible and induce cantilever bending in the opposite direction towards the sample. Short-range

attractive forces like van der Waals interactions provoke a jump-to-contact near the sample surface. Further approaching deflects the cantilever as it is pushed against the surface. Given that the sample is non-deformable, the cantilever deflection equals the displacement of the z-piezo. In contrast, soft and deformable samples yield a non-linear contact regime (cf. Figure 2.6B). The cantilever is approached up to a predefined setpoint and subsequently retracted **III**. In the case of adhesive surfaces, the cantilever sticks to the surface and deflects towards the sample **IV**. A hysteresis is observed as the cantilever adheres to the sample longer than its initial contact when approaching the sample. When the restoring force of the cantilever exceeds the adhesive force, the cantilever jumps off contact **V**. Finally, the cantilever returns to its non-deflected equilibrium position **VI**.[28, 29]

2.1.3 Nanoindentation by Atomic Force Microscopy

Elastic bodies deform when an external force is applied to them. The Young's modulus describes a material's elasticity and defines how the body deforms under external mechanical stress. Consequently, applying defined forces to an elastic body allows one to determine its elasticity.[50]

AFM force spectroscopy is the method of choice for studying elastic properties on the nanoscale and especially for µm-sized objects. *E.g.* single cells or microgel particles can be characterized [15, 81–85] and tissue mechanics [14, 25, 86, 87] or elastic properties of polymeric or biomaterials can be investigated [88, 89]. The general principle of AFM-based nanoindentation relies on deforming the subject of interest by indenting it with a cantilever-based indenter. The resulting force vs. deformation relation is extracted from the nanoindentation experiment and fitted to a suitable continuum contact model to extract the elastic properties.

The indentation of a silica colloidal probe into a soft hydrogel particle is depicted schematically in Figure 2.6A, and an exemplary force vs. deformation curve is visible in Figure 2.6B. The forces increase gradually with the deformation of the soft bead when the cantilever is ramped towards it. In contrast, forces increase infinitely when the same colloidal probe is ramped against a rigid substrate, *e.g.* a glass slide (cf. blue curve in Figure 2.6B).

The simplest and earliest continuum contact model for contact mechanics was derived by Heinrich Hertz in 1881.[90] Hertz described a fully elastic contact between two elastic bodies, — here, a non-deformable silica microsphere and soft microgel bead — with the radii R_1 and R_2. Moreover, the model assumes the absence of any surface forces (*i.e.* adhesion, electrostatics, sterics, friction, etc.) and bodies consisting of homogeneous

materials (continuum model). Then, the force F is related to deformation δ of the microspheres by

$$F = \frac{4}{3}\sqrt{R_{12}}E_{12}\delta^{\frac{3}{2}} \tag{2.14}$$

with $\frac{1}{R_{12}} = \frac{1}{R_1} + \frac{1}{R_2}$ and $\frac{1}{E_{12}} = \frac{1-\nu_1^2}{E_1} + \frac{1-\nu_2^2}{E_2}$. ν_1 and ν_2 denote the Poisson ratio, E_{12} is the reduced Young's modulus, and R_{12} defines the reduced radius of the two bodies in contact.[90] In the context of a rigid indenter deforming a much softer material ($E_1 \gg E_2$), the relation of force and deformation simplifies to Eq. 2.15.

$$F = \frac{4}{3}\sqrt{R_{12}}\frac{E_2}{1-\nu_2^2}\delta^{\frac{3}{2}} \tag{2.15}$$

In the case of a spherical indenter, *e.g.*, a spherical colloidal probe indenting a bulk material $R_2 \to \infty$, the reduced radius equals the radius of the colloidal probe ($R_{12} = R_1$).

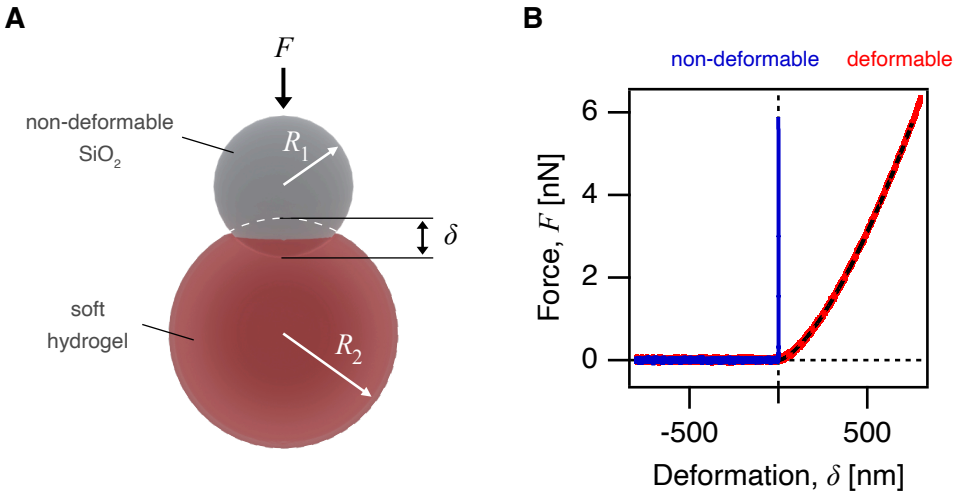

Figure 2.6. **A** Schematic of a non-deformable SiO_2 colloidal particle with the radius R_1 deforming a softer bead with R_2. **B** Force vs. deformation profile acquired on a non-deformable surface (glass, blue) and a soft sample (PAAm microgel $E < 10$ kPa red) probed with a colloidal probe. The dashed line represents a fit to the deformation data according to the classical Hertz model [90].

Sneddon [91] expanded the relation between force and deformation to an arbitrary indenter geometry. Eq. 2.16 defines the force-deformation relation for a conical indenter, where θ denotes the cone's half-angle.[91]

$$F = \frac{2}{\pi}\tan\theta\frac{E_2}{1-\nu_2^2}\delta^2 \tag{2.16}$$

The Hertz model considers the bodies in contact, independent of the surrounding medium. However, for an AFM indentation experiment, the spherical sample with the radius R_2 is placed onto a solid support. Hence, the overall interaction is more complex, and the description by the Hertz model becomes insufficient, especially for small R_2 and large ratios R_1/R_2.[83, 92, 93] Figure 2.7 contrasts both configurations. While only the indenter exerts a force F_{ind} onto the sample in the case of the Hertz model [90] (cf. Figure 2.7A), an additional force F_{sub} acts on the sample when placed on a planar non-deformable substrate. Double contact models account for the deformation at the indenter-sample contact δ_{12} and the substrate-sample contact δ_{32} (cf. Figure 2.7B).[82, 83, 92]

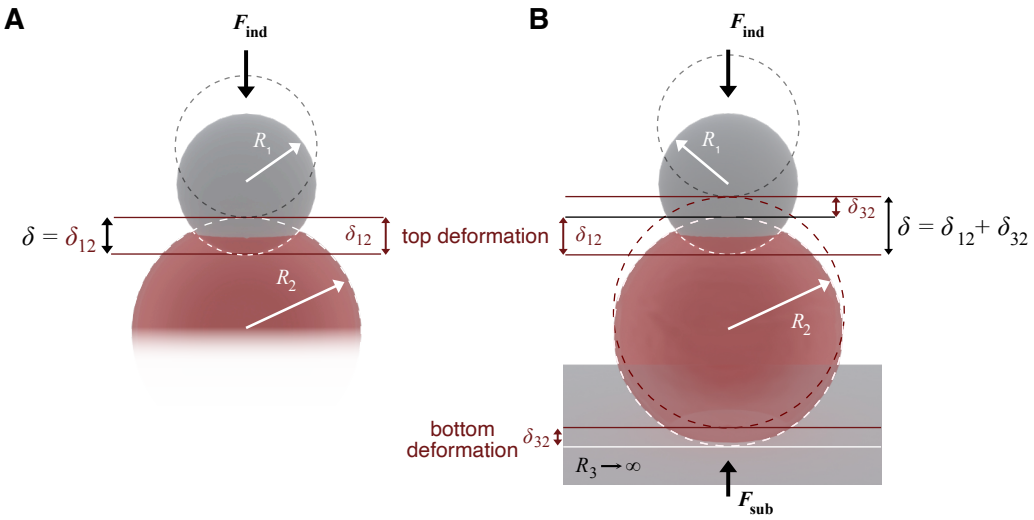

Figure 2.7. **A** The Hertz model [90] describes the contact of a spherical indenter with a spherical sample. Deformation only occurs at the indenter-sample contact ($\delta = \delta_{12}$) caused by the force F_{ind}. **B** The double contact model [83, 92] takes the deformation at the substrate sample contact δ_{32} into account. The total deformation δ is the sum of the deformation at the indenter contact δ_{12} and the deformation at contact with the substrate δ_{32}.

It is assumed that forces and the resulting deformation only act within the respective half-sphere and are independent of each other. Then, the total deformation δ is the sum of the top deformation δ_{12} caused by the indenter and bottom deformation δ_{32} induced by the substrate (cf. Figure 2.7). A correction factor k, which considers the reduced radii of the indenter-sample contact R_{12} and the substrate-sample contact R_{32}, expresses the deviation of the double-contact model from the classical Hertzian contact.

$$\delta = \delta_{12} + \delta_{32} = \left[\frac{3}{4}\frac{F(1-\nu_2^2)}{E_2\sqrt{R_{12}}}\right]^{\frac{2}{3}} + \left[\frac{3}{4}\frac{F(1-\nu_2^2)}{E_2\sqrt{R_{32}}}\right]^{\frac{2}{3}} \tag{2.17}$$

$$\delta = \left[\frac{3}{4}\frac{F(1-\nu_2^2)}{E_2\sqrt{R_{12}}}\right]^{\frac{2}{3}}\frac{1}{k} \text{ with } k = \frac{{R_{32}}^{\frac{1}{3}}}{{R_{32}}^{\frac{1}{3}} + {R_{12}}^{\frac{1}{3}}} \tag{2.18}$$

The force vs. deformation relation for a spherical indenter with the radius R_1 indenting a spherical sample with the radius R_2 on a planar substrate with $R_3 \rightarrow \infty$ is

$$F = \frac{4}{3}\sqrt{R_{12}}\frac{E_2}{1-\nu_2^2}\delta^{\frac{3}{2}}k^{\frac{3}{2}}. \tag{2.19}$$

While the force scales with $F \propto \delta^{\frac{3}{2}}$ similar to the Hertz model [90], the dimensions of the indenter and sample define the absolute forces at a given deformation [92].

The previous paragraphs discussed nanoindentation from the viewpoint of particulate soft matter. However, nanoindentation is also relevant to characterize the elastic properties of (thin) films or bulk materials, or larger biological samples like tissues.[14, 94, 95] Besides static force measurement, dynamic nanomechanical AFM modes are increasingly used to map local variation in stiffness.[96–99] However, as these aspects are not directly relevant to understanding the experiments conducted in this thesis, the interested reader is kindly referred to the standard books and reviews which cover the fundamentals of AFM-based nanoindentation and its application across various fields in greater detail.[14, 50, 95, 97, 100–104] These sources also cover adhesive continuum contact models, like Johnson-Kendall-Roberts (JKR) [105] or Derjaguin-Müller-Toporov (DMT) [106] and their unifying approach, the Maugis theory [107].

2.1.4 Picobalance

The previous sections explained how AFM cantilevers are commonly used to sense interaction forces. However, the application range of cantilevers can reach beyond: for instance, oscillating cantilevers have been used for biomolecular detection, to trace polymerization reactions [79] and detect small mass changes in the past.[78–80] In 2017, Martinez-Martin et al. [108] introduced an inertial picobalance, a cantilever-based mass balance integrated into an AFM. The mass detection is based on a resonator's, here the cantilever's, frequency shift when an external mass is attached. Since its invention, the picobalance has been used primarily in the biological context, i.e., for weighing entire living cells attached to an AFM cantilever. [108–112].

The central piece of the picobalance is a cantilever, to which a sample, i.e., a cell or a colloidal object, is attached. The cantilever is excited by an intensity-modulated laser operated by a function generator.[108] The excitation laser is focused close to the clamped end of the cantilever beam and locally heats the material. The resulting gradient induces a mechanical response, i.e., the modulated oscillation of the resonator.[56, 113,

114] Photothermal excitation is advantageous to conventional excitation by a shaking piezo in liquid as it excites only the cantilever and not the surrounding liquid. It generates clear resonance peaks with high amplitudes and Q factors.[113, 115] A second laser reads out the cantilever oscillation using the optical lever technique.[27] A lock-in amplifier extracts the cantilever oscillation's frequency and phase with respect to the modulation signal. A phase-locked-loop (PLL) maintains a constant phase shift (90°) between the excitation signal created by the function generator and the cantilever response by adjusting the excitation frequency accordingly. Thereby, the frequency is monitored over time, which is related to the attached mass (Eq. 2.22–2.24).[108] Simultaneous optical or fluorescence microscopy allows observation of the cantilever and sample throughout, which is mandatory to trace cell movement over the experiment.[108] Figure 2.8 displays the instrumental setup of the inertial picobalance and its working principle.

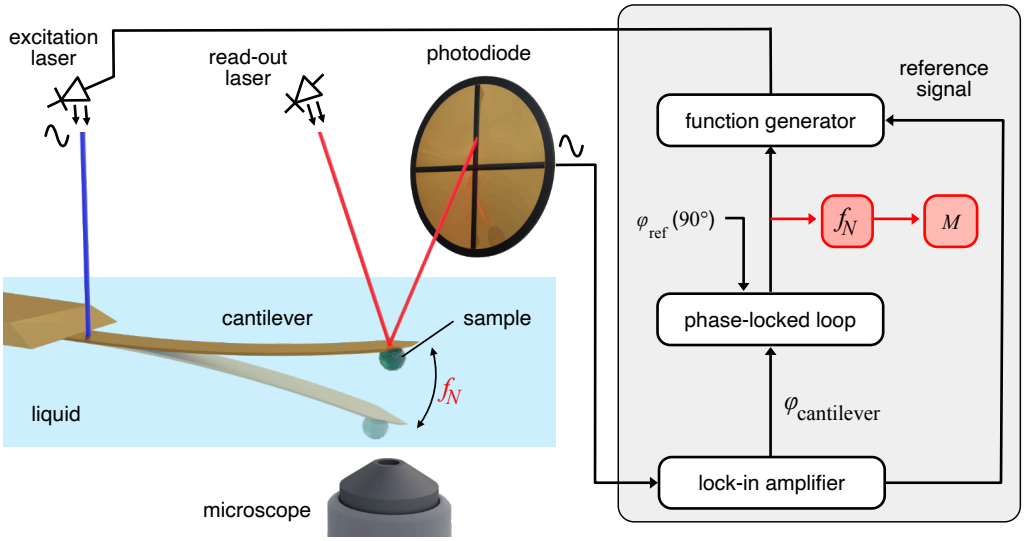

Figure 2.8. Schematic of the picobalance using a cantilever as a microscopic mass sensor in a liquid cell. The cantilever is driven photothermally by an intensity-modulated excitation laser close to its clamped end. A second laser reflects off the free end to a position-sensitive photodiode to read out the cantilever oscillation. The lock-in amplifier extracts the frequency and phase of the cantilever oscillation. A phase-locked-loop retains a constant phase shift of 90° with respect to the excitation signal by adjusting the excitation frequency at the function generator. The natural frequency of the microresonator f_N can be traced and converted into a mass. Optical or fluorescence microscopy enables optical control of the cantilever and the sample, e.g., the cell, throughout the experiment.

The cantilever's amplitude and phase response to the photothermal excitation are frequency dependent (cf. Fig. 2.9) and can be described by a driven, underdamped harmonic oscillator. The resonator's amplitude A is

$$A = a\frac{f_N^2}{\sqrt{(f_N^2 - f^2)^2 + \frac{f_N f}{Q_f}}} + a_1 f + a_2 \tag{2.20}$$

with the driving frequency f, the natural frequency f_N, and the quality factor $Q_f > 1$. a_1 and a_2 account for the excitation amplitude and higher mode oscillations. Similarly, the corresponding phase is described by Eq. 2.21.

$$\varphi = \arctan\left(\frac{Q_f(f_N^2 - f^2)}{f_N f}\right) + b_1 f + b_2. \tag{2.21}$$

b_1 and b_2 account for phase lags of the photothermal drive and electronics and the impact of higher oscillation modes, respectively.[78, 79]. The phase, i.e., the difference between the excitation signal and the cantilever's response, is 90° at the natural frequency f_N.

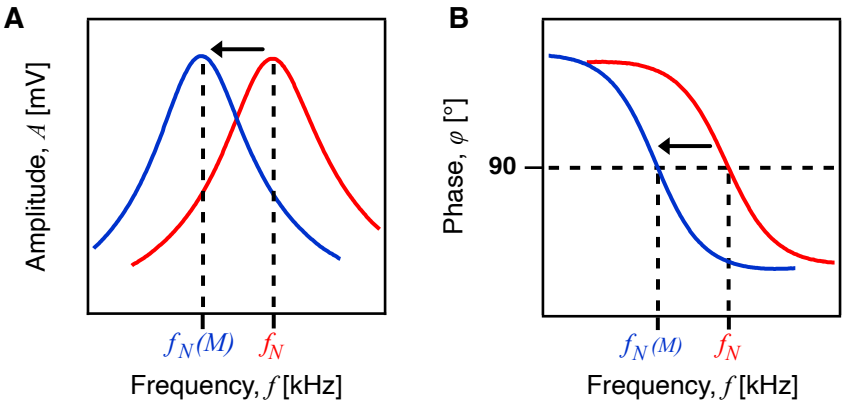

Figure 2.9. **A** Amplitude and **B** phase response of a photothermally driven cantilever without (red) and with (blue) added mass. The natural frequency f_N shifts to a lower frequency $f_N(M)$ when a mass M is attached to the cantilever. At f_N the phase, i.e., the difference between the excitation and the cantilever response, is 90°.

The natural frequency of the cantilever f_N depends on its effective mass m^* and the spring constant k_c. When a sample with the apparent mass M is attached (blue curves in Fig. 2.9), the frequency shifts to $f_N(M)$.

$$f_N(M) = \frac{1}{2\pi}\sqrt{\frac{k_c}{m^* + M}} \tag{2.22}$$

Subtracting the natural frequency f_N of the bare cantilever from the frequency $f_N(M)$ obtained after attaching the sample allows to determine the apparent sample mass.

$$M = \frac{k}{4\pi^2}\left[\frac{1}{(f_N - \Delta f_N)^2} - \frac{1}{{f_N}^2}\right], \tag{2.23}$$

A correction factor is used to compensate for the final position of the sample, e.g., the cell. The factor $\frac{1}{\psi^2(x_c)}$ accounts for the location of the mass on the cantilever when determining the sample mass m_{PB} from the apparent mass M (Eq. 2.24).[108, 116]

$$m_{PB} = M\frac{1}{\psi^2(x_c)} \tag{2.24}$$

ψ describes the oscillation amplitude and follows Eq. 2.25 for rectangular cantilevers

$$\psi(x) = \alpha\left[\sin(\xi x) - \sinh(\xi x) + \frac{(\sin(\xi L) + \sinh(\xi L))\,(\cosh(\xi x) - \cos(\xi x))}{\cosh(\xi L) + \cos(\xi L)}\right] \tag{2.25}$$

with $1 + \cos(\xi L)\cosh(\xi L) = 0$. The parameter α normalizes the oscillating amplitude to $\psi(L)^2 = 1$.[108]

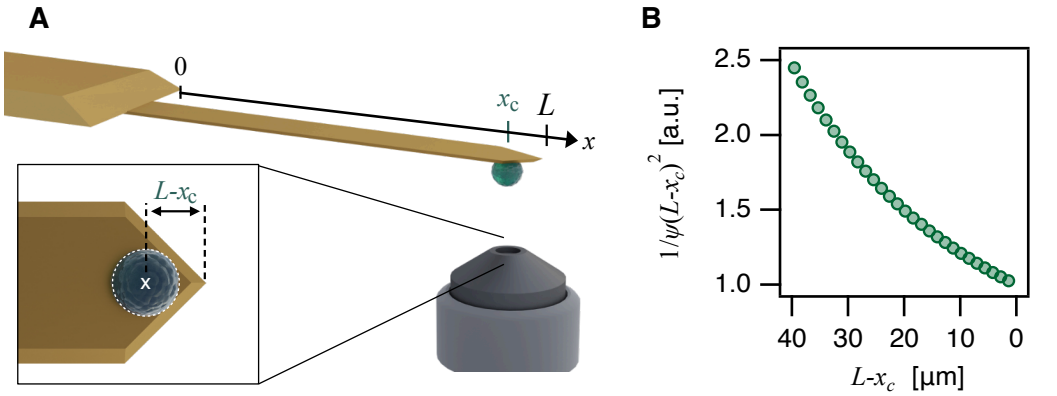

Figure 2.10. Evaluating the mass from a frequency shift in a picobalance experiment requires knowledge of the sample location on the cantilever. **A** The position of the mass x_c on the cantilever with respect to the length L can be assessed by optical microscopy. **B** A correction factor $\frac{1}{\psi^2(L-x_c)}$ depending on $L - x_c$ is required to convert the effective mass (cf. Eq. 2.24) and is plotted exemplarily for a cantilever with a length $L = 150$ µm.

Detecting small mass changes with the picobalance requires a high instrumental sensitivity and mass resolution. Instrumentally, the minimal detectable mass depends on the minimal detectable frequency shift, which is described by

$$\delta(\Delta f) = \sqrt{\frac{f_N k_B T B}{\pi k_c Q_f A^2}}. \tag{2.26}$$

k_B denotes the Boltzmann constant, T the temperature, spring constant k_c, f_N the natural frequency, Q quality factor and amplitude A of the oscillating cantilever. B refers to the measurement bandwidth related to the setup's time resolution.[108, 117, 118] Photothermal excitation allows for amplifying the cantilever amplitude while increasing the quality factor of the resonance at the same time.[113, 114] Capturing fast processes in situ requires optimizing the time resolution of the data acquisition. However, optimizing the accessible time scale requires a trade-off in mass resolution as Eq. 2.26 shows.[108] Finally, the mass sensitivity S_m, i.e. the frequency response Δf_N of the cantilever to an mass change ΔM

$$S_m = -\frac{\Delta f_N}{\Delta M} \cong \frac{2 f_N}{m^*} \tag{2.27}$$

governs which masses can be traced in a picobalance experiment.[80, 118, 119] A high-resonance cantilever, with small effective mass m^* is favorable. Decreasing the top-view dimensions leads to a smaller effective mass. Milling rectangular holes into the cantilever using a focused ion beam (FIB) and thereby decreasing m^* enhances the sensitivity further.[118]

2.2 Electrochemistry and Electrode Processes

Electrochemical processes occur at an electrode interface with the surrounding electrolyte solution.[120, 121] Hence, combining electrochemistry with interface analytical techniques allows the study of electrode processes directly at the interface and tracing electrochemical reactions in real time - examples include IR spectroscopy, X-ray scattering, ellipsometry, quartz crystal microbalance (QCM) and AFM.[122–129] In the following basic electrode processes and electroanalytical tools are briefly introduced. Additionally, a glance is thrown into instrumentation for electrochemistry in combination with AFM and QCM, which is relevant to this thesis.

2.2.1 Electrochemical Instrumentation

An electrochemical cell requires at least two electrodes: the working electrode (WE) at which the electrochemical process of interest takes place, and a counter electrode to close the electric circuit.[120, 121] However, redox processes occurring at the electrode interface can alter its properties. Consequently, the half-cell potentials may change significantly over time, resulting in undesired side effects in electrochemical experiments. Thus, a third electrode is commonly used in electroanalysis to overcome these potential error sources (cf. Figure 2.11). A potentiostat controls the potential at the working

electrode (WE) with respect to a reference electrode (RE). A voltmeter measures the potential difference, and a high-ohmic resistance prevents current flow through the RE. Consequently, its half-cell potential remains unchanged throughout the measurement, forming a reliable potential reference.[120, 121] Commonly, metal salt electrodes enclosed in metal salt solution and separated by a salt bridge from the analyte electrolyte, such as silver/silver chloride (Ag|AgCl|KCl) or saturated calomel electrode SCE ($Hg|HgCl_2|KCl$), are utilized.[120, 121, 130] An ampere meter measures the current flow between the WE and the CE. The CE should ideally be nonpolarizable so that the total potential change corresponds to the change in the potential of the WE. Noble metals like platinum are commonly used as inert CE materials to reduce the risk of contamination through electrochemical degradation, e.g., the release of metal ions into the analyte solution.[120, 121]

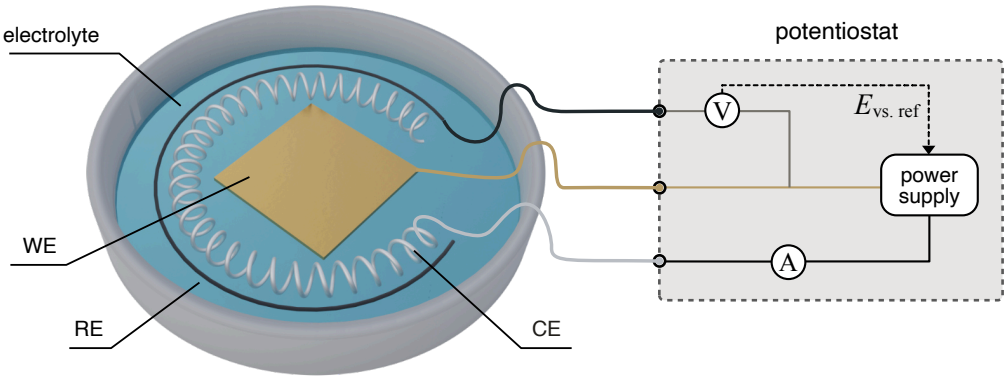

Figure 2.11. Electrochemical cell with a three-electrode configuration. A potentiostat controls the potential of the working electrode (WE). The potential is referenced to a reference electrode (RE) connected via a high-ohmic resistance. The potentiostat adjusts the current flow through the counter electrode to keep the working electrode at a constant potential as set externally. A noble metal counter electrode (CE) completes the electric circuit.

Electrode setups can also be implemented directly into AFM setups to study interfacial electrode processes.[131, 132] For instance, a conductive substrate can be used as a macroscopic WE and probed by AFM.[18, 131] Integrating the WE onto the cantilever enables studying electrode processes directly or manipulating colloidal objects.[64, 132, 133] Scanning electrochemical microscopy is an AFM technique that entirely relies on cantilever-integrated nanoelectrodes.[129, 134–136]

In AFM electrochemical cells, a pseudo RE, e.g., a chlorinated silver wire, is commonly employed due to its simple handling and small dimensions.[18, 131, 132] However, pseudo REs, in contrast to true reference electrodes, only approximate thermal equilibrium and depend on the ion concentration (e.g. Cl^- for a chlorinated Ag-wire) according to the Nernst equation (Eq. 2.29). Thus, drift during the experiment cannot be excluded

entirely, and their potential cannot be calculated. Hence, pseudo-REs require calibration with a known redox couple (e.g., ferrocene, cyanidoferrate) added to the analyte solution or by comparing the electrode's potential to a true reference electrode.[137] The latter approach has been employed to verify the pseudo RE potential throughout the experiments presented in Chapters 5 and 6.

2.2.2 Electrode Processes

Two processes typically occur at an electrode interface: (i) Faradaic processes are characterized by a charge transfer at the electrode, e.g., by chemical redox reactions, including metal deposition or dissolution. The electron flux through the electrode can be analyzed and is referred to as faradaic current I_{faraday}. (ii) Non-faradaic processes transfer no charge at the electrode-liquid interface. Such processes include polarization, adsorption, and desorption of ions. Although no charge carrier crosses the electrode interface, charges are moved by rearrangements within the solution, e.g., by restructuring the electric double layer (EDL). Resulting currents are capacitive currents $I_{\text{capacitive}}$.[120, 121]

Faradaic processes

During a faradaic process, the charge Q transferred at the electrode is described by Faraday's law (Eq. 2.28).[138]

$$m_i = \frac{QM_w(i)}{zF} \tag{2.28}$$

The mass m_i of an involved species i is proportional to the molecular weight $M_w(i)$ of i and inversely proportional to the number of electrons z transferred to form i. In a potentiostatic experiment, the current is typically the directly measured quantity, which is related to the charge by $Q = \int I dt$.[120, 121]

In the simplest case of a faradaic process, an oxidized species O is converted into a reduced species R by an electron transfer of electrons (e^-) at an electrode interface. n defines the number of electrons transferred during the reaction.

$$O + ne^- \rightleftharpoons R$$

One example adhering to this process is the electrodeposition or dissolution of a metal M and its corresponding cation M^+. Under which conditions the half-reactions occur is determined by the half-cell potential of the redox reaction. For example, the half-cell

potential specifies if a metal immersed in a metal salt solution is stable or is oxidized, yielding the respective metal cation. The Nernst equation (cf. Eq. 2.29) describes the electrode potential E concerning the standard electrode potential of the half-cell $E = E^{\ominus}$ in thermodynamic equilibrium.[120, 121]

$$E = E^{\ominus} + \frac{RT}{nF} \ln \frac{a_O}{a_R} \tag{2.29}$$

F represents the Faraday constant, T the temperature, R the universal gas constant, n the number of electrons transferred, and the standard conditions are defined as $C^{\ominus} = 1\ \mathrm{mol\,L^{-1}}$ and $P^{\ominus} = 1$ bar. Provided sufficient dilution, the concentrations are valid approximations for the activities of the oxidized species a_O and the reduced species a_R. The activity of solid metals is described as infinite.[120, 121]

Cyclic voltammetry and mass transport

Cyclic voltammetry (CV) is a widely used potentiostatic sweep technique to study electrochemical processes like the redox reaction introduced in the previous paragraph. In a CV experiment, the potential is swept between a maximal and a minimal potential E_{max} and E_{min} at a constant sweep rate. The current is monitored continuously and displayed depending on the applied potential.[120, 121, 139] Figure 2.12 sketches a cyclic voltamogram (CV) of a redox couple using a micro- and a macroelectrode.

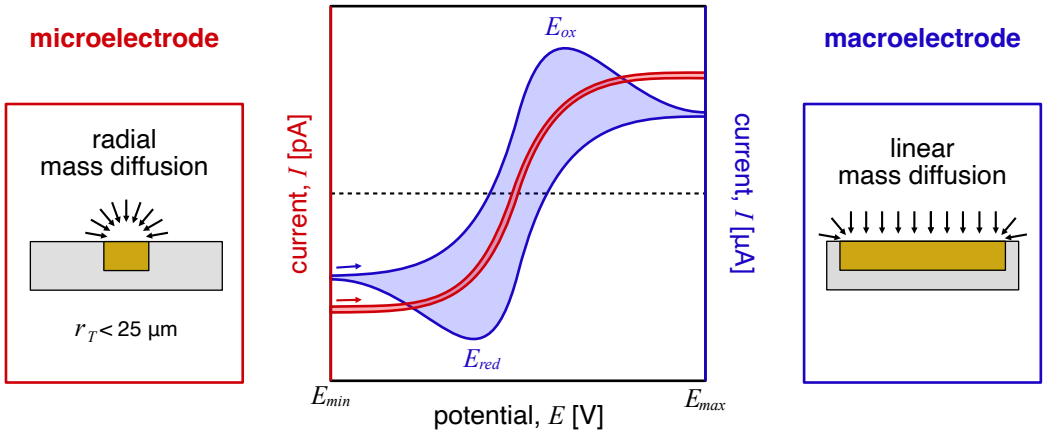

Figure 2.12. Cyclic voltammetry is a common technique to analyze the electrochemical reactions of a redox couple. An exemplary cyclic voltammogram of the same species using a micro- and a macroelectrode is displayed. The size of the electrode area significantly impacts the current response. Radial mass diffusion dominates at microelectrodes with a $r_T < 25$ µm, while the mass transfer to the electrode is predominantly linear at macroelectrodes.

Macroelectrodes on laboratory scales have electrode areas in the $\mathrm{cm^2}$-range. When the potential is swept from E_{min} to more positive potentials in the presence of a redox

couple, no significant faradaic currents are sensed as long as E is significantly smaller than the standard potential $E^{\ominus}$ of the redox couple. Close to $E^{\ominus}$, the current rises as the reduced species is oxidized. A distinct current peak is visible, resembling the maximum electron transfer rate. At this point, the reaction rate is dominated by the diffusion of reduced species to the electrode. Sweeping the potential beyond this peak current, further depletion slows the mass transfer of the reduced species to the electrode. The resulting reduced reaction rate leads to lower currents.[120, 121, 139] When inverting the sweep direction, the oxidized species is reduced again. Similar to the oxidative peak, a reductive peak is observed due to the oxidative species' depletion and consequential reduced mass transport.

In contrast to the macroscopic electrode, the current response of a microelectrode not only deviates in magnitude, i.e., a much lower current range due to the reduced electrode size, but it also shows a different shape. Microelectrodes neither show scan-direction-dependent behavior nor do they show distinct oxidative/reductive peaks. The cause of the difference in current response arises from diffusion behavior at the microelectrode in contrast to its macroscopic counterpart.[120, 121, 139]

A microelectrode is defined by its characteristic (smallest) dimension $r_T < 25$ µm, e.g., the radius of a disk-like or the width of a band-like electrode.[120, 121, 140–143] Beyond the geometries mentioned above, (hemi)spherical, cylindric, or ring-shaped microelectrodes or microelectrode-arrays are used for specific applications.[142, 144] Here, a disk-like electrode with a radius r_T implemented in an insulating carrier material is considered in contrast to a macroscopic electrode concerning their mass transfer properties (illustrations in Figure 2.12). Mass transport in solution occurs through diffusion, migration, and convection.[120] In an unstirred aqueous solution with sufficient supporting electrolytes, migration and convection are negligible. Thus, diffusion governs the mass transport of the species i, which is consumed at the electrode. The flux $J_i(x,t)$ follows Fick's first law of diffusion [145]

$$J = -D_i \left(\frac{\partial C_i(x)}{\partial x} \right) \tag{2.30}$$

with the diffusion coefficient D_i.[120] The reaction rate at the electrode interface is typically significantly higher than the mass transfer to the electrode, governed by the diffusion limitation, which defines the reaction rate. The current is proportional to the concentration gradient $\frac{\partial C_i(x)}{\partial x}$ of the species i, which depends on the current flux of reactant from the bulk to the interface. The mass transport of the reactant i, i.e., the oxidative species O is predominantly axial (along the coordinate x) for a macroelectrode. In contrast, radial transport dominates at a microelectrode with characteristic dimension r_T.[120]

Eq. 2.31 describes the steady-state current i_{ss} in a diffusion-limited process.

$$i_{ss} = \frac{nFA\sqrt{D_i}C^*}{\sqrt{\pi t}} + \frac{nFAD_iC^*}{r_T} \tag{2.31}$$

The first term is time-dependent and arises from the Cotrell equation.[120] It describes the axial diffusion on planar electrodes. For microelectrodes, the diffusion layer's extension exceeds the microelectrode's radius (or characteristic dimension) after a relatively short time (i.e., a few seconds), and the time-dependent axial term vanishes. Then, the steady-state current i_{ss}(microelectrode) only depends on the time-independent second term, governed by the diffusion coefficient D_i and its critical dimension r_T.[120, 121, 140, 142, 143] The steady state is reached once the extension of the diffusion layer is larger than the critical dimension of the electrode, i.e., the electrode radius. The steady state is established rapidly, typically within seconds, which allows for the study of mass transport processes. In contrast, establishing a steady-state condition at macroscopic electrodes would be much more time-consuming or impossible on experimentally relevant time scales, as the axial term in Eq. 2.31 dominates.[120, 121]

Due to their unique properties, microelectrodes are widely employed and have further evolved in electroanalysis since their introduction.[120, 121, 141–143, 146] Moreover, microelectrodes or even smaller nanoelectrodes are also fundamental for electrochemical scanning probe techniques, like scanning ion conductance microscopy (SICM) [147], scanning electrochemical microscopy (SECM) [129, 148] or electrochemical force spectroscopy [132, 149, 150]. Micro- or nanoelectrodes have readily been integrated into AFM cantilevers by various nanoscale deposition and insulation techniques.[133, 134, 150–155] Successful design and fabrication of such electrochemical probes facilitate studying interfacial charges [156], nanoscale biosensing [157], analysis of photocatalytic materials [153] and probing electroactive materials like PEDOT:PSS [132, 150].

2.2.3 Electrochemical Quartz Crystal Microbalance

One method that allows real-time tracking of electrochemical processes is the electrochemical quartz crystal microbalance (EQCM).[158–160] The EQCM, like any quartz crystal microbalance (EQCM), detects frequency changes of a quartz crystal upon adding a mass, e.g., during a deposition or adsorption process. The working principle of the QCM relies on the inverse piezoelectric effect, i.e., the mechanical response of a piezoelectric material to an external potential applied across opposite sites.[121, 161] QCM employs an AT-cut α-quartz with two Au thin-film electrodes vapor-deposited onto opposite faces, which functions as a mass sensor (cf. Figure 2.13A). The adsorption or deposition process occurs at the top electrode (cf. Figure 2.13B).

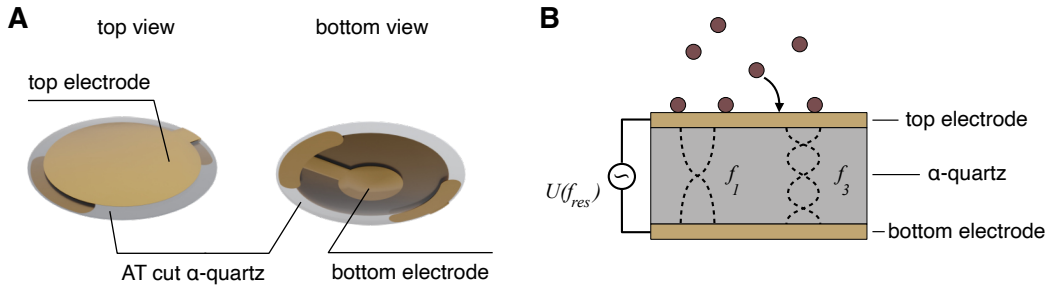

Figure 2.13. Quartz crystal microbalance (QCM). **A** Top and bottom view of a quartz-crystal resonator. **B** Applying an alternating voltage between the resonator's top and bottom electrodes induces a shear oscillation. Adsorption of a sample to the top electrode induces frequency shift.

Applying a sinusoidal voltage across the two electrodes induces a shear oscillation as depicted for the first (f_1) and third (f_3) harmonic in Figure 2.13B.[161] Impedance analysis [162], or the ring-down technique [163] are used to readout the frequency shift. The excitation signal is interrupted in the latter case, and the oscillation decay is evaluated.[161, 163] Evaluation of the bandwidth, in addition to the resonance frequency, opens up the extraction of additional sample properties, particularly relevant for soft, swollen, and viscoelastic systems.[161] However, complex modeling might be necessary for quantitative analysis.[161, 164]

Sauerbrey [165] discovered that the mass $m_{\text{Sauerbrey}}$, deposited onto a piezoelectric resonator, is proportional to its resonance frequency normalized to the number of its harmonic f/n, provided the deposit is sufficiently thin and rigid.

$$\Delta f/n = -C\Delta m_{\text{Sauerbrey}} \tag{2.32}$$

$$C = \frac{2f_0^2}{A\sqrt{\rho_q \mu_q}} = 17.7\ \text{ng}\,\text{cm}^{-2}\,\text{Hz}^{-1} \tag{2.33}$$

The proportionality constant C represents the sensitivity and depends on the fundamental frequency of the quartz resonator f_0, its active area A, and material properties like the density $\rho_q = 2.648\ \text{g}\,\text{cm}^{-3}$ and shear modulus $\mu_q = 2.947 \cdot 10^{11}\ \text{g}\,\text{cm}^{-1}\,\text{s}^{-2}$ for an AT-cut quartz crystal.[161] Provided that a deposit is sufficiently rigid, thin, and homogenous, the Sauerbrey equation directly correlates the frequency shift with the deposited mass.[161, 165]

Combining the QCM with electrochemistry enables the study of electrode processes that result in mass changes at the electrode.[158, 160, 164] These include electropolymerization, [166, 167] and electrodeposition of metals [128, 159, 162, 168–170] and polymers [171], investigation of electroactive or electroresposive films [164, 172]. Moreover, EQCM is increasingly valued in energy storage and battery research [127, 128, 173–175].

In the EQCM, the top electrode serves a dual purpose: it is the WE, at which the electrochemical reaction occurs, and it detects the resulting mass change via the induced frequency shift. Figure 2.14A illustrates the setup of such an EQCM. A platinum sheet acts as a CE, and a miniaturized RE is immersed in the electrolyte solution to complete the three-electrode configuration. Due to the dual function of the top electrode, a capacitor (high-pass filter) and an inductor (low-pass filter) are used to electrically separate the excitation and readout of the oscillation from the electrochemical circuit and eliminate any interference.[161]

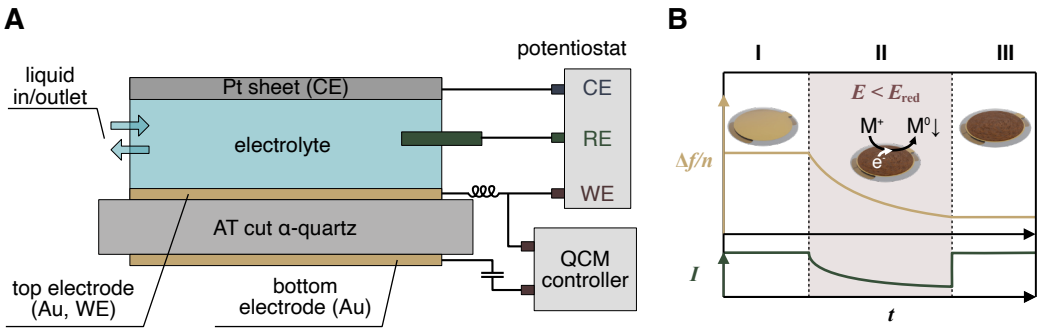

Figure 2.14. Electrochemical quartz crystal microbalance (EQCM). **A** Schematic of an EQCM setup, including the three-electrode configuration implemented into a QCM liquid cell. The top electrode of the QCM-crystal serves a dual purpose as the WE and mass sensor. **B** Sketch of the electrodeposition a metal M from a metal salt solution comprising M^+ ions upon applying a reductive potential E_{red} monitored by the EQCM: **I** equilibration without an external potential; **II** electrodeposition of M to the WE (top electrode) by applying $E < E_{red}$ induces a negative frequency shift and current flow; **III** the electrodeposition process stops once the applied potential is switched off.

The electrodeposition of metals such as copper or silver has been used experimentally to calibrate the sensitivity of quartz crystal resonators by determining the frequency change depending on the electrochemical mass according to Faraday's Law (Eq. 2.28).[159, 176, 177] Figure 2.14B outlines such an electrodeposition experiment containing three parts: **I** The resonator is equilibrated in the electrolyte solution at zero frequency shift, as long as no external potential is applied. **II** The electrodeposition at a reductive potential E_{red} induces a current and frequency response, which are sensed simultaneously. **III** When the potentiostat is switched off, a stable frequency and no current flow are detected if the deposit is stable in the electrolyte solution. Otherwise, the dissolution of the deposit could be followed.

References

(1) Voigtländer, B., *Scanning Probe Microscopy*; Springer: Berlin, Heidelberg, 2015.

(2) Binnig, G.; Rohrer, H.; Gerber, C.; Weibel, E. *Phys. Rev. Lett.* **1982**, *49*(1), 57–61.

(3) Binnig, G.; Rohrer, H. *Angew. Chem. Int. Ed.* **1987**, *26*(7), 606–614.

(4) Binnig, G.; Rohrer, H. *Rev. Mod. Phys.* **1987**, *59*(3), 615–625.

(5) Binnig, G.; Quate, C.; Gerber, C. *Phys. Rev. Lett.* **1986**, *56*(9), 930–933.

(6) Giessibl, F. J. *Jpn. J. Appl. Phys.* **1994**, *33*(6S), 3726.

(7) *Atomic Force Microscopy in Liquid*; Baró, A. M., Reifenberger, R. G., Eds.; Wiley: 2012.

(8) *Scanning Probe Microscopy in Industrial Applications*; Yablon, D. G., Ed.; Wiley: 2013.

(9) Weisenhorn, A. L.; Hansma, P. K.; Albrecht, T. R.; Quate, C. F. *Appl. Phys. Lett.* **1989**, *54*(26), 2651–2653.

(10) Zhang, Z.; Said, S.; Smith, K., et al. *Adv. Energy Mater.* **2021**, *11*(38), 2101518.

(11) Orji, N.; Badaroglu, M.; Barnes, B., et al. *Nat. Electron.* **2018**, *1*(10), 532–547.

(12) Zhong, J.; Yan, J. *RSC Advances* **2016**, *6*(2), 1103–1121.

(13) Variola, F. *Phys. Chem. Chem. Phys.* **2015**, *17*(5), 2950–2959.

(14) Krieg, M.; Fläschner, G.; Alsteens, D., et al. *Nat. Rev. Phys.* **2019**, *1*, 41–57.

(15) Viljoen, A.; Mathelié-Guinlet, M.; Ray, A., et al. *Nat. Rev. Methods Primers* **2021**, *1*(1), 63.

(16) Tsukruk, V. V.; Singamaneni, S., *Scanning Probe Microscopy of Soft Matter*; Wiley: Weinheim, 2011.

(17) Joshua, A.; Cheng, G.; Lau, E. *Appl. Surf. Sci. Adv.* **2023**, *17*, 100448.

(18) Kuznetsov, V.; Papastavrou, G. *J. Phys. Chem. C* **2014**, *118*(5), 2673–2685.

(19) Helfricht, N.; Mark, A.; Dorwling-Carter, L.; Zambelli, T.; Papastavrou, G. *Nanoscale* **2017**, *9*(27), 9491–9501.

(20) Kawai, S.; Foster, A.; Björkman, T., et al. *Nat. Commun.* **2016**, *7*, 11559.

(21) Butt, H.-J.; Kappl, M.; Mueller, H., et al. *Langmuir* **1999**, *15*(7), 2559–2565.

(22) Hughes, M.; Dougan, L. *Rep. Prog. Phys.* **2016**, *79*(7), 076601.

(23) Puchner, E.; Gaub, H. *Curr. Opin. Struct. Biol.* **2009**, *19*(5), 605–614.

(24) Giessibl, F. J. *Mater. Today* **2005**, *8*(5), 32–41.

(25) Cho, D.; Aguayo, S.; Cartagena-Rivera, A. *Biomaterials* **2023**, *303*, 122389.

(26) Liu, Y.; Li, X.; Zhang, Y., et al. *Small* **2024**, *20*(1), e2303838.

(27) Meyer, G.; Amer, N. M. *Appl. Phys. Lett.* **1988**, *53*(12), 1045–1047.

(28) Butt, H.-J.; Cappella, B.; Kappl, M. *Surf. Sci. Rep.* **2005**, *59*(1-6), 1–152.

(29) Cappella, B.; Dietler, G. *Surf. Sci. Rep.* **1999**, *34*(1-3), 1–104.

(30) Butt, H.-J. *Biophys. J.* **1991**, *60*(6), 1438–1444.

(31) Ducker, W. A.; Senden, T. J.; Pashley, R. M. *Nature* **1991**, *353*(6341), 239–241.

(32) Derjaguin, B. *Kolloid-Zeitschrift* **1934**, *69*(2), 155–164.

(33) Montes Ruiz-Cabello, F.; Trefalt, G.; Maroni, P.; Borkovec, M. *Phys. Rev. E* **2014**, *90*(1), 012301.

(34) Ma, N.; Wang, X.; Zhang, M., et al. *Langmuir* **2023**, *39*(17), 5956–5969.

(35) Wei, Y.; Dong, Y.; Ji, X., et al. *J. Mol. Liq.* **2022**, *350*, 118506.

(36) Neugirg, B. R.; Helfricht, N.; Czich, S., et al. *Polymer* **2016**, *102*, 363–371.

(37) Muir, I.; Meagher, L.; Gee, M. *Langmuir* **2001**, *17*(16), 4932–4939.

(38) Sato, K.; Ijuin, A.; Imai, Y.; Hotta, Y. *Polym. Compos.* **2020**, *41*(12), 5209–5215.

(39) Sittl, S.; Das, M.; Helfricht, N.; Petekidis, G.; Papastavrou, G. *Coll. Surf. A* **2024**, *697*, 134319.

(40) Helfricht, N.; Doblhofer, E.; Bieber, V., et al. *Soft Matter* **2017**, *13*(3), 578–589.

(41) Pussak, D.; Behra, M.; Schmidt, S.; Hartmann, L. *Soft Matter* **2012**, *8*(5), 1664–1672.

(42) Erath, J.; Schmidt, S.; Fery, A. *Soft Matter* **2010**, *6*(7), 1432–1437.

(43) Meister, A.; Gabi, M.; Behr, P., et al. *Nano Lett.* **2009**, *9*(6), 2501–2507.

(44) Dörig, P.; Ossola, D.; Truong, A., et al. *Biophys. J.* **2013**, *105*(2), 463–472.

(45) Kuznetsov, V.; Papastavrou, G. *Rev. Sci. Instrum.* **2012**, *83*(11), 116103.

(46) Specht, A.; Krämer, D.; Helfricht, N.; Papastavrou, G. *Langmuir* **2025**, *41*(10), 6515–6527.

(47) Mark, A.; Helfricht, N.; Rauh, A.; Karg, M.; Papastavrou, G. *Small* **2019**, *15*(43), e1902976.

(48) Gan, Y. *Rev. Sci. Instrum.* **2007**, *78*(8), 081101.

(49) Yuan, C.; Zhang, D.; Gan, Y. *Rev. Sci. Instrum.* **2017**, *88*(3), 031101.

(50) *Handbook of Nanoindentation with biological applications*; Oyen, M. L., Ed.; Jenny Stanford Publishing: New York, 2019.

(51) Drake, B.; Prater, C.; Weisenhorn, A., et al. *Science* **1989**, *243*(4898), 1586–1589.

(52) Dufrêne, Y.; Ando, T.; Garcia, R., et al. *Nat. Nanotechnol.* **2017**, *12*(4), 295–307.

(53) Zhong, Q.; Inniss, D.; Kjoller, K.; Elings, V. *Surf. Sci.* **1993**, *290*(1-2), L688–L692.

(54) Schäffer, T. E.; Cleveland, J. P.; Ohnesorge, F.; Walters, D. A.; Hansma, P. K. *J. Appl. Phys.* **1996**, *80*(7), 3622–3627.

(55) Umeda, N.; Ishizaki, S.; Uwai, H. *J. Vac. Sci. Technol. B* **1991**, *9*(2), 1318–1322.

(56) Ratcliff, G. C.; Erie, D. A.; Superfine, R. *Appl. Phys. Lett.* **1998**, *72*(15), 1911–1913.

(57) Jarvis, S.; Lantz, M.; Dürig, U.; Tokumoto, H. *Appl. Surf. Sci.* **1999**, *140*(3-4), 309–313.

(58) Rosa-Zeiser, A.; Weilandt, E.; Hild, S.; Marti, O. *Meas. Sci. Technol.* **1997**, *8*(11), 1333–1338.

(59) Bruker *Application note: Introduction to Bruker's ScanAsyst and PeakForce Tapping AFM Technology* **2011**, *133*.

(60) JPK Instruments *Application note: QI™ mode - Quantitative Imaging with the NanoWizard ® 3 AFM* **2011**.

(61) Nievergelt, A.; Banterle, N.; Andany, S.; Gönczy, P.; Fantner, G. *Nat. Nanotechnol.* **2018**, *13*(8), 696–701.

(62) Lorenzoni, M.; Evangelio, L.; Verhaeghe, S., et al. *Langmuir* **2015**, *31*(42), 11630–11638.

(63) Nellist, M.; Chen, Y.; Mark, A., et al. *Nanotechnology* **2017**, *28*(9), 095711.

(64) Knittel, P.; Mizaikoff, B.; Kranz, C. *Anal. Chem.* **2016**, *88*(12), 6174–6178.

(65) Sader, J. E.; Larson, I.; Mulvaney, P.; White, L. R. *Rev. Sci. Instrum.* **1995**, *66*(7), 3789–3798.

(66) Butt, H.-J.; Siedele, P.; Seifert, K., et al. *J. Microsc.* **1993**, *169*(1), 75–84.

(67) Hazel, J. L.; Tsukruk, V. V. *Thin Solid Films* **1999**, *339*(1-2), 249–257.

(68) Khan, A.; Philip, J.; Hess, P. *J. Appl. Phys.* **2004**, *95*(4), 1667–1672.

(69) Gibson, C.; Alastair Smith, D.; Roberts, C. *Nanotechnology* **2005**, *16*(2), 234–238.

(70) Georgakaki, D.; Mitridis, S.; Sapalidis, A. A.; Mathioulakis, E.; Polatoglou, H. M. *Measurement* **2013**, *46*(10), 4274–4281.

(71) Kim, M.-S.; Choi, J.-H.; Kim, J.-H.; Park, Y.-K. *Measurement* **2010**, *43*(4), 520–526.

(72) Te Riet, J.; Katan, A. J.; Rankl, C., et al. *Ultramicroscopy* **2011**, *111*(12), 1659–1669.

(73) Sader, J. E. *J. Appl. Phys.* **1998**, *84*(1), 64–76.

(74) Cleveland, J. P.; Manne, S.; Bocek, D.; Hansma, P. K. *Rev. Sci. Instrum.* **1993**, *64*(2), 403–405.

(75) Hutter, J. L.; Bechhoefer, J. *Rev. Sci. Instrum.* **1993**, *64*(7), 1868–1873.

(76) Butt, H.-J.; Jaschke, M. *Nanotechnology* **1995**, *6*(1), 1–7.

(77) Proksch, R.; Schäffer, T. E.; Cleveland, J. P.; Callahan, R. C.; Viani, M. B. *Nanotechnology* **2004**, *15*(9), 1344–1350.

(78) Braun, T.; Barwich, V.; Ghatkesar, M., et al. *Phys. Rev. E* **2005**, *72*(3 Pt 1), 031907.

(79) Bircher, B. A.; Duempelmann, L.; Renggli, K., et al. *Anal. Chem.* **2013**, *85*(18), 8676–8683.

(80) Ghatkesar, M. K.; Barwich, V.; Braun, T., et al. *Nanotechnology* **2007**, *18*(44), 445502.

(81) Girardo, S.; Träber, N.; Wagner, K., et al. *J. Mater. Chem. B* **2018**, *6*(39), 6245–6261.

(82) Daza, R.; González-Bermúdez, B.; Cruces, J., et al. *J. Mech. Behav. Biomed. Mater* **2019**, *95*, 103–115.

(83) Dokukin, M.; Guz, N.; Sokolov, I. *Biophys. J.* **2013**, *104*(10), 2123–2131.

(84) Pérez-Domínguez, S.; Kulkarni, S.; Pabijan, J., et al. *Nanoscale* **2023**, *15*(40), 16371–16380.

(85) Kumachev, A.; Tumarkin, E.; Walker, G. C.; Kumacheva, E. *Soft Matter* **2013**, *9*(10), 2959.

(86) Stylianou, A.; Mpekris, F.; Voutouri, C., et al. *Acta Biomater.* **2022**, *154*, 324–334.

(87) Wenderott, J.; Flesher, C.; Baker, N., et al. *Sci. Rep.* **2020**, *10*(1), 20423.

(88) Xu, D.; Harvey, T.; Begiristain, E., et al. *J. Mech. Behav. Biomed. Mater.* **2022**, *133*, 105329.

(89) Mokhtari, A.; Tala-Ighil, N.; Masmoudi, Y. A. *J. Mater. Eng. Perform.* **2022**, *31*(4), 2715–2722.

(90) Hertz, H. *J. Reine Angew. Mathematik* **1882**, *1882*(92), 156–171.

(91) Sneddon, I. N. *Int. J. Eng. Sci.* **1965**, *3*(1), 47–57.

(92) Glaubitz, M.; Medvedev, N.; Pussak, D., et al. *Soft Matter* **2014**, *10*(35), 6732–6741.

(93) Raßmann, N.; Trippmacher, S.; Specht, A., et al. *ACS Appl. Nano. Mater.* **2025**, *8*(11), 5383–5398.

(94) Miyake, K.; Satomi, N.; Sasaki, S. *Appl. Phys. Lett.* **2006**, *89*(3), 031925–031921.

(95) Kilpatrick, J.; Revenko, I.; Rodriguez, B. *Adv. Healthc. Mater.* **2015**, *4*(16), 2456–2474.

(96) Cohen, S.; Kalfon-Cohen, E. *Beilstein J. Nanotechnol.* **2013**, *4*, 815–833.

(97) Garcia, R. *Chem. Soc. Rev.* **2020**, *49*(16), 5850–5884.

(98) Young, T. J.; Monclus, M. A.; Burnett, T. L., et al. *Meas. Sci. and Technol.* **2011**, *22*(12), 125703.

(99) Cartagena-Rivera, A.; Wang, W.; Geahlen, R.; Raman, A. *Sci. Rep.* **2015**, *5*, 11692.

(100) Oyen, M. L. *Int. Mater. Rev.* **2014**, *59*(1), 44–59.

(101) Tsukruk, V. V.; Singamaneni, S. In *Scanning Probe Microscopy: Fundamentals and Practices*; Wiley: Weinheim, 2011, pp 99–151.

(102) Jacobs, T. D. B.; Mathew Mate, C.; Turner, K. T.; Carpick, R. W. In *Scanning Probe Microscopy in Industrial Applications: Nanomechanical Characterization*, Yablon, D. G., Ed.; Wiley: 2013, pp 15–48.

(103) Lin, D.; Horkay, F. *Soft Matter* **2008**, *4*, 669–682.

(104) Cappella, B., *Mechanical Properties of Polymers Measured through AFM Force-Distance Curves*; Springer International Publishing: Cham, 2016.

(105) Johnson, K. L.; Kendall, K.; D., R. A. *Proc. R. Soc. London A* **1971**, *324*(1558), 301–313.

(106) Derjaguin, B.; Muller, V.; Toporov, Y. *J. Coll. Interface Sci.* **1975**, *53*(2), 314–326.

(107) Maugis, D. *J. Coll. Interface Sci.* **1992**, *150*(1), 243–269.

(108) Martínez-Martín, D.; Fläschner, G.; Gaub, B., et al. *Nature* **2017**, *550*(7677), 500–505.

(109) Herzog, S.; Fläschner, G.; Incaviglia, I., et al. *Nat. Commun.* **2024**, *15*(1), 1751.

(110) Fläschner, G.; Roman, C.; Strohmeyer, N.; Martinez-Martin, D.; Müller, D. *Nat. Commun.* **2021**, *12*(1), 2922.

(111) Colombo, F.; Villiou, M.; Taheri, F., et al. *Adv. NanoBiomed Res.* **2023**, *3*(7), 2200156.

(112) Cuny, A.; Tanuj Sapra, K.; Martinez-Martin, D., et al. *Nat. Commun.* **2022**, *13*(1), 3483.

(113) Ramos, D.; Tamayo, J.; Mertens, J.; Calleja, M. *J. Appl. Phys.* **2006**, *99*(12), 124904.

(114) Kiracofe, D.; Kobayashi, K.; Labuda, A.; Raman, A.; Yamada, H. *Rev. Sci. Instrum.* **2011**, *82*(1), 013702.

(115) Ge, L. K.; Tuniz, A.; de Sterke, C. M., et al. *Adv. Sens. Res.* **2024**, *3*(8), 2300136.

(116) Cuny, A. P.; Martínez-Martín, D.; Fläschner, G. *SoftwareX* **2019**, *10*, 100303.

(117) Albrecht, T. R.; Grütter, P.; Horne, D.; Rugar, D. *J. Appl. Phys.* **1991**, *69*(2), 668–673.

(118) Incaviglia, I.; Herzog, S.; Fläschner, G., et al. *Nano Lett.* **2023**, *23*(2), 588–596.

(119) Shen, Z.; Shih, W. Y.; Shih, W.-H. *Rev. Sci. Instrum.* **2006**, *77*(6), 065101.

(120) Bard, A. J.; Faulkner, L. R.; White, H. S., *Electrochemical Methods: Fundamentals and Applications*; John Wiley & Sons: Hoboken, 2022.

(121) Eliaz, N.; Gileadi, E., *Physical Electrochemistry: Fundamentals, Techniques, and Applications*; John Wiley & Sons: 2019.

(122) Neubauer, D.; Scharpf, J.; Pasquarelli, A.; Mizaikoff, B.; Kranz, C. *Analyst* **2013**, *138*(22), 6746–6752.

(123) Baggio, B.; Grunder, Y. *Annu. Rev. Anal. Chem.* **2021**, *14*(1), 87–107.

(124) Wang, W.; Yan, H.; Gu, Y.; Yan, J.; Mao, B. *Annu. Rev. Anal. Chem.* **2024**, *17*(1), 103–126.

(125) Shi, X.; Qing, W.; Marhaba, T.; Zhang, W. *Electrochim. Acta* **2020**, *332*, 135472.

(126) Broch, L.; Johann, L.; Stein, N.; Zimmer, A.; Beck, R. *Rev. Sci. Instrum.* **2007**, *78*(6), 064101.

(127) Levi, M. D.; Daikhin, L.; Aurbach, D.; Presser, V. *Electrochem. Commun.* **2016**, *67*, 16–21.

(128) Vanoppen, V.; Johannsmann, D.; Hou, X., et al. *Adv. Sens. Res.* **2024**, *3*(9), 2400025.

(129) Bard, A. J.; Mirkin, M. V., *Scanning Electrochemical Microscopy*; CRC Press: Boca Raton, 2022.

(130) *Handbook of Reference Electrodes*; Inzelt, G., Lewenstam, A., Scholz, F., Eds.; Springer Berlin Heidelberg: Berlin, Heidelberg, 2013.

(131) Kuznetsov, V.; Papastavrou, G. *Langmuir* **2012**, *28*(48), 16567–16579.

(132) Karg, A.; Rößler, T.; Mark, A., et al. *Langmuir* **2021**, *37*(46), 13537–13547.

(133) Karg, A.; Kuznetsov, V.; Helfricht, N.; Lippitz, M.; Papastavrou, G. *Sci. Rep.* **2023**, *13*(1), 7885.

(134) Kranz, C.; Friedbacher, G.; Mizaikoff, B., et al. *Anal. Chem.* **2001**, *73*(11), 2491–2500.

(135) Kranz, C.; Mizaikoff, B.; Lugstein, A.; Bertagnolli, E. In *ACS Symposium Series: Environmental Electrochemistry*; American Chemical Society: Washington, DC, 2002, pp 320–333.

(136) Kranz, C. *Electroanalysis* **2016**, *28*(1), 35–45.

(137) Inzelt, G. In *Handbook of Reference Electrodes*; Springer Berlin Heidelberg: Berlin, Heidelberg, 2013, pp 331–332.

(138) Faraday, M. *Phil. Trans. R. Soc.* **1834**, *124*, 77–122.

(139) Elgrishi, N.; Rountree, K. J.; McCarthy, B. D., et al. *J. Chem. Educ.* **2018**, *95*(2), 197–206.

(140) Aoki, K. *Electroanalysis* **1993**, *5*(8), 627–639.

(141) Beriet, C.; Pletcher, D. *J. Electroanal.Chem.* **1993**, *361*(1-2), 93–101.

(142) Forster, R. J. *Chem. Soc. Rev.* **1994**, *23*(4), 289.

(143) Heinze, J. *Angew. Chem. Int. Ed.* **1993**, *32*(9), 1268–1288.

(144) Morf, W. E. *Anal. Chim. Acta* **1996**, *330*(2-3), 139–149.

(145) Fick, A. *Ann. Phys.* **1855**, *170*(1), 59–86.

(146) Zoski, C. G. *Electroanalysis* **2002**, *14*(15-16), 1041–1051.

(147) Hansma, P.; Drake, B.; Marti, O.; Gould, S.; Prater, C. *Science* **1989**, *243*(4891), 641–643.

(148) Izquierdo, J.; Knittel, P.; Kranz, C. *Anal. Bioanal.Chem.* **2018**, *410*(2), 307–324.

(149) Daboss, S.; Lin, J.; Godejohann, M.; Kranz, C. *Anal. Chem.* **2020**, *92*(12), 8404–8413.

(150) Knittel, P.; Zhang, H.; Kranz, C.; Wallace, G.; Higgins, M. *Nanoscale* **2016**, *8*(8), 4475–4481.

(151) Eifert, A.; Smirnov, W.; Frittmann, S., et al. *Electrochem. Commun.* **2012**, *25*, 30–34.

(152) Eifert, A.; Mizaikoff, B.; Kranz, C. *Micron* **2015**, *68*, 27–35.

(153) Caniglia, G.; Horn, S.; Kranz, C. *Faraday Discuss.* **2025**, *257*(0), 224–239.

(154) Knittel, P.; Higgins, M.; Kranz, C. *Nanoscale* **2014**, *6*(4), 2255–2260.

(155) Hellmann, A.; Neusser, G.; Daboss, S., et al. *Anal. Chem.* **2024**, *96*(8), 3308–3317.

(156) Caniglia, G.; Tezcan, G.; Meloni, G.; Unwin, P.; Kranz, C. *Annu. Rev. Anal. Chem.* **2022**, *15*(1), 247–267.

(157) Hellmann, A.; Schundner, A.; Frick, M.; Kranz, C. *Curr. Opin. Electrochem.* **2023**, *39*, 101282.

(158) Buttry, D. A.; Ward, M. D. *Chem. Rev.* **1992**, *92*(6), 1355–1379.

(159) Gileadi, E.; Tsionsky, V. *J. Electrochem. Soc.* **2000**, *147*(2), 567–574.

(160) Hillman, A. R. *J. Sol. State Electrochem.* **2011**, *15*(7-8), 1647–1660.

(161) Johannsmann, D., *The Quartz Crystal Microbalance in Soft Matter Research*; Springer International Publishing: Cham, 2015.

(162) Bund, A.; Schwitzgebel, G. *Electrochim. Acta* **2000**, *45*(22-23), 3703–3710.

(163) Rodahl, M.; Höök, F.; Krozer, A.; Brzezinski, P.; Kasemo, B. *Rev. Sci. Instrum.* **1995**, *66*(7), 3924–3930.

(164) Easley, A. D.; Ma, T.; Eneh, C. I., et al. *J. Pol. Sci.* **2022**, *60*(7), 1090–1107.

(165) Sauerbrey, G. *Z. Phys.* **1959**, *155*(2), 206–222.

(166) Antonio, J. L.; Martins, V. L.; Córdoba de Torresi, S. I.; Torresi, R. M. *Electrochim. Acta* **2019**, *324*, 134887.

(167) Zhao, M.; Tang, X.; Zhang, H.; Gu, C.; Ma, Y. *Electrochem. Commun.* **2021**, *123*, 106913.

(168) Leppin, C.; Langhoff, A.; Höfft, O.; Johannsmann, D. *Electroanalysis* **2021**, *33*(12), 2529–2538.

(169) Biermann, M.; Leppin, C.; Langhoff, A., et al. *Analyst* **2024**, *149*(7), 2138–2146.

(170) Friedt, J.-M.; Choi, K. H.; Frederix, F.; Campitelli, A. *J. Electrochem. Soc.* **2003**, *150*(10), H229.

(171) Sadman, K.; Wang, Q.; Chen, S.; Delgado, D.; Shull, K. *Langmuir* **2017**, *33*(8), 1834–1844.

(172) Lin, C.; Luo, S. *Langmuir* **2021**, *37*(42), 12476–12486.

(173) Lemaire, P.; Dargon, T.; Alves Dalla Corte, D., et al. *Anal. Chem.* **2020**, *92*(20), 13803–13812.

(174) Ji, Y.; Yin, Z.-W.; Yang, Z., et al. *Chem. Soc. Rev.* **2021**, *50*(19), 10743–10763.

(175) Shpigel, N.; Levi, M.; Sigalov, S.; Daikhin, L.; Aurbach, D. *Acc. Chem. Res.* **2018**, *51*(1), 69–79.

(176) Gabrielli, C.; Keddam, M.; Torresi, R. *J. Electrochem. Soc.* **1991**, *138*(9), 2657–2660.

(177) Hu, J.; Huang, X.; Xue, S., et al. *Electrochem. Commun.* **2020**, *116*, 106744.

Synopsis

3

This thesis is written in a cumulative manner, comprising four different subprojects which have been published [1–4] in peer-reviewed journals. The following section will outline the context of this thesis, evolving from the individual subprojects, and highlight their connection. The individual projects are presented throughout chapters 4-7.

3.1 Outline

An ever-advancing analytic toolbox fuels progress in developing and understanding materials. For soft matter science, analytical techniques are essential to trace the assembly process and to investigate a material's structure and physicochemical properties.

Atomic force microscopy (AFM) is a widely used and highly appreciated technique in soft matter research [5, 6], and it was the primary analytical tool throughout this thesis to investigate soft matter assembly and probe its properties. By combining AFM with other techniques, like electrochemistry or correlating its results with techniques such as SAXS, its analytical capabilities were increased further. Combinatorial strategies allowed access to the understanding of interfacial processes of soft matter at the nano- to microscale by accessing different physicochemical and material properties simultaneously or complementarily. The AFM cantilever itself can serve multiple purposes: to access interaction forces quantitatively [7], as an indenter [8, 9], for biosensing [10], as a nanoelectrode [11, 12], and to detect mass changes [13, 14]. Throughout this thesis, AFM cantilevers functioned as nanoindenters (Chapters 5 and 7), microelectrodes (Chapter 6), mass sensors (Chapter 6) and were used to study the nanostructure soft matter (Chapter 4 and 5).

This thesis developed AFM-based techniques to study soft matter systems. The first two chapters **Colloidal Nanoassembly** (Chapter 4) and **Electrogelation** (Chapter 5) took their motivation from the assembly and structural characterization of soft matter. AFM-based techniques were transferred and adapted to successfully study the assembly and the characteristics of the soft matter formed. In the later chapters **Electrochemical Picobalance** (Chapter 6) and **Microgel Nanoindentation** (Chapter 7), the advancement and development of AFM techniques, also in combination with electrochemistry, resembled the primary focus. Figure 3.1 outlines these four subprojects schematically.

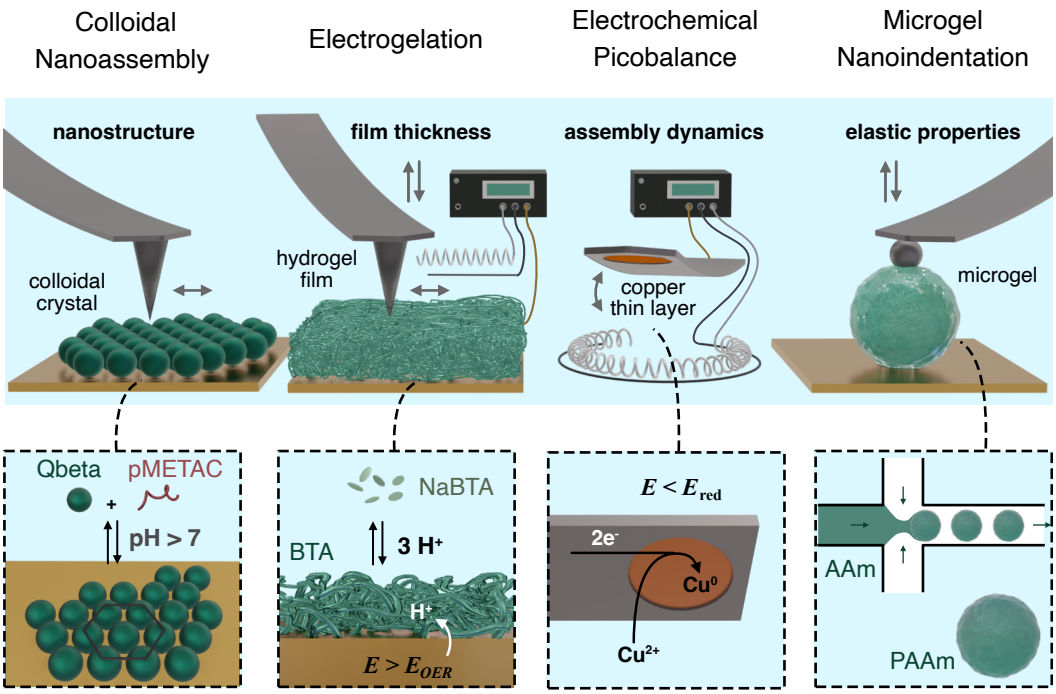

Figure 3.1. Overview of the thesis consisting of the subprojects **Colloidal Nanoassembly** (Chapter 4), **Electrogelation** (Chapter 5), **Electrochemical Picobalance** (Chapter 6), and **Microgel Nanoindentation** (Chapter 7). Different materials have been assembled throughout this thesis. AFM-based techniques have been developed to characterize the nanostructure, film thickness, assembly dynamics, and elastic properties.

The first subproject **Colloidal Nanoassembly** (Chapter 4, [1]) introduced a simple, scalable approach to assembling bio-nanocolloids in the presence of polycations into a highly ordered colloidal crystals. Analysis of small-angle X-ray scattering (SAXS) data proposed that the nanocolloids pack into superstructures with 2D-hexagonal order in suspension. An immobilization strategy to transfer the colloidal crystals from the suspension to a solid support was developed, which enabled the acquisition of real-space topographic images of the colloidal assemblies in liquid via advanced AFM imaging. The nanostructure data acquired by AFM in liquid acquired real-space proof of the suspected hexagonal packing of Qbeta and was correlated to the SAXS data on the same system by Fourier transformation.

The second subproject **Electrogelation** (Chapter 5, [2]) built another soft matter system, namely a soft hydrogel film. Small molecular-weight hydrogelators were assembled into fibrillar hydrogel films from an electrode interface by a process called electrogelation. The AFM-based nanoindentation technique was adapted to determine the thickness of electrogelated hydrogel films in the swollen state. By relating the hydrated film thickness acquired by nanoindentation to the dried film thickness determined by AFM imaging,

it was possible to comprehensively determine the influence of the assembly conditions on the resulting film thickness. Ultimately, these AFM-based thickness measurements opened the door for growing soft hydrogel thin films with controlled thickness.

The third subproject **Electrochemical Picobalance** (Chapter 6, [3]) transferred the electrochemical film formation from a macroscopic electrode directly to the cantilever, i.e., on an integrated microelectrode. Thus, by integrating electrochemistry with an AFM-based mass balance, the microelectrode's dynamic current response could be directly correlated to the resulting mass changes according to Faraday's law. This novel technique was calibrated using the well-studied process of electrochemical copper deposition, with a mass resolution of $\lesssim 1$ pg. However, its application potential reaches further, e.g., for directly tracing processes like electrogelation of hydrogels or single-entity bioelectrics.

The final subproject **Microgel Nanoindentation** (Chapter 7, [4]) addressed the instrumental challenges of AFM-based elasticity measurements on two types of microgel particles with cell-relevant size and Young's modulus as synthesized by droplet microfluidics. While AFM-based nanoindentation is the gold standard for soft particulate systems, a comprehensive assessment of all influential parameters had not yet been conducted. The project answered long-discussed questions on the adequate choice of indenter geometry, contact model, and impact of experimental parameters for elasticity measurements on single microgels through extensive experimental assessment.

3.1.1 Soft Matter Assembly and Characterization

Self-assembly is a ubiquitous process that creates hierarchically ordered and functional structures. Prominent examples of self-assembly in nature are lipid bilayers and the folding of proteins. In both cases, self-assembly introduces a distinct structure and leads to functionality. Inspired by nature, chemists and materials scientists follow similar strategies to create building blocks and use self-assembly to create functional superstructures and materials.[15–18] Building blocks for assembly can be manifold, ranging from individual low molecular weight compounds [19, 20], lipids, and peptides [21] via (bio)polymers to various (bio)colloids [16, 22]. In this thesis, functional soft matter materials, i.e., a colloidal crystal and supramacromolecular fibrillar structures which form a soft hydrogel film, have been fabricated through self-assembly guided by the interaction of a biocolloid and a polycation or an electrochemically induced pH shift. In both projects, existing AFM-based tools, advanced topographic imaging in air and liquid, and nanoindentation have been adapted to elucidate structural properties and materials characteristics that were otherwise inaccessible.

pH-Responsive Virus-Based Colloidal Crystals for Advanced Material Platforms

Using preassembled structures such as bacteriophages to construct novel functional materials has several advantages. Viruses, like bacteriophages, are precision-designed nano-colloids with a well-defined structure, shape, and surface chemistry.[23, 24] Moreover, their production can easily be scaled [25, 26] while modification allows for further functionalization and customization to meet specific needs [27, 28].

In the **Colloidal Nanoassembly** project, a scalable and straightforward approach to form pH-responsive colloidal crystals using the *Qubervirus durum* (Qbeta) bacteriophage was developed by the Salentinig group (University of Fribourg).[1] Qbeta consists of an icosahedral protein capsid with a diameter of ≈ 29 nm [29] as visible by TEM (Figure 3.2A). The interaction with the synthetic polycationic poly[2-(methacryloyloxy)ethyl]trimethylammonium chloride] (pMETAC) drives colloidal self-assembly of Qbeta into colloidal superstructures (Figure 3.2B). The pH and chain length of the polycation influence the self-assembly. Hence, pMETAC was synthesized in two different lengths (pMETAC1 M_w ≈ 3.3 kDA and pMETAC2 M_w ≈ 16.5 kDa) to study the impact on the self-assembly.

At pH>7, Qbeta formed colloidal crystals when the shorter pMETAC1 (≈ 3.3 kDa) was added in a ratio 1:50 (w:w) in suspension. The interaction of Qbeta and pMETAC1 across a broad pH range (3.0-9.0) and varied ratios of Qbeta and pMETAC1 (1:0.2-1:100) was investigated in-depth by small-angle X-ray scattering (SAXS) to map the

assembly conditions. The assembly of Qbeta/pMETAC1 into colloidal crystals was already indicated by Bragg reflections in the SAXS data at pH 7 and above at ratios 1:5—1:50 Qbeta/pMETAC1.

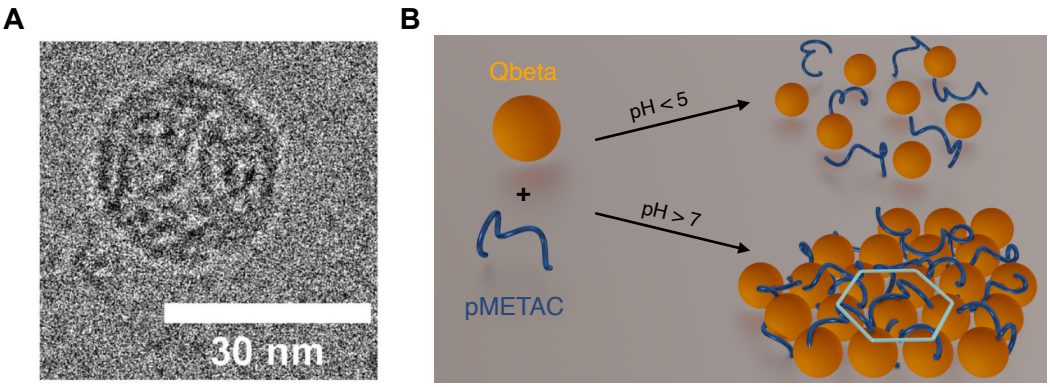

Figure 3.2. Self-assembly of Qbeta bacteriophages into colloidal suprastructures. **A** TEM image of a Qbeta bacteriophage with a diameter of ≈ 29 nm. **B** Qbeta assembled into well-ordered structures when pMETAC was added at pH > 7 and disassembled at pH < 5.

SAXS is a bulk method that yields data averaged across the entire sample volume acquired in reciprocal space. Modeling the scattering curves allowed the extraction of structural characteristics, but did not provide real-space structure information. The SAXS data acquired by our collaborators at the University of Fribourg suggested three §D aggregates with 2D hexagonal packing of Qbeta/pMETAC1 in suspension. However, so far, the proposed structure could not be verified in real space due to the fragile character of the assembly that forms in suspension.

In contrast, AFM imaging allows for the characterization of the structure of soft matter on the nanoscale in real space. These AFM measurements were the responsibility of the Department of Physical Chemistry II in Bayreuth. The prerequisite for the AFM experiments was that the sample was attached to a solid support. To analyze the colloidal crystals formed in suspension by AFM, these had to be transferred onto a supporting substrate without damaging or altering the fragile structures. Freshly cleaved ultra-flat gold substrates [30] provided a low roughness, high-energetic surface to which the colloidal crystals, preassembled in solution, adhered sufficiently well. The successful transfer of the colloidal suprastructures to a solid support was the first important step to image the nanostructure in real space. The fragile and soft character of assembly, paired with the nanoscale structural features and liquid environment, required a careful choice of an AFM imaging mode and extensive optimization of the AFM imaging parameters. PeakForce Tapping with soft cantilevers and very low force setpoints allowed the acquisition of topographic images of the colloidal crystals in liquid for the first time. Long (> 12 h) equilibration times of the sample and cantilever in the buffered measurement

solution were required to reduce thermal instrumental drift. The resulting AFM images (cf. Figure 3.3A) of the nanoassemblies (1:50 Qbeta/pMETAC1, pH 7) showed indeed hexagonal nanostructures with high lateral resolution as observed in suspension by SAXS. In the following, a quantitative comparison of both structures had been attempted.

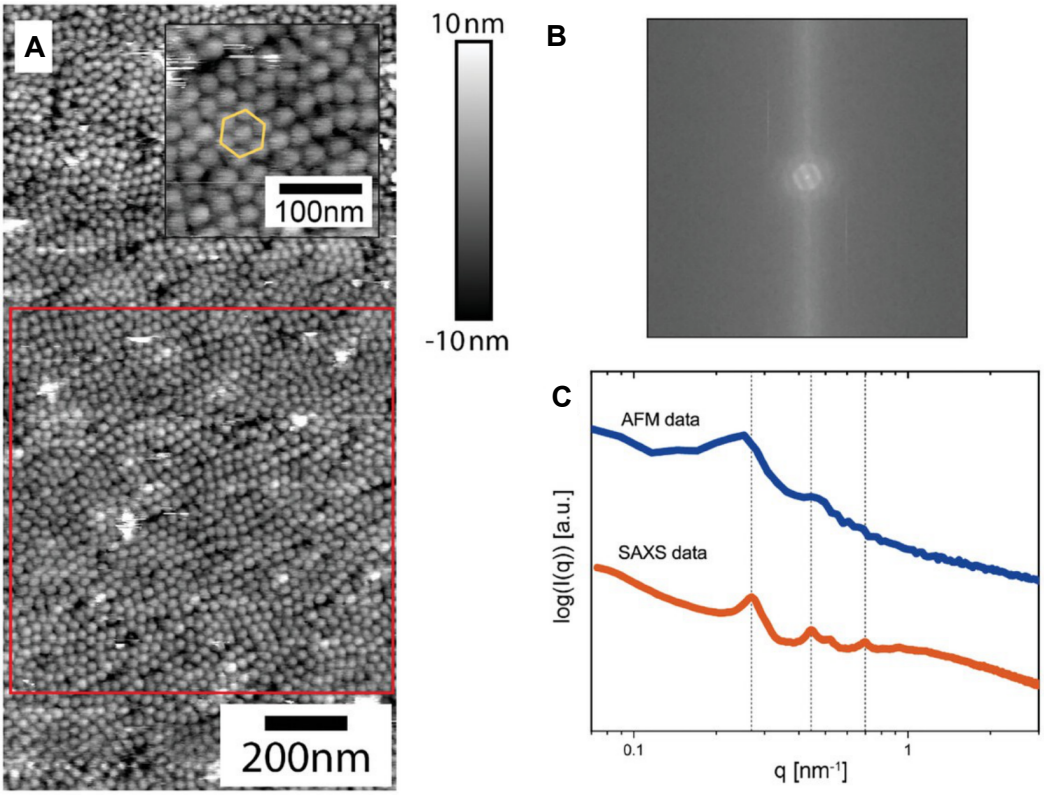

Figure 3.3. Hexagonal patterns of Qbeta in the presence of pMETAC1. **A** AFM height image acquired in PeakForce Tapping mode in liquid reveals a well-ordered hexagonal packing of Qbeta assembled with pMETAC1. **B** 2D FFT analysis of the area marked with a red square, underlines the ordered character of the nanostructures. **C** Azimutal integration of the FFT spectrum intensities (blue) and SAXS curve (orange) shows similar peak positions as indicated by the dashed guide to the eye.

The hexagonal pattern spanned large areas reaching several hundred nanometres. Moreover, the center-center spacing of the Qbeta capsides in height profiles in the AFM images was ≈ 29 nm which is the exact distance expected from the TEM of single Qbeta and the Bragg reflections in SAXS data acquired in suspension. However, we aimed not only to reveal the real space nanostructure but also to directly overlay the results from SAXS acquired in suspension and the AFM data measured on a solid support. Thus, we applied a two-dimensional fast Fourier transform (FFT) to the AFM data to calculate a scattering spectrum (Figure 3.3B). Azimutal integration yielded a one-dimensional scattering curve, analogous to the SAXS data in reciprocal space (Figure 3.3C). The scattering peaks in both scattering curves, i.e., the SAXS reciprocal data and the FFT of the AFM image, were

located at similar positions. Despite minor deviations and smearing of the scattering peaks of the AFM curve, which could be attributed to AFM's finite data sets of domains in contrast to SAXS, a good agreement of real-space and reciprocal space was obtained. Hence, we could prove that the hexagonal packing of the nanocolloids extracted from modeling the SAXS curves matched the nanostructure of the colloidal assemblies in real space.

Beyond proving the structure by correlating SAXS and AFM, the chemical surface composition of Qbeta when adding pMETAC1 was investigated by X-ray photoelectron spectroscopy (XPS). Additionally, in-situ examination of the assembly process by DLS showed that the process follows diffusion-limited aggregation. Moreover, it could be demonstrated that the colloidal crystals were stable at pH > 7 and at temperatures $< 60°C$. Furthermore, Qbeta maintained its biological activity after separation from the liquid phase at a slightly reduced rate compared to the suspended form. This broad range of conditions underlined the versatility of this straightforward assembly strategy and the broad application potential of the colloidal crystals in biomedicine and nanotechnology.

The **Colloidal Nanoassembly** project assembled biocolloids with a polyelectrolyte into a well-ordered structure. The suspension pH and the length of the polycation governed the assembly. AFM was correlated with SAXS, operating in reciprocal and real space, respectively, to study the structural properties of colloidal crystals in-depth. The successful transfer of the nanostructures from suspension to the surface and the adaptation and optimization of advanced AFM imaging were crucial to proving the hexagonal packing of the colloids. All AFM-related work has been performed in Bayreuth at the chair of Physical Chemistry II.

Electrogelation: Controlled Fast Formation of Micrometer-Thick Films From Low-Molecular Weight Hydrogelators

The first project introduced an easy and scalable approach to assembling bio-colloids into functional colloidal crystals in suspension. However, building blocks for self-assembly can be even smaller, e.g., low molecular weight compounds.

The second project **Electrogelation** investigated the growth of hydrogel films based on low molecular weight hydrogelators (LMWHG). LMWHG are a special class of compounds that reversibly assemble into supramacromolecular, often fibrous structures via non-covalent interactions.[19, 31, 32] The fibrous network swells in the surrounding liquid to form a hydrogel. The high water content, softness, and inherent responsiveness to external stimuli like temperature and pH make soft LMWHG films attractive for life-science applications. However, immobilization strategies or surface-mediated

hydrogelation approaches and respective characterization techniques are required to use them as functional coatings.

Conventional coating techniques like drop casting or spin coating show limited possibilities to form very soft hydrogels or thin hydrogel films. Moreover, they only work for planar surfaces. One alternative approach for coating conductive substrates with a hydrogel film is electrodeposition. Silk proteins and other biopolymers like alginate or chitosan have been assembled into films by electrochemical deposition to metal surfaces, albeit high potentials are typically required.[33–40] In contrast, the electrogelation of low molecular weight hydrogelators is reported sparsely.[41–43] Electrogelation refers to processes in which the sol-gel transition is induced by an electrochemical trigger, e.g., reduction or oxidation of a redox mediator or electrochemical shift in pH at the electrode interface. Then, a hydrogel film grows directly from the conductive substrate. To control the assembly process and, in turn, the hydrogel film thickness, adequate tools are needed to measure the film thickness. Optical or fluorescence microscopy techniques work well for dense and thick polymeric layers. However, very soft and thin layers cannot be traced by such techniques. Thus, to study the early stages of film growth, different techniques are required, which have been developed in the framework of this thesis.

Within the **Electrogelation** project, we employed a simple technique to grow µm-thick soft hydrogel films electrochemically within very short timeframes (15 to 120 s). A pH-responsive low molecular weight compound *N,N',N"*-Tris(4-carboxyphenylene)-1,3,5-benzenetricarboxamide (BTA) assembled into fibrillar structures which formed a hydrogel network upon applying an external potential. We chose BTA to establish adequate analytical techniques to assess the thickness during the early stages of hydrogel film formation by electrogelation. BTA is a pH-responsive LMWHG that assembled into fibrous structures upon protonating its terminal carboxyl functionalities (Figure 3.4A).[44] The pH shift required for the electrogelation of BTA was based on the proton generation at the working electrode interface with the BTA solution.[45] A sufficiently large potential to facilitate electrochemical water splitting was applied. The protons generated in the oxygen-evolution reaction (OER) shift the pH locally to the acidic regime. BTA was protonated near the electrode interface, forming a hydrogel film (Figure 3.4B). We proved the successful formation of the expected fibrous structure by acquiring AFM and SEM images of dried electrogelated BTA films in Figure 3.4C,D.

The primary interest was accessing and then controlling the thickness of the hydrogel films. The films were too thin and too low in contrast to the surrounding medium due to the high water content, preventing them from being traced optically. Quartz crystal microbalance (QCM), a technique that is used to track polymer film swelling and electropolymerization processes, reaches its limits with increasing film thickness due

to hydrodynamic effects. We developed techniques based on AFM that overcame the above-described limitations.

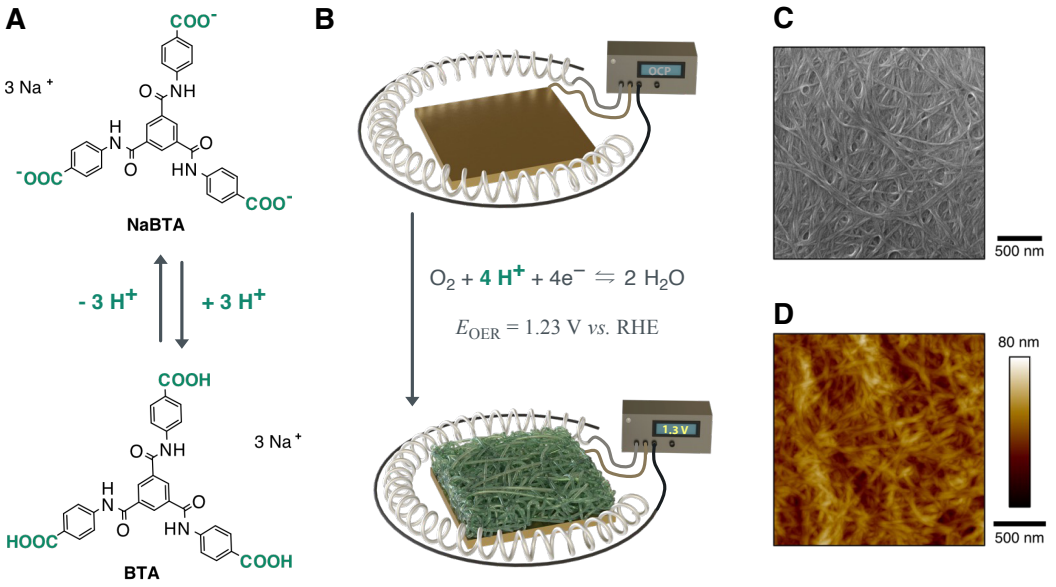

Figure 3.4. **A** pH triggered assembly of NaBTA (dissolved) to BTA (assembled). **B** Electrogelation of BTA into hydrogel films is induced by locally shifting the pH to the acidic regime. The oxygen evolution reaction (OER) generates protons at the working electrode. BTA self-assembled into fibrillar hydrogel films due to the protonation of its terminal groups. **C** SEM and **D** AFM height sensor images of the dried BTA films reveal the fibrillar structure.

The thickness of polymeric films is typically studied by scratching the film and determining the step height on AFM images along the edge of the scratch (Figure 3.5A). This scratching and imaging approach was successful for dried BTA films. We observed the expected film thickness increase with electrogelation time, i.e., the time for which an external potential was applied to the WE (Figure 3.5B). However, a hydrogel loses its characteristic of a swollen network upon drying. Hence, we aimed to study the film thickness in its native, swollen state. Meanwhile, the scratching and imaging approach was straightforward for dried BTA films; it was unsuitable for very soft, swollen hydrogel films. To overcome this limitation, we adapted another AFM-based method, which was successfully used on much thinner lipid bilayers and much stiffer polyelectrolyte thin films [46, 47]. Instead of moving the cantilever laterally, the sharp tip was pushed through, i.e., indented vertically into the film until the non-deformable electrode was reached (Figure 3.5C). Thus, this technique was referred to as full-nanoindentation. An exemplary force vs. distance relation of the full-nanoindentation experiment is depicted in (Figure 3.5D). The initial contact point of the tip with gel marked the farthest extension of the hydrogel film from the electrode. Further indenting the tip into the film resulted in increasing forces, due to the mechanical response of the hydrogel. This mechanical response can also be used to determine elastic properties (cf. **Microgel**

Nanoindentation, Chapter 7). Here, however, nanoindentation was primarily used to determine the hydrogel film thickness. The non-monotonous increase in force during the "piercing process" reflected the fibrous character of the hydrogel. Forces increased infinitely once the tip contacted the non-deformable electrode. The distance between the initial contact with the hydrogel and the contact with the rigid substrate corresponded to the BTA film thickness in the swollen state. Thus, by adapting the full-indentation method, we were able to investigate the electrogelated hydrogel film thickness in its natural hydrated state for the first time.

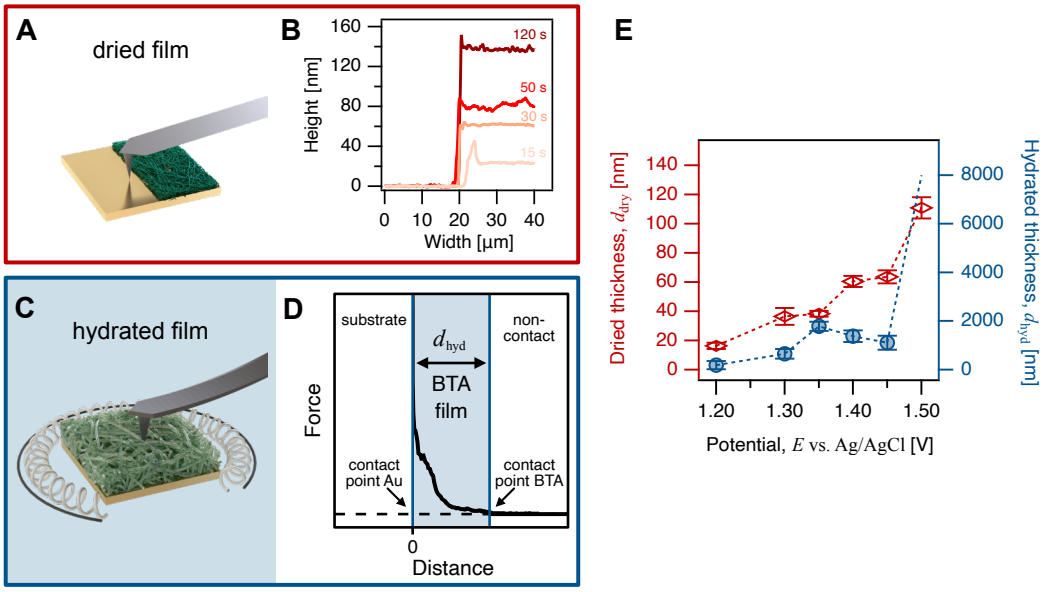

Figure 3.5. The BTA film thickness was studied via two different AFM-based techniques: imaging at the edge of a scratch in the dried state (red, **A**, **B**) and nanoindentation in the hydrated state (blue, **C**, **D**). Panel **A** and **C** illustrate the two techniques; **B** averaged cross-sections as determined by AFM imaging at the edge of a scratch in dried BTA films; **D** representative force vs. distance curve acquired by indenting a hydrated BTA film. The distance between the contact point with the gel and the contact point with the substrate represented the BTA film thickness. **E** Thickness of the same electrogated hydrogel film in hydrated and dried states for different potentials.

The hydrated film thickness determined by nanoindentation and the dried film thickness for a series of electrogelation potentials showed similar trends (cf. Figure 3.5E). Based on mass conservation during the drying process of the hydrogel films, we calculated a swelling factor (29 ± 15), i.e., the ratio of d_{hyd} and d_{dry}. Thereby, we could relate the hydrated and the dried thickness as determined by the two different AFM-based approaches.

We found three main parameters that influenced the electrogelation process and, hence, could be used to control the thickness of the hydrogel film: the electrogelation time,

the electrogelation potential, which was applied to the working electrode, and the concentration of the LMWHG in the gelation solution (cf. Figure 3.6).

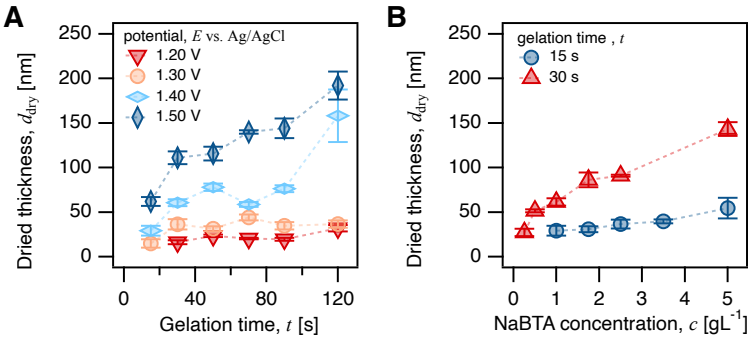

Figure 3.6. The thickness of electrogelated hydrogel films could be controlled via the assembly conditions: electrogelation time, the applied potential, and the LMWHG concentration. **A** Film thickness vs. time plots for different potentials and constant concentration; **B** Film thickness vs. BTA concentration plot for different gelation times at a constant potential.

The film thickness could be controlled throughout a range of one order of magnitude by adjusting the electrogelation time ($15-120$ s), potential ($1.2-1.5$ V). Moreover, it became evident that LMWHG concentrations $5-10$ fold lower than bulk concentrations were sufficient to electrogelate hydrogel thin films. Furthermore, we could control the film thickness with an accuracy of ≈ 10 nm.

The **Electrogelation** project introduced an easy one-pot method that allowed assembling soft hydrogel coatings with controlled thickness within $15-60$ s at comparably low potentials. Adapting two AFM-based techniques, namely full-nanoindentation and imaging at a scratch, enabled the thickness characterization in different stages of the assembly process and under varied conditions. Establishing these techniques allowed to study the influence of assembly parameters. Finally, the methodological advancement enabled the assembly of LMWHG into hydrogel films to be controlled. The control over the electrogelation, i.e., the assembly, and the AFM-based film characterization techniques can easily be transferred to other responsive LMWHG or hydrogel thin films.

3.1.2 Advanced Atomic Force Microscopy Techniques for Soft Matter

The picobalance was initially designed to investigate single-living cells gravimetrically.[14] Like soft hydrogels, cells comprise a complex structure and a high water content. The picobalance can trace mass changes of loosely attached complex soft matter with high mass resolution. However, this resolution has not yet been corroborated by implemented techniques. Integrating the existing AFM-based mass balance with electrochemistry in this work opened up the possibility of developing a new method to trace electrochemical assembly processes by current and gravimetric response simultaneously. The working principle, validation, and calibration of the here-developed **Electrochemical Picobalance** and the development of custom-made electrochemical mass probes used by this technique are introduced in the following section.

AFM-based nanoindentation is the gold standard for determining the elastic properties of particulate soft matter like cells or their synthetic mimics, microgels. However, fundamental instrumental questions regarding the indenter geometry choice, adequate contact mechanics modeling, and the impact of measurement parameters have not yet been addressed. The **Microgel Nanoindentation** project extensively and systematically reassessed AFM-based elasticity measurements to tackle exactly these questions. An in-depth investigation on two model systems allowed us to reevaluate, refine, and enhance the current state-of-the-art in nanoindentation of particulate soft matter. Based on the comprehensive and systematic investigation of all influential parameters, like the tip geometry, contact models, experiment design, and measurement settings, the project concluded with best-practice advice for other researchers in the field.

Electrochemical Picobalance: Proof-of-Principle for an Electrochemical Cantilever-based Mass Balance

Thickness studies of LMWHG films are challenging due to the highly swollen character of non-covalently crosslinked hydrogels. Standard methods to study film thickness and film growth in situ, like the quartz crystal microbalance (QCM), reflectometry, ellipsometry, and optical microscopy, work nicely for rigid inorganic materials or dense, non-swollen polymer films. However, there are hydrodynamic limitations to the thickness of swollen soft matter with shear oscillations used for QCM tracking. Even at the lowest possible concentration and potential, the BTA film outgrows the upper EQCM detection limit within seconds. The energy dissipation is enormous due to the highly swollen hydrogel network, which is only loosely bound to the surface of the QCM sensor. Thus, there is a tremendous need to develop new instrumental techniques or adapt existing methods to overcome the current limitations.

One method that allows for tracing mass changes in complex soft matter dynamically is the picobalance. The picobalance is an AFM-based technique designed to study the mass of individual cells and fluctuations throughout the proliferation cycle of a cell.[14] A single cell is attached to an AFM cantilever. As the natural resonance of a resonator changes when an external mass is added, the sample mass and its evolution over time can be tracked by recording the frequency shift. Due to the high precision of frequency analysis, small mass changes down to the picogram regime can be resolved. Moreover, the picobalance can discriminate the object mass of complex soft matter, like cells, from its liquid surroundings, even at tiny differences in density. Hence, this method meets the general requirements to trace the dynamics of soft matter assembly, e.g., the assembly of a hydrogel film.

We developed the **Electrochemical Picobalance** with the long-term objective of investigating electrochemical assembly, like electrogelation, and processes related to organic bioelectrics by an AFM-based technique in situ and dynamically. To achieve an electrochemically active setup, we needed to transfer the working electrode from a macroscopic substrate mounted to an AFM fluid cell, as used in the **Electrogelation** project, directly onto an AFM cantilever. Thus, we developed modified AFM cantilevers, so-called electrochemical balance probes (EBPs), with an integrated planar microelectrode on an otherwise fully insulated cantilever (cf. Figure 3.8). Based on a previously developed process to fabricate electrochemical colloidal probes via a masking technique [48], we enhanced and adapted the insulation procedure to meet the requirements for use in the electrochemical picobalance. Defect-free insulation of the cantilever chip and arm was essential for quantitative measurements in the electrochemical picobalance. Any potential defect in the insulation could lead to electrochemical deposition outside the designated microelectrode. Then, the deposited mass would either not be tracked or could not be accounted for correctly during the evaluation, i.e., the conversion of the detected frequency shift into the mass. Thus, we opted for a dual insulation strategy. The cantilever chip was coated in a thick layer of red insulating varnish with enhanced scratch resistance and mechanical stability (cf. red coating in Figure 3.7A). The lever arm was coated with a transparent thin layer of electropaint (cf. blueish coating in Figure 3.7A) through a multi-step procedure with intermittent curing phases. The resulting insulating layer on the lever arm was sufficiently flexible to allow for cantilever oscillations, and its transparency ensured that the cantilever could still be excited photothermally and the optical lever technique in the AFM could read out its movement. Figure 3.7A illustrates a successfully insulated EBP with a microelectrode area and displays a respective EBP photograph. The microelectrode located close to the free end of the cantilever arm was visible in the SEM images in Figure 3.7B.

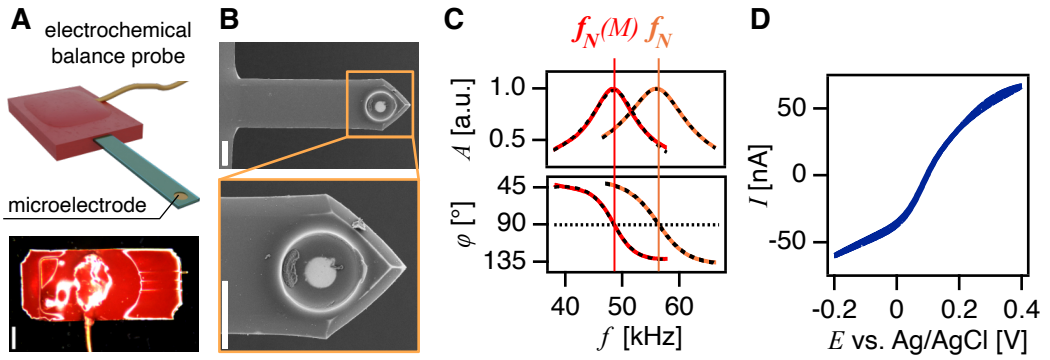

Figure 3.7. Electrochemical balance probes (EBPs) with purpose-tailored characteristics have been developed for the electrochemical picobalance. **A** Illustration and photograph of an EBP with the scalebar representing 500 µm. **B** SEM images of the insulated cantilever arm bearing an approximately circular microelectrode at the free end (zoom-in). Scale bars represent 20 µm. EBPs function as mass sensors and microelectrodes: **C** The phase $\varphi(f)$ and amplitude $A(f)$ response of an EBP to photothermal excitation in the picobalance. The natural resonance f_N (orange) shifts to $f_N(M)$ when an external mass is attached to it (red). **D** Cyclic voltammogram of the EBP microelectrode in cyanidoferrate solution.

We individually verified the electrochemical and gravimetric performance of the EBPs before implementing them in the combined electrochemical picobalance setup. The EBP structure was more complex than a conventional cantilever. An EBP comprised a silicon cantilever core with an Au-coating enclosed by a thin layer of electropaint insulation. Thus, we verified their suitability for mass detection independently from the electrochemical setup by 'weighing' external masses, i.e., tungsten microspheres. Figure 3.7C displays frequency sweeps without and with an external added mass M, i.e., a tungsten bead. The theoretical mass calculated from the particle dimension and density agreed with the mass determined from the resonance frequency shifts in the picobalance. The picobalance mass $m_{\mathbf{PB}}$ was calculated according to

$$M = \frac{k}{4\pi^2}\left[\frac{1}{(f_N - \Delta f_N)^2} - \frac{1}{{f_N}^2}\right] \tag{3.1}$$

$$m_{PB} = C \cdot M \tag{3.2}$$

with the apparent mass M, spring constant k and considering a correction factor $C = \frac{1}{\psi^2(x_c)}$ for the mass position on the EBP.[14] In the second step, we validated the electrochemical performance of the EBP by cyclic voltammetry in cyanidoferrate solution (Figure 3.7D), which provided microelectrode properties.

Figure 3.8 illustrates the fully operational electrochemical picobalance setup. The successful development and independent verification of the EBPs' gravimetric and electrochemical performance were essential for developing the electrochemical picobalance.

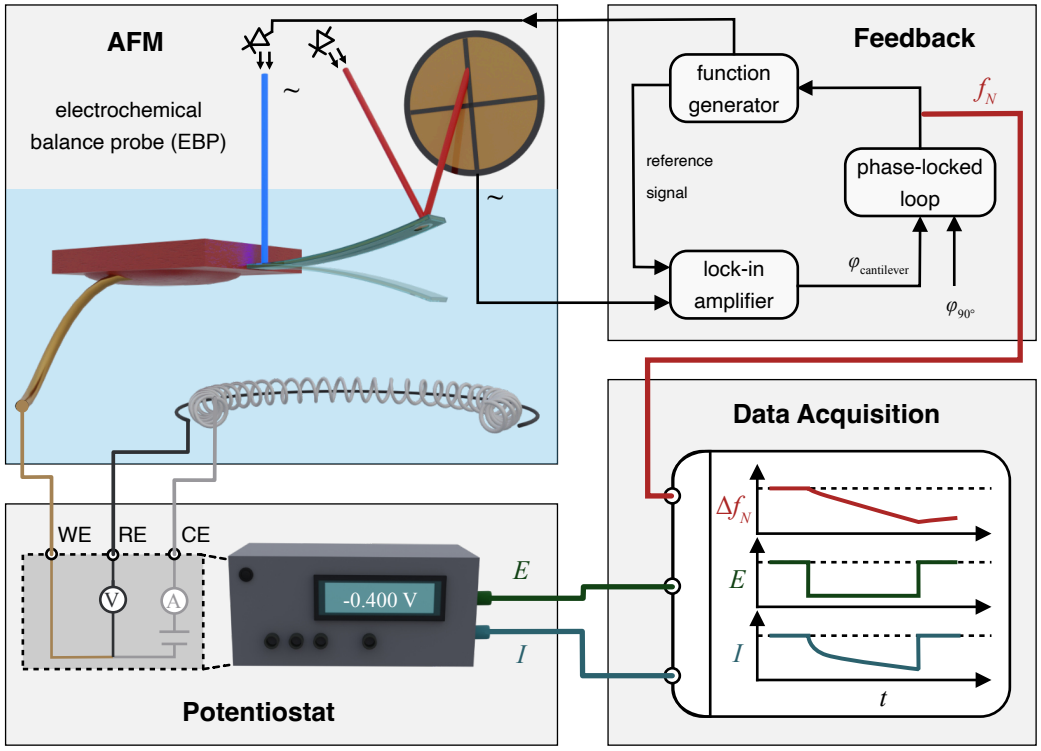

Figure 3.8. Setup and working principle of the electrochemical picobalance. A potentiostat controls the three-electrode setup integrated into the picobalance. The counter and reference electrodes are implemented into the fluid cell of the picobalance, while the microelectrode on the insulated cantilever serves as the working electrode. An intensity-modulated laser (blue) drives the cantilever to oscillation. The cantilever oscillation is detected with a second laser (red) using the optical lever technique. A phase-locked loop-based feedback maintains a constant phase by adjusting the excitation frequency modulated by the function generator. A data acquisition unit captures all signals from the AFM and electrochemical setup.

We established a picobalance setup based on a commercial AFM with photothermal excitation.[49] The EBPs were driven by a photothermal excitation laser, which was operated externally using a lock-in amplifier. The lock-in amplifier also comprised the phase-locked loop (PLL) responsible for tracking the resonance frequency shift due to the added mass. The picobalance setup was integrated with a three-electrode electrochemical cell controlled by a potentiostat to build the electrochemical picobalance. The microelectrode integrated into the custom-developed EPBs functioned as the WE. A platinum CE and Ag/AgCl RE were incorporated into the AFM fluid cell. The EBP served a dual purpose in the electrochemical picobalance; it was the mass sensor and held the WE, the integrated microelectrode. An external data acquisition unit monitored all relevant signals from the potentiostat (potential, current) and the picobalance (frequency, amplitude, phase) with a common timestamp for direct gravimetric and electrochemical readout correlation.

The here-developed electrochemical picobalance had to be verified and calibrated. Copper electrodeposition ($Cu^{2+} \longrightarrow Cu^0$) was used for the proof-of-feasibility (Figure 3.9A), analogously to a standard calibration approach for macroscopic electrochemical mass balances, the EQCM. By applying a reductive potential, Cu^{2+} was reduced and assembled into rigid thin layers on the microelectrode of the EBP. Thus, we could verify the novel method independent of possible effects by the softness and deformability of a hydrogel. Moreover, the gravimetric response of the picobalance could be directly confirmed by the electrochemical mass using Faraday's law of electrolysis (cf. Figure 3.9B, C).

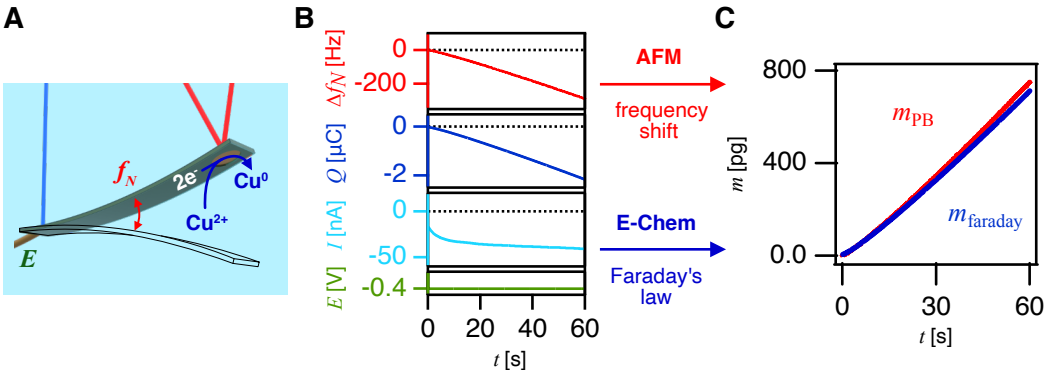

Figure 3.9. Proof-of-feasibility of the electrochemical picobalance. **A** Illustration of the electrodeposition of copper at the EBP microelectrode. **B** The electrochemical picobalance traced the frequency shift $\Delta f_N(t)$ and current response $I(t)$ of the EBP simultaneously, during electrodeposition induced by a reductive potential E. **C** The frequency shift Δf_N and the transferred charge $Q = \int I dt$ were converted to the masses m_{PB} and $m_{faraday}$. The high agreement between the picobalance and the Faraday mass verified the working principle of the electrochemical picobalance.

The frequency shift $f_N(t)$ during the electrodeposition of copper was traced by the picobalance and was converted into the picobalance mass. Simultaneously, the current $I(t)$ was monitored. Integrating the current signal yielded the total charge transfer at the electrode $Q = \int I dt$ during electrodeposition, which correlated with the frequency shift detected by the picobalance (cf. Figure 3.9B). The amount of copper deposited was proportional to the electrons transferred to the electrode according to Faraday's law $m_{faraday} = -\frac{QM_W}{zF}$ with the Faraday constant F and z electrons transferred to form a compound of the molecular weight M_w. The gravimetric mass detected by the picobalance agreed throughout the entire copper deposition process with the electrochemical mass according to Faraday's law (cf. Figure 3.9C). These experiments marked not only the first successful dynamic depositions at the electrochemical picobalance, simultaneously traced gravimetrically and electrochemically. More importantly, they proved the quantitative gravimetric accuracy of the newly developed technique with a current resolution limit of $\lesssim 1$ pg. However, an even higher mass resolution could be achieved by optimizing the electronics, as AD converter artifacts of the employed electronics

supposedly caused the current limitation. We conducted comparable copper deposition experiments at the electrochemical quartz crystal microbalance (EQCM) and determined the mass sensitivities for both techniques. Meanwhile, the mass sensitivity normalized to the electrode was higher for the EQCM (460 $ng\,cm^{-1}\,Hz^{-1}$ vs. 17.5 $ng\,cm^{-1}\,Hz^{-1}$), the electrochemical picobalance had a significantly higher absolute mass sensitivity (2.44 $pg\,Hz^{-1}$ vs. 19.8×10^{-3} $pg\,Hz^{-1}$) and higher absolute mass resolution (1 pg and $\approx$ 10 ng).

Overall, the **Electrochemical Picobalance** was successfully developed, its working principle was verified by copper deposition, and its gravimetric response and sensitivity were calibrated using Faraday's law of electrolysis. The proof-of-feasibility showed that electrochemical techniques like chronoamperometry or cyclic voltammetry could be directly used in the picobalance on cantilever-integrated microelectrodes. Custom-designed and fabricated EBPs were essential not only for the electrochemical picobalance but also for introducing a new multifunctional AFM probe to the cantilever portfolio. Adding the electrochemical picobalance to the existing AFM toolbox enlarged it to trace dynamic electrode processes simultaneously by its current and gravimetric response on the EBPs with a current resolution of down to $\lesssim$ 1 pg. The integration of the AFM-based mass balance with an electrode directly implemented into the mass sensor opens up new applications within and beyond soft matter assembly. In contrast to the AFM-based techniques used in **Electrogelation**, the electrochemical picobalance enables continuous dynamic tracking of the growth process. Beyond, the **Electrochemical Picobalance** could also be a powerful method in single-entity electrochemistry and for investigating cell response to electrical stimuli or electrical signal pathways on the cellular level, in the future.

Determining the Elastic Modulus of Microgel Particles by Nanoindentation

The elasticity of a material, defined by its Young's modulus, is a key characteristic of hydrogels and is of utmost relevance in the context of biomaterials. For instance, cell growth in tissue engineering can be enhanced by tuning the elasticity of the matrix.[50, 51] Moreover, particulate hydrogels, often called microgels, are used to mimic cells, for example, in developing biofabrication processes.[52–55] The final project of this thesis, **Microgel Nanoindentation**, enhanced and developed AFM-based nanoindentation on particulate soft matter. Due to their target application in biofabrication, microgels with cell-relevant size and elastic properties were required. The LMWHG hydrogels presented in the project on **Electrogelation** are significantly softer than cells. Thus, we moved to covalently crosslinked hydrogels based on polyacrylamide (PAAm) and ene-functionalized polyoxazoline (POx) with thiol-functionalized hyaluronic acid (POx-HASH) for the **Microgel Nanoindentation** project. PAAm is a standard microgel system,[56] meanwhile,

POx-HASH has been proposed for bioink applications.[57, 58] By combining a standard and an application-relevant system, we could verify that our experimental findings and resulting method refinement are relevant to different kinds of particulate soft matter.

Microgels with monodisperse size distribution and elasticity in the cell-relevant regime could be synthesized by droplet microfluidics. Two immiscible fluids were directed across a junction, where shear forces created uniform microdroplets of the hydrogel precursor. The precursor droplets were gelated, e.g., by covalent crosslinking of the network. The crosslinking density defined the microgel's final elastic properties, which allowed to tune the elastic properties.[56] By this approach, two types of microgels with cell-relevant size ($d \approx 25-30$ µm) and elastic moduli (< 10 kPa) were fabricated for this project.

Different techniques can characterize such microgels' elasticity, with AFM-based nanoindentation being the gold standard. Even though nanoindentation by AFM is widely used to study Young's moduli of particulate hydrogels, several central questions remained open. While describing the elastic deformation of bulk materials without adhesion is relatively straightforward, thin films or spherical objects like microgels or cells exhibit a more complex behaviour. Models accounting for the finite sample thickness in thin films [59–61] and the double contact model taking the deformation at the substrate-sample in addition to the indenter-sample contact for microgel or spherical cells into account [62–64] have been introduced. Even though the double contact model for particulate soft matter nanoindentation has been around for over a decade, it has been used very sparsely so far. The simpler Hertz model is commonly employed for particulate soft matter without verifying its validity, especially for microgels. Lack of a systematic and extensive experimental proof for the double contact could be one of the reasons. Moreover, although the Young's modulus is a material's property, significant deviations have been observed when different indenter types (e.g., a sharp tip and a colloidal probe) have been employed on the same sample.[56, 62] Thus, there is a fundamental instrumental knowledge gap in a standard method employed to determine the elastic properties of microgels and comparable particulate soft matter.

The **Microgel Nanoindentation** project addressed these questions systematically using six different indenter geometries for AFM nanoindentation on two distinct microgel systems — PAAm and POx-HASH. We modified commercially available cantilevers to create a cantilever library comprising six different indenter geometries. Figure 3.10A displays SEM images of the respective indenter geometries: The indenter selection included α a commercial sharp tip indenter with a conical tip (half angle $\theta = 25°$) and β a commerical rounded tip ($R = 1$ µm) which has been designed specifically for biological applications. This geometry resembles an intermediate between the cone and larger spherical indenters. We fabricated two different types of spherical indenters, i.e., colloidal probes γ and δ with different radii, smaller ($R = 3.3$ µm) and comparable to

the microgel radius ($R = 10.5$ µm), by attaching silica microspheres to tipless cantilevers. Additionally, ε a tipless cantilever was used to create a plate-plate configuration. However, as AFM cantilevers are mounted at a tilt angle, microgels were deformed with the tilt angle by the tipless cantilevers. To assess and eliminate potential impacts of the tilt angle, we custom-build tilt-corrected indenters, so-called wedge cantilevers ζ, by attaching a "wedge" to the free end of tipless cantilevers.

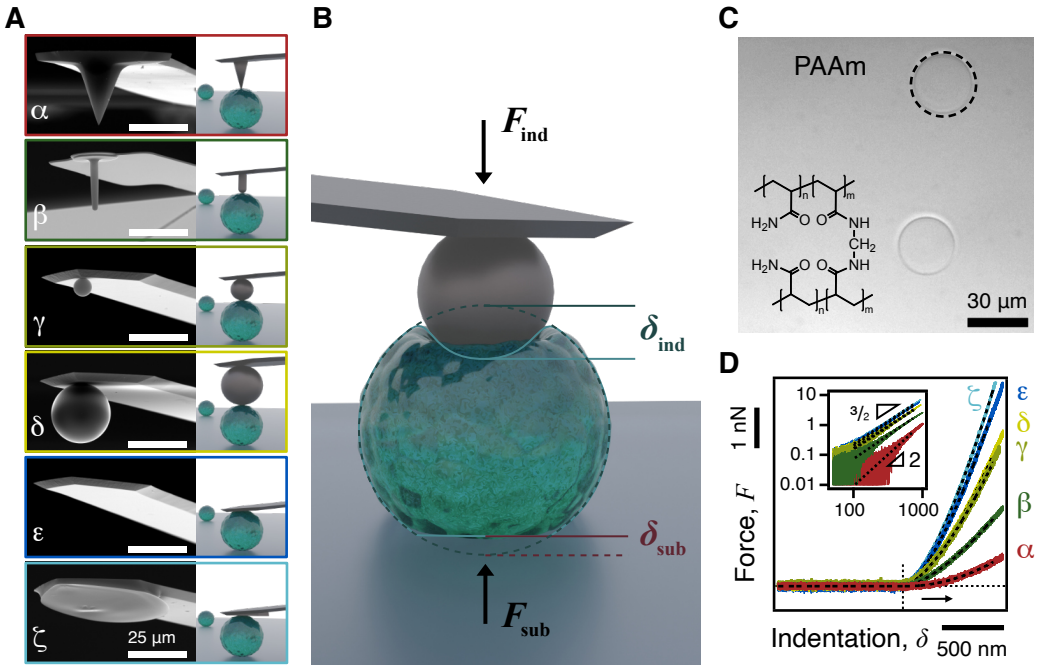

Figure 3.10. **A** Experimental design to indent the same microgel particle with six different indenter geometries ($\alpha - \zeta$). SEM images of α conical sharp tip; β a rounded tip; γ small and δ large colloidal probes; ε tipless and a ζ wedged cantilever compensating for the tilt of the lever arm. **B** Illustration of an AFM nanoindentation experiment using a colloidal probe indenter. **C** Optical microscopy image of PAAm microsphere. **D** Representative force vs. indentation profiles acquired with geometries $\alpha - \zeta$ on the same PAAm microgel particle. The inset shows the power law dependency of the force with the indentation ($F \propto \delta^2$ for α and $F \propto \delta^{\frac{3}{2}}$ for $\beta - \zeta$).

We employed six types of indenters to assess the impact of indentation geometry on Young's moduli. However, instead of measuring a large number of particles, we opted for a different approach. We indented the same microgel particle with all six indenters for a selection ($n = 5$) of particles (insets in Figure 3.10A).

Figure 3.10B illustrates the indentation process and resulting interaction geometry for a colloidal probe deforming a microgel particle. Representative force vs. indentation profiles acquired with geometries $\alpha - \zeta$ (cf. Figure 3.10D) on a PAAm microgel particle (Figure cf. 3.10C) demonstrated the different force-indentation relations depending on the indenter shape and size. Overall forces increased with the size of the indenter at the same indentation depth. Moreover, the power law relation $F \propto \delta^2$ for the

conical indenter α and $F \propto \delta^{\frac{3}{2}}$ for the spherical and planar geometries $\beta - \zeta$ have been determined in accordance with the contact models.

Two models are primarily used throughout the literature on elasticity measurements for microgel and spherical cells: (i) The simple Hertz model [65] that only considers deformation at the indenter-sample contact is still a standard in the literature. (ii) The simplified double contact model [62–64] additionally takes the deformation at the sample-substrate contact into account (Figure 3.10B) but has been employed sparsely. Since the Young's modulus is a material's property, no difference in elasticity should be measured using different indenter geometries, provided the contact model describes the interaction geometry adequately.

We used both models to evaluate the data acquired on the five selected PAAm microgel particles with indenters $\alpha - \zeta$ (Figure 3.11A). Meanwhile, apparently higher Young's moduli were calculated with decreasing indenter size when the data were evaluated using the classical Hertz model. Moreover, we could show that the data for the conical indenter is prone to higher inaccuracies, as its geometry is less well defined in contrast to, e.g., a spherical colloidal probe. The discrepancies between the Young's moduli by different geometries were decreased significantly when the SDC model was used instead. The remaining discrepancies were assigned to the adhesive interaction of the sample and the supporting substrate (cf. Figure 3.11B) by pairing the AFM indentation experiments with total internal reflection fluorescence (TIRF) microscopy and finite element simulations. We introduced a dimensionless parameter Λ as a measure of the adhesive strength, related to the ratio of the adhesive radius r_{adh} and the particle radius r_{part}. To determine r_{adh} experimentally, a fluorescently labeled batch with otherwise comparable properties of the PAAM microgels was fabricated. TIRF microscopy of fluorescent-labeled particles (Figure 3.11C) provided an upper limit for the adhesion radius and the resulting predeformation stress exerted on the microgel particle. Finite element simulation of the predeformation for different Λ values (Figure 3.11D) and the deformation process using indenters $\alpha - \zeta$ comparable to the experiments were performed. Apparent moduli for all geometries were extracted by fitting the simulated interaction profiles to the SDC model (Figure 3.11E). The deviation of the apparent Young's modulus in contrast to the Young's modulus fixed in the simulation increased with Λ, i.e., with the strength of the adhesive interaction, which was the cause for apparently deviating moduli depending on the indenter geometry. By normalizing the experimental moduli to the apparent moduli for the respective geometry, we could demonstrate that Λ lies in a specific range for each microgel type. These findings underlined that, in general, the SDC models describe elasticity measurements by AFM-nanoindentation more adequately.

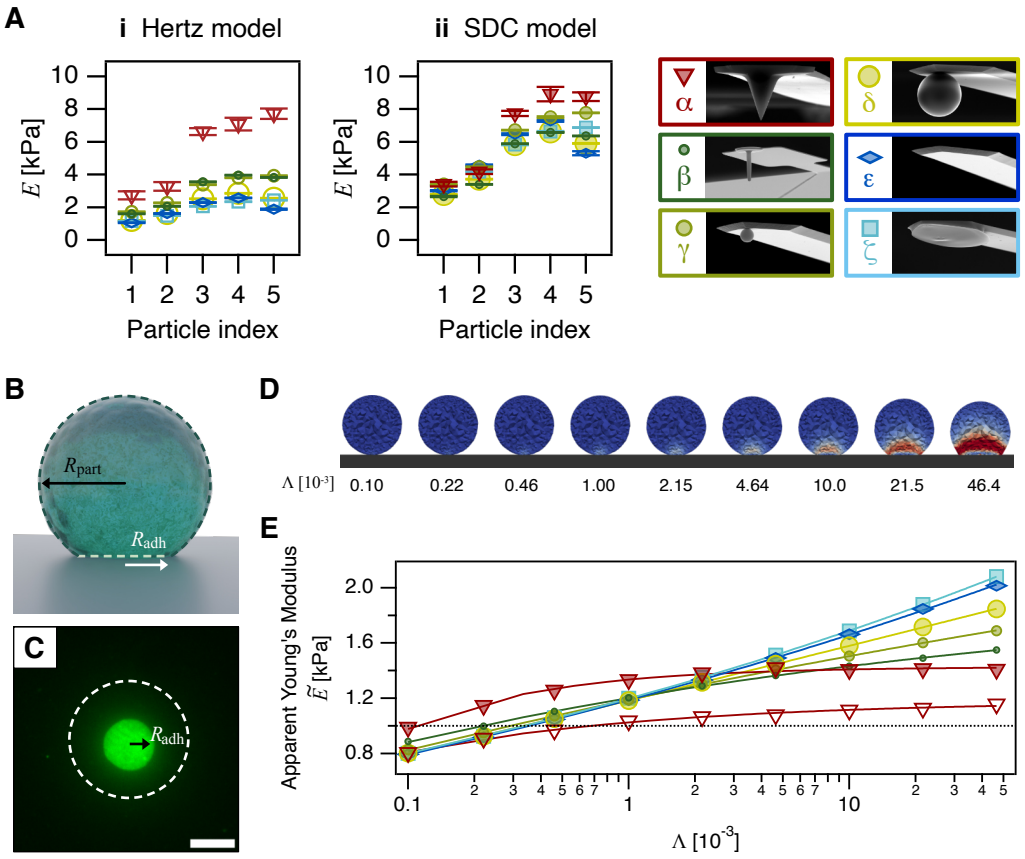

Figure 3.11. Indenter geometry and contact models for AFM-based nanoindentation on microgels. **A** Young's moduli of the same 5 microgel particles determined with $\alpha - \zeta$ according to (i) the Hertz model and (ii) the SDC model. **B** Visualization of the adhesion radius r_{adh} of a microgel particle with the radius r_{part}. **C** TIRF image of a fluorescent-labeled microgel particle attached to a glass slide with a contact area defined by r_{adh}. **D** Prestress of a microgel particle by finite element simulations depending on the dimensionless number Λ, which describes the adhesion between the particle and the substrate. **E** Apparent Young's moduli $\tilde{E}$ depending on Λ differ between the indenter geometry ($\alpha - \zeta$).

Apparent discrepancies between the geometries vanish when the substrate adhesion's influence is considered. Thus, our findings indicate that previously observed discrepancies in Young's moduli determined with different indenter geometries on the same system likely arose from using inadequate contact models like the Hertz model, paired with different contributions of the particle-substrate adhesion. The inaccuracies of the Young's moduli due to particle-substrate adhesion are reduced even further for smaller indenter sizes in the framework of the SDC model.

The impact of experimental parameters beyond the indenter geometry on the elasticity was elucidated to establish best-practice guidelines for the AFM-based nanoindentation of particulate soft matter (cf. Fig. 3.12). First, we showed that off-center contact between the indenter and the sample reduced the curve quality and underestimated the Young's

modulus. Thus, a force-based approach to locate the microgel apex instead of solely optically aligning the cantilever was used throughout this work and is recommended for similar investigations in the future. Moreover, we assessed the impact of experimental parameters on the elasticity measurements. The ramping velocity of the indentation has to be slow enough for hydrodynamic reasons, i.e., to prevent apparent stiffening of the sample caused by insufficient relaxation of the hydrogel. The indentation depth can also impact Young's modulus, e.g., if the microgel shows an elasticity gradient caused by the crosslinking mechanism. Furthermore, the indentation depth has to be adequate for the size of the indenter, i.e., not violate the small indentation limit assumed in the contact model.

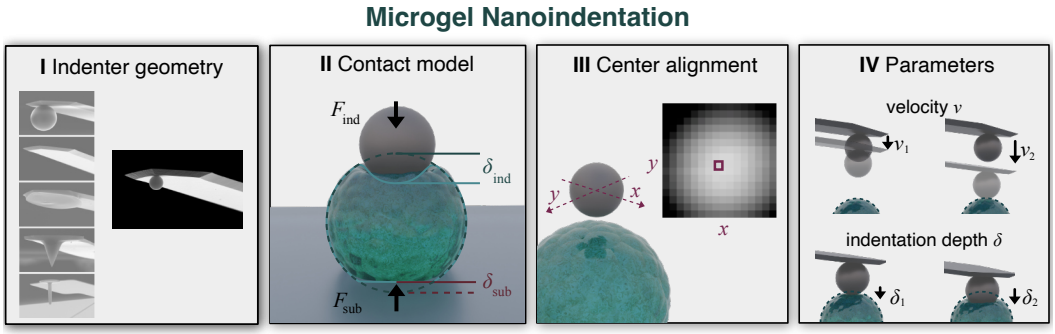

Figure 3.12. Key aspects to be considered for an AFM nanoindentation experiment. **I** Indenter geometry; **II** contact model; **III** center alignment of the indenter to the sample; and **IV** measurement parameters like the ramping velocity v and the indentation depth δ.

Figure 3.12 summarizes all relevant aspects to be considered from an instrumental perspective for any AFM-based elasticity study on particulate soft matter. The indenter should be chosen based on practical considerations when the SDC model is used (**I**): A small colloidal probe γ provides a suitable combination of a well-defined spherical geometry that is large enough to support a sufficient indentation depth with a small impact of the adhesive substrate interaction. The experimental data and simulations proposed that the SDC model describes the data more accurately (**II**). Tip-sample alignment by the AFM-based force mapping approach enhances the position accuracy compared to optical alignment, preventing the underestimation of the Young's modulus (**III**). Finally, the ramping velocity and indentation depth must be reassessed for any new sample and indenter combination to ensure precise experimental results (**IV**). The here-presented values could be used as a starting point. By following these steps and accurately reporting all experimental parameters precisely, the accuracy, reproducibility, and cross-study comparability of reported moduli of particulate soft matter like microgels or cells can be ensured.

The findings of **Microgel Nanoindentation** project were essential to establishing and verifying a new technique that inverts the role of indenter and substrate.[66] To re-

alize the inverted interaction geometry, fluidic force microscopy (FluidFM) is used to reversibly aspirate the microgel to the aperture of a microchanneled cantilever and ramp it against a substrate. This approach allows direct access to the impact of particle adhesion, either by ramping the same particle against a number of surfaces with varied surface functionalization or by inherently varying the suction pressure to tune the particle cantilever interaction. Comparing elasticity data acquired by both conventional nanoindentation and inverse nanoindentation using FluidFM on the same batches of PAAm and POx-HASH microgels, yielded agreeing moduli. Thereby, the novel approach was validated. Influential parameters for the conventional nanoindentation, like the indentation velocity and depth, remain valid also for the inverse nanoindentation. Potentially higher hydrodynamic effects at compared velocities due to the larger indenter size have to be considered compared to the conventional colloidal probe approach. In turn, the time-consuming step of indenter alignment can be avoided as the microgel is automatically centered to the aperture of the microchanneled cantilever. Thus, the novel technique opens up for high-throughput measurements, which allow for studying the distribution of Young's moduli frequently observed within microgel batches in greater depth. This work is not part of this thesis. However, it builds on and contributes together with **Microgel Nanoindentation** project to the method development for soft matter nanoindentation.

Overall, the **Microgel Nanoindentation** demonstrated how method evaluation and development, here by comprehensively reassessing all relevant influential factors of a widely used technique, builds a foundation for future studies in the field.

3.2 Individual Contributions to Joint Publications

The projects presented in this thesis were collaborative projects with colleagues from our group, other departments at the University of Bayreuth, and national and international partner institutions. In the following, the individual contributions of all authors for the respective publications will be declared. Corresponding authors are marked with asterisks.

Chapter 4: pH-responsive Virus-based Colloidal Crystals for Advanced Material Platforms

Bettina Tran, Samuel Watts, Jules D. P. Valentin, Nadine Raßmann, Madeleine Ramstedt, Georg Papastavrou and Stefan Salentinig*

We published this article in *Advanced Functional Materials*, **2024**, *34*(37), 2402257.

Bettina Tran synthesized and characterized the polymer, produced and purified the virus, and acquired and analyzed the small angle X-ray scattering (SAXS), X-ray photoelectron spectroscopy (XPS), electrophoresis, and dynamic light scattering (DLS) data. Moreover, she wrote the first version of the manuscript and assisted with the atomic force microscopy (AFM) data analysis for the AFM-SAXS correlation. **Dr. Samuel Watts** and **Dr. Jules Valentin** produced and purified the virus, revised the manuscript, and were involved in scientific discussions. **I** designed and conducted the AFM experiments, analyzed the AFM data, was involved in scientific discussions, and edited and revised the manuscript. **Prof. Dr. Georg Papastavrou** was involved in scientific discussions, and revised and edited the manuscript. **Prof. Dr. Madeleine Ramstedt** was involved in the XPS measurements and analysis, scientific discussions, and revised and edited the manuscript. **Prof. Dr. Stefan Salentinig** supervised the project, was involved in scientific discussions, and revised and edited the manuscript.

Chapter 5: Electrogelation: Controlled Fast Formation of Micrometer-Thick Films from Low-Molecular Weight Hydrogelators

Nadine Raßmann, Melina Weber, Roman E. J. Glaß, Klaus Kreger, Nicolas Helfricht, Hans-Werner Schmidt, and Georg Papastavrou*

We published this article in *Langmuir*, **2023**, *39*(48), 17190-17200.

Prof. Dr. Georg Papastavrou, **Dr. Nicolas Helfricht** and **I** conceptualized the project. **I** did the data acquisition and formal analysis, including electrogelating the hydrogel films, designing and conducting all AFM experiments in the dried and swollen state, and analyzing the AFM data. Moreover, **I** compiled all figures, wrote the initial version of the manuscript. **I** supervised **Roman E. J. Glaß** on a day-to-day basis during his bachelor's thesis. He prepared the electrodes, performed the electrochemical characterization of the electrodes, and electrogelated some of the hydrogel films for characterization in the dried state and revised the manuscript. **Melina Weber** synthesized and purified the BTA molecule was involved in scientific discussions, revised and edited the manuscript. **Dr. Nicolas Helfricht**, **Dr. Klaus Kreger** and **Prof. Dr. Hans-Werner Schmidt** were involved in scientific discussions and revised and edited the manuscript. **Prof. Dr. Georg Papastavrou** supervised the project, was involved in scientific discussions, and revised and edited the manuscript.

Chapter 6: Electrochemical Picobalance: Proof-of-Principle for an Electrochemical Cantilever-Based Mass Balance

Nadine Raßmann, Roman E. J. Glaß, Nicolas Helfricht and Georg Papastavrou*

We submitted this article to *Electrochimica Acta*, **2025**, (manuscript number ISSIS-2024-S-25-01530), where it is currently under revision.

Prof. Dr. Georg Papastavrou, **Dr. Nicolas Helfricht** and **I** conceptualized the project. **I** verified the picobalance setup, designed and conducted all picobalance and EQCM experiments. Furthermore, **I** wrote the scripts for data analysis, analyzed the experimental data, compiled all figures, and wrote the initial version of the manuscript. **Roman E. J. Glaß** implemented and improved the fabrication process for the cantilever-based electrochemical mass sensors. He produced all electrochemical balance probes for the picobalance measurements and assisted with their electrochemical characterization. He was involved in scientific discussions and revised the final version of the manuscript. **Dr. Nicolas Helfricht** was involved in conceptualization and scientific discussions, and revised and edited the manuscript. **Prof. Dr. Georg Papastavrou** supervised the project, was involved in scientific discussions, wrote a part of the initial version, and revised and edited the manuscript.

Chapter 7: Determining the Elastic Modulus of Microgel Particles by Nanoindentation

Nadine Raßmann[#], Steffen Trippmacher[#], Agnes Specht, Katinka Theis, Tamino Rößler, Sebastian Wohlrab, Richard Kellnberger, Sahar Salehi, Hendrik Bargel, Nicolas Helfricht, Krystyna Albrecht, Thomas Scheibel, Jürgen Groll, Stephan Gekle and Georg Papastavrou[*]

[#] These authors contributed equally.

We published this article in *ACS Applied Nano Materials*, **2025**, *8*(11), 5383-5398.

Prof. Dr. Georg Papastavrou, **Dr. Nicolas Helfricht** and **I** conceptualized the project. **I** designed and performed all AFM indentation experiments, evaluated the AFM data, compiled the figures, and wrote most of the manuscript. **Steffen Trippmacher** and **Tamino Rößler** synthesized the PAAm and the fluorescence labeled microgels. Moreover, **Steffen Trippmacher** fabricated the wedge cantilevers, conducted the TIRF experiments, and performed some preliminary indentation experiments. He revised and edited the manuscript. **Katinka Theis** synthesized the POx-HASH microgels and revised the manuscript. **PD Dr. Sahar Salehi** and **Dr. Hendrik Bargel** assisted with the TIRF measurements, participated in scientific discussions, and revised the manuscript. **Agnes Specht** participated in the early indentation experiments leading to this study, was involved in scientific discussions, and revised the manuscript. **Sebastian Wohlrab** and **Richard Kellnberger** conducted the finite element simulations for the adhesion of the microgels. Furthermore, **Richard Kellnberger** and **Prof. Dr. Stephan Gekle** wrote the simulations-related part of the manuscript, revised the manuscript, and were involved in scientific discussions. **Dr. Nicolas Helfricht** was involved in scientific discussions and revised and edited the manuscript. **Dr. Krystyna Albrecht**, **Prof. Dr. Thomas Scheibel**, **Prof. Dr. Jürgen Groll** acquired funding, were involved in scientific discussions, and revised the manuscript. **Prof. Dr. Georg Papastavrou** acquired funding, supervised the project, was involved in scientific discussions, and revised and edited the manuscript.

References

(1) Tran, B.; Watts, S.; Valentin, J. D. P., et al. *Adv. Funct. Mater.* **2024**, *34*(37), 2402257.

(2) Raßmann, N.; Weber, M.; Glaß, R., et al. *Langmuir* **2023**, *39*(48), 17190–17200.

(3) Raßmann, N.; Glaß, R.; Helfricht, N.; Papastavrou, G. *Electrochim. Acta* **2025**, *540*, 146907.

(4) Raßmann, N.; Trippmacher, S.; Specht, A., et al. *ACS Appl. Nano. Mater.* **2025**, *8*(11), 5383–5398.

(5) Tsukruk, V. V.; Singamaneni, S., *Scanning Probe Microscopy of Soft Matter*; Wiley: Weinheim, 2011.

(6) Joshua, A.; Cheng, G.; Lau, E. *Appl. Surf. Sci. Adv.* **2023**, *17*, 100448.

(7) Butt, H.-J.; Cappella, B.; Kappl, M. *Surf. Sci. Rep.* **2005**, *59*(1-6), 1–152.

(8) Krieg, M.; Fläschner, G.; Alsteens, D., et al. *Nat. Rev. Phys.* **2019**, *1*, 41–57.

(9) *Handbook of Nanoindentation with biological applications*; Oyen, M. L., Ed.; Jenny Stanford Publishing: New York, 2019.

(10) Raiteri, R.; Grattarola, M.; Butt, H.-J.; Skládal, P. *Sens. Actuators. B Chem.* **2001**, *79*(2-3), 115–126.

(11) Kranz, C.; Friedbacher, G.; Mizaikoff, B., et al. *Anal. Chem.* **2001**, *73*(11), 2491–2500.

(12) Eifert, A.; Smirnov, W.; Frittmann, S., et al. *Electrochem. Commun.* **2012**, *25*, 30–34.

(13) Bircher, B. A.; Duempelmann, L.; Renggli, K., et al. *Anal. Chem.* **2013**, *85*(18), 8676–8683.

(14) Martínez-Martín, D.; Fläschner, G.; Gaub, B., et al. *Nature* **2017**, *550*(7677), 500–505.

(15) Mendes, A.; Baran, E.; Reis, R.; Azevedo, H. *Interdiscip. Rev. Nanomed. Nanobiotechnol.* **2013**, *5*(6), 582–612.

(16) McLellan, J.; Lu, Y.; Jiang, X.; Xia, Y. In *Nanostructure Science and Technology: Nanoscale Assembly*, Huck, W. T. S., Ed.; Springer US: Boston, MA, 2005, pp 187–216.

(17) Ferreira, N.; Ferreira, L.; Cardoso, V., et al. *Europ. Polym. J.* **2018**, *99*, 117–133.

(18) Kopeček, J.; Yang, J. *Angew. Chem. Int. Ed.* **2012**, *51*(30), 7396–7417.

(19) De Loos, M.; Feringa, B. L.; van Esch, J. H. *Eur. J. Org. Chem.* **2005**, *2005*(17), 3615–3631.

(20) Draper, E. R.; Adams, D. J. *Chem* **2017**, *3*, 390–410.

(21) Sinha, N.; Langenstein, M.; Pochan, D.; Kloxin, C.; Saven, J. *Chem. Rev.* **2021**, *121*(22), 13915–13935.

(22) Huang, Y.; Wu, C.; Chen, J.; Tang, J. *Angew. Chem. Int. Ed.* **2024**, *63*(9), e202313885.

(23) Watts, S.; Tran, B.; Salentinig, S. *Chimia* **2022**, *76*(10), 846–851.

(24) Korpi, A.; Anaya-Plaza, E.; Välimäki, S.; Kostiainen, M. *Rev. Nanomed. Nanobiotechnol.* **2020**, *12*(1), e1578.

(25) João, J.; Lampreia, J.; Prazeres, D.; Azevedo, A. *Biotechnol. Adv.* **2021**, *49*, 107758.

(26) Wang, Y.; Douglas, T. *Acc. Chem. Res.* **2022**, *55*(10), 1349–1359.

(27) Gillitzer, E.; Willits, D.; Young, M.; Douglas, T. *Chem. Commun.* **2002**, *38*(20), 2390–2391.

(28) Hommersom, C.; Matt, B.; van der Ham, A.; Cornelissen, J.; Katsonis, N. *Org. Biomol. Chem.* **2014**, *12*(24), 4065–4069.

(29) Gorzelnik, K.; Zhang, J. *Prog. Biophys. Mol. Biol.* **2021**, *160*, 79–86.

(30) Stamou, D.; Gourdon, D.; Liley, M., et al. *Langmuir* **1997**, *13*(9), 2425–2428.

(31) Adams, D. J. *JACS* **2022**, *144*(25), 11047–11053.

(32) Morris, K.; Chen, L.; Raeburn, J., et al. *Nat. Commun.* **2013**, *4*, 1480.

(33) Bressner, J.; Marelli, B.; Qin, G., et al. *J. Mater. Chem. B* **2014**, *2*(31), 4983–4987.

(34) Elia, R.; Michelson, C.; Perera, A., et al. *J. Biomed. Mater. Res. B Appl. Biomater.* **2015**, *103*(8), 1602–1609.

(35) Lu, Q.; Huang, Y.; Li, M., et al. *Acta Biomater.* **2011**, *7*(6), 2394–2400.

(36) Qu, Y.; Hong, G.; Liu, L.; Sasaki, K.; Chen, X. *Dent. Mater. J.* **2019**, *38*(5), 813–820.

(37) Cheng, Y.; Luo, X.; Betz, J., et al. *Soft Matter* **2011**, *7*(12), 5677–5684.

(38) Betz, J.; Cheng, Y.; Tsao, C., et al. *Lab Chip* **2013**, *13*(10), 1854–1858.

(39) Cheng, Y.; Luo, X.; Betz, J., et al. *Soft Matter* **2010**, *6*(14), 3177–3183.

(40) Gray, K.; Liba, B.; Wang, Y., et al. *Biomacromolecules* **2012**, *13*(4), 1181–1189.

(41) Raeburn, J.; Zamith Cardoso, A.; Adams, D. *Chem. Soc. Rev.* **2013**, *42*(12), 5143–5156.

(42) Raeburn, J.; Alston, B.; Kroeger, J., et al. *Mater. Horiz.* **2014**, *1*(2), 241–246.

(43) Johnson, E.; Adams, D.; Cameron, P. *JACS* **2010**, *132*(14), 5130–5136.

(44) Bernet, A.; Albuquerque, R. Q.; Behr, M.; Hoffmann, S. T.; Schmidt, H.-W. *Soft Matter* **2012**, *8*(1), 66–69.

(45) Helfricht, N.; Mark, A.; Behr, M., et al. *Small* **2017**, *13*(31), 1700962.

(46) Uzüm, C.; Hellwig, J.; Madaboosi, N.; Volodkin, D.; von Klitzing, R. *Beilstein J. Nanotechnol.* **2012**, *3*, 778–788.

(47) Li, J.; Sullan, R.; Zou, S. *Langmuir* **2011**, *27*(4), 1308–1313.

(48) Karg, A.; Rößler, T.; Mark, A., et al. *Langmuir* **2021**, *37*(46), 13537–13547.

(49) Adams, J.; Frederix, P.; Bippes, C. *Rev. Sci. Instrum.* **2021**, *92*(12), 129503.

(50) Yi, B.; Xu, Q.; Liu, W. *Bioact. Mater.* **2022**, *15*, 82–102.

(51) Vining, K.; Mooney, D. *Nat. Rev. Mol. Cell. Biol.* **2017**, *18*(12), 728–742.

(52) Raz, N.; Li, J. K.; Fiddes, L. K., et al. *Macromolecules* **2010**, *43*(17), 7277–7281.

(53) Kumachev, A.; Tumarkin, E.; Walker, G. C.; Kumacheva, E. *Soft Matter* **2013**, *9*(10), 2959.

(54) Kim, E.; Lee, H. *J. Pol. Sci.* **2022**, *60*(11), 1670–1699.

(55) Labriola, N.; Mathiowitz, E.; Darling, E. *Biomater. Sci.* **2016**, *5*(1), 41–45.

(56) Girardo, S.; Träber, N.; Wagner, K., et al. *J. Mater. Chem. B* **2018**, *6*(39), 6245–6261.

(57) Reineke, B.; Paulus, I.; Löffelsend, S., et al. *Biofabrication* **2024**, *16*(2), 025038.

(58) Brand, J.; Forster, L.; Böck, T., et al. *Macromol. Biosci.* **2022**, *22*(4), e2100274.

(59) Akhremitchev, B. B.; Walker, G. C. *Langmuir* **1999**, *15*(17), 5630–5634.

(60) Domke, J.; Radmacher, M. *Langmuir* **1998**, *14*(12), 3320–3325.

(61) Dimitriadis, E.; Horkay, F.; Maresca, J.; Kachar, B.; Chadwick, R. *Biophys. J.* **2002**, *82*(5), 2798–2810.

(62) Daza, R.; González-Bermúdez, B.; Cruces, J., et al. *J. Mech. Behav. Biomed. Mater* **2019**, *95*, 103–115.

(63) Glaubitz, M.; Medvedev, N.; Pussak, D., et al. *Soft Matter* **2014**, *10*(35), 6732–6741.

(64) Dokukin, M.; Guz, N.; Sokolov, I. *Biophys. J.* **2013**, *104*(10), 2123–2131.

(65) Hertz, H. *J. Reine Angew. Mathematik* **1882**, *1882*(92), 156–171.

(66) Specht, A.; Trippmacher, S.; Raßmann, N., et al. *Small* **2025**, *21*, e05367.

Part II

Scientific Publications

4

pH-responsive Virus-based Colloidal Crystals for Advanced Material Platforms

Bettina Tran, Samuel Watts, Jules D. P. Valentin, Nadine Raßmann, Madeleine Ramstedt, Georg Papastavrou and Stefan Salentinig*

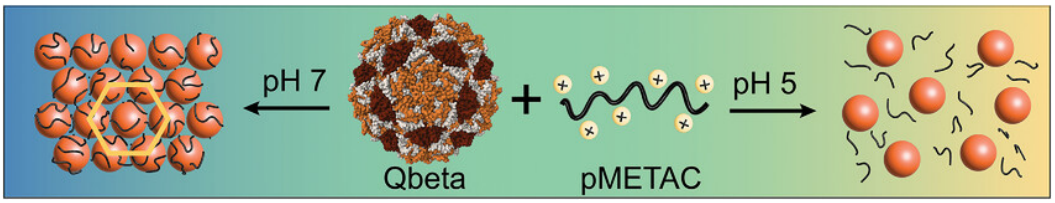

„pH-responsive Virus-based Colloidal Crystals for Advanced Material Platforms“,

Advanced Functional Materials, **2024**, *34*(37), 202402257.

Abstract

Bacteriophages have a well-defined nanoscale size, shape, and surface chemistry, making them promising candidates for creating advanced biomaterials for applications including biocatalysis, drug delivery, and biosensing. This study demonstrates the self-assembly of the $\approx$ 29 nm *diameter bacteriophage Qbeta (Qubevirus durum) with the synthetic polycation, poly [2-(methacryloyloxy)ethyl] trimethylammonium chloride (pMETAC), into compartmentalized colloidal crystals. The pH and the polymer chain length tune their self-assembly and the resulting structure, with the potential for further chemical modification or loading with bioactive molecules. Small angle X-ray scattering (SAXS), multi-angle dynamic light scattering (DLS), and atomic force microscopy (AFM) are used for studying the Qbeta self-assembly into the geometrically ordered aggregates. The suprastructures form at* pH $>$ 7.0 *and disassemble at* pH $<$ 7.0. *Zeta potential measurements and X-ray photoelectron spectroscopy (XPS) show pMETAC adsorption onto the negatively charged Qbeta surface. The colloidal crystal formation is achieved without chemically modifying the Qbeta surface. Additionally, the Qbeta/pMETAC suprastructures can be easily separated from the suspension as macroscopic aggregate, maintaining their activity. Their simple preparation allows for large-scale production of advanced materials in food and health science applications and nanotechnology. The insights from this study will further advance the tailored design and production of novel colloidal materials.*

4.1 Introduction

Nature uses colloidal structurization to customize material properties and biological function. Examples include collagen structurization in bone and dental tissues or actin structures in the cytoskeleton and muscles.[1–6] Drawing inspiration from this to design novel structured materials allows for innovations across diverse fields, spanning health sciences, food technology, and energy research. They can be used, for instance, as vehicles for enzyme and drug delivery, electrodes for energy conversion, antimicrobial surfaces, and nanoreactors.[7–9]

Peptides and lipids have been used to create various structured materials.[10–13] Applying pre-assembled viruses in this process could facilitate the design of complex hierarchical functional material. For example, exploiting viral particles such as bacteria viruses (phages) as foundational elements for novel structures offers a notable advantage due to their well-defined nanoscale surface characteristics, shapes, sizes, mechanical stability, and biological functions.[14] Viruses are precision-designed by nature, built from the self-assembly of peptide monomers into a highly organized protein nanocage.

Their shapes span from cylindrical and tailed to spherical, depending on the specific phage variant.[14] Their intrinsic biocompatibility and the active research on scalable production make them prime candidates for designing advanced biomaterials.[15–17] Their well-defined structural and functional properties can be bioengineered on demand.[18] Tailoring the functional groups on the protein nanocage surface can enable them to immobilize in precise orientations onto surfaces.[19] The manipulation of the protein nanocage self-assembly process is also achievable through surface modification of these functional groups. [20, 21] An alternate route for tailoring the ordered assembly of virus capsids is based on DNA templating.[22] These materials are promising therapeutic agents in phage therapy.[16, 23–25] Expanding their scope, they can be utilized as energy generators or biosensors within the food industry, exemplifying their far-reaching potential.

The phage Qbeta (*Qubevirus durum*), belonging to the *Fiersviridae* family, consists of an icosahedral protein capsid containing single-strand RNA and replicates selectively in *Escherichia coli*.[26–28] Qbeta has been widely studied and used as a model system for pathogenic viruses such as norovirus and rotavirus due to their structural similarities.[29, 30] It has a diameter of 29.4 nm with a net negative charge at pH values above its isoelectric point (IEP) of $\approx$ 4.3.[31] Any interaction properties should be governed mainly by its surface properties and size due to its isotropic shape.[31] Therefore, Qbeta potentially serves as a simple and solid foundation for protein-based nanostructured material due to its well-known properties and small size.

The fundamental understanding of the interaction between the viral particles and other involved building blocks will guide the design and development of advanced structured materials. Extensive research has been reported on the interaction mechanisms between polyelectrolytes and charged nanoparticles.[32–35] However, most focus has been on homogenous spherical particles, with few studies on heterogeneously charged, core-shell particles such as phages.[36, 37] The insights from investigations on homogeneous particles may not seamlessly translate to viral particles exhibiting a core-shell structure, intricate surface charge distribution, and heterogeneously exposed functional groups.[31]

In this study, the control over the interaction of Qbeta is achieved with a custom-designed polyelectrolyte, the polycation poly [2-(methacryloyloxy)ethyl] trimethylammonium chloride (pMETAC, refer to Figure S1, Supporting Information, Section 8.1). It is synthesized at defined chain lengths through atom transfer radical polymerization (ATRP) and contains a cationic quaternary ammonium group per repeating unit. pMETAC is widely used in different fields, for instance, as a flocculant in wastewater treatment, for developing antimicrobial surfaces, or in gene delivery vectors.[38–40]

To our knowledge, this study demonstrates the first formation of highly geometrically organized colloidal crystals through the self-assembly of Qbeta mediated by a polycationic polymer. The study comprehensively examines how composition, polymer chain length, and pH influence supramolecular structures, providing insights into protein nanocage self-assembly with polyelectrolytes. This understanding is key for controlling material parameters, including morphology, size, and structure. These resulting biocompatible and degradable materials are promising for various potential applications in the biomedical and nanotechnology fields.

4.2 Results and Discussion

4.2.1 Synthesis and Characterization of pMETAC

Two different chain lengths of pMETAC were synthesized via ATRP. The primary chosen molecular weight of 3.3 kDa aligns with the size range typically observed for antimicrobial peptides, whereas the 16.5 kDa variant represents a comparably larger structure,[41] referred to as pMETAC1 and pMETAC2, respectively. After synthesis, a comprehensive pMETAC characterization was performed using gel permeation chromatography (GPC), nuclear magnetic resonance (NMR), and Raman spectroscopy.

^{1}H-NMR confirmed the polymerization of the METAC monomers to pMETAC. The hydrogen signal associated with the C=C double bonds at δ 6.31 ppm and 5.94 ppm disappeared after the reaction (cf. Figure S1B, Supporting Information, Section 8.1).[42] This finding agrees with the Raman analysis, where the C=C vibration and its associated hydrogen vibrations at 1640 cm^{-1} (C=C stretch), 1409 cm^{-1} (C=C$-$H$_2$ bending, in-plane), and at 895 cm^{-1} (C=C$-$H$_2$ bending, out of plane) are absent in the pMETAC spectrum (cf. Figure S1C, Supporting Information, Section 8.1). pMETAC polymers were assessed via aqueous GPC. pMETAC1 displayed a dispersity index (DI) defined as the ratio of the weight averaged (M_W) and number averaged molecular weight (M_n) of the polymer with DI $= M_W/M_n =$ 3.3 kDa/2.65 kDa $=$ 1.26. For pMETAC2, the DI $=$ 16.5 kDa/11.04 kDa $=$ 1.49. The repeat unit length (RU) was approximated at 1.75 $\pm$ 0.17 Å through hexamer simulations (simulation details can be found in the Supporting Information, Section 8.1). Utilizing the degree of polymerization extracted from M_n (refer to Equation S3, Supporting Information, Section 8.1), the estimated lengths for pMETAC1 and pMETAC2 were calculated as 20.7 and 91.4 Å, respectively.

The polymers were further studied with small angle X-ray scattering (SAXS) in virus dilution buffer (VDB, composition cf. Materials and Methods in the Supporting Information, Section 8.1) at different pH values between 3.0 and 9.0, see Figure S2 (Supporting

Information, Section 8.1). A broad peak with a maximum at scattering vector magnitude, $q \approx 1.1$ nm^{-1} for pMETAC1 and $q \approx 0.8$ nm^{-1} for pMETAC2 was observed. These peaks, corresponding to realspace dimensions of $d = 2\pi/q = 5.7$ nm and 7.9 nm, respectively, can be associated with the apparent center-to-center distance between the positively charged polymer coils in solution.[43] The larger d value for pMETAC2 compared to pMETAC1 agrees qualitatively with the differences in the molecular weight determined by GPC analysis. The peak position and scattering profiles do not change with pH between 3.0 and 9.0. This finding suggests that the interpolymer interaction and polymer conformation remain mostly unchanged in this pH range (cf. Figure S2, Supporting Information, Section 8.1), as the quaternary ammonium cation remains positively charged at all these pH values.

4.2.2 Qbeta/pMETAC Self-Assembly in Water

The colloidal structure of Qbeta in VDB was analyzed before and after adding pMETAC at different pH values between 3.0 and 9.0. Figure S3A (Supporting Information, Section 8.1) shows the SAXS curve for Qbeta in VDB at pH 3.0 and 9.0 at optimized Qbeta concentrations for the SAXS study. The Qbeta concentration was estimated by plague forming unit (PFU) counting, measuring the infective particles per milliliter (PFU mL^{-1}). A Qbeta sample at $\approx 10^{13}$PFU mL^{-1} gave a signal with reasonable signal-to noise and negligible scattering from inter-particle correlations in SAXS. The Qbeta concentration in this sample was estimated to ≈ 1 mgmL^{-1}, in agreement with a previous study.[44] This concentration estimate was further validated with SAXS using a protein of known molecular weight as standard (cf. Supporting Information, Section 8.1).

The SAXS patterns are characteristic of nanoscale particles with a Guinier region below $q \approx 0.2$ nm^{-1}. At higher q values ($0.2 < q < 1$ nm^{-1}), the scattering curves show maxima and minima, characteristic of the quasi-spherical (icosahedral) virus particles. A modified low-q $\left(q < 0.2 \text{ nm}^{-1}\right)$ scattering has been observed for suspensions of viruses only at pH 3.0. This SAXS curve shows a power-law behavior with an exponent of ≈ -3.0 at this pH and no Guinier region. This curve shape results from aggregates larger than the maximum dimension that can be accurately resolved with the SAXS setup ($\pi/q_{\text{min}} \approx 45$ nm). The low-q aggregation behavior of Qbeta agrees with previous reports.[30]

The size and shape of Qbeta were obtained from the SAXS data using the generalized-independent Fourier transformation (GIFT) method (details can be found in the Materials and Method section in the Supporting Information, Section 8.1). The resulting pair-distance distribution ($p(r)$) function is characteristic of spherical particles with diameters

≈ 29 nm at pH 7.0 (cf. Figure S3B, Supporting Information, Section 8.1). The representative cryogenic-transmission electron microscopy (cryo-TEM) image of the Qbeta at pH 7.0, presented in Figure 4.1, confirms the results on size and shape from SAXS, showing an icosahedral particle with diameters ≈ 29 nm. These findings agree with previous reports on the size and shape of Qbeta.[30, 45, 46] At pH 9.0, a shift in the $p(r)$ function can be observed that arises due to changes in the electron density of the buffer media after pH adjustments.[47]

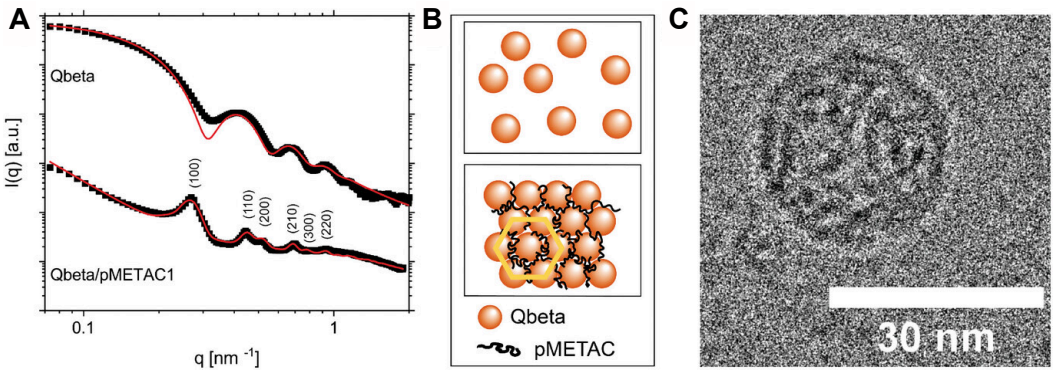

Figure 4.1. Qbeta/pMETAC1 (1:50 weight ratio) self-assembly at pH 7.0. The curves were displaced vertically for better visibility. **A** Black squares represent the experimental SAXS data; red lines are the best possible fits of Equation S9 (Supporting Information, Section 8.1) to the experimental SAXS data of Qbeta and the Qbeta/pMETAC1 assembly. The peaks in the SAXS curve are further identified by their Miller indices (hkl). **B** is an artistic representation of the data showing the Qbeta in a hexagonal arrangement, marked in yellow, with polymers on the surface and in the voids. It is worth noting that the icosahedral Qbeta is represented as spheres. **C** Cryo-TEM image showing icosahedral Qbeta with a diameter of ≈ 29 nm at pH 7.0 in VDB. The zoomed-out overview image is presented in Figure S5 (Supporting Information, Section 8.1).

Supramolecular Qbeta materials were created for the first time by adding pMETAC1 or pMETAC2 to the Qbeta suspension. The structure and pH-responsive interactions between Qbeta and pMETAC1, and pMETAC2 were systematically investigated in VDB at pH values between 3.0 and 9.0. The SAXS curves of Qbeta/pMETAC1 and Qbeta/pMETAC2 at a mass ratio of 1:50 in this pH range are presented in Figure S4A, B (Supporting Information, Section 8.1). The scattering of Qbeta aggregates dominates the sample Qbeta/pMETAC1 at pH 5.0 and 3.0. At pH 7.0 and 9.0, Bragg reflections of colloidal crystals appear in the presence of pMETAC1, cf. Figure 4.1A. The q-positions of the peaks are at $0.27, 0.44, 0.48, 0.70, 0.81$, and $0.95\ \mathrm{nm}^{-1}$. The corresponding peak ratio of $1/\sqrt{3}/\sqrt{4}/\sqrt{7}/\sqrt{9}/\sqrt{12}$ is characteristic of a 2-dimensional (D) hexagonal structure as represented in Figure 4.1B. The lattice constant, a, calculated from the first-order reflection using Equation 4.4, is 27.8 ± 1.4 nm. This agrees with the dimensions of Qbeta of ≈ 29 nm from the SAXS and cryo-TEM analysis reported above.

To further analyze the structures of the highly geometrically ordered Qbeta/pMETAC1 composite material at pH 7.0, model-dependent fitting of the SAXS data was performed. A spherical core-shell model with added Gaussian coil scattering ($P_G(q)$) to account for the polymer scattering contributions from the Qbeta sample (protein and RNA) was used (cf. Equation S9, Supporting Information, Section 8.1, where $S_{hex}(q) = 1$ and $N = 0$). The best possible fit of this equation to the experimental data of Qbeta alone is presented in Figure 4.1A. The inner radius was 10.1 ± 1.2 nm, and the protein shell thickness was 2.7 ± 0.1 nm. The calculated scattering from the analytical model agrees well with the experimental data, given that the SAXS signal provides statistical information on all components in the sample, including impurities. These impurities may be responsible for the smearing of the local minima in the experimental scattering curve, which is not accounted for in the analytical model. Minor fractions of coexisting bacteria and virus fragments with sizes in the nanometer-range, are seen in some TEM images (cf. Figure S6, Supporting Information, Section 8.1).

For the highly ordered Qbeta/pMETAC1 structures, the spherical core-shell form factor model was multiplied with the structure factor of a 2D hexagonal lattice ($S_{hex}(q)$). (cf. Equations S6 and S10, Supporting Information, Section 8.1). For the model to represent the overall scattering curve, an additional power law model was included to account for the contribution of larger aggregates at low q values (cf. Equation S9, Supporting Information, Section 8.1). Detailed fitting parameters can be found in Table S1 (Supporting Information, Section 8.1). For the assembly, a core radius of 16.2 ± 0.2 nm with a shell thickness of 1.6 ± 0.5 nm and lattice constant of 27.8 ± 0.1 nm was obtained from the best possible fit of the model to the experimental data (cf. Figure 4.1). The fitted radius of Qbeta in the assembly, with an overall radius of 17.8 ± 0.5 nm, is larger when compared to the obtained radius of 12.8 ± 1.2 nm, for Qbeta alone. This increase in the radius with apparently larger core dimensions and reduced shell thickness indicates the adsorption of pMETAC1 to the virus surface with related modifications in the excess electron density in this region.

Atomic force microscopy (AFM) images of the assemblies were acquired in buffer to further analyze the Qbeta/pMETAC1 suprastructures at pH 7.0 (cf. Figure 4.2). In Figure 4.2A and Figure S7 (Supporting Information, Section 8.1), the representative topographical AFM images reveal a hexagonal pattern with a center-to-center distance of ≈ 29 nm from the AFM height profile. The hexagonal lattice spacing obtained at the 2D interface from the AFM image is consistent with the one obtained from the SAXS analysis of 3D bulk structures.

A fast Fourier transformation (FFT) algorithm was used to calculate the 2D Fourier spectrum of the AFM image (Figure 4.2B). This spectrum is related to the SAXS data, which are also in the reciprocal space. The radial integration of the 2D spectrum into a

1D scattering curve allowed us to directly compare the structure in the AFM image with the experimental SAXS data of the same sample in buffer (Figure 4.2C). The calculated scattering pattern agrees reasonably with the experimental SAXS data. The smearing of the FFT peaks from the AFM data can be attributed to factors including compromised statistics on the image, the limited contrast of the image, and imaging artifacts. All those effects, in combination with the cross-terms of the form factor of the spherical particles, contribute to frequency overlay from the imaging process, leading to smeared features and insufficient statistics for a higher resolution scattering pattern in the overall q range.

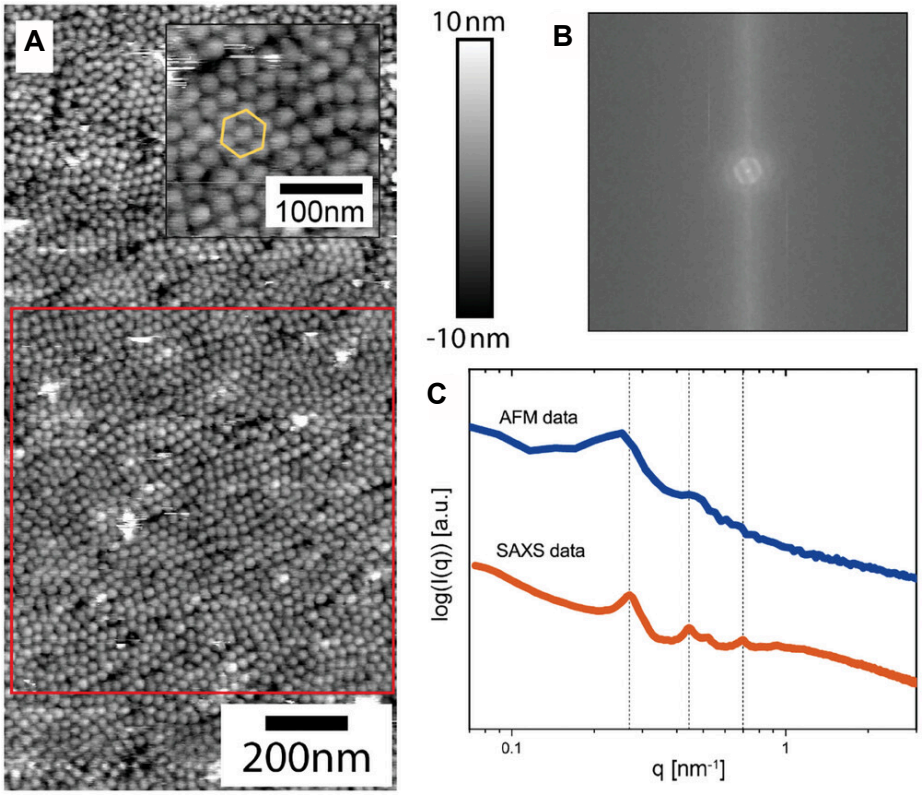

Figure 4.2. **A** Representative AFM image shows the ordered Qbeta-pMETAC1 assembly measured in VDB at pH 7.0. The inset shows an enlarged area with the hexagonal arrangement of the Qbeta marked in yellow. **B** FFT spectrum of the image area, marked with a red square in **A**. **C** The scattering pattern was obtained from the radial integration of the intensities in the FFT image (blue line) and the experimental SAXS data (orange line). The vertical lines guide the eye to compare selected peak positions between the curves, and scattering patterns were displaced vertically.

The influence of the ratio Qbeta/pMETAC1 on the structure formation was evaluated on weight ratios of 0:1, 1:100, 1:50, 1:20, 1:10, 1:5, 1:2, 1:1, 1:0.5, 1:0.2, and 1:0 as shown in Figure 4.3. In Figure 4.3A, the SAXS curves corresponding to Qbeta/pMETAC1 ratios between 1:1 and 1:50 show a low-q power-law decay of the I(q) with an exponent of −3.5

to −4, which is characteristic of attractive inter-particle interactions (aggregation).[48] Additionally, Bragg reflections are evident in the SAXS patterns for the ratios of 1:5 to 1:20, with peak maxima at q values of 0.26, 0.46, 0.69, and 0.95 nm^{-1}. These peaks result from a 2D hexagonal structure with a lattice parameter of 27.7 nm, similar to the sample at Qbeta/pMETAC1 at 1:50 ratio presented in Figure 4.1. Referring to Figure 4.3A, for ratios 1:1 and 1:2, an upturn at low-q but no Bragg reflections can be seen. This observation indicates that this Qbeta/pMETAC1 ratio is a threshold for forming colloidal crystals. Upon increasing the ratio to 1:100, the Bragg peaks and the low-q upturn diminish in the scattering. The low-q region of the I(q) showed a power-law decay with an exponent of ≈ −2.1, comparable to that of the pMETAC1 alone (sample 0:1). This implies that the number of aggregates present is insignificant. Likely, charge inversion occurs at this high pMETAC1 concentration, stabilizing the pMETAC-coated Qbeta.

To study this effect, zeta potential and conductivity measurements were conducted on Qbeta/pMETAC1 samples at pH 7.0, employing a range of ratios (1:0, 1:0.2, 1:0.5, 1:1, 1:5, 1:10, 1:50, 1:100) as illustrated in Figure 4.3B.

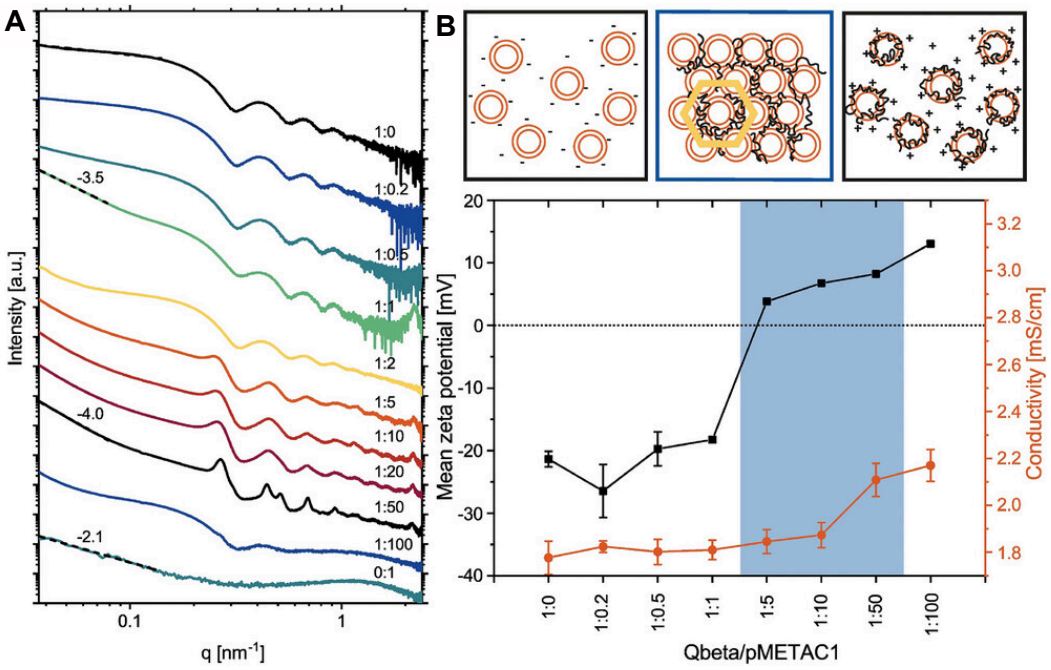

Figure 4.3. **A** SAXS data of Qbeta/pMETAC1 at pH 7.0 at varying composition. For better comparison, the curves have been shifted vertically on the arbitrary unit axis. **B** Zeta potential (black squares) and conductivity (orange circles) of Qbeta/pMETAC1 at pH 7.0 at different weight ratios with the artistic views of the structure at different Qbeta/pMETAC1 ratios. A hexagonal arrangement of Qbeta within the suprastructures is observed in the composition range highlighted in blue and the hexagonal lattice is marked in yellow in the corresponding graphical representation.

The zeta potential of Qbeta was -21.4 ± 1.3 mV, consistent with previous reports.[30, 31] Until Qbeta/pMETAC1 of 1:1, the zeta potential was relatively constant at ≈ -20 mV. As the quantity of pMETAC1 increased, an incremental rise in zeta potential from -18.3 to 3.9 mV was evident. At the 1:5 ratio, charge inversion was observed. This goes with a slow, gradual increase until an inflection point, indicating a change in adsorption behavior. A steeper conductivity increase is followed due to the overcharging of the Qbeta until saturation, with additional free pMETAC1 ions in the surrounding water phase. This effect has been observed previously when adding polyelectrolytes to functionalized polystyrene particle suspension.[49]

The onset of aggregation aligned closely with the zeta potential values reaching a magnitude of < 10 mV upon pMETAC1 addition. Further increasing the pMETAC concentration to Qbeta/pMETAC1 at 1:100 led to charge inversion and a significant amount of free pMETAC1 with the zeta potential increasing to 13 mV. Repulsive interactions between the now positively charged particles trigger de-aggregation and free pMETAC1. This behavior agrees with the observations from the SAXS analysis. While the scattering of virus particles dominates the signal at low and high pMETAC1, Bragg peaks from colloidal crystals appear when the zeta potential magnitude is below 10 mV (cf. Figure 4.3).

SAXS was used to analyze the stability of the Qbeta and the Qbeta/pMETAC1 at 1:50 colloidal crystals upon heating and salt addition. The SAXS patterns for Qbeta are comparable up to ≈ 60°C (cf. Figure S8A, Supporting Information, Section 8.1). At 80°C, changes in the low-q region of I(q) are observed due to temperature-triggered structural modifications that are irreversible upon cooling to 20°C. This agrees with previous reports on the protein capsid alteration, with an onset at ≈ 60°C, depending on the environment.[50, 51] A similar behavior is reflected in the Qbeta/pMETAC1 at 1:50 colloidal crystals. The hexagonal structure was stable between 20°C and 60°C, with no major change in SAXS curves (cf. Figure S8B, Supporting Information, Section 8.1). However, the scattering patterns change significantly with a decrease in the intensity of the Bragg reflections, when heated to 80°C.

Increasing the ionic strength of the suspension by adding NaCl had a major effect on the colloidal structure of the Qbeta/pMETAC sMelf-assemblies. The Bragg reflections of the hexagonal Qbeta self-assemblies at 10 mM NaCl disappeared ≥ 30 mM NaCl (cf. Figure S9, Supporting Information, Section 8.1). This shows that electrostatic interactions between the Qbeta and pMETAC mainly control the structure formation in this system. Therefore, stable conditions for the suprastructures are at low ionic strength.

The influence of the polymer chain length was studied by mixing Qbeta with the roughly $4-5\times$ longer pMETAC2 (3.3 kDa vs. 16.5 kDa) at mass-ratio 1:50 at varying pH from

3.0 to 9.0. Based on Figure S4B (Supporting Information, Section 8.1), the SAXS curves indicate the presence of Qbeta/pMETAC2 aggregates as there is an upturn in low-q scattering across all measured pH values from attractive interactions. As the pH value increases, the intensities of the minima and maxima in the scattering curve decrease at higher q-values, suggesting a change in scattering contrast within the Qbeta/pMETAC aggregates due to the higher intensity of the Gaussian chain scattering. At pH 7.0 and 9.0, the SAXS curves displayed a broad peak ≈ 0.26 nm^{-1} and relatively weak reflections with maxima $\approx 0.46, 0.68$, and 0.92 nm^{-1}. The broad and weak reflections make it challenging to determine the structure type accurately. The positions of the broad peaks were comparable to the sharper reflections from the hexagonal phase in the Qbeta/pMETAC1 assembly discussed above. This indicates that less ordered colloidal crystals were formed in the presence of pMETAC2 compared to pMETAC1.

Inorganic salts were added to Qbeta suspensions at pH 7.0 to analyze whether simple charge screening can induce colloidal crystal formation. The ionic strength upon the salt addition was aligned with that of the pMETAC-containing samples at pH 7.0. The pMETAC1 charge was calculated from the number-averaged molecular mass (2.65 kDa) by assuming that each repeating unit holds one cationic quaternary amine for interaction (cf. Equations S3 and S12-S17, Supporting Information and in the Experimental Section part of the Supporting Information, Section 8.1). Therefore, NaCl 0.25,0.5, and 1 M and $MgCl_2$ (0.125, 0.25, and 0.5 M were added instead of pMETAC. The lowest salt concentration at 0.25 M matches the estimated charges from when pMETAC is added.

Figure S10 (Supporting Information, Section 8.1) shows that as the salt concentrations increase, the maxima and minima in the SAXS curve of the Qbeta form factor scattering become less pronounced. This behavior may result from the increased electron density of the buffer from salt addition, which decreases the excess electron density (scattering contrast) of Qbeta. No Bragg reflections were observed in the Qbeta samples with the mono- and divalent cations, even at concentrations exceeding the theoretical charge available from pMETAC. These findings demonstrate that charge screening induced by inorganic salt is insufficient for colloidal crystal formation. Specific interactions between Qbeta and the polycations are necessary.

It has been shown that low valency ions tend to induce instability of latex particles by charge screening, while polyelectrolytes adsorb onto the particle surface.[52] The combination of charge interactions and the linear arrangement of the charges induces the formation of the colloidal structure. In the case of Qbeta/pMETAC1, the electrostatically driven self-assembly is stable over up to more than 50°C but susceptible to changes in the ionic strength.

Further investigation into the chain-length dependent mechanism shows that pMETAC1 is sufficiently short (≈ 21 Å), likely allowing the locally flat attachment onto the virus surface in a so-called train conformation.[53] When a particle interacts with a considerably smaller polymer, the polymers can wrap around it,[34, 35] likely the case for this study's Qbeta/pMETAC structures. Even though pMETAC2 is roughly 4.5-5 times longer (≈ 91 Å) than pMETAC1, it is still short compared to the size of the virus particle. The finding that Qbeta can aggregate into colloidal crystals with pMETAC1 and less organized structures with pMETAC2 shows that the length of the polycation is important in the structure formation.

The small polymer chain length of pMETAC1 and 2, compared to the Qbeta, differs from previous works, where polyelectrolyte-patchy-charged particle interactions were mainly studied with a chain length similar to or larger than the nanoscale-sized spherical particles.[34, 37, 54–56] The polyelectrolyte chain length influenced the attachment onto spherical particles such as silica or poly(styrene sulfate) latex particles.[32, 57]

The 2D hexagonal structure observed in the Qbeta/pMETAC aggregates suggests that the interactions among the pMETAC and viruses are anisotropic. For homogeneously interacting spheres, the attractive interaction may prefer the formation of closed cubic hard-sphere packing. The hexagonal structure in this system may result from the inhomogeneous charge distribution on the Qbeta surface.[29, 58] The inhomogeneous charge distribution from various polyelectrolytes on different polymer particles, such as amidine or sulfate latex surfaces, was shown before.[59] The specific adsorption of pMETAC onto Qbeta sufficiently screens its surface charge, bringing them close enough that attractive forces, such as van der Waals forces, start to dominate and structures aggregate forms.[32] The heterogeneous charge distribution on the Qbeta surface may also allow pMETAC to connect between particles. Such "specific" polymer bridging could explain why pMETAC2 forms assemblies with reduced order. Similar observations were made when simulating the interaction of polyelectrolytes with globular proteins.[36, 56] However, we can not exclude that the hexagonal structure is a secondary minimum on the complex energy hypersurface of such a system. Weak interactions may hinder the system from reaching a potentially lower energy state, allowing it to form face-centered cubic (fcc) structures.[60, 61] Furthermore, the order of the structure can be reduced by longer bridging segments.

4.2.3 In Situ Dynamic Light Scattering Study of Qbeta pMETAC Aggregation

The assembly mechanism of Qbeta/pMETAC structures is studied with in situ multi-angle dynamic light scattering (DLS). The aggregation rate constants are calculated from the change in the apparent R_H with time.[62] The multi-angle approach provides additional information on the homogeneity of the process, as the signal at each scattering angle is weighted with the particle size (large particles scatter to smaller angles; small particles to larger ones). The scattering angles were chosen to analyze the aggregation simultaneously at 39° for large particles, at 90° as intermediate, and at 124° for small particles.

For the Qbeta/pMETAC1 sample at a mass ratio 1:1 in a total concentration of 0.005 wt% (Qbeta and pMETAC1) at pH 7.0, the aggregation started within seconds after mixing (cf. Figure 4.4). Lowering the mass ratio to Qbeta/pMETAC 1:1 was chosen to achieve aggregation kinetics within the DLS time resolution range. The initial step of the aggregation process was fast, reaching ≈ 400 nm within the first 10 min, and slowed down to plateau at an apparent R_{H} of ≈ 1000 nm after one hour. All measured scattering angles (39, 90, 124°) show comparable aggregation behavior, and the calculated polydispersity index (PDI) values fluctuated around 0.5. This highlights the relative homogeneity of the Qbeta/pMETAC aggregation process. Similar behavior was observed for the Qbeta/pMETAC aggregation at both chain lengths at pH 9.0 and Qbeta/pMETAC2 at pH 5.0 (cf. Figure S12, Supporting Information, Section 8.1).

In contrast, the DLS results for Qbeta/pMETAC1 at pH 5.0 and 3.0, and pMETAC2 at pH 3.0 did not show the formation of large aggregates. An apparent R_{H} of up to 200 nm is observed at the smallest scattering angle (39°), giving weight to large aggregates (cf. Figure S12, Supporting Information, Section 8.1). The signal at larger scattering angles reflects R_{H} values < 150 nm for these samples. Based on the results, the interaction between Qbeta and pMETAC1 is not very strong when the pH is at or below 5.0. These pH values are close to the isoelectric point of Qbeta, and the electrostatic interaction of Qbeta with pMETAC is reduced. Only minor aggregation can be observed when focusing on large particles at the lowest scattering angles. The aggregation reaction's equilibrium appears to have shifted toward Qbeta/pMETAC oligomers that remain static over time and do not exhibit further growth. This observation agrees with the findings from the SAXS analysis. Large and compact aggregates containing multiple repeat units are essential for generating Bragg reflections in the scattering patterns, as demonstrated by the samples at pH 7.0 and 9.0, but not for pH 5.0.

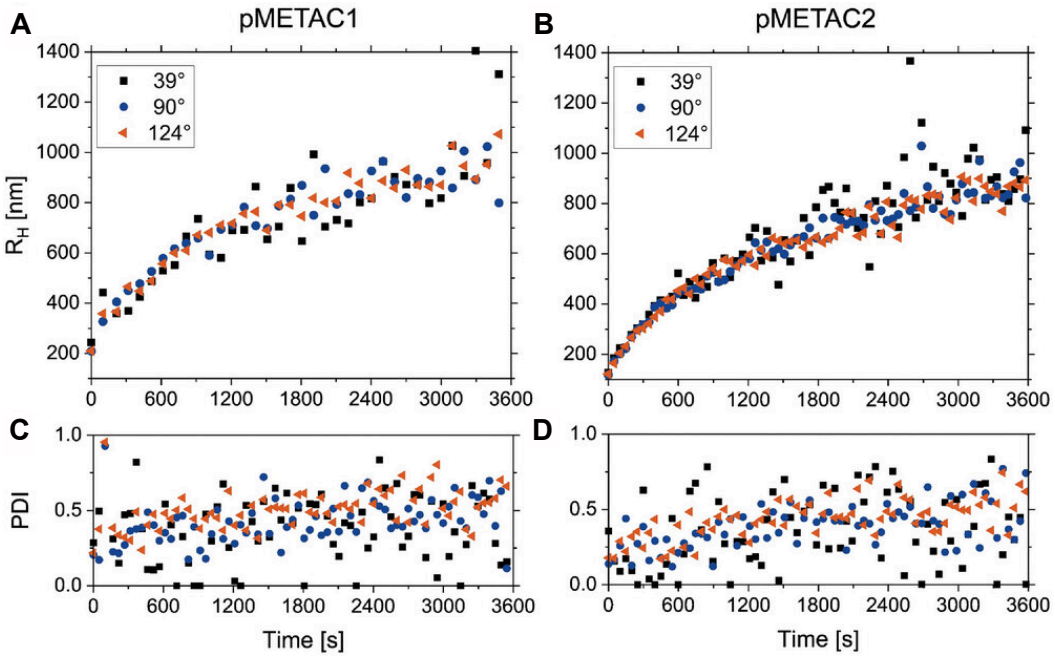

Figure 4.4. Aggregation kinetics of Qbeta with pMETAC at a fixed ratio of 1:1 and pH 7.0 studied in situ using time-resolved DLS at different scattering angles. **A** Evolution of R_H over time for Qbeta in the presence of pMETAC1; **B** pMETAC2; **C** and **D** show the corresponding polydispersity plots. The DLS autocorrelation curves are presented in Figure S11 (Supporting Information, Section 8.1)

Qbeta/pMETAC2 exhibits comparable aggregation behavior across the pH range from 5.0 to 9.0 from DLS. A noticeable disparity arises in the SAXS analysis when the pH is lowered to 5.0, revealing a reduction in order and aggregation. These results suggest that the pMETAC chain length is critical in the Qbeta aggregation and structurization process.

To gain more insight into the detailed kinetics and to investigate the influence of the Qbeta/pMETAC1 ratio, the self-assembly process was further studied at pH 7.0. When the ratio of Qbeta to pMETAC1 was changed from 1:1 to 1:0.5, 1:0.2, to 1:0.1, the R_{H} increase was less homogeneous over the observed scattering angles (cf. Figure 4.4, Figure S14, Supporting Information, Section 8.1), indicating multi-modal particle size distributions. Additionally, the formation of smaller aggregates at a R_{H} range of 600 nm for 1:0.5, 50 nm for 1:0.2, and 25 nm for 1:0.1, was observed, suggesting an insufficient amount of polymers for forming larger aggregates. As the SAXS experiment has shown (cf. Figure 4.4), at ratios below 1:2, no Bragg reflection could be observed. The low-q upturn becomes less pronounced at these low polymer concentrations, indicating the formation of less and smaller aggregates, in agreement with DLS.

For Qbeta/pMETAC2 the ratio was varied from 1:1, 1:0.5, 1:0.2 to 1:0.1 (cf. Figure 4.4; Figure S14, Supporting Information, Section 8.1), analogous to pMETAC1. The main difference was that even for the ratio 1:0.5, a homogeneous time-dependent aggregation, yielding large aggregates of $R_H \approx 1000$ nm, was observed. This behavior contradicts the heterogenous 600 nm-sized aggregates for Qbeta/pMETAC1 at a 1:0.5 ratio. It can be concluded that large aggregates can be formed at a broader range of conditions for pMETAC2. Therefore, longer chains promote the formation of aggregates. This observation agrees with the revisited Schulze-Hardy rule, where the critical coagulation concentration (CCC) decreases with increasing valence for multivalent counterions.[63]

For more quantitative analysis, the time-resolved DLS data were fitted for all samples at a 1:1 ratio at pH 7.0 and 9.0 and the Qbeta /pMETAC2 1:0.5 ratio at pH 7.0 (cf. Table S2, Supporting Information, Section 8.1). The diffusion-limited cluster aggregation (DLCA) model was chosen because the primary driving force behind the aggregation process is considered to be the charge interactions of the anionic Qbeta with the cationic pMETAC at sufficiently high concentrations. From the fitting parameter A (cf. Equation S22, Supporting Information, Section 8.1), the aggregation rate is similar for Qbeta/pMETAC1 at 1:1 and Qbeta/pMETAC2 at 1:1 at the same pH, resulting in apparent average R_H values ≈ 1000 nm. This finding implies that the aggregation rate depends mainly on the pH and, thus, the surface charge of Qbeta but less on the difference in the pMETAC chain length. An exception can be seen for Qbeta/pMETAC2 1:0.5 at pH 7.0, where the aggregation rate is higher than at a 1:1 ratio. At a 1:0.5 ratio, the charge modification is lower due to the lower amount of pMETAC, as observed from the zeta potential (Figure 4.3B). Still, the lower ionic strength could benefit the aggregation of longer chains. It has been shown that the interaction between cationic polymers and functionalized latex particles with heterogeneous charge distributions increased aggregation rates at low ionic strength.[33, 62]

For the Qbeta/pMETAC1 system, fitting the DLCA model to the DLS data results in a D_f between 1.9 and 2.36. The calculated D_f values are larger than typical D_f, 1.75-1.85, obtained from DLCA and indicate reaction-limited cluster aggregation (RLCA).[64] This can result from thermally-driven restructuring to the denser cluster, especially if the inter-particle interactions are weak. A similar behavior has been observed with gold nanoparticles interacting with cationic surfactant.[65]

A further cause for denser clusters has been shown by increased concentration of polyelectrolytes such as poly(allylamine hydrochloride) or poly-diallyldimethylammonium chloride to screen the charges of silica nanoparticles.[37] This charge screening effect also applies to Qbeta/pMETAC aggregates and can explain the higher D_f than expected from the DLCA model for simple particle aggregation. For Qbeta, the higher surface

charge at pH above 7.0 leads to a stronger attraction between the patchy regions, favoring rearrangement to reduce repulsion between the adsorbed pMETAC.[30, 31]

The DLS results demonstrate the effect of the Qbeta/pMETAC1 ratio and their self-assembly into suprastructures. For Qbeta/pMETAC1, an optimal ratio is found based on charge balance, which agrees with the zeta potential analysis. The particle size increases at sufficiently high pMETAC1 concentration (from Qbeta/pMETAC = 1:0.5), leading to large aggregates. At low particle concentrations, this process is slow enough to be studied by DLS. Upon increasing the particle concentration, the rate at which the particles collide increases, and the aggregation rate increases, however, the mechanism stays the same.

In summary, pMETAC induces charge screening and destabilization of Qbeta in suspension and tailors the structure of the aggregates with a given chain length. Rearrangement into a more efficient packing, crucial to forming colloidal crystals, is likely due to repulsive forces between Qbeta/pMETAC1 assemblies and free pMETAC1 in solution. Therefore, the analysis of the DLS data completes the conclusions on the aggregation from SAXS, zeta potential analysis, and AFM with additional kinetic information.

4.2.4 Qbeta/pMETAC of Surface Chemistry

X-ray photoelectron spectroscopy (XPS) provides the chemical composition of the outermost surface of a sample, with a typical information depth of < 10 nm.[66, 67] Thus, in the case of Qbeta, primarily the protein capsid is probed by XPS analysis.[67] Cryogenic XPS was performed to detect any alterations in the chemical composition on the surface of the phage after exposure to the polymer. These measurements were conducted with the assembly Qbeta/pMETAC at 1:50 at pH 7.0 (cf. Figures S16 and S17, and Table S3, Supporting Information, Section 8.1) and comparing its surface chemistry to its pure components. Survey spectra of the phages in the buffer showed the presence of O, N, C, Na, Cl, and P. However, Na, Cl, and P mainly originated from the buffer, while O was from the buffer and the phage surface. N and C originated only from the phages. The C 1s spectrum was fitted with four components relating to aliphatic C at 285.0 eV, C atoms with an O or N neighbor at 286.4 eV, C in peptide bonds at 288.2 eV, and C with two O neighbors, e.g., in esters, at 288.7 eV (Figure S17, Supporting Information, Section 8.1). The N 1s spectrum of the phage sample showed a main peak at 400.1 eV, which corresponds to N in amides or peptide bonds.[68] This peak had a shoulder at 401.5 eV arising from protonated groups (Figure S17, Supporting Information, Section 8.1). Survey spectra of the polymer samples showed the presence of C, N, O, and Cl. For samples with the shorter polymer, Br was also detected. C 1s spectra for pMETAC were fitted with three peaks representing aliphatic C at 285.0 eV C with N or O neighbor at 286.4 eV, and C in esters at 289.1 eV. The quaternary ammonium groups in the polymer

were observed in N 1s spectra at 402.6-402.7 eV (Figures S1 and S17, Supporting Information, Section 8.1). The spectra acquired from phages with polymer show the presence of both species in the analysis volume, in line with the observations from DLS and SAXS of an overlayer of polymers coating the surface of the phages. Three peaks can be observed in N 1s spectra from the assembly corresponding to NH and protonated NH at the phage surface, at low binding energy, and quaternary ammonium groups from the polymer at higher binding energy (cf. Figure S17 and Table S3, Supporting Information, Section 8.1). A unique peak relating to the phage is also observed in the C 1s spectra of the assembly since the polymer does not contain C in peptide bonds (at 288.2 eV). Furthermore, the COO peak corresponds to esters, observed in the phages at 288.7 eV, shifts to 289.1 eV, similar to that of the polymer, when the polymer is present in the sample and coats the phage surface. The similarity of the XPS data between the pure phage and the assembled phage-polymer system suggests that no significant alteration in the form of surface reorganization of Qbeta takes place during the adsorption of the polymer onto the surface of the phage, confirming a physical adsorption process.

4.2.5 Infectivity of Qbeta and Qbeta pMETAC1 Aggregates

The Qbeta suprastructures were formed at Qbeta/pMETAC1 at 1:50 and separated as macroscopic aggregate from the liquid using centrifugation. The gel-like aggregate was resuspended in VDB buffer at pH 7.0 by gentle mixing with a pipette. The viral infectivity was studied by using a plaque assay (a detailed procedure can be found in the methods section of the Supporting Information, Section 8.1). The infectivity of Qbeta/pMETAC1 at 1:50 after centrifugation and separation was comparable to the original suspension. Compared to the unbound Qbeta, a 2.2 log reduction was observed (cf. Figure S18, Supporting Information, Section 8.1). This results from the fact that Qbeta is bound in the aggregates, hence the assay allows to count the number of infectious aggregate particles rather than infectious Qbeta particles. Overall, this proof of concept experiment demonstrates the separation of bactericidal Qbeta/pMETAC1 =1:50 suprastructured aggregates from the buffer. This opens future opportunities to develop novel phagebased materials, such as antimicrobial films. The aggregates' response to their environment, such as ionic strength and pH, may open the possibility of tailoring the suprastructures into a functional phage delivery system. Additionally, the fast and simple method of separating intact phages in the presence of pMETAC1 as macroscopic aggregates could be further developed into a virus extraction technology.

4.3 Conclusion

This study demonstrates advanced nanopatterned biomaterials from the self-assembly of the 29 nm protein nanocage Qbeta with a polycationic polymer. Upon interacting with pMETAC, Qbeta self-assembles into pH- and composition-responsive colloidal crystals. The pMETAC chain length is shown to influence the self-assembly process and structure strongly.

SAXS analysis confirms the formation of highly ordered, nanopatterned materials when Qbeta is combined with pMETAC of 3.3 kDa at a ratio of $\approx$ 1:50 (w/w). The Qbeta structure and surface chemistry are not modified in this process, and cryoXPS indicates non-covalent adsorption of the polymer onto the phage surface. Analysis of the SAXS and liquid AFM data demonstrate the formation of hexagonally packed Qbeta structures at pH 7.0. The pH of the suspension triggers structural transformation in the suprastructures. At pH $<$ 7.0, the long-range order of the suprastructures reduces, and the aggregates eventually disassemble at and below pH 5.0.

When the pMETAC chain length is increased to 16.5 kDa, the crystal-like ordering of the Qbeta decreases, as seen by the smearing of the Bragg reflections in the SAXS data. Zeta potential analysis demonstrates specific adsorption of the pMETAC, with charge inversion and disintegration of structures at elevated pMETAC content. Time-resolved light scattering studies showed that the self-assembly of the viruses with the polymers is homogenous and follows the diffusion-limited aggregation process. Rearrangement into the ordered structure is enabled due to the patchy-charge surface nature of Qbeta, which gets enhanced by the adsorbed pMETAC.

The thermodynamically stable Qbeta self-assemblies are mainly controlled by electrostatic interaction and are highly susceptible to changes in the ionic strength and temperature at or above 60°C. The Qbeta/pMETAC suprastructures could be separated from the liquid using centrifugation. The solid aggregate maintained its biological activity, albeit in a reduced form compared to free Qbeta in suspension.

Further optimizations of the composition may be required based on the desired conditions. Nevertheless, the versatility of bacteriophage provides inherent advantages, such as the scalability of synthesis and the customizability by bioengineering its surface properties. Pursuing suprastructured materials typically involves multiple steps in the synthesis. The simple production process presented in this work is transferable to other systems. It is feasible for large-scale production, targeting applications in biomedicine, food, and nanotechnology. The suprastructures can be further encapsulated or dispersed as particles with various loadings of, for instance, drugs and nutrients in the core of the protein cage.

4.4 Experimental Section

Synthesis and Virus Propagation

Poly [2-(methacryloyloxy)ethyl] trimethylammonium chloride (pMETAC) was synthesized with the activator generated by electron transfer (AGET) ATRP.[69, 70] Details on the synthesis and the material used can be found in the Materials and Methods part of the Supporting Information (Section 8.1). Qbeta was propagated in *Escherichia coli* strain W1485 and purified using ultra-centrifugation filtration. A detailed protocol can be found in the Supporting Information (Section 8.1).

Small-Angle X-Ray Scattering

SAXS measurements were conducted in the laboratory and at the Austrian SAXS beamline at Elettra (Trieste, Italy) at two beamtimes. Laboratory SAXS measurements were conducted on the SAXSpoint 5.0 (Anton Paar, Graz, Austria) coupled to a MetalJet D2 X-ray source (Excillum, Kista, Sweden). An X-ray beam with a wavelength λ, of 0.134 nm 9.3 keV and sample-to-detector distance was 1608.1 mm , providing a q-range from 0.04−2.4 nm^{-1}. The scattering vector magnitude q was calculated with Eq. 4.1, where n is the refractive index, which is virtually unity for X-rays in this study, θ is the scattering angle.

$$q = \frac{4\pi n}{\lambda} \sin\left(\frac{\theta}{2}\right) \tag{4.1}$$

The scattering and diffraction images were recorded using a 2D EIGER R 1M detector (Dectris Ltd., Baden, Switzerland) with a total area of 77.10 ×79.65 mm^2 and pixel size of 75 × 75 μm^2. The resulting 2D scattering patterns were radially integrated into the 1D $I(q)$ functions using SAXSanalysis 4.20 (Anton Paar, Graz, Austria). The temperature was kept at 25°C if not mentioned otherwise. Measurements were done in sextet to check for beam damage, and the average of the results was used. No beam damage was observed. The scattering curves were corrected for transmittance. Buffer scattering was measured with all samples and subtracted as background from the scattering curves.

For temperature scans, the sample was heated to the desired temperature and equilibrated for 5 min in a sample holder for vertical capillaries, which is temperature controlled by a Peltier device. The measurement was taken over a time span of 2 h.

At the Austrian SAXS beamline, an X-ray beam with a wavelength of 0.154 nm (8 keV) and sample-to-detector distance was 1753 mm and 906.2 mm was used, providing a q-range from 0.05 to 4.2 nm^{-1} and 0.07 to 7.4 nm^{-1}. The scattering patterns were recorded using a Pilatus3 1M detector (Dectris Ltd., Baden, Switzerland) with a total

area of 169 × 179 mm^2 and pixel size of 172 × 172 μm^2. The resulting 2D scattering patterns were azimuthally integrated into the 1D $I(q)$ functions using SAXSDOG.[71] The temperature was kept at 25°C. Measurements were done in quadruplets to check for beam damage, and the average of the results was used. No beam damage was observed. The scattering curves were corrected for transmittance using a semitransparent beam stop. Buffer scattering was subtracted as background from all samples as background.

SAXS Data Analysis

The SAXS data were analyzed using the generalized indirect Fourier transformation (GIFT) method[72, 73] and further analyzed with model-dependent fitting with SASfit.[74]

The scattering intensity I(q) of N monodisperse, homogeneous, and spherical particles is described by the product of the form factor $P(q)$ and the structure factor $S(q)$:

$$I(q) = NS(q)P(q) \tag{4.2}$$

The GIFT method allows the simultaneous fitting of $P(q)$ and $S(q)$ by selecting a suitable $S(q)$ model.[72, 74–77] With this method direct information on the size, shape of the particles, and their internal structure are obtained.[78–81] Further details on the GIFT method can be found in the Supporting Information (Section 8.1).

The virus structure before and after interaction with pMETAC was also analyzed with the spherical core-shell form factor model (cf. Equation S6, Supporting Information, Section 8.1) combined with a structure factor model for hexagonal structures (cf. Equation S10, Supporting Information, Section 8.1) to obtain the overall scattering intensity of the assembly $I_{\text{assembly}}(q)$, taking into account of additional factors (cf. Equation S9, Supporting Information, Section 8.1).[82–84] The detailed model and fitting procedure are described in the Supporting Information (Section 8.1). The data were fitted up to $q = 0.89$ nm^{-1} due to the low signal-to-noise ratio above that value.

For samples showing diffraction patterns, the Bragg peaks in the scattering curves, which correspond to the reflections from the planes defined by their hkl Miller indices, were assigned to the space groups of the liquid crystalline structures.

$$d_h = \frac{2\pi}{q_h} \tag{4.3}$$

$$\frac{1}{d^2{}_{hkl}} = \frac{4}{3}\frac{\left(h^2 + hk + k^2\right)}{a^2} \tag{4.4}$$

where q_{hkl} is the q-value of the Bragg peak corresponding to the reflection from the hkl Miller planes and d_{hkl} is the corresponding interplanar spacing. The lattice constant a was calculated from d_{hkl} using Equations 4.3 and 4.4, assuming a 2D hexagonal close-packed system. This structure provided the best possible fit to all peaks out of all the tested symmetries.[85]

Cryogenic Transmission Electron Microscopy

Qbeta has been prepared for cryogenic transmission electron microscopy and for negative staining TEM. Samples for cryo-TEM were prepared on Quantifoil Holey Carbon Grids of Type R 2/2 Cu 300 (Quantifoil Micro Tools GmbH, Großlöbichau, Germany). Negative glow discharging for 30 s at 25 mA was performed in PELCO easiGlow (Ted Pella, inc., USA). Vitrifying of 4 µL sample was performed on Vitrobot, FEI (ThermoFisher Scientific) at 20°C under 95% relative humidity. The sample suspension was adsorbed for 10 s, blotted for 5 s and plunge frozen into liquid ethane. All samples were stored under liquid nitrogen until imaging.

Grids were loaded by the autoloader system into Titan Krios G2 300 kV TEM (FEI). Images were recorded with K2 BioQuantom, energy filtered direct electron detector using Digital Micrograph software (Gatan, Inc. USA). 33000x magnification resulted in a recorded pixel size of 4.37 Å.

Atomic Force Microscopy

The colloidal Qbeta-pMETAC assemblies were deposited onto ultra-flat Au surfaces for AFM imaging in VDB at pH 7.0. Au substrates were fabricated by a template-assisted procedure [86, 87] based on silicon wafers (CrysTec, Berlin, Germany) to create an ultra-flat and fresh Au surface for every experiment. The Qbeta (1 mg mL^{-1}) and pMETAC 15 wt% solution were mixed in a volumetric 1:1 ratio by vortexing for 2 × 10 s until a turbid liquid had formed. Tiny droplets of the suspension were incubated on a fresh ultra-flat Au surface for 10 min. The VDB, prepared as described above, was exchanged several times to remove unbound components. The samples were equilibrated in the buffer in the AFM overnight to reduce thermal drift.

AFM images were acquired on a Dimension ICON equipped with a Nanoscope V controller (Bruker, Santa Barbara, USA) in PeakForce Tapping mode. Silicon nitride cantilevers SNL-A (Bruker, Santa Barbara, USA) with a typical resonance frequency of 65 kHz and a nominal spring constant of 0.35 N m^{-1} were operated at a PeakForce frequency of 1 kHz, a PeakForce setpoint of 8 mV, Peak Force Amplitude of 10 nm and a tip velocity of 300 nm s^{-1} in VDB.

AFM Data Processing

A first-order plane fit and first-order flattening procedure was applied to the height sensor channel of the AFM images in NanoscopeAnalysis (version 1.80, Bruker, Santa Barbara, USA). A fast Fourier transform (FFT) of a 926 nm × 926 nm sized image section and its azimuthal integration was performed using Python (NumPy package fft.fft2) to obtain the calculated 1D scattering pattern from the AFM data. A filter (Tukey window) was priory applied to avoid edge effects leading to artifacts during the FFT.

Electrophoretic Mobility Analysis

The electrophoretic mobility, μ_e, was determined by phase analysis light scattering on a Litesizer 500 (Anton Paar, Graz, Austria). The wavelength of the laser was 658 nm, the laser power was 40 mW, and the scattering angle was either 15° or 175°, optimized automatically through the build-in algorithm of the device. The temperature was 25°C for all measurements. The zeta-potential, ζ, was calculated with Henry's equation.[88]

$$\mu_e = \frac{2\varepsilon_r \varepsilon_0 \zeta \mathrm{f(ka)}}{3\eta} \tag{4.5}$$

ε_r is the relative permittivity of VDB of 76.64, ε_r is the permittivity of vacuum of $8.854 \times 10^{-12} \mathrm{CV}^{-1}\ \mathrm{m}^{-1}$, f(ka) is the Henry function, approximated to 1.5 by the Smoluchowski approximation,[89] and η is the viscosity of the solvent (VDB, 0.904 mPa s). The samples were diluted 20-fold and vortexed before being measured five times, applying a voltage of 50 V.

At the same time, the current I was measured on the same samples at the applied voltage V. From this, the conductivity σ is calculated (Equation 4.6), where L is the distance between the electrodes and S is the surface area.

$$\sigma = \frac{I}{V} \cdot \frac{L}{S} \tag{4.6}$$

Dynamic Light Scattering

Multi-angle DLS measurements were carried out with a light scattering goniometer (CGS-8F, ALV Langen, Germany) and a solid-state laser (Coherent Verdi V5, with a wavelength, λ, of 532 nm and max. power of 5 W) with single-mode fiber detection optics (OZ from GMP, Zurich, Switzerland), 8 fiber-optic detectors, and ALV 7004 correlators with fast expansion (ALV, Langen, Germany). Measured angles were in the range between 34.0 and 144.5°.

Qbeta and pMETAC in VDB were separately adjusted to pH 3.0, 5.0, 7.0, and 9.0. Immediately before the measurement, the components were mixed with a 1 mL pipette by 10x loading and unloading in a 5 mL DLS vial. Time-dependent DLS measurements were conducted with 10 s of accumulation over 1 h to monitor the kinetics of aggregation. The total volume of the sample was 2 mL at an estimated total concentration of 0.002-0.005 wt%, depending on the ratio of Qbeta to pMETAC (1:1, 1:0.5, 1:0.2, 1:0.1). The refractive index and viscosity of water, $n = 1.33$ and $\eta = 0.89 \times 10^{-3}$ Pa s and temperature of 25°C were used for all measurements.

The DLS autocorrelation functions were fitted with the Cumulant method. The apparent hydrodynamic radius (R_H) was determined from the diffusion coefficient using the Stokes-Einstein equation (cf. Materials and Methods in the Supporting Information, Section 8.1 for details).[90] The diffusion-limited cluster aggregation (DLCA) model was used to compare the aggregation behavior of the Qbeta under different conditions based on the time-dependent DLS data (cf. Materials and Methods in the Supporting Information, Section 8.1 for details).[91]

X-ray Photoelectron Spectroscopy

XPS spectra were acquired on a Kratos Axis Ultra DLD spectrometer with a monochromated Al Kalpha source operated at 150 W as previously described.[67] All spectra were acquired with a hybrid lens system, an analysis area of 0.3 by 0.7 mm, and using the inbuilt charge neutralizing system of the spectrometer. The binding energy scale was referenced to aliphatic carbon at 285.0 eV. The survey spectra were collected using an analyzer pass energy of 160 eV, while high-resolution spectra were collected using a pass energy of 20 eV. The polymeric samples were measured as a powder at room temperature (21°C), while samples containing the phages were measured as a suspension in VDB at pH 7.0 under cryogenic conditions. For cryo-XPS, a small quantity of the liquid samples (15 — 20 µL) was placed with an automatic pipette onto the pre-cooled copper stub (—170°C) inside the loading chamber, which immediately froze the droplet. The sample holder was transferred into the analyzing chamber, and analyzed under cryogenic conditions using liquid nitrogen cooling. Data analysis was performed in CasaXPS, Casa Software Ltd. using a Shirley background and Gaussian-Lorentzian (GL30) peak shapes.[92]

Acknowledgements

The Swiss National Science Foundation funded this work through project no. 186251 and the National Center of Competences in Research (NCCR) Bioinspired Materials. The authors thank the CERIC-ERIC Consortium for access to the Austrian SAXS beamline at the Elettra Synchrotron (outstation of the Institute of Inorganic Chemistry, Graz University of Technology) and Heinz Amenitsch for technical support. The authors further acknowledge Nico Bruns and Sara R. Velasquez for the technical support with GPC measurements and Linda Sandblad with electron microscopy. Open access funding provided by Université de Fribourg.

4.5 Supporting Information

The Supporting Information has been restricted to the Supplementary Figure of the AFM experiment. The full version of the Supporting Information is available in the Appendix (chapter 8.1).

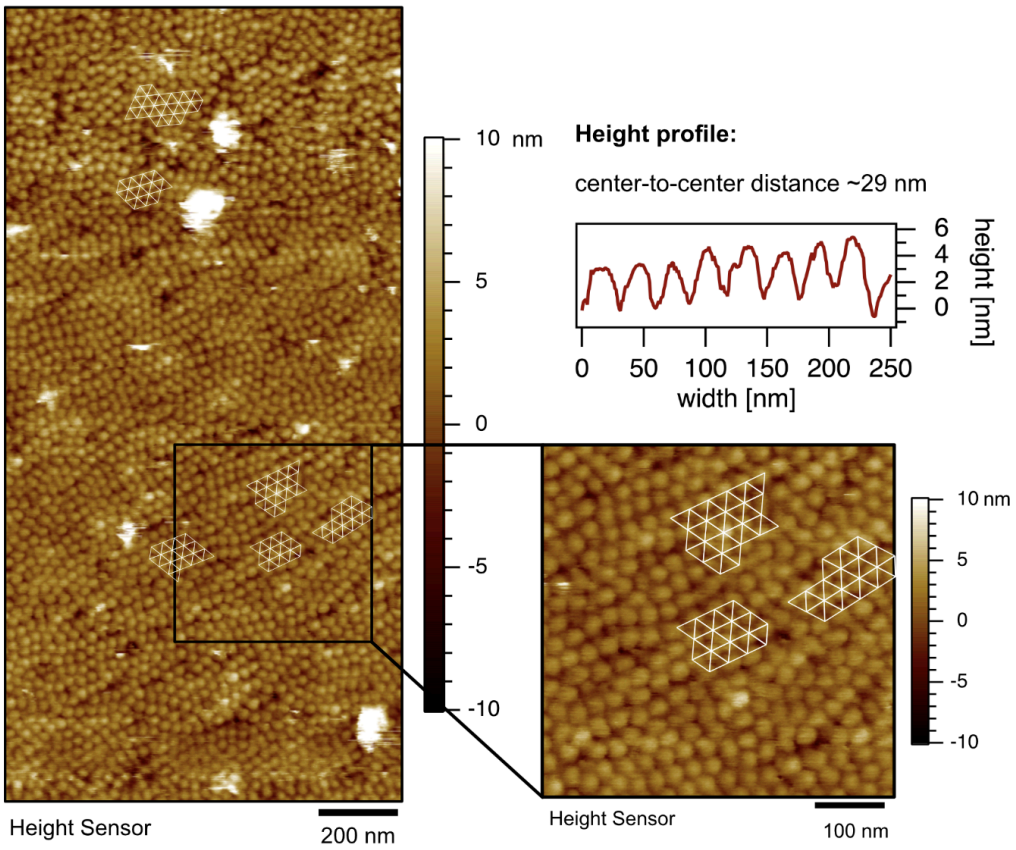

Figure 4.5. AFM image of Qbeta/pMETAC1 assembly acquired in VDB. Hexagonal arrangements were marked with a white pattern. The enlarged height profile indicates a center-to-center distance of ≈ 29 nm for the Qbeta in this structure.

References

(1) Yao, H.; Ge, J.; Mao, L.; Yan, Y.; Yu, S. *Adv. Mater.* **2014**, *26*(1), 163–187.

(2) Elsharkawy, S.; Mata, A. *Adv. Healthc. Mater.* **2018**, *7*(18), e1800178.

(3) Chen, C.; Kuang, Y.; Zhu, S., et al. *Nat. Rev. Mater.* **2020**, *5*(9), 642–666.

(4) Koushik, T.; Miller, C.; Antunes, E. *Adv. Healthc. Mater.* **2023**, *12*(9), e2202766.

(5) Gotti, C.; Sensini, A.; Zucchelli, A.; Carloni, R.; Focarete, M. L. *Appl. Mater. Today* **2020**, *20*, 100772.

(6) Dos Remedios, C.; Chhabra, D.; Kekic, M., et al. *Physiol. Rev.* **2003**, *83*(2), 433–473.

(7) Koyani, R.; Pérez-Robles, J.; Cadena-Nava, R. D.; Vazquez-Duhalt, R. *Nanotechnol. Rev.* **2017**, *6*(5), 405–419.

(8) Buller, S.; Strunk, J. *J. Energy Chem.* **2016**, *25*(2), 171–190.

(9) Roy, A.; Chatterjee, K. *Nanoscale* **2021**, *13*(2), 647–658.

(10) Sinha, N.; Langenstein, M.; Pochan, D.; Kloxin, C.; Saven, J. *Chem. Rev.* **2021**, *121*(22), 13915–13935.

(11) Gontsarik, M.; Yaghmur, A.; Ren, Q.; Maniura-Weber, K.; Salentinig, S. *ACS Appl. Mater. Interfaces* **2019**, *11*(3), 2821–2829.

(12) Zabara, M.; Ren, Q.; Amenitsch, H.; Salentinig, S. *ACS Appl. Bio Mater.* **2021**, *4*(6), 5295–5303.

(13) Salentinig, S. *Curr. Opinin. Colloid Interface Sci.* **2019**, *39*, 190–201.

(14) Watts, S.; Tran, B.; Salentinig, S. *Chimia* **2022**, *76*(10), 846–851.

(15) João, J.; Lampreia, J.; Prazeres, D.; Azevedo, A. *Biotechnol. Adv.* **2021**, *49*, 107758.

(16) Wang, Y.; Douglas, T. *Acc. Chem. Res.* **2022**, *55*(10), 1349–1359.

(17) Souza, G.; Molina, J.; Raphael, R., et al. *Nat. Nanotechnol.* **2010**, *5*(4), 291–296.

(18) Korpi, A.; Anaya-Plaza, E.; Välimäki, S.; Kostiainen, M. *Rev. Nanomed. Nanobiotechnol.* **2020**, *12*(1), e1578.

(19) O'Connell, L.; Marcoux, P.; Roupioz, Y. *ACS Biomater. Sci. Eng.* **2021**, *7*(6), 1987–2014.

(20) Gillitzer, E.; Willits, D.; Young, M.; Douglas, T. *Chem. Commun.* **2002**, *38*(20), 2390–2391.

(21) Hommersom, C.; Matt, B.; van der Ham, A.; Cornelissen, J.; Katsonis, N. *Org. Biomol. Chem.* **2014**, *12*(24), 4065–4069.

(22) Seitz, I.; Saarinen, S.; Kumpula, E., et al. *Nat. Nanotechnol.* **2023**, *18*(10), 1205–1212.

(23) Cardinale, D.; Carette, N.; Michon, T. *Trends Biotechnol.* **2012**, *30*(7), 369–376.

(24) Edwardson, T.; Levasseur, M.; Tetter, S., et al. *Chem. Rev.* **2022**, *122*(9), 9145–9197.

(25) Gordillo Altamirano, F.; Barr, J. *Clin. Microbiol. Rev.* **2019**, *32*(2), e00066–18.

(26) Rūmnieks, J.; Tārs, K. In *Virus Protein and Nucleoprotein Complexes*, Harris, J., Bhella, D., Eds.; Springer: Singapore, 2018, pp 281–303.

(27) Gorzelnik, K.; Zhang, J. *Prog. Biophys. Mol. Biol.* **2021**, *160*, 79–86.

(28) Callanan, J.; Stockdale, S.; Adriaenssens, E., et al. *Microb. Genom.* **2021**, *7*(11), 000686.

(29) Cui, Z.; Gorzelnik, K.; Chang, J., et al. *PNAS* **2017**, *114*(44), 11697–11702.

(30) Watts, S.; Maniura-Weber, K.; Siqueira, G.; Salentinig, S. *Small* **2021**, *17*(30), e2100307.

(31) Armanious, A.; Aeppli, M.; Jacak, R., et al. *Environ. Sci. Technol.* **2016**, *50*(2), 732–743.

(32) Dickinson, E.; Eriksson, L. *Adv. Colloid Interface Sci.* **1991**, *34*, 1–29.

(33) Popa, I.; Gillies, G.; Papastavrou, G.; Borkovec, M. *J. Phys. Chem. B* **2009**, *113*(25), 8458–8461.

(34) Chodanowski, P.; Stoll, S. *J. Chem. Phys.* **2001**, *115*(10), 4951–4960.

(35) Winkler, R. G.; Cherstvy, A. G. In *Advances in Polymer Science: Polyelectrolyte Complexes in the Dispersed and Solid State I*; Springer Berlin Heidelberg: Berlin, Heidelberg, 2013, pp 1–56.

(36) Samanta, R.; Halabe, A.; Ganesan, V. *J. Phys. Chem. B* **2020**, *124*(22), 4421–4435.

(37) Holkar, A.; Toledo, J.; Srivastava, S. *AIChE J.* **2021**, *67*(12).

(38) Moore, C.; Gao, W.; Fatehi, P. *Polymers* **2021**, *13*(22), 3871.

(39) Raynold, A.; Li, D.; Chang, L.; Gautrot, J. *Nat. Commun.* **2021**, *12*(1), 6445.

(40) Watts, S.; Gontsarik, M.; Lassenberger, A., et al. *Adv. Mater. Interf.* **2023**, *10*(8).

(41) Gan, B.; Gaynord, J.; Rowe, S.; Deingruber, T.; Spring, D. *Chem. Soc. Rev.* **2021**, *50*(13), 7820–7880.

(42) Visnevskij, C.; Makuska, R. *Macromolecules* **2013**, *46*(12), 4764–4771.

(43) Plazzotta, B.; Diget, J.; Zhu, K.; Nyström, B.; Pedersen, J. *J. Polym. Sci. B Polym. Phys.* **2016**, *54*(19), 1913–1917.

(44) Watts, S.; Hänni, E.; Smith, G., et al. *J. Colloid Interface. Sci.* **2024**, *657*, 971–981.

(45) Golmohammadi, R.; Fridborg, K.; Bundule, M.; Valegård, K.; Liljas, L. *Structure* **1996**, *4*(5), 543–554.

(46) Gorzelnik, K.; Cui, Z.; Reed, C., et al. *PNAS* **2016**, *113*(41), 11519–11524.

(47) Mykhaylyk, O. O.; Ryan, A. J.; Tzokova, N.; Williams, N. *J. Appl. Crystallogr.* **2007**, *40*(s1), s506–s511.

(48) Schmidt, P. W. *J. Appl. Crystallogr.* **1982**, *15*(5), 567–569.

(49) Barany, S. *Adv. Colloid Interface Sci.* **2015**, *222*, 58–69.

(50) Bauer, D.; Li, D.; Huffman, J., et al. *J. Virol.* **2015**, *89*(18), 9288–9298.

(51) Manzenrieder, F.; Luxenhofer, R.; Retzlaff, M.; Jordan, R.; Finn, M. *Angew. Chem. Int. Ed. Engl.* **2011**, *50*(11), 2601–2605.

(52) Szilagyi, I.; Sadeghpour, A.; Borkovec, M. *Langmuir* **2012**, *28*(15), 6211–6215.

(53) Netz, R. R.; Andelman, D. *Phys. Rep.* **2003**, *380*(1-2), 1–95.

(54) Chaplain, V.; Janex, M. L.; Lafuma, F.; Graillat, C.; Audebert, R. *Colloid Polym. Sci.* **1995**, *273*(10), 984–993.

(55) Carnal, F.; Stoll, S. *J. Phys. Chem. B* **2011**, *115*(42), 12007–12018.

(56) Pandav, G.; Pryamitsyn, V.; Errington, J.; Ganesan, V. *J. Phys. Chem. B* **2015**, *119*(45), 14536–14550.

(57) Kleimann, J.; Gehin-Delval, C.; Auweter, H.; Borkovec, M. *Langmuir* **2005**, *21*(8), 3688–3698.

(58) Armanious, A.; Agnarsson, B.; Lundgren, A.; Zhdanov, V. P.; Höök, F. *J Phys. Chem. C* **2021**, *125*(41), 22733–22746.

(59) Borkovec, M.; Papastavrou, G. *Curr. Opin. Coll. Interf. Sci.* **2008**, *13*(6), 429–437.

(60) Kratky, K. W. *Chem. Phys.* **1981**, *57*(1-2), 167–174.

(61) Pronk, S.; Frenkel, D. *J. Chem. Phys.* **1999**, *110*(9), 4589–4592.

(62) Szilagyi, I.; Szabo, T.; Desert, A., et al. *Phys. Chem. Chem. Phys.* **2014**, *16*(20), 9515–9524.

(63) Trefalt, G.; Szilágyi, I.; Borkovec, M. *Colloid Polym. Sci.* **2020**, *298*(8), 961–967.

(64) Wu, H.; Lattuada, M.; Morbidelli, M. *Adv. Colloid Interface Sci.* **2013**, *195-196*, 41–49.

(65) Liu, J.; Shih, W.; Sarikaya, M.; Aksay, I. *Phys. Rev. A* **1990**, *41*(6), 3206–3213.

(66) Baer, D.; Artyushkova, K.; Brundle, C., et al. *J. Vac. Sci. Technol. A* **2019**, *37*(3), 031401.

(67) Shchukarev, A.; Backman, E.; Watts, S., et al. *Front. Chem.* **2021**, *9*, 666853.

(68) Rouxhet, P. G.; Genet, M. J. *Surf. Interface Anal.* **2011**, *43*(12), 1453–1470.

(69) Wang, J.-S.; Matyjaszewski, K. *JACS* **1995**, *117*(20), 5614–5615.

(70) Matyjaszewski, K.; Jakubowski, W.; Min, K., et al. *PNAS* **2006**, *103*(42), 15309–15314.

(71) Burian, M.; Meisenbichler, C.; Naumenko, D.; Amenitsch, H. *J. Appl. Crystallogr.* **2022**, *55*(Pt 3), 677–685.

(72) Fritz, G.; Bergmann, A.; Glatter, O. *J. ChemPhys.* **2000**, *113*(21), 9733–9740.

(73) Bergmann, A.; Fritz, G.; Glatter, O. *J. Appl. Crystallogr.* **2000**, *33*(5), 1212–1216.

(74) Breßler, I.; Kohlbrecher, J.; Thünemann, A. *J. Appl. Crystallogr.* **2015**, *48*(Pt 5), 1587–1598.

(75) Brunner-Popela, J.; Glatter, O. *J. Appl. Crystallogr.* **1997**, *30*(4), 431–442.

(76) Brunner-Popela, J.; Mittelbach, R.; Strey, R., et al. *J. Chem. Phys.* **1999**, *110*(21), 10623–10632.

(77) Weyerich, B.; Brunner-Popela, J.; Glatter, O. *J. Appl. Crystallogr.* **1999**, *32*(2), 197–209.

(78) Glatter, O. *J. Appl. Crystallogr.* **1977**, *10*(5), 415–421.

(79) Glatter, O. *J. Appl. Crystallogr.* **1980**, *13*(6), 577–584.

(80) Glatter, O. *J. Appl. Crystallogr.* **1981**, *14*(2), 101–108.

(81) Glatter, O.; Hainisch, B. *J. Appl. Crystallogr.* **1984**, *17*(6), 435–441.

(82) Pedersen, J. S. *Adv. Colloid Interf. Sci.* **1997**, *70*, 171–210.

(83) Förster, S.; Fischer, S.; Zielske, K., et al. *Adv. Colloid. Interface Sci.* **2011**, *163*(1), 53–83.

(84) Förster, S.; Timmann, A.; Konrad, M., et al. *J. Phys. Chem. B* **2005**, *109*(4), 1347–1360.

(85) *International Tables for Crystallography*; Aroyo, M. I., Ed.; International Union of Crystallography: Chester, England, 2016.

(86) Stamou, D.; Gourdon, D.; Liley, M., et al. *Langmuir* **1997**, *13*(9), 2425–2428.

(87) Kuznetsov, V.; Papastavrou, G. *Langmuir* **2012**, *28*(48), 16567–16579.

(88) Delgado, A. V.; González-Caballero, F.; Hunter, R. J.; Koopal, L. K.; Lyklema, J. *Pure Appl. Chem.* **2005**, *77*(10), 1753–1805.

(89) Hunter, R. J., *Zeta Potential in Colloid Science – Principles and Applications*; Academic Press: Cambridge, 1981.

(90) Koppel, D. E. *J. Chem. Phys.* **1972**, *57*(11), 4814–4820.

(91) Sabín, J.; Prieto, G.; Ruso, J.; Messina, P.; Sarmiento, F. *Phys. Rev. E Stat. Nonlin. Soft Matter Phys.* **2007**, *76*(1 Pt 1), 011408.

(92) Wagner, C. D.; Davis, L. E.; Zeller, M. V., et al. *Surf. Interface Anal.* **1981**, *3*(5), 211–225.

5

Electrogelation: Controlled Fast Formation of Micrometer-Thick Films from Low-Molecular Weight Hydrogelators

Nadine Raßmann, Melina Weber, Roman E. J. Glaß, Klaus Kreger, Nicolas Helfricht, Hans-Werner Schmidt, and Georg Papastavrou*

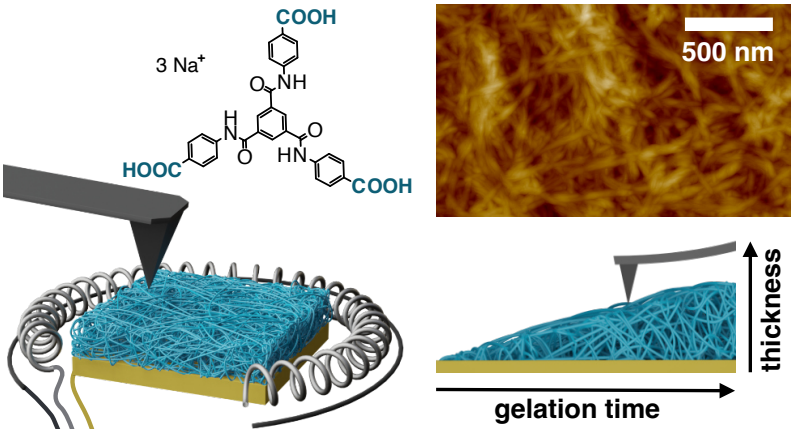

Reprinted with permission from:

„Electrogelation: Controlled Fast Formation of Micrometer-Thick Films from Low-Molecular Weight Hydrogelators “

Langmuir, **2023**, *39*(48), 17190-17200.

Abstract

The controlled electrochemical deposition of hydrogels from low-molecular weight hydrogelators (LMWHGs) allows for the defined formation of thin films on electrodes. Here, the deposition of fibrillar networks consisting of N,N',N"-tris(4-carboxyphenylene)-1,3,5-benzenetricarboxamide (BTA) onto ultraflat gold electrodes has been studied. This process, also termed electrogelation, is based on a local change in the pH due to electrolysis of water at the electrode. The protonation of the BTA sodium salt leads to self-assembly into supramolecular fibrillar structures mainly via hydrogen bonding of the uncharged molecules. The resulting hydrogel film was characterized in terms of its thickness by atomic force microscopy (AFM). Two different AFM-based techniques have been used: ex situ imaging of dried films and in situ nanoindentation of the hydrated hydrogel films. The deposition process was studied as a function of gelator concentration, applied potential, and gelation time. These parameters allow control of the film thickness to a high degree of accuracy within a few tenths of nanometers. Film formation takes place in a few seconds at moderate applied potentials, which is beneficial for biomedical applications. The results obtained for the BTA presented here can be transferred to any type of pH-responsive LMWHG and many reversibly formed hydrogel films.

5.1 Introduction

Electrodeposition under potentiostatic or galvanostatic control has a long history. The deposition of metals on electrodes can be traced back directly to Faraday and is still today highly relevant for industrial processes like galvanization.[1] Electropolymerization allows the formation of polymeric films on electrodes with control over film morphology and thickness.[2, 3] Electropolymerization is a bottom-up route for forming high-molecular weight polymers from monomers directly on the electrode. By contrast, the electrodeposition of polyelectrolytes is a top-down approach, in which already synthesized polymers, primarily polyelectrolytes, adsorb to the electrode.[4–6] The potential applied to the electrode governs the process in both cases. The term 'electrogelation' is currently used for a broad range of electrodeposition processes. Most often this term describes the formation of physical networks formed by organic gelator molecules due to a local pH change by electrolysis of water [7, 8] or the oxidation and reduction of a secondary agent, such as hydroquinone [9–11] or hydrogen peroxide [12]. These two processes have in common that no direct oxidation or reduction of the gelator takes place while they are still bottom-up deposition processes. This approach has been utilized for the electrochemical assembly of films of biopolymers such as chitosan,[13–17] alginate,[18–20] agarose,[21] and silk.[22–28]

Low-molecular weight hydrogelators (LMWHGs) are small molecules that form typically fibrillar structures via secondary interactions in aqueous media upon application of external stimuli, such as pH changes, the presence of specific ions, or temperature changes.[29] During this change of conditions, LMWHGs form physical networks in the entire volume of the liquid, resulting in a macroscopic sol–gel transition.[10, 11, 30, 31] The sol–gel transition/hydrogelation, however, can also take place on electrodes [7, 13–28, 32] even though the electrogelation of LMWHGs on an electrode has been reported only sparsely in the literature.[9, 11, 32–34] Interestingly, the electrogelation of LMWHG based on dipeptides by a hydroquinone oxidation-mediated pH shift at an electrode interface[9, 11, 33] takes place at potentials (< 1.5 V) considerably lower than that of the electrochemically induced formation of silk-gels (≈ 25 V),[22–24] which make LMWHGs appealing candidates for biomedical applications.

Here, we comprehensively studied the electrogelation of a LMWHG, namely, *N,N',N"*-tris(4-carboxyphenylene)-1,3,5-benzenetricarboxamide (BTA hereafter). 1,3,5-Benzenetricarboxamides are, in general, widely used due to their robust self-assembly into supramolecular nanofibers.[35] Among the plethora of molecular structures, several 1,3,5-benzenetricarboxamides, particularly with polar peripheral side groups, are known to yield supramolecular structures in aqueous media upon being heated or cooled.[36–39] In particular, derivatives of 1,3,5-benzenetricarboxamides with peripheral aromatic carboxylic acid groups can form hydrogels in water with a change in pH to the acidic regime. Adding dilute HCl or glucono-delta-lactone, protonates the initially used trisodium salt of the BTA (NaBTA), which becomes insoluble in water, resulting in self-assembly into a fibrillar network.[40]

In the past, primarily optical and fluorescence microscopy techniques have been utilized to study electrochemically induced gel growth.[13–16, 41] However, these microscopical techniques are best suited for films with thicknesses of several micrometers. Such thicknesses are typical for hydrogel films of silks or biopolymers on electrodes [13–16] but not the early stages of synthetic LMWHG films on electrodes. Electrochemical quartz crystal microbalance (EQCM) can provide in principle a highly sensitive technique for the adsorbed mass. However, for hydrogel films, simple approximations, such as the Sauerbrey equation, cannot be applied due to their high water content.[42] So far, EQCM has been used to study only electrodeposited polyelectrolyte films to the best of our knowledge.[15, 43] Hence, different surface analytical approaches must be introduced to follow the growth of electrogelated BTA films in their early stages. Here, atomic force microscopy (AFM) is utilized to determine the film thickness. By combining AFM imaging on gold electrodes and AFM-based nanoindentation, we can directly characterize the thickness of the electrodeposited hydrogel layer in the hydrated and dried state. We demonstrate that BTA film formation, and especially film thickness, can be controlled

to a high degree of accuracy, i.e., few tenths of nanometers, by gelation time, gelator concentration, and applied potential.

5.2 Experimental Section

Synthesis of BTA

Synthesis and purification of the *N,N',N"*-tris(4carboxyphenylene)-1,3,5-benzenetricarboxamide trisodium salt are described in the Supporting Information 5.5.1.

Electrode Preparation

Ultraflat Au electrodes on a glass support were prepared by a template-assisted procedure.[44, 45] Briefly, a silicon wafer (10mm in diameter, p-Typ, CrysTec GmbH, Berlin, Germany) was cleaned by a modified three-step RCA cleaning procedure.[46] The wafer was sonicated in 2 vol% Hellmanex III (Hellma GmbH & Co. KG, Müllheim, Germany) in MilliQ grade water (resistivity of $> 18\ M\Omega\,cm^{-1}$, IQ7000, Merck Millipore, Darmstadt, Germany) at 40°C for 20 min and rinsed extensively with MilliQ water. In the next step, the silicon wafer was sonicated in a 3:1 (v:v) mixture of 2-propanol (p.a., VWR Chemicals, Darmstadt, Germany) and MilliQ water. Then, the wafer was thoroughly washed with MilliQ water. In a third step, the wafer was exposed to a 5:1:1 (v:v:v) mixture of MilliQ water, ammonia (25%, p.a., VWR Chemicals), and hydrogen peroxide (30 (w:v)%), Fisher Scientific, Schwerte, Germany) at 80°C for 20 min. Finally, the wafer was rinsed extensively with MilliQ water again and ultimately dried under a nitrogen stream. A 100 nm thin layer of Au (99.99%, Agosi, Pforzheim, Germany) was deposited onto the silicon wafer by thermal evaporation in a Mini Coater (MICO, Tectra GmbH, Frankfurt, Germany). Glass slides (11 mm × 11 mm × 1 mm, crown glass, Glasagentur Glenewinkel, Duingen, Germany) were cleaned with the same procedure as described for the silicon wafer. The cleaned glass slides were subsequently glued to the evaporated Au layer by using a temperature curing two-component epoxy glue (Epotec 377, Epoxy Technology Europe GmbH, Augsburg, Germany). The glue was cured at 150°C for 1 h Before usage, the ultraflat Au electrodes were stripped of the wafer and electrical contact was established by attaching silver wires (diameter of 0.25 mm, insulated with PTFE, Advent Research Materials, Witney, U.K.) using conductive silver paint (Plano GmbH, Wetzlar, Germany). The insulation of the silver wire was partially removed for attachment, and the new electric contact with the Au electrode was insulated using red insulating varnish (GC Electronics, Rockford, IL) that was cured at 80°C for 1 h.

Electrogelation

A three-electrode setup was implemented into a commercial AFM fluid cell (Asylum Research, Oxford Instruments, Santa Barbara, CA). A platinum wire (diameter of 0.127 mm, Alfa Aesar, Thermo Fisher GmbH, Kandel, Germany) was coiled to create a sufficiently large electrode area with respect to the area of the working electrode and was employed as the counter electrode (CE). The PTFE insulation of a silver wire (diameter of 0.25 mm, insulated with PTFE, Advent Research Materials) was partially removed, and AgCl was deposited on the wire by means of an ACl-01 chlorinator (npi electronic GmbH, Tamm, Germany). This wire was positioned in the cell as a quasi-reference electrode (quasi RE) and calibrated with respect to a commercial Ag/AgCl electrode (RE-5B 3 M NaCl, BASi, West Lafayette, IN). The potential of ultraflat Au electrodes employed as working (WE) electrodes was controlled by means of a potentiostat (CHi 750E, CH Instruments Inc., Austin, TX).

All electrodes and the AFM fluid cell were thoroughly rinsed with MilliQ water, 10 mM KOH (1 M KOH, Titrisol, Merck, Darmstadt, Germany) to dissolve potential residues of BTA gel, and MilliQ water before and after every use. Electrogelation was conducted in NaBTA solutions prepared from 10 mM NaCl (BioUltra, Sigma-Aldrich, Merck) at pH 5.0 (adjusted with 1 M HCl, Titrisol, Merck). For 1 $g\,L^{-1}$ NaBTA, an overall pH value of 6.0 ± 0.1 has been determined. A critical pH of 5.4 has been determined previously from titration experiments.[47] The NaBTA concentration varied between 0.25 $g\,L^{-1}$ and 5 $g\,L^{-1}$ for the concentration-dependent experiments. Prior to electrogelation, the NaBTA solution was filtered through a syringe filter with a pore size of 0.22 µm (PES, Carl Roth GmbH, Karlsruhe, Germany) and degassed in a desiccator for at least 1 h. The open circuit potential of the electrochemical cell was monitored in advance for every experiment for 300 s to verify equilibrium conditions. A fixed potential in the range of 1.20–1.50 V vs. Ag/AgCl was applied to the working electrode for a preset time ranging between 15 s and 120 s. The process was monitored by recording the current flow between the working electrode and the counter electrode. Eventually, the solution was carefully exchanged with MilliQ water four times to remove residues of the electrolyte as well as excess BTA molecules without damaging the hydrogel film. The BTA films were carefully covered and left to dry completely in a fume hood overnight before they were used for the *ex situ* experiments.

In situ Thickness of BTA Films Determined by AFM

The BTA hydrogel film thickness was determined *in situ* by an AFM full indentation approach that has been employed previously.[48, 49] A sharp tip AFM cantilever was moved toward the gel and pushed through it until the underlying substrates had been reached,

which corresponds to the constant compliance region in the force-distance profile. The spring constants of sharp tip cantilevers (CSC17 Cr-Au, MikroMasch) with a typical resonance frequency of 13 kHz were calibrated using the thermal noise method[50] and ranged from 0.29 to 0.37 $N\,m^{-1}$. The cantilevers were cleaned by dipping into a sequence of solvents: MilliQ water, ethanol (p.a., VWR Chemicals), acetone (p.a., VWR Chemicals), ethanol, and MilliQ water, successively. Finally, the cantilevers were treated with air plasma in a low-pressure plasma cleaner (Zepto, Diener electronic, Ebhausen, Germany) for 90 s before any measurement. The same fluid cell that was used for the *ex situ* gelation was mounted into a MFP 3D AFM instrument equipped with an ARC II controller (Asylum Research, Oxford Instruments, Santa Barbara, CA), which was installed on an inverted optical microscope (Axio Observer Z.1, Zeiss, Oberkochen, Germany). Electrogelation for *in situ* experiments was performed in a similar manner as described above for the *ex situ* experiments. The cantilever was retracted at a minimum 100 µm above the working electrode surface. The system was equilibrated for 30 min after the potential had been switched off to minimize drifts during the AFM measurements; 256 individual force vs. distance curves were acquired in a 16 × 16 grid on an 80 µm × 80 µm sized area. The cantilever was moved toward the substrate covered with BTA hydrogel at a tip velocity of 0.5 $\mu m\,s^{-1}$ at each position until a deflection setpoint of $1.0 - 1.5$ V, depending on the film thickness, was reached. The resulting cantilever deflection was sufficient to completely penetrate the soft hydrogel and reach contact with the underlying hard electrode in the constant compliance region. The optical lever sensitivity was calibrated after the acquisition of data on a BTA free part of the ultraflat Au substrate, which was separated from the electrode area. The cantilever was ramped against the substrate, and the optical lever sensitivity was extracted from the constant compliance region of the force vs. distance curves. After electrogelation, the solution in the measurement cell was carefully exchanged with MilliQ water four times, and the BTA films were left to dry in a fume hood overnight.

Raw AFM data was converted into force vs. distance profiles via previously used home-written procedures [45] in Igor Pro (Wavemetrics, Portland, OR), taking the optical lever sensitivity and spring constant of the cantilever into account. The gel thickness was determined by evaluating the distance between the initial interaction visible in the force curve and the hard contact with the Au substrate. The initial interaction was predefined as the distance at which the force exerted on the cantilever exceeds five standard deviations of the noncontact noise ($F > 5\sigma_{nc}$) and was evaluated by a home-written procedure in Igor Pro.

Determining the Thickness and Roughness of Dried Films by AFM

The thickness of the dried BTA films was determined by AFM imaging at the edge of a scratch. The films were scratched using a pipet tip to remove the film partially, meanwhile preventing damage to the underlying gold electrode. The 40 µm × 40 µm (512 × 512 pixels) AFM images were acquired in TappingMode using a Dimension Icon AFM instrument (Bruker, Santa Barbara, CA) equipped with a NanoScope V controller controlled by NanoScope software (version 9.3, Bruker). OMCL AC160TS cantilevers (Olympus, Tokyo, Japan) with a nominal resonance frequency of 300 kHz and a nominal spring constant of 26 $N\,m^{-1}$ were driven to a typical free amplitude of 500 mV and scanned across the edge of a scratch at a rate of 0.2 Hz. A plane fit and first-order flattening were applied to the AFM images under exclusion of the area covered by BTA using NanoScope analysis software (version 1.8, Bruker). The BTA film thickness across the whole image area was determined by averaged cross sections by using the internal step height function of the NanoScope analysis software. A minimum of three images per film were analyzed.

Additional AFM TappingMode images on a scan area of 5 µm × 5 µm (512 × 512 pixels) were acquired on the BTA films to determine their roughness. The internal roughness function of the NanoScope analysis software was used to calculate the root-mean-square roughness after applying a plane fit and first-order flattening to the AFM images.

5.3 Results and discussion

5.3.1 Electrogelation by Local Acidification at an Electrode Interface

N,N',N"-tris(4-carboxyphenylene)-1,3,5-benzenetricarboxamide (BTA) is a supra-molecular pH-responsive low-molecular weight hydrogelator (LMWHG) (cf. Figure 5.1A).[40] Acidification of the solution facilitates self-assembly of the BTA molecules into a hydrogel of fibrillar structure. The transition from the dissolved state of the BTA trisodium salt (NaBTA) (basic regime) to the fibrillar hydrogel structure (acidic regime) originates from the protonation of the carboxyl groups. Decreased solubility and weaker intermolecular repulsion of the BTA in water trigger the self-assembly into fibrillar structures.[40] Here, all solutions of NaBTA were prepared by addition of the salt to a pH 5.0 electrolyte solution and 10 mM NaCl, leading to an overall pH of 6.0 ± 0.1 for 1 $g\,L^{-1}$ NaBTA. A critical pH of 5.4 has been determined previously from titration experiments.[47] Under alkaline conditions, the deprotonation of the COOH groups and reestablishment of the electrostatic repulsion lead to BTA disassembly and dissolution of the hydrogel.

Shifting the pH to the acidic regime, as required for the formation of supramolecular fibrils, can also be achieved by electrolysis of water provided that sufficiently positive potentials are applied to an electrode immersed in a NaBTA solution.[34] Figure 5.1B illustrates how such a pH change at an electrode leads to the formation of an electrogelated film. Protons are generated by the so-called oxygen evolution reaction (OER) at the working electrode (WE):[1]

$$O_2 + 4\,H^+ + 4\,e^- \rightleftharpoons 2\,H_2O, \quad E_{OER} = 1.23\ \text{V vs. RHE}$$

Already relatively low applied potentials Φ on the order of 1.20 V vs. Ag/AgCl, which corresponds to 1.70 V vs. RHE (i.e., reversible hydrogen electrode), generate enough protons despite the rather high overpotentials of the OER on gold.[51] The local acidification of the electrode interface by the OER leads to protonation of NaBTA and induces the self-assembly of BTA molecules. A fibrillar BTA hydrogel network forms on the electrode.[34]

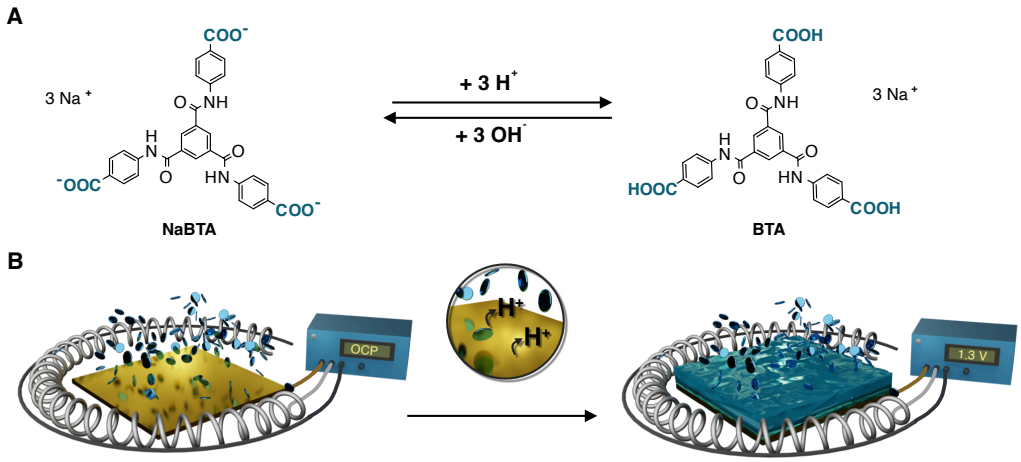

Figure 5.1. **A** The three carboxyl groups of the soluble trisodium salt of *N,N',N"*-tris(4-carboxyphenylene)-1,3,5-benzenetricarboxamide (NaBTA) are protonated under sufficiently acidic conditions. The protonated BTA molecules assemble into fibrillar hydrogels due to weaker intermolecular repulsion. The assembly process can be reversed by shifting the pH to the alkaline regime.[34] **B** Assembly of BTA into a hydrogel can be induced by local acidification in the vicinity of the working electrode in a three-electrode electrochemical setup. The local decrease in pH results from proton generation by the oxygen evolution reaction at the working electrode. The hydrogel film formed at the electrode is comparable to that resulting in bulk from a pH shift in solution.

To better control the OER, a three-electrode setup has been used to have full control of the potential at the working electrode.[1] The electrochemical cell has been incorporated directly in a commercial AFM fluid cell (cf. Figure 5.1B) [45, 52, 53] to allow for *in situ* AFM measurements. Ultraflat template stripped gold substrates have been utilized as working electrodes[45, 54] on which electrogelation takes place. A chlorinated silver

wire was used as the quasi-reference electrode (RE), and a platinum wire as the counter electrode (CE) has been placed in a circular manner around the WE.[53, 54]

5.3.2 Morphology of Electrogelated BTA Films

BTA hydrogels make up an extended network of fibrils with a diameter in the range of $25 - 100$ nm.[34] Figure 5.2 shows the fibrillar structure of dried BTA hydrogel films as prepared by electrogelation at 1.30 V vs. Ag/AgCl for 30 s in a solution of 1 $\mathrm{g\,L^{-1}}$ NaBTA salt at pH 5. 10 mM NaCl was added as the background electrolyte to increase solution conductivity. Electrogelated gels were characterized in the dried state by atomic force microscopy (AFM) in TappingMode (Figure 5.2A) and scanning electron microscopy (SEM) (Figure 5.2B). Both techniques show practically the same fibrous entangled structure of the BTA gel on gold electrodes. A similar structure has been reported previously for BTA gels.[34, 40] The electrogelated films show a roughness (r_{rms}) of < 10 nm in the dried state determined by AFM on a scan area of 25 µm, which is comparable across several spots on at least two different films.

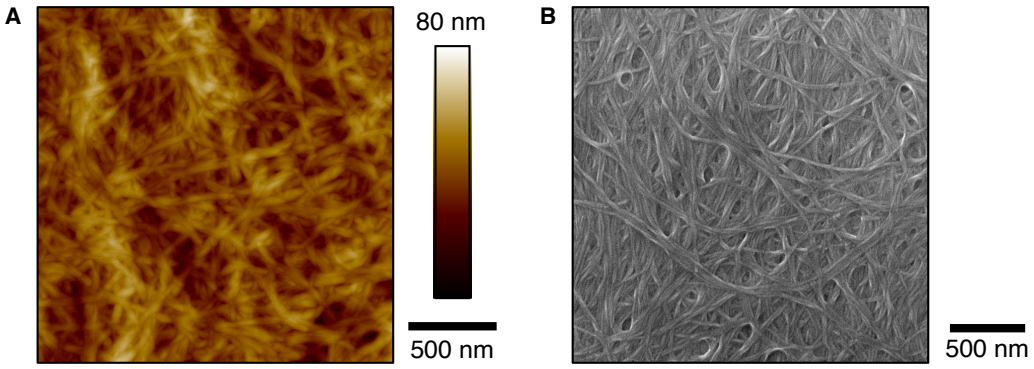

Figure 5.2. Fibrillar morphology of BTA films electrogelated at 1.30 V vs. Ag/AgCl for 30 s from 1 $\mathrm{g\,L^{-1}}$ NaBTA in 10 mM NaCl on an Au electrode surface in the dried state. **A** *Ex situ* AFM image acquired in TappingMode in air and **B** SEM image after drying and sputter coating.

5.3.3 Film Thickness as Determined by *ex situ* AFM Imaging

To follow the film growth of electrogelated BTA films, we used two AFM-based approaches. For the first approach, the electrogelation process has been stopped after defined time intervals, and the electrode has been removed from the electrochemical cell and dried after rinsing. After drying, the BTA hydrogel film was locally removed by applying a small scratch without damaging the Au electrode, which allows the film thickness to be determined by AFM TappingMode imaging. This scratching approach is used frequently

to determine the thickness of soft films on hard surfaces.[49] Electrogelated hydrogel films as obtained from LMWHGs have a high water content of > 90%, which is typical for hydrogels. Hence, imaging of such soft and very fibrillar structures (cf. Figure 5.2) is not feasible in the swollen state. However, due to material conservation, the thickness in the dried state represents a good indicator of how much BTA has been electrogelated on the electrode. However, the film thickness will be clearly underestimated and is not comparable to that of the hydrated state.

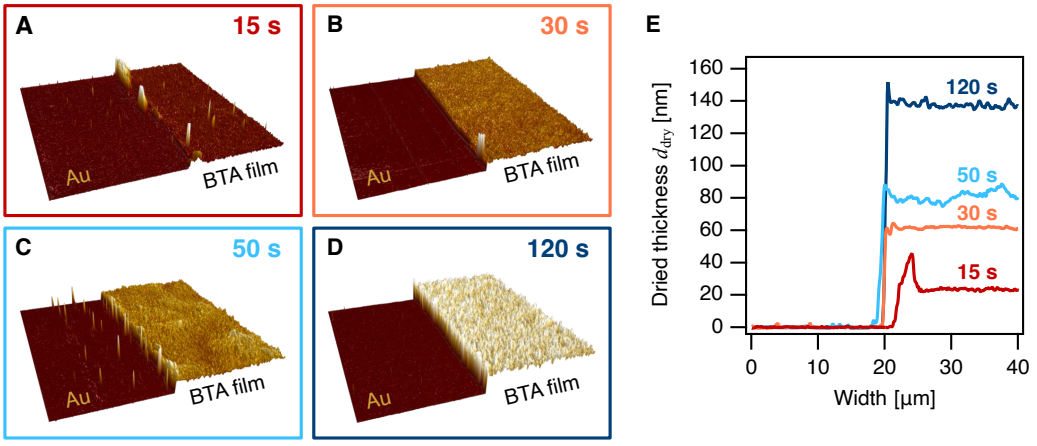

Figure 5.3. *Ex situ* AFM TappingMode images (40 µm × 40 µm) illustrating the evolution of electrogelated BTA films as a function of gelation time (1.40 V vs. Ag/AgCl from a 1 gL^{-1} NaBTA solution in 10 mM NaCl at pH 5). The film thickness can be compared directly from cross sections of the images at the edge of BTA films at different gelation times: **A** 15 s, **B** 30 s, **C** 50 s, and **D** 120 s. **E** Compilation of averaged cross sections from the AFM images shown in panels **A-D**.

Panels A-D of Figure 5.3 show a series of AFM images of the topography of dried BTA films and the underlying ultraflat Au electrode. The latter area was laid bare by carefully scratching the film. Comparison of the measured heights allows for a direct determination of the film thickness in the dried state. A large scan area of 40 µm × 40 µm was chosen to eliminate edge effects and to image a sufficient area of the underlying Au electrode within the scratched area. The BTA films have been obtained by electrogelation at 1.40 V vs. Ag/AgCl from a 1 gL^{-1} BTA solution at pH 5 in 10 mM NaCl. The electrogelation time, i.e., the time interval during which an external potential has been applied, varied from 15 s to 120 s. The respective cross sections of the height profiles (cf. Figure 5.3E) from the single images corroborate a monotonically increasing thickness of electrogelated BTA films as a function of gelation time. The height in the dried state increases from approximately 20 nm (dried) after 15 s to 135 nm (dried) after 120 s.

5.3.4 Film Growth Traced by *in situ* Nanoindentation

The second AFM-based technique is not based on scanning over the surface laterally but on pressing into the sample. It is termed nanoindentation and allows the tip to be pressed through the hydrogel film. This technique can be performed *in situ*, i.e., in the electrochemical cell filled with the BTA solution after electrogelation has been conducted. The electrochemical cell is identical to that utilized before and has been used previously for direct force measurements under potentiostatic control of the sample (cf. Figure 5.4A).[45, 52, 53] We determined the BTA film thickness directly after electrogelation by a full indentation method, which has been originally developed to determine the thickness of polyelectrolyte multilayers and lipid bilayers.[48, 49]

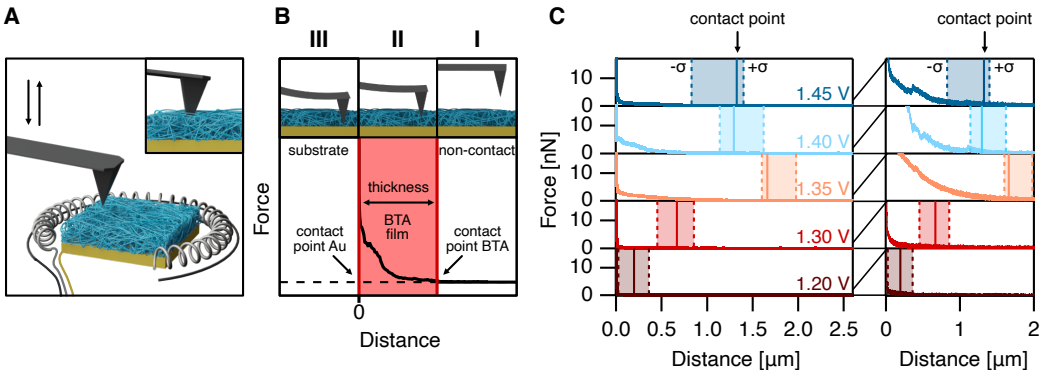

Figure 5.4. *In situ* determination of hydrated BTA film thickness by nanoindentation with the sharp tip of an AFM instrument. **A** Schematic illustration of the experimental setup. An electrochemical cell is integrated into the fluid cell of an AFM allowing to perform nanoindentation experiments in situ. **B** Exemplary force vs. distance curve for the indentation of electrogelated BTA films. Three regimes can be distinguished. **I** The tip is far away from the sample, and no interaction takes place. **II** Upon further approach, the tip touches the BTA film (contact point) and subsequently indents the film, which leads to increasingly repulsive forces. **III** Finally, the cantilever pierces the soft hydrogel film and reaches the nondeformable AuBTA interface at the electrode, which leads to a sharp increase in repulsive force. This point is defined as "zero distance", and the distance to the first contact point provides an estimate for the layer thickness.[48, 49] **C** Exemplary force profiles (left) for potentials between 1.20 V and 1.45 V versus Ag/AgCl and a gelation time of 30 s. Close-up (right) at 2 nN illustrating the contact point (solid line) with the BTA gel for the corresponding curve. The shaded areas mark one standard deviation of the mean for the whole data set of all force vs. distance curves acquired at the specified potential.

Here, the electrogelated BTA film is indented until the point that the tip reaches the underlying incompressible substrate (i.e., full indentation).[48, 49] An AFM cantilever with a sharp tip was chosen to facilitate the complete penetration of the BTA hydrogel film. If the tip pushes through the film and reaches the practically incompressible Au electrode, the so-called "constant compliance region" in the force vs. distance curve starts. In this constant compliance regime of the force curve, the displacement of the

z-piezo is directly proportional to the deflection of the cantilever. After conversion of the z-piezo displacement to the separation distance between the tip and sample, the constant compliance region is represented as a vertical increase in force with no change in separation distance due to the incompressibility of the substrate. In Figure 5.4B, which shows an exemplary force vs. distance curve, this part of the force curve is marked as region **III**. By contrast, for sufficiently large separation distances, practically no interaction between the tip and surface takes place. As a consequence, the force acting on the cantilever is negligible and does not change with separation distance (cf. region **I** in Figure 5.4B). However, with a decrease in the separation between the tip and film, the tip comes into with the electrogelated film (cf. region **II** in Figure 5.4B) and the film is compressed, which leads to a nonlinear force response due to the viscoelasticity of the hydrogel (cf. region **II** in Figure 5.4B).

The film thickness can be estimated from these force vs. distance profiles, like that shown in panels B and C of Figure 5.4, as the difference between the zero distance of the constant compliance region and the contact point. However, for practical purposes, the accurate definition of the latter is not without unambiguity. Here, we follow an approach that has also been widely used in tracing multiple adhesion events.[55] The cantilever is subject to thermal excitations and thus shows random noise deflection with a certain standard deviation σ_{nc} in the noncontact regime. We defined a threshold of $n\sigma_{nc}$ above this thermal noise floor as a criterion for the onset of contact between the tip and electrogelated film. Here, a threshold of $5\sigma_{nc}$ has been chosen. For $3\sigma_{nc}$, some false contact points were assigned, which could be attributed to local variations in the noncontact regime, rather than interaction with the gel that results in an overestimation of the film thickness. By contrast, for $10\sigma_{nc}$, significant interaction forces were applied before the attribution of contact. Thereby, a systematic underestimation of film thickness would have taken place. Figure 5.5 demonstrates that the choice of the threshold does not lead to a qualitative change in the determination of film thickness, which will be discussed below.

Figure 5.4C compiles some exemplary force profiles that have been acquired 30 min after the electrogelation process had reached completion to harmonize data acquisition and reduce drift during AFM measurements on freshly electrogelated BTA films. During the electrogelation, the cantilever was immersed in the solution but placed sufficiently far away from the electrode. The potentials applied for the electrogelation were varied between 1.20 V and 1.45 V vs. Ag/AgCl, while the other parameters remained constant [electrogelation time of 30 s as well as a 1 $g\,L^{-1}$ NaBTA solution (pH 5) and 10 mM NaCl, respectively]. An analogous data set for a shorter electrogelation time (15 s) is presented in Figure 5.9. For all of the profiles shown in Figure 5.4C, we marked the contact point (as identified by the threshold of $5\sigma_{nc}$) by a solid line. To preclude artifacts by plastic

deformation of the films after the full indentation experiments, the measurements were conducted on a 16 point × 16 point grid on an area of 80 µm × 80 µm. In total, a set of > 250 force vs. distance curves were acquired and evaluated per film. The center of each shaded area gives the average position of the contact point for all positions on the grid, while the solid line indicates the position of the contact point for the shown force profile. The shaded area extends one standard deviation in each direction for the position over all contact points found for the force curves on this type of film and hence represents the variation of the film thickness determined for the different films.

The large variation for the film thickness, even within one sample (cf. Figure 5.4C), is attributed to the fibrillar film structure of the BTA hydrogel films, as shown in Figure 5.2. The fibrils with diameters of several tenths of nanometres are protruding into the solution and form a complex, relatively heterogeneous structure. The BTA hydrogel films on the electrode are thus much less smooth than the polyelectrolytes or lipid layers.[48, 49] The insets for the low-force regime in Figure 5.4C show exemplary cases of how complex interaction profiles originate from the reorientation of fibrils due to the external force exerted by the tip. The tip can break through one fiber or layer, corresponding to a short force decrease until contact to the next underlying fiber is established and forces continue to increase again.

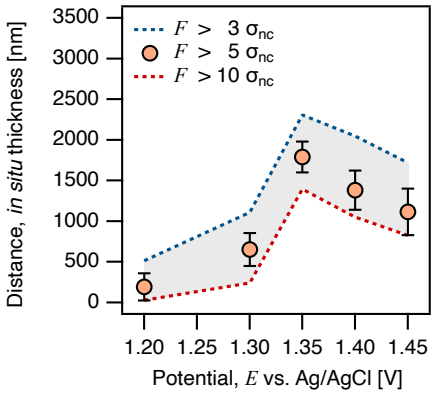

Figure 5.5. *In situ* thickness of electrogelated BTA films as a function of external potential for a gelation time of 30 s and 1 g L^{-1} NaBTA in 10 mM NaCl at pH 5. The data points correspond to a threshold force $F_c > 5\sigma_{nc}$ as an indicator for the contact point of the AFM tip with the BTA film. For comparison, the results (dashed lines) for two additional threshold values of $> 3\sigma_{nc}$ (blue) and $> 10\sigma_{nc}$ (red) are shown.

Figure 5.5 summarizes the *in situ* data for the film thickness as obtained from the nanoindentation measurements. The film thickness of the BTA hydrogel in its swollen state is shown as a function of the applied potential, which has been varied from 1.20 V to 1.45 V vs. Ag/AgCl. Electrogelation took place for 30 s (Figure 5.5), and similar data for a shorter gelation time (15 s) can be found in Figure 5.9. The other parameters

remained constant during the experiments (1 gL^{-1} NaBTA, 10 mM NaCl, pH 5). At gelation potentials of < 1.50 V vs. Ag/AgCl, forces as weak as 10–20 nN were sufficient to fully indent through the hydrogel film. For the combination of an applied potential of 1.50 V and a gelation time of 30 s, the film thickness reached >8 µm, which could no longer be measured due to the limited z-range of piezo of the AFM instrument. A similar trend for film thickness vs. gelation potential has been found for a gelation time of 15 s (cf. Sections 5.5.2 and 5.5.3 of the Supporting Information).

5.3.5 Determining the Swelling Factor Between the Hydrated and Dried State

Due to mass conservation, the BTA film thickness in hydrated and dried states must be strongly related and should be approximately proportional. The resulting proportionality factor is termed swelling factor.[56–58] Note that here, as opposed to other notations, we refer not to volume or mass ratio swelling factor [58] but solely to the increase in thickness in the axial direction. To determine the swelling factor, thickness d has been determined *in situ* in the hydrated state (d_{hyd}) and then *ex situ* in the dried state (d_{dry}). Thus, swelling factor χ is given by the equation $\chi = \frac{d_{hyd}}{d_{dry}}$. In Figure 5.6A, the corresponding film heights have been compiled. Both data sets always originate from the same films: one time measured *in situ* (filled data points) directly after finishing the gelation process and one time after drying *ex situ* (empty data points). Note the different scaling of the data by a factor 60.

Figure 5.6A illustrates that the thickness of the film increases with potential independently if the BTA film height has been determined in the hydrated and dried states. The same finding has been observed for other *in situ* vs. *ex situ* data sets with variation of potential and at a different gelation time (cf. Figure 5.10). However, a large scattering of ratio $\frac{d_{hyd}}{d_{dry}}$ can be observed, which we attribute to the fibrillar, heterogeneous structure of the films, in particular, in the hydrated state. Moreover, the nonmonotonous behavior occurring in the potential range of 1.35-1.40 V vs. Ag/AgCl was present also in other data sets and will be discussed below as it might be attributed to changes in the underlying gold substrate. Despite the scattering of swelling factor χ between the films, we find that the average for $\frac{d_{hyd}}{d_{dry}}$ over all films studied (cf. panel **I** of Figure 5.6B) provides a reasonable estimate for the swelling factor, which is here 29 ± 15. This overall value is consistent with the swelling factor determined for different experimental series, and the single swelling values fall within the standard deviation. It should be noticed that the swelling factor for the film prepared at 1.50 V exceeds by a factor of at least 2 the value for χ determined for the smaller potentials and has not been included. We attribute this

deviation to the increasing level of formation of gas bubbles at higher potentials [59] that lead to an inhomogeneous and inflated film.

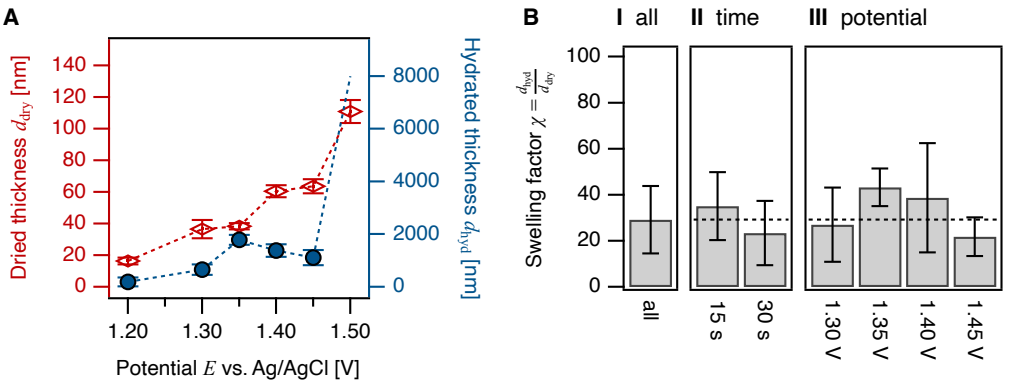

Figure 5.6. Determination of the swelling factor $\chi = \frac{d_{\text{hyd}}}{d_{\text{dry}}}$ between the hydrated and dried states of the BTA hydrogel films. **A** BTA film thickness as determined *in situ* (hydrated) and *ex situ* (dried) for BTA films electrogelated at different potentials (1.20 − 1.50 V vs. Ag/AgCl). The BTA film prepared at 1.50 V exceeded the z-piezo range of the AFM instrument and, therefore, the upper limit of the in situ method. **B I** Mean swelling factor $\chi = \frac{d_{\text{hyd}}}{d_{\text{dry}}}$ over all measurements, **II** swelling factors $\chi = \frac{d_{\text{hyd}}}{d_{\text{dry}}}$ for different gelation times and 1.30 V, and **III** swelling factors $\chi = \frac{d_{\text{hyd}}}{d_{\text{dry}}}$ for different potentials and a constant gelation time (30 s). The mean swelling ratio over all data is indicated by the dashed line in panels **II** and **III**.

Hence, the film thickness as determined in the dried state provides a sufficiently good approximation for the expected film thickness in the hydrated state. Thus, the wider parameter space of gelator concentration, electrogelation time, and applied potential can be mapped by the less time-consuming *ex situ* AFM technique in the dried state. Moreover, as no material is lost during drying, the height of the dried film provides, in our opinion, a more suitable measure for the total amount of material deposited on the electrode during electrogelation. Due to the collapsed state, local lateral variations in thickness are less pronounced than those in the hydrated state. However, the underlying assumption of the constant homogeneity or density of the electrogelated film independent of thickness and applied potential cannot be verified in the framework of the experimental techniques available.

5.3.6 Effect of Applied Potential, Gelation Time, and BTA Concentration on Film Thickness

The film thickness of an electrogelated BTA hydrogel is controlled by three fundamental parameters: (i) the applied potential, which is related to the rate of proton generation at

the electrode interface, (ii) the time during which the potential was applied, and (iii) the NaBTA concentration in the solution. We chose the *ex situ* imaging approach (cf. Figure 5.3) for the in-depth study of these parameters. Figure 5.7A plots the film thickness as a function of electrogelation time for four different applied potentials, ranging between 1.20 V and 1.50 V vs. Ag/AgCl. For these experiments, the other parameters, i.e., the NaBTA concentration, were kept constant at 1 $g\,L^{-1}$ and the background electrolyte (pH 5 and 10 mM NaCl) remained unchanged. Figure 5.7B plots the film thickness as a function of NaBTA concentration in a range of 0.25–5 $g\,L^{-1}$ for two different gelation times (15 and 30 s) and a constant potential of 1.40 V vs. Ag/AgCl. For all data shown, the film thickness is represented as the mean value of at least three AFM images per film. Individual films show small variations in thickness. The variation between different films electrogelated under identical conditions has been addressed for selected conditions (cf. Figure 5.12).

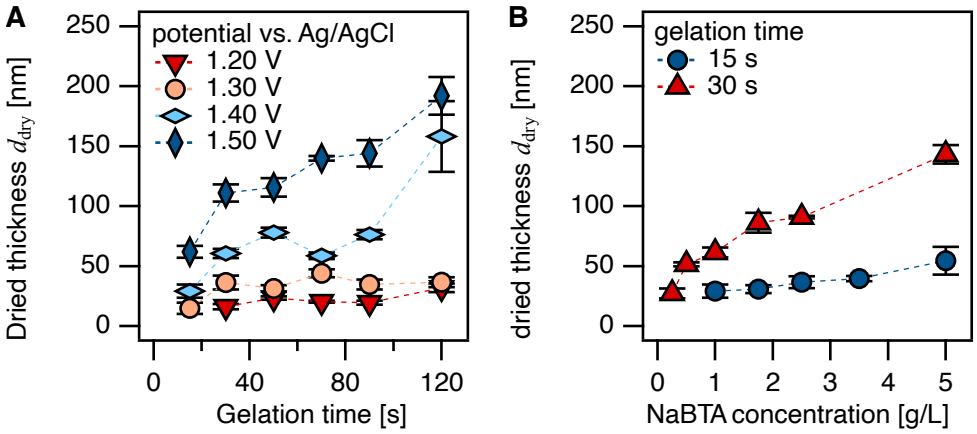

Figure 5.7. **A** Thickness of electrogelated BTA films as a function of gelation time (15-120 s) for four different potentials between 1.20 V and 1.50 V vs. Ag/AgCl and BTA concentration of 1 $g\,L^{-1}$ NaBTA. **B** BTA film thickness as a function of NaBTA concentration in the range of $0.25-0.50\ g\,L^{-1}$ for two gelation times (15 s and 30 s) and a constant potential of 1.40 V vs. Ag/AgCl. The background electrolyte composition was always 10 mM NaCl and pH 5

Figure 5.7 corroborates that the thickness of the BTA films increased with electrogelation time, as expected. In total, over longer electrogelation intervals, more protons are generated and these are diffusing farther from the electrode–electrolyte interface. Hence, the pH gradient is progressing farther from the electrode–electrolyte interface and allows for gelation of BTA at larger separation distances away from the electrode. Nevertheless, significant film thicknesses, which were sufficient to ensure complete coverage of the electrode surface, were already reached within the first 15–30 s for all potentials applied, which underlines the fast reaction rate constant for the formation of the fibrillar structures.

After this initial period of < 30 s, hydrogel formation continues, albeit at a slightly reduced rate. Plausibly, electrogelation slows with gelation time as the already formed gel hinders the diffusion of protons from the electrode and NaBTA molecules must diffuse from the bulk solution to the electrode. In some studies of electrogelation, a direct correlation between the total charge and the film thickness has been reported.[7] However, here, we opted for potentiostatic rather than galvanostatic control of the electrode mainly with respect to the uncertainties for the potentials at which the OER takes place in the case of the latter. The currents determined during the electrogelation progress decayed over time, approaching a plateau after approximately 15–30 s. Decreasing currents with time are an indication of a slowed electron transfer and, in turn, reduced the electrogelation rates. Corresponding current vs. time plots are shown in the Supporting Information (cf. Figure 5.15). Unfortunately, due to our experimental setup, the area of the electrode could not be controlled to a sufficiently high degree of accuracy to allow for a quantitative evaluation of the limiting currents. Our findings are in accordance with Leisk et al., who reported an exponential decay of current during silk electrogelation that they attributed to an insulating effect of the growing gel front.[25] We observed a steady increase in gel thickness up to 200 nm at higher potentials. Electrogelation of BTA, which is a LWMH, seems to be comparable in terms of film growth to another LWMHG [32] and the electrodeposition of polyelectrolytes as described by van Tassel and co-workers.[4] In both cases, a nearly linear increase in thickness with time has been observed at least for the first stages of film formation. Electrogelation allows us to increase the thickness of the films by a factor of ≤ 6 by tuning the gelation potential within the specified range and keeping the gelation time constant. Via combination of the control of both the gelation time and the potential, within the studied range, the hydrogel film thickness can be adjusted by ≤ 1 order of magnitude.

Another essential parameter for the electrogelation process is the NaBTA concentration in solution. Figure 5.7B shows the gel thickness as a function of NaBTA concentration in the range from 0.25 to 5 $g\,L^{-1}$ at a constant potential of 1.40 V vs. Ag/AgCl and for gelation times of 15 and 30 s. Electrogelation was possible at NaBTA concentrations as low as 0.25 $g\,L^{-1}$ and gelation times as short as 30 s. Hence, electrogelation allows the use of concentrations that are nearly 1 order of magnitude lower than the critical gelation concentration of 2 $g\,L^{-1}$ reported by Bernet et al. for the formation of a BTA gel in the bulk.[40] The presence of a solid interface might play a crucial role in allowing these lower concentrations. In contrast to bulk gelation, the pH is altered only locally, which limits the extension of the gel to the vicinity of the electrode.[7]

The best results, regarding control of the growth and homogeneity of the films, were achieved using NaBTA concentrations in the range of 1.0–2.5 $g\,L^{-1}$, albeit electrogelation was taking place under all conditions. In general, the increase in the NaBTA concentration

led to thicker films; for example, going from 1 $g\,L^{-1}$ to 5 $g\,L^{-1}$ NaBTA resulted in 2−2.5-fold thicker films depending on the gelation time.

5.3.7 Secondary Effects on the Working Electrode

As discussed in the previous sections, the BTA hydrogel exhibits a fibrillar and highly swollen character, which makes it harder to sharply define the interface between the BTA gel and the solution compared with the dried state. Increasing the applied potential leads to an increased rate of oxygen formation in the OER, which in turn increases the rate of formation of gaseous bubbles on the electrode. Excessive entrapment of oxygen bubbles in the hydrogel film is here undesired;[59] bursting of such bubbles, especially larger ones, tends to leave cavities and holes in the hydrogel film. The formation and release of gas bubbles could also lead to the transfer of material from the film into the solution, which might provide an explanation for the nonmonotonous film thickness increase as a function of the externally applied potential (cf. Figure 5.5 and Figure 5.6A). On the contrary, with decreasing potential, gelation time, and BTA concentration below the here-presented lower boundaries, no or an incomplete coverage of the electrode has been observed. However, we believe that other electrochemical reactions taking place at the electrode also contribute to the nonmonotonous increase in film thickness with potential.

Above a certain threshold, the externally applied potential will not only lead to the OER but also initiate further reactions of the electrode itself. Gold electrodes under acidic conditions and in the presence of chloride ions are known to be subject of the formation of oxide layers.[51, 60–62] Linear potential sweeps were performed under conditions analogous to those of electrogelation (cf. Figure 5.13, 5.14). The respective voltammogram shows a shoulder between approximately 1.20 V and 1.35 V vs. Ag/AgCl, which is compatible with the onset of formation for such an oxide layer.[60, 62] The formation of such an oxide layer would lead to a potential drop in the oxide layer, thus leading to reduced OER rates and less effective electrogelation. Additional side reactions such as $2\,Cl^- + 2\,e^- \rightleftharpoons Cl_2(g)$ and $Cl_2 + H_2O \rightleftharpoons Cl^-(aq) + HOCl(aq) + H^+(aq)$ are also possible.[63] The presence of such side reactions on the electrode surface can be confirmed by linear sweep voltammograms of a BTA-containing and bare solution for the gold electrode used here (cf. the Supporting Information, Figure 5.15). Most likely, a combination of these side reactions, including the formation of an oxide layer, takes place and thus provides an explanation for the nonmonotonic BTA electrogelation as function of the applied potential (cf. Figure 5.5 and 5.6A).

5.4 Conclusion

To determine the thickness of thin hydrogel films with sufficient accuracy, an *in situ* nanoindentation technique had to be developed, which could be integrated in an electrochemistry AFM fluid cell. This new experimental approach allowed us to study fibrillar hydrogel films from LMWHGs with thicknesses in the hydrated state between 100 nm and 5 µm. By contrast, comparable studies of LMWHG hydrogel films concentrated on much thicker films.[32]

Electrochemically based deposition of NaBTA at potentials of 1.30–1.40 V vs. Ag/AgCl and concentrations of approximately 1 $g\,L^{-1}$ provide the best control over the film thickness. Thus, with relatively small potentials and low NaBTA concentrations, it is possible to deposit hydrogel films on a conductive surface of practically arbitrary form within a few seconds. The results presented here can be readily adapted to other reversibly formed hydrogels and LMWHGs that are triggered by local pH changes. For perspective, electrogelation facilitates a simple, one-pot reaction under mild conditions to coat any conductive surface by means of a soft hydrogel coating within a minute.

Such direct and fast preparation of thin films could be interesting for surface modification of conductive surfaces with potential applications in corrosion protection or biomedical coatings. For example, silk has been used in the past for coating of implants [64] and silk films can be also deposited by electrogelation.[23, 24, 28] Moreover, the responsiveness of many LMWHGs, including BTA, to local changes of pH facilitates the active degradation of the films or the release of encapsulated therapeutics once desired.[65]

Acknowledgements

The authors thank S. Sittl for his help with SEM imaging and A. Frank and S. Gumbel for support with the synthesis of BTA. N.R. thanks the VCI for granting the Kekulé Fellowship and acknowledges support by the Elite Network of Bavaria (ENB) through the study program “Macromolecular Science” and the University of Bayreuth Graduate School.

5.5 Supporting Information

5.5.1 Synthesis, Purification and Characterization of *N,N',N"*-tris(4-carboxy-phenylene)-1,3,5-benzenetricarboxamide trisodiumsalt

N,N',N"-tris(4-carboxyphenylene)-1,3,5-benzenetricarboxamide (BTA) has been synthesized as sodium salt derivative (NaBTA) according to literature procedures.[66] 5.43 g (39.6 mmol) of 4-aminobenzoic acid (≥ 99 %, Sigma-Aldrich Chemie GmbH, Steinheim, Germany) dissolved in 10 mL of THF (99.9 % extra pure, anhydrous, stabilized with BHT, ThermoFisher GmbH, Kandel, Germany) and 3.19 g (12 mmol) of 1,3,5-benzenetricarbonyl trichloride (> 98.0 %, Tokyo Chemical Industry Co, Ltd., Tokyo, Japan) dissolved in 10 mL THF were simultaneously given to a suspension of 8.39 g (79.2 mmol) Na_2CO_3 (≥ 99 %, Carl Roth GmbH + Co. KG, Karlsruhe, Germany) in 30 mL THF. After stirring for 20 h at room temperature the solution was transferred into 300 mL desalted water. The solution was acidified to pH 2 using HCl (37 %, VWR Chemicals, Darmstadt, Germany) and a suspension of the BTA was obtained. The precipitate was filtered off, was washed with 400 mL of water and dried under vacuum at 60 °C. Subsequently, the BTA was suspended in 200 mL desalted water and 2.6 mL NaOH (50 − 52 %) (≥ 98 %, Sigma-Aldrich Chemie GmbH, Steinheim, Germany) were added dropwise until pH 13 was reached and further stirred for 20 min to obtain the trisodium salt NaBTA. The solution was precipitated in 1200 mL of 2-propanol, filtrated and dried under vacuum at 60°C yielding 6.2 g of a yellowish powder. Subsequently, 0.9 g of the trisodium salt of the BTA (NaBTA) was dissolved in 100 mL of water and precipitated again in 800 mL of 2-propanol. This step was repeated two times yielding 0.80 g of a white powder.

MS (70 eV):m/z (%): 403 (1), 329 (22), 193 (100), 165 (19), 120 (18), 65 (16)
^{1}H-NMR (300 MHz, D_2O) δ (ppm) = 8.43 (s, 3H), 7.82 (d, 6H), 7.79 (d, 6H)

5.5.2 Exemplary Force vs. Distance Curves Acquired at Different Gelation Potentials for a Shorter Gelation Time

We used an AFM nanoindentation method to determine the thickness of electrogelated BTA films (cf. Figure 5.4) in their hydrated state in situ. Force vs. distance curves were acquired in a potential range of 1.20 V to 1.50 V vs. Ag/AgCl at two different gelation times, 30 s (cf. Figure 5.4C) and 15 s (cf. Figure 5.8), respectively. The trends observed at 15 s are in accordance with the observations for the longer gelation time. In tendency, higher forces up to > 10 nN for films created at a potential of 1.50 V vs. Ag/AgCl were required to completely push through the hydrogel with increasing potential, meanwhile the distance of first interaction inclined. In contrast to the data sets acquired after 30 s gelation time, the gel thickness generated at 1.50 V vs. Ag/AgCl for 15 s remained within the detection range of our method. The insets on the low force regime once again reveal the complexity of the interaction of the cantilever with the fibrous network of the BTA hydrogel. A non-monotonic increase in interaction force with indentation depth into the film was observed as discussed for the longer gelation time.

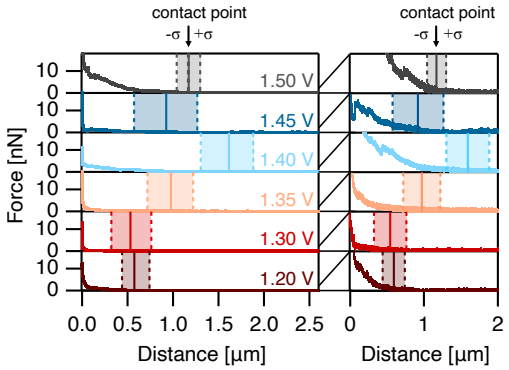

Figure 5.8. Exemplary force profiles (left side) pushing through the BTA films generated at potentials between 1.20 V and 1.50 V vs. Ag/AgCl for 15 s from a 1 $g\,L^{-1}$ NaBTA solution in 10 mM NaCl, pH 5. Zoom-in (right side) at 2 nN magnifies the regions of the contact point (solid line) with the BTA hydrogel for the corresponding curve. The shaded areas mark one standard deviation of the mean for the whole data set. The distance of 0 nm has been attributed to the respective piercing point.

5.5.3 Evaluation of the Hydrated Gel Thickness at Different Gelation Potentials for a Shorter Gelation Time

The hydrated thickness of the BTA gel was extracted from force vs. distance curves as the distance between the first contact of the cantilever with the soft hydrogel and the hard contact with the gold substrate underneath. We defined a force threshold of $n\sigma_{nc}$ above the noise generated by thermal fluctuation of the cantilever in the non-contact regime as an unambiguous criterion for the onset of contact between tip and the electrogelated film. Figure 5.9 presents the hydrated film thickness dependent on the applied potential during electrogelation for 15 s from a 1 $\mathrm{g\,L^{-1}}$ NaBTA solution in 10 mM NaCl pH 5. All data points were determined employing a force threshold of $5\sigma_{nc}$, which was found to be the most accurate across the whole parameter range. All data points lay within the range defined by $3\sigma_{nc}$ and $10\sigma_{nc}$, respectively. A force threshold of $3\sigma_{nc}$ lead to an overestimation of the gel thickness, as some local variations in force before an actual interaction were considered. In contrast, significant interaction occurred before the contact point if $10\sigma_{nc}$ was used which underestimates the actual extension of the gel.

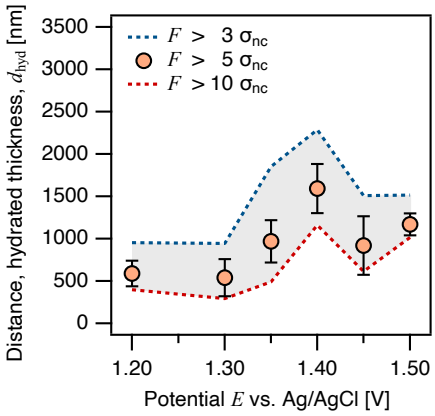

Figure 5.9. Evaluation of the hydrated gel thickness at a gelation potential of 1.20 V – 1.50 V vs. Ag/AgCl and a gelation time of 15 s from a 1 g/L NaBTA solution in 10 mM NaCl pH 5 using a force threshold of $F > 5\sigma_{nc}$ to determine the contact point with the gel. All data points lay between the boundaries of a force threshold of $F > 3\sigma_{nc}$ (blue) and $F > 10\sigma_{nc}$ (red) which show similar trends with potential (dashed lines).

5.5.4 Swelling Factor: Shorter Gelation Time and Influence of the Force Threshold During Hydrated Gel Thickness Evaluation

Figure 5.10 compiles the hydrated gel thickness as determined in situ and the thickness after drying for the same films. BTA was electrogelated for 15 s with applied potentials ranging from 1.20 V to 1.50 V vs. Ag/AgCl. Evaluating the dried gel thickness for films electrogelated at 1.20 V was not possible, as no complete coverage of the electrode by BTA was achieved within 15 s.

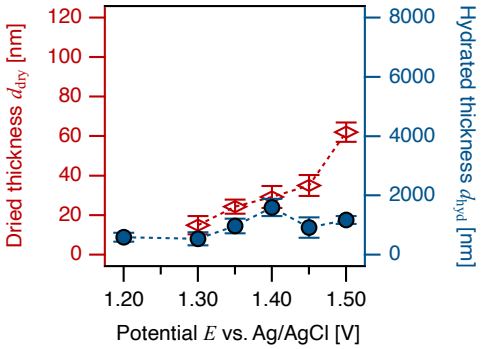

Figure 5.10. Hydrated BTA film thickness as determined in situ and thickness in dried statedepending on the gelation potential in the range of 1.20 V to 1.50 V vs. Ag/AgCl at a gelation time of 15 s. Films were electrogelated from a 1 $g\,L^{-1}$ NaBTA solution in 10 mM NaCl, pH 5.

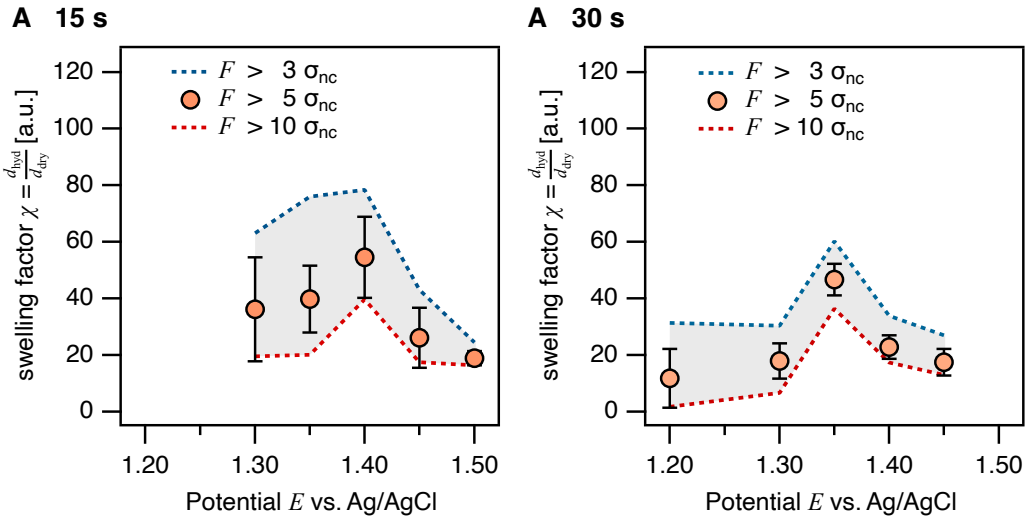

Figure 5.11. Influence of the force threshold $F > n\sigma_{nc}$ on the swelling factor $\frac{d_{hyd}}{d_{dry}}$ calculated from the in situ thickness and film thickness after drying. Films were electrogelated at potentials between 1.20 V and 1.50 V vs. Ag/AgCl for fixed gelation intervals of **A** 15 s; **A** 30 s from a 1 $g\,L^{-1}$ NaBTA solution containing 10 mM NaCl pH 5. All data points for a force threshold of $F > 5\sigma_{nc}$, which was employed for in situ height evaluation, lay between the boundaries of a force threshold of $F > 3\sigma_{nc}$ (blue) and $F > 10\sigma_{nc}$ (red) which show similar trends with potential (dashed lines).

The swelling factor χ (cf. Figure 5.5, 5.11) was calculated as the ratio of the hydrated film thickness and dried gel height of the BTA film ($\chi = \frac{d_{\mathrm{hyd}}}{d_{\mathrm{dry}}}$) for several combinations of parameters, e.g., applied potential and gelation period, respectively. As for all other data, a force threshold of $F > 5\sigma_{nc}$ was considered for evaluating the hydrated hydrogel thickness. Figure 5.11 shows calculated swelling factors χ under consideration of three force thresholds, $F > 3\sigma_{nc}$ (blue line), $F > 5\sigma_{nc}$ (orange markers), and $F > 10\sigma_{nc}$ (red line), respectively. Similar potential dependent trends were observed for the different force thresholds and all data points fall within the range of $3\sigma_{nc}$ and $10\sigma_{nc}$.

5.5.5 Reproduction of Dried Gel Thickness for one Time Teries at a Selected Potential

We studied the three main influencing parameters, the applied potential, duration of the electrogelation and BTA concentration to control the thickness of the hydrogel films. Low variations in dried thickness were found for individual films. To estimate the variation between films electrogelated at comparable conditions, duplicates of selected gelation conditions were studied. We chose the 1.40 V time series for reproduction.

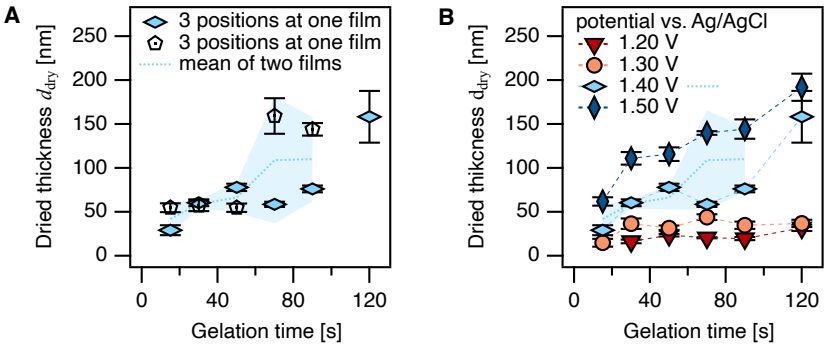

Figure 5.12. Reproduction of the times series acquired at 1.40 V vs. Ag/AgCl from a 1 $\mathrm{g\,L^{-1}}$ NaBTA solution in 10 mM NaCl pH 5. **A** Dried gel thickness for several gelation times at a constant gelation potential of 1.40 V vs. Ag/AgCl. Data points show the mean dry height and the standard deviation per film. The mean of two films (dashed line) and its propagated error (shaded area) were calculated. **B** Thickness of dried BTA films depending on the gelation time at potentials between 1.20 V and 1.50 V vs. Ag/AgCl at 1 $\mathrm{g\,L^{-1}}$ NaBTA concentration (cf. Figure 5.7B) with appended data of the reproduction of the 1.40 V series.

The thickness of two films was studied at three positions per film and the results are contrasted in Figure 5.12A. The markers represent the average thickness within the respective film meanwhile the mean of the two films with propagated errors is displayed as a shaded area. The mean of two films was appended to the gelation period and applied potential dependent representation of the dry gel thickness (cf. Figure 5.7A,

5.12B). The data show a variation of thickness between individual films electrogelated at comparable conditions. However, the trend of increasing film thickness with time remains clear, also within the context of the data acquired for electrogelated films at higher and lower gelation potentials.

5.5.6 Linear Sweep Voltammograms

Secondary electrode reactions besides the OER are supposed to take place. For instance, gold electrodes can undergo oxide formation, especially under acidic conditions and in the presence of chloride ions.[51, 60, 61] In our system, OER and oxide formation might occur partly competingly in a potential window. In consequence, the production of oxygen and thus the progress of electrogelation can become less effective upon the formation of a gold oxide layer. It should be pointed out that not only the building up of the oxide layer but also its presence will reduce the efficiency of the OER. However, further side reactions are possible such as $2\,Cl^- + 2\,e^- \rightleftharpoons 2Cl_2(g)$ and $Cl_2(g) + H_2O \rightleftharpoons HOCl(aq) + H^+(aq)$, respectively.

Linear sweep voltammetry (LSV) was performed in the potential range of 0.10 V to 1.50 V vs. Ag/AgCl under electrogelation conditions (1 $g\,L^{-1}$ NaBTA, 10 mM NaCl pH 5).

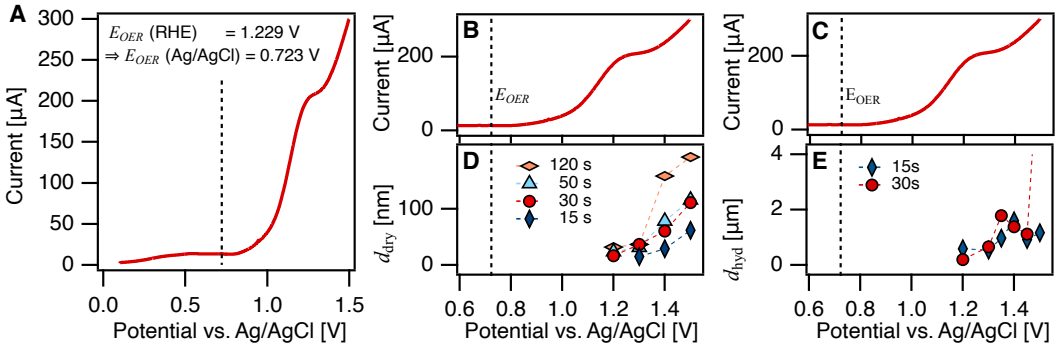

Figure 5.13. **A** Linear sweep voltammogram in 1 $g\,L^{-1}$ NaBTA, 10 mM NaCl pH 5 from 0.10 V to 1.50 V vs. Ag/AgCl. **B** and **C** zoom-in on the potential range relevant for electrogelation. Potential dependent **D** dry gel thickness d_{dry} and **E** hydrated gel thickness hyd presented in the same potential range as the linear sweeps in **B** and **C**. Dashed lines mark the theoretical potential of the oxygen evolution reaction $E_{OER} = 0.723$ V vs. Ag/AgCl under experiment conditions (pH 5).

Figure 5.13A shows the presence of a shoulder in the voltammogram between 1.20 V – 1.35 V vs. Ag/AgCl. A sudden increase in hydrogel thickness can be observed at potentials > 1.35 V (cf. Figure 5.13B, D). This increase could be attributed to the increased effectivity at potentials significantly larger than oxide formation. Furthermore, the potential range of non-monotonous increasing film thickness can be traced also to the

hydrated state (cf. Figure 5.13E), which equally corresponds to the shoulder observed by LSV.

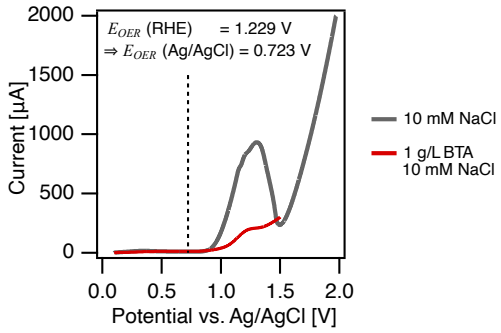

Figure 5.14. Linear sweep voltammograms from 0.10 V to 1.50 V vs. Ag/AgCl comparing a solution without and with BTA containing 1 gL^{-1} NaBTA. Both aqueous solutions are prepared with 10 mM NaCl, pH 5

For completeness, also current vs. time diagrams are shown in Figure 5.15.

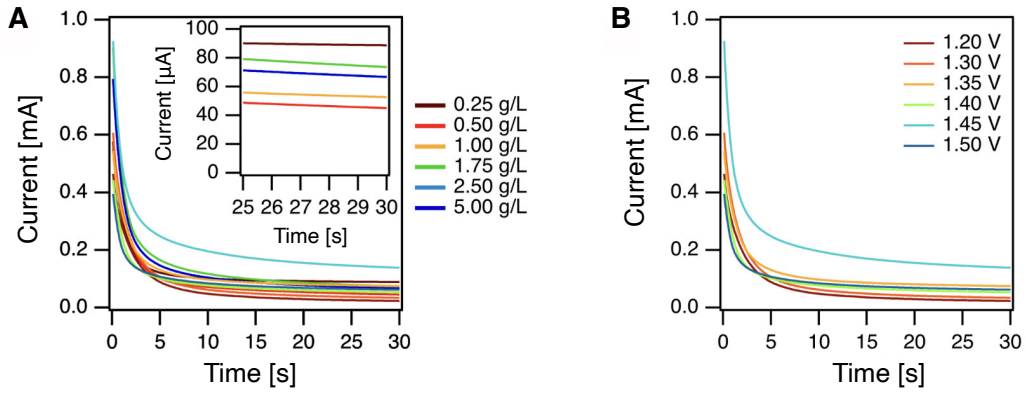

Figure 5.15. Current vs. time plots for 30 s electrogelation of BTA. **A** Plots have been acquired at a constant potential of 1.40 V vs. Ag/AgCl. **B** Plots have been acquired for 1 gL^{-1} BTA at different potentials.

These were acquired different BTA concentrations and applied potentials, respectively. It has to be pointed out that due to the way, the Au-electrodes have been contacted, no normalization to the electrode area could be carried out. Hence, a quantitative evaluation of the limiting current has not been possible.

References

(1) Bard, A. J.; Faulkner, L. R.; White, H. S., *Electrochemical Methods: Fundamentals and Applications*; John Wiley & Sons: Hoboken, 2022.

(2) Cosnier, S. *Anal. Bioanal. Chem.* **2003**, *377*(3), 507–520.

(3) Ibanez, J.; Rincón, M.; Gutierrez-Granados, S., et al. *Chem. Rev.* **2018**, *118*(9), 4731–4816.

(4) Ngankam, A.; Van Tassel, P. *Langmuir* **2005**, *21*(13), 5865–5871.

(5) Van Tassel, P. R. *Curr. Opin. Colloid. Interface Sci.* **2012**, *17*(2), 106–113.

(6) Rydzek, G.; Ji, Q.; Li, M., et al. *Nano Today* **2015**, *10*(2), 138–167.

(7) Yan, K.; Ding, F.; Bentley, W., et al. *Soft Matter* **2014**, *10*(3), 465–469.

(8) Lakshminarayanan, V.; Poltorak, L.; Sudhölter, E. J.; Mendes, E.; van Esch, J. *Electrochim. Acta* **2020**, *350*, 136352.

(9) Johnson, E.; Adams, D.; Cameron, P. *JACS* **2010**, *132*(14), 5130–5136.

(10) Raeburn, J.; Zamith Cardoso, A.; Adams, D. *Chem. Soc. Rev.* **2013**, *42*(12), 5143–5156.

(11) Patterson, C.; Dietrich, B.; Wilson, C.; Mount, A.; Adams, D. *Soft Matter* **2022**, *18*(5), 1064–1070.

(12) Patterson, C.; Panja, S.; Liu, W., et al. *Mater. Chem. Front.* **2023**, *7*(13), 2671–2675.

(13) Cheng, Y.; Luo, X.; Betz, J., et al. *Soft Matter* **2010**, *6*(14), 3177–3183.

(14) Gray, K.; Liba, B.; Wang, Y., et al. *Biomacromolecules* **2012**, *13*(4), 1181–1189.

(15) Liu, Y.; Zhang, B.; Gray, K. M., et al. *Soft Matter* **2013**, *9*(9), 2703–2710.

(16) Yan, K.; Xiong, Y.; Wu, S., et al. *ACS Appl. Mater. Interfaces* **2016**, *8*(30), 19780–19786.

(17) Lei, M.; Qu, X.; Liu, H., et al. *Adv. Funct. Mater.* **2019**, *29*(18).

(18) Cheng, Y.; Luo, X.; Betz, J., et al. *Soft Matter* **2011**, *7*(12), 5677–5684.

(19) Cheng, Y.; Luo, X.; Tsao, C., et al. *Lab Chip* **2011**, *11*(14), 2316–2318.

(20) Betz, J.; Cheng, Y.; Tsao, C., et al. *Lab Chip* **2013**, *13*(10), 1854–1858.

(21) Liu, Y.; Cheng, Y.; Wu, H., et al. *Langmuir* **2011**, *27*(12), 7380–7384.

(22) Bressner, J.; Marelli, B.; Qin, G., et al. *J. Mater. Chem. B* **2014**, *2*(31), 4983–4987.

(23) Elia, R.; Michelson, C.; Perera, A., et al. *J. Biomed. Mater. Res. B Appl. Biomater.* **2015**, *103*(8), 1602–1609.

(24) Elia, R.; Michelson, C.; Perera, A., et al. *J. Biomater. Appl.* **2015**, *29*(9), 1247–1255.

(25) Leisk, G.; Lo, T.; Yucel, T.; Lu, Q.; Kaplan, D. *Adv. Mater.* **2010**, *22*(6), 711–715.

(26) Lin, Y.; Xia, X.; Shang, K., et al. *Biomacromolecules* **2013**, *14*(8), 2629–2635.

(27) Lu, Q.; Huang, Y.; Li, M., et al. *Acta Biomater.* **2011**, *7*(6), 2394–2400.

(28) Qu, Y.; Hong, G.; Liu, L.; Sasaki, K.; Chen, X. *Dent. Mater. J.* **2019**, *38*(5), 813–820.

(29) Adams, D. J. *JACS* **2022**, *144*(25), 11047–11053.

(30) Morris, K.; Chen, L.; Raeburn, J., et al. *Nat. Commun.* **2013**, *4*, 1480.

(31) Dong, R.; Pang, Y.; Su, Y.; Zhu, X. *Biomater. Sci.* **2015**, *3*(7), 937–954.

(32) Zaldivar, G.; Feng, J.; Lizarraga, L., et al. *Adv. Mater. Interf.* **2023**, *10*(16), 2300046.

(33) Raeburn, J.; Alston, B.; Kroeger, J., et al. *Mater. Horiz.* **2014**, *1*(2), 241–246.

(34) Helfricht, N.; Mark, A.; Behr, M., et al. *Small* **2017**, *13*(31), 1700962.

(35) Cantekin, S.; de Greef, T.; Palmans, A. *Chem. Soc. Rev.* **2012**, *41*(18), 6125–6137.

(36) Palmans, A. R. A.; Vekemans, J. A. J. M.; Meijer, E. W., et al. *Chem. Commun.* **1997**, *32*(22), 2247–2248.

(37) Leenders, C.; Albertazzi, L.; Mes, T., et al. *Chem. Commun.* **2013**, *49*(19), 1963–1965.

(38) Kumar, D. K.; Jose, D. A.; Dastidar, P.; Das, A. *Chem. Mater.* **2004**, *16*(12), 2332–2335.

(39) Lee, S.; Lee, J.; Lee, C.; Jung, Y.; Kim, J. *Langmuir* **2011**, *27*(5), 1560–1564.

(40) Bernet, A.; Albuquerque, R. Q.; Behr, M.; Hoffmann, S. T.; Schmidt, H.-W. *Soft Matter* **2012**, *8*(1), 66–69.

(41) Seibt, S.; With, S.; Bernet, A.; Schmidt, H.; Förster, S. *Langmuir* **2018**, *34*(19), 5535–5544.

(42) Reviakine, I.; Johannsmann, D.; Richter, R. *Anal. Chem.* **2011**, *83*(23), 8838–8848.

(43) Sadman, K.; Wang, Q.; Chen, S.; Delgado, D.; Shull, K. *Langmuir* **2017**, *33*(8), 1834–1844.

(44) Stamou, D.; Gourdon, D.; Liley, M., et al. *Langmuir* **1997**, *13*(9), 2425–2428.

(45) Kuznetsov, V.; Papastavrou, G. *Langmuir* **2012**, *28*(48), 16567–16579.

(46) Kern, W.; Puotinen, D. A. *RCA Rev.* **1970**, *31*, 187–206.

(47) Behr, M. Supramolecular hydrogels based on 1,3,5-benzene tricarboxamides, Ph.D. Thesis, Bayreuth, Germany: University of Bayreuth, Macromolecular Chemistry I, 2014.

(48) Li, J.; Sullan, R.; Zou, S. *Langmuir* **2011**, *27*(4), 1308–1313.

(49) Uzüm, C.; Hellwig, J.; Madaboosi, N.; Volodkin, D.; von Klitzing, R. *Beilstein J. Nanotechnol.* **2012**, *3*, 778–788.

(50) Hutter, J. L.; Bechhoefer, J. *Rev. Sci. Instrum.* **1993**, *64*(7), 1868–1873.

(51) Yang, S.; Hetterscheid, D. G. H. *ACS Catalysis* **2020**, *10*(21), 12582–12589.

(52) Rentsch, S.; Siegenthaler, H.; Papastavrou, G. *Langmuir* **2007**, *23*(17), 9083–9091.

(53) Karg, A.; Rößler, T.; Mark, A., et al. *Langmuir* **2021**, *37*(46), 13537–13547.

(54) Kuznetsov, V.; Papastavrou, G. *J. Phys. Chem. C* **2014**, *118*(5), 2673–2685.

(55) Gergely, C.; Senger, B.; Voegel, J., et al. *Ultramicroscopy* **2001**, *87*(1-2), 67–78.

(56) Zhu, J.; Marchant, R. *Expert Rev. Med. Devices* **2011**, *8*(5), 607–626.

(57) Kipcak, A. S.; Ismail, O.; Doymaz, I.; Piskin, S. *J. Chem.* **2014**, *2014*(1), 281063.

(58) Sievers, J.; Sperlich, K.; Stahnke, T., et al. *J. Appl. Polym. Sci.* **2021**, *138*(18), 50326.

(59) Iwata, R.; Zhang, L.; Wilke, K. L., et al. *Joule* **2021**, *5*(4), 887–900.

(60) Brummer, S. B.; Makrides, A. C. *J. Electrochem. Soc.* **1964**, *111*(10), 1122.

(61) Tabor, R.; Morfa, A.; Grieser, F.; Chan, D.; Dagastine, R. *Langmuir* **2011**, *27*(10), 6026–6030.

(62) Bentley, C.; Kang, M.; Unwin, P. *JACS* **2016**, *138*(39), 12755–12758.

(63) Kiamco, M.; Zmuda, H.; Mohamed, A., et al. *Sci. Rep.* **2019**, *9*(1), 2683.

(64) Schacht, K.; Scheibel, T. *Curr. Opin. Biotechnol.* **2014**, *29*, 62–69.

(65) Guillaume-Gentil, O.; Graf, N.; Boulmedais, F., et al. *Soft Matter* **2010**, *6*(17), 4246.

(66) Qin, H.; Dotson, D.; Torres, E.; Dey, S. K.; Alvarez, F. *Milliken Company* **2015**, *US 9193845 B2*.

6

Electrochemical Picobalance: Proof-of-Principle for an Electrochemical Cantilever-Based Mass Balance

Nadine Raßmann, Roman E. J. Glaß, Nicolas Helfricht and Georg Papastavrou*

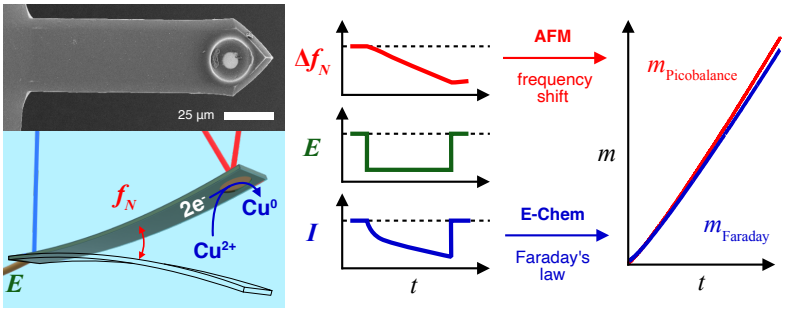

„Electrochemical Picobalance: Proof-of-Principle for an Electrochemical Cantilever-Based Mass Balance“,

Electrochimica Acta, **2025**, *540*, 149607.

Abstract

Since the introduction of Faraday's law, the combination of electrochemical methods with gravimetric techniques has been pursued very actively in the field of electrochemistry. Here, we present a proof-of-concept to combine electrochemical methods with the recently introduced picobalance, which originates from atomic force microscopy (AFM). The picobalance is a cantilever-based technique that can measure mass changes in the order of a few picograms. The development of fully insulated cantilevers with an integrated microelectrode (electrochemical balance probes, EBPs) was an essential prerequisite for the electrochemical picobalance. The electrochemical deposition of copper allowed for a highly defined and continuous deposition of mass on the EBP. By comparing the faradaic current and the mass signal of the picobalance, the mass sensitivity of the latter has been determined as 4.6 $\mathrm{fg\,\mu m^{-2}\,Hz^{-1}}$ *(or* $460 \approx \mathrm{ng\,cm^{-2}\,Hz^{-1}}$*). This value can be readily compared to the one for the electrochemical quartz microbalance (EQCM), which has been used here as a benchmark under the same conditions (17.5* $\mathrm{ng\,cm^{-2}\,Hz^{-1}}$*). However, in contrast to the EQCM, the picobalance is capable of measuring absolute masses as low as one picogram. The here-presented electrochemical picobalance allows for applications in electropolymerization, organic electronics, and bioelectrochemistry*

6.1 Introduction

Material deposition on electrodes is a universal process in electrochemistry, which is often referred to as electrodeposition.[1, 2] Starting with Faraday, mass deposition was essential for developing electrochemical concepts.[3] Faraday's law of electrolysis states a direct relation between the transferred charge at the interface of an electrode and the deposited mass of a metal.[1, 3] Historically, Faraday established it based on experimental data for the deposition of copper onto macroscopic electrodes. The mass change was determined gravimetrically.[1, 3] Following this landmark experiment, gravimetric detection by the associated faradaic current became a standard technique in electrochemistry,[4–7] biomedical sensing, and energy storage applications.[8–11]

Electrochemistry has a long history of being integrated with various surface analytical techniques to further characterize the solid/liquid interface of an electrode under potentiostatic control. Examples include IR-spectroscopy, optical microscopy, ellipsometry, X-ray reflectometry, and atomic force microscopy (AFM).[5, 12–17] One technique that allows for directly determining the mass deposited on an electrode is the quartz crystal microbalance (QCM), which is among the most utilized surface analytical techniques

in combination with electrochemistry.[4, 9, 18] The QCM dates back to the early experiments of Sauerbrey in the 1950s, who employed the inverse piezoelectric effect for microgravimetric studies.[19] The QCM detects a piezoelectric resonator's frequency or amplitude shift due to the deposited mass.[20] Originally, QCMs have been primarily used in the gas phase and are still employed as a monitoring device to determine the mass deposited by physical vapor deposition, such as thermal evaporation or sputter coating.[21, 22] According to the Sauerbrey equation, the deposited mass and the resulting frequency shift are directly proportional.[19] However, this equation is only valid for sufficiently thin and rigid layers.

The principle of QCM also allows for the operation in a liquid environment.[20, 23, 24] QCM in liquid enables not only for applications such as biosensing [25] but also to follow interfacial electrode processes.[5, 9, 18, 26–29] In this respect, electrochemical deposition with Faraday's law is often used to calibrate electrochemical QCM (EQCM) setups or new resonator designs.[30–32] It should be noted that for a QCM operated in liquid, water will also be bound to the surface of the QCM sensor while it is oscillating. Tightly bound water can include much more than only ions of the double layer, especially when extended layers of organic material protrude into the solution.[24] Hence, QCM in liquid determines the so-called wet mass in contrast to other techniques such as optical reflectometry.[24, 33] In the case of extended layers, hydrodynamic damping can be used to estimate properties, such as thickness and elastic behavior.[20] One technique used to address hydrodynamic damping is referred to as QCM with dissipation monitoring (QCM-D) and is based on short excitation sequences to the sensor whose subsequent damping is followed.[24, 34] QCM-D has also been used in combination with electrochemistry, for example, in the context of electropolymerization [35, 36] and electrogelation [37, 38].

Recently, a new technique to determine masses and mass changes of isolated, micrometer-sized objects has been introduced. This technique is founded on AFM and is often referred to as picobalance.[39] The picobalance is also based on the resonance shift of a mechanical microresonator like the QCM. However, in contrast to the shear oscillations of a QCM crystal, the picobalance is based on the oscillations of a cantilever commonly used in atomic force microscopy (AFM).[39, 40] The cantilever oscillations are induced by photothermal excitation using a modulated IR laser focused near the clamped end of the cantilever beam.[41, 42] The cantilever's deflection during oscillation is read out by an additional laser that is reflected on the free end of the cantilever (optical light lever technique).[43] Any changes in the mass immobilized at the end of the cantilever result in a change of its resonance frequency. Recording frequency sweeps with and without an attached mass and fitting the respective phase and amplitude response with a driven and damped oscillator yields the resonance frequency. The mass can then be calculated

from the difference in resonance frequency. The corresponding frequency shift can also be detected continuously using a phase-locked loop (PLL). The PLL maintains a constant phase shift of 90° by adjusting the excitation frequency in accordance with the mass change at the cantilever.

Originally, the picobalance was developed with the aim to detect the mass fluctuation in single living cells with millisecond and piconewton resolution over time scales of days.[39] So far, the picobalance has mainly been employed in a biological context.[40, 44–46] It should be noted that other microresonators are sometimes also referred to as 'picobalances'. However, these techniques are not AFM-based.[47, 48]

Electrochemistry has a long history of hyphenating with other techniques, such as ellipsometry, spectroscopy, and QCM. Here, we developed the electrochemical picobalance, which adds another gravimetric technique that is sensitive to the smallest mass changes on an absolute scale. Within this feasibility study, we demonstrated by electrochemical techniques that indeed the mass resolution of the AFM-based picobalance is on the order of 1 picogram. The preparation of special AFM cantilevers, which could also act as electrochemical sensors bearing integrated µm-sized electrodes,[49, 50] has been further developed and adapted to the requirements for the picobalance measurements. In our proof-of-feasibility of an electrochemical picobalance, we show that Faraday's law of electrolysis can also be used to correlate current and deposited mass. Thus, 'classical' electrochemical techniques, such as cyclic voltammetry and chronoamperometry, can be readily combined with the picobalance setup. With the advent of organic electronics and the strong current interest in electrically addressing cells, the combination of electrochemistry and picobalance will open new possibilities for single-cell electrochemistry.[51, 52] Moreover, the picobalance technique will allow for overcoming hydrodynamic limits of EQCM for electropolymerization and electrogelation when thick polymer films are present on the sensor.[24, 53]

6.2 Experimental

Fabrication of Electrochemical Balance Probes

The electrochemical probes for the picobalance were fabricated from commercial gold-coated tipless AFM cantilevers (HQ:NSC35-C/tipless/Cr-Au, MikroMasch, Sofia, Bulgaria). These cantilevers have a nominal spring constant of 5.4 $N\,m^{-1}$ and a nominal resonance frequency of 150 kHz. The two lever arms, which were not used, i.e., NSC35-A and B on the chip, were removed beforehand. We modified a previously published procedure for the preparation of electrochemical colloidal probes [49] to meet the requirements for our microelectrode mass sensors. The cantilevers were electrically

contacted and, afterward, completely insulated, leaving an approximately circular gold electrode area uncoated.

Briefly, the cantilevers were cleaned by dipping them alternatingly in MilliQ water (resistivity $> 18\ M\Omega\,cm^{-1}$, Merck Millipore, Darmstadt, Germany) and EtOH (p.A., VWR, Darmstadt, Germany). Subsequently, the cantilevers were exposed to air plasma (Zepto, Diener Electronics, Ebhausen, Germany) for 180 s, dipped into EtOH, and left to dry in air. The later electro-active area, i.e., microelectrode, had been protected by spherical polystyrene particles (PS, with a nominal diameter of 30 µm, microparticles, Berlin, Germany). This sacrificial particle masked the future electrode area during the following insulating steps and was successively removed after finalizing the insulating process. For this purpose, a PS microsphere (nominal diameter 30 µm, PS-R-30.0, Microparticles, Berlin, Germany) was placed on the free end of the cantilever using a micromanipulator (DC-3K, Märzhäuser, Ebhausen, Germany) equipped with etched tungsten wires under the control of an optical fixed-stage microscope (Axio Examiner D1, Zeiss, Oberkochen, Germany). The particle transfer and immobilization are enabled by capillary forces. A similar approach has been reported previously by us for the preparation of electrochemical colloidal probes.[49] Afterward, the cantilever was tempered at 200°C in a reflux oven for 180 s (Protoflow S, LKPF Laser, and Electronics AG, Garbsen, Germany) to increase the contact area of the priorly placed PS-particle. Furthermore, electrical contact was established by attaching a polyimide-insulated silver wire (0.125 mm, Advent Research Material, Oxford, United Kingdom, insulation partially removed) to the cantilever chip using conductive silver paint (Acheson silver DAG 1415, Plano, Marburg, Germany). A small droplet of UV curable glue (NOA 63, Norland Products, Cranbury, USA) was applied to the contact to seal it electrically and provide mechanical support. The cantilever chip was insulated by carefully dipping it into 1:1 (w:w) diluted red insulating varnish (4228, MG Chemicals., Burlington, Canada) with the dedicated thinner (4354, MG Chemicals, Burlington, Canada) using a micromanipulator under optical control with a digital microscope (Supereyes, Shenzhen Supereyes Co. Ltd., Shenzhen, China). After drying at room temperature for > 12 h, the insulating coating was cured in a reflux oven at 80°C for 1 h.

The cantilever was insulated using a cathodic paint (ClearClad HSR, LHV coatings, Birmingham, United Kingdom). For this purpose, the paint was diluted 1:5 in MilliQ water, stirred for > 24 h, and filtered through a syringe filter (PES, hydrophilic, 0.22 µm, Carl Roth, Karlsruhe, Germany) immediately before use. The paint was deposited in a two-electrode configuration with a platinum sheet (15 mm^2, 99.95%, Goodfellow, Hamburg, Germany) acting as the counter electrode. The deposition was conducted three times at -3.0 V for 120 s using a potentiostat (PGU BI-1000, Ingenieurbüro Peter Schrems, Münster, Germany). The cantilevers were gently dipped in MilliQ water before

and after every deposition step. After the third step, the cantilever was removed from the suspension without being dipped into MilliQ water. It was left to dry at room temperature for 15 min before curing the coating at 160°C for 20 min in a reflux oven. This deposition cycle was repeated three times. Finally, the sacrificial PS microsphere was removed from the cantilever using a micromanipulator equipped with an etched tungsten wire. Due to the masking effect of the PS particle during the different insulating steps, an approximately circular non-insulated gold electrode at the free end of the cantilever was obtained (cf. Figure 6.1 and Figure 6.12). We refer to these cantilevers with integrated electrodes in the electrochemical picobalance experiments as 'electrochemical balance probes' (EBP).

The spring constants of the used EBPs were calibrated according to the procedure introduced by Cleveland et al. [54] after the electrodeposition or added mass experiments. Briefly, a minimum of 7 individual tungsten beads were picked up with each cantilever under ambient conditions. The microspheres adhered to the EBPs, primarily due to capillary forces. The spring constant was determined from the shift of the resonance frequency and the theoretical particle mass, calculated from the bead diameter and particle position on the cantilever, which was determined by optical microscopy for each attached particle.

Picobalance Setup

The picobalance setup is based on a commercial AFM (Drive, Nanosurf AG, Liestal, Switzerland) equipped with a CX controller (Nanosurf AG, Liestal, Switzerland). Two different lasers are available in the used AFM: i) a photothermal excitation laser (CleanDrive, $\lambda = 785$ nm), which drives the cantilever's oscillation, and ii) a readout laser ($\lambda = 840$ nm) to detect the cantilever deflection. Optical control is realized by placing the AFM setup on top of an inverted optical microscope (Axiovert 200, Zeiss, Oberkochen, Germany). A commercial fluid cell (Asylum Research, Oxford Instruments, Santa Barbara, USA) with exchangeable glass bottom discs (diameter 35 mm, Irlbacher Blickpunkt Glas, Schönsee, Germany) was used for measurements in liquid.

Resonance Shifts by Added Mass

The mass sensing by the electrochemical balance probes was verified by attaching tungsten microspheres ($\rho = 19.25\ \mathrm{g\,cm^{-3}}$ [55]) with variable sizes to the modified electrochemical cantilevers in 0.1 mM aqueous HCl pH 4 (Titrisol, Sigma-Aldrich, Merck, Darmstadt, Germany). The mass determined by the picobalance has been compared to the theoretical mass calculated based on the dimensions and density of the respective particles. The electrochemical balance probes were exposed to UV/ozone treatment

(UVO-Cleaner, Jelight Co. Inc., Irvine, USA) for 10 min before immersing them into a 1 $g\,L^{-1}$ aqueous solution of polyethyleneimine (PEI, hyperbranched, M_W 25000 $g\,mol^{-1}$ LS, Sigma-Aldrich, Merck, Darmstadt, Germany) for 30 min. Excess PEI was removed by carefully dipping the electrochemical balance probes several times into MilliQ water.

Cantilevers were driven to oscillation using the additional photothermal laser.[56] The system was operated using the picobalance software (v1.2.6.0, Nanosurf AG, Liestal, Switzerland) and the CX control software (v3.10.5.14, Nanosurf AG, Liestal, Switzerland). Frequency sweeps in liquid were acquired before and after picking up single microspheres from a glass slide (11 mm × 11 mm × 1 mm) glued to the glass bottom disc to compensate for the additional height of the contact wire on the cantilever chip of the electrochemical balance probe. In order to attach the mass, the EBP was aligned above a particle and then approached. Surface forces, such as van der Waals and mostly capillary forces, held the particles on the EBP when retracting it from the surface. Attached particles could be removed by crossing the liquid-air interface. The successful removal of the attached particles was verified once the resonance frequency returned to its initial value and corroborated by optical microscopy. The phase sweeps were fit to Eq. 6.2 to extract the resonance frequency of the cantilever without f_N and with an attached mass $f_N(M)$. The actual size of the microspheres and their respective position on the cantilever were evaluated from optical microscopy images. The apparent mass M was calculated using Eq. 6.5 and was corrected for the position following Eq. 6.6 to obtain the actual particle mass m_{PB}.

Electrochemical Picobalance

The electrochemical picobalance setup has been implemented on the Drive AFM setup described above. A photograph of the entire setup and key components is available in the supplementary materials (Section 6.5.1, cf. Figure 6.8). Using the CX control Software (v3.10.5.14, Nanosurf AG, Liestal, Switzerland) in user mode allowed to externally operate the photothermal excitation using an additional lock-in amplifier (MFLI 500 kHz, Zürich Instruments, Zürich, Switzerland) in phase-locked loop (PLL) mode. The excitation amplitude was fixed at 500 mV, which resulted in an oscillation amplitude of 3-5 nm. The PLL adjusted the excitation frequency to maintain a constant phase shift of 90° between the excitation and the response of the resonator. The shift in the cantilever's resonance frequency Δf_N was monitored to trace the mass evolution over time. No effects due to swelling or degradation of the electropaint coating of the EBP have been observed.

Here, the integrated electrode on the EBPs acted as the working electrode in a three-electrode setup, and the applied potential was controlled using a CHi 750 E bipotentiostat

(CH Instruments, Austin, USA). A coiled platinum wire (0.1 mm, 99.99%, Goodfellow, Huntingdon, United Kingdom) acting as a counter electrode (CE) and a chlorinated wire as a pseudo reference electrode (pseudo-RE) were placed in a circular manner into the fluid cell around the position of the electrochemical balance probes acting as WE. The pseudo-RE was fabricated by electrochemically depositing AgCl onto a partially insulated Ag-wire (0.25 mm, PTFE insulated, Advent Research Materials, Oxford, United Kingdom) using an automated chlorider (ACl-01, npi electronic, Tamm, Germany). The offset of the pseudo-RE was verified against a commercial Ag/AgCl electrode (RE-5B, 3 M NaCl, BASi, West Lafayette, USA).

All signals from the lock-in amplifier (frequency shift, amplitude, phase) and the potentiostat (potential, current) were captured simultaneously using a low noise data acquisition system (Axon Digidata 1550 B, Axon Instruments, Molecular Devices, San Jose, USA) with a common time stamp. The data were verified using the raw data from the potentiostat for data analysis.

Cu Deposition Traced by the Electrochemical Picobalance

Copper was deposited electrochemically onto the µm-sized Au electrode at the free end of an electrochemical balance probe utilizing the three-electrode configuration inside the electrochemical picobalance setup specified above. To avoid damage to the electrical insulation of the cantilevers, these home-build EBPs were fixated by paraffin wax (Paraplast, Sigma Aldrich, Merck, Darmstadt, Germany) to the cantilever holder rather than using any standard clamping mechanism. Moreover, the wax provided an additional insulating layer to the cantilever chip. Before electrodeposition, each electrochemical balance probe was characterized by cyclic voltammetry (CV) in the range −0.2 V to +0.4 V vs. Ag/AgCl at a scan rate of 50 $mV\,s^{-1}$ in an electrochemical analyte solution containing 5 mM potassium hexacyanidoferrate(II) ($K_4[Fe(CN)_6]$, > 98.5%, Sigma-Aldrich, Darmstadt, Germany), 5 mM potassium hexacyanoferrate(III) ($K_3[Fe(CN)_6]$, > 99.0%, Sigma-Aldrich Darmstadt, Germany), and 100 mM potassium nitrate (> 99.0%, Carl-Roth, Karlsruhe, Germany) in MilliQ water. These CV experiments were performed in the electrochemical picobalance setup directly before Cu deposition. The analyte solution was replaced by MilliQ water thrice before exchanging the solution thrice for 10 mM H_2SO_4 (99.99%, Sigma-Aldrich, Merck, Darmstadt, Germany). A reference experiment was conducted by applying −0.4 V vs. Ag/AgCl for 60 s with a potentiostat (CHi 750 E bipotentiostat, CH Instruments, Austin, USA) without any copper added to the supporting electrolyte solution. Then, the solution was exchanged for the electrolyte solution containing 3 mM $CuSO_4$ (99%, Grüssing, Filsum, Germany) in 10 mM H_2SO_4 (99.99%, Sigma-Aldrich, Merck, Darmstadt, Germany). During the copper electrodeposition, Cu^{II} was reduced to Cu^0 by applying $E_{red} = -0.4$ V vs. Ag/AgCl

for 60 s with a potentiostat. The frequency shift, current, and potential were traced as specified above.

Data Analysis for the Electrochemical Picobalance

The mass of the deposited copper was evaluated by two different methods: On the one hand, based on the total charge transferred through the working electrode according to Faraday's law of electrolysis (m_{faraday}, Eq. 6.11) and on the other hand, by acquiring the frequency shift recorded by the AFM-based picobalance and evaluating it by purposely-written procedures in Igor Pro (v. 8.04 Wavemetrics, Portland, USA) (m_{PB}, Eq. 6.5, 6.6). The position and dimension of the electrode on the cantilever were determined from SEM images by means of FiJi [57] using the free hand tool to outline the electrode area and the centroid function to determine the center of mass, i.e., the center of the electrode area (cf. Figure 6.12). A similar approach was used previously to determine the location and center of mass of cells on AFM cantilevers for picobalance experiments.[39, 44, 45, 58] The effective mass M was corrected for the mass position to calculate the actual deposited mass m_{PB} by Eq. 6.6.

Cu Deposition in the Electrochemical Quartz Crystal Microbalance (EQCM)

Copper electrodeposition on macroscopic quartz sensors (5 MHz, 14 mm, Cr-Au, Quartz Pro, Jarfälla, Schweden) was conducted in a commercial quartz crystal microbalance (QCM) setup (QSense Explorer, Biolin Scientific, Göteborg, Schweden) equipped with a closed electrochemistry module (QEM401, Biolin Scientific, Göteborg, Schweden). In this setup, the QCM sensor acts as WE. The three-electrode configuration in the electrochemical QCM-cell was realized by a platinum sheet used as CE and an Ag/AgCl as RE (Dri-Ref 2SH, World Precision Instruments, Sarasota, USA). The QCM sensors were cleaned by immersing them into a 5:1:1 (v:v:v) of MilliQ water, ammonia (25 (w:v) %, VWR International S. A. S, Rosny-sous-Bois, France), and hydrogen peroxide (30 (w:v) %, Fisher Scientific, Schwerte, Germany) at 75°C for 5 min. Subsequently, the sensors were thoroughly rinsed with MilliQ water and dried in a stream of nitrogen. The offset of the RE was verified against a commercial RE (RE-5B, 3 M NaCl, BASi, West Lafayette, USA). For the copper deposition, −0.4 V vs. Ag/AgCl was applied to the QCM sensor WE for 60 s using a potentiostat (Zennium, Zahner-Elektrik, Kronach, Germany). Measurements were conducted in an aqueous solution containing 10 mM $CuSO_4$ (99 %, Grüssing, Filsum, Germany) and 10 mM H_2SO_4 (99.99 %, Sigma-Aldrich, Merck, Darmstadt, Germany) supporting electrolyte in a constant flow of 100 µL min^{-1} facilitated by a peristaltic pump (IPC multichannel dispensing pump, ISMATEC, Cole-Parmer, Wertheim, Germany).

Frequency shifts were converted into mass shifts using the Sauerbrey equation 6.12.[19] The third overtone was used for evaluation. However, comparable results were obtained for higher oscillation modes. The Faraday mass was determined similarly to the electrochemical picobalance according to Eq. 6.11.

Scanning Electron Microscopy Images of Electrochemical Balance Probes

We analyzed the EBPs by scanning electron microscopy (SEM) after sputter coating a thin layer of platinum ($d = 2$ nm) using a field emission SEM (Leo 1530, Zeiss, Oberkochen, Germany) operated at 3 kV acceleration voltage and a working distance of 8.1 mm with an ET detector.

6.3 Results and Discussions

In the following, it is demonstrated how the AFM-based picobalance, which was initially developed to study small mass fluctuations in cells[39], was adapted to also follow small mass changes on µm-sized electrodes during dynamic electrochemical experiments. Faraday's law allowed for a direct correlation between deposited mass and simultaneously acquired current. However, an essential prerequisite for electrochemical experiments with the picobalance were fully insulated cantilevers with an integrated microelectrode.

6.3.1 Preparation of Electrochemical Balance Probes

The preparation of suitable electrochemical probes is central for performing electrochemical experiments by AFM, such as scanning electrochemical microscopy [50, 59, 60], nanomanipulation [61], or direct force measurements [49, 62, 63]. Here, we adapted a template-assisted procedure originally developed to prepare electrochemical colloidal probes [49]. However, electrochemical probes for the picobalance have a highly defined electrode area at the end of the AFM cantilever as a primary requirement. Therefore, we opted for a simplified approach where a circular microelectrode was obtained by masking the later electrode area using a sacrificial particle and applying an insulating coating for the rest of the cantilever. The respective cantilevers will be denoted as electrochemical balance probes (EBPs) throughout this work, and 6.1 provides a comprehensive overview of the required preparation steps and the characterization of EBPs

The individual steps of the manufacturing process are displayed in Figure 6.1A ($\alpha - \zeta$). The electrochemical balance probes (EBPs) were fabricated based on commercial gold-coated conductive cantilevers (α). The future electrode area located at the free end of the EBP was masked by attaching a sacrificial polystyrene (PS) particle (β). Annealing the cantilever and PS bead above its glass transition temperature at 200°C for 180 s generated an increased, approximately circular contact area (γ). Subsequently, the gold-coated cantilever chip was contacted with an insulated silver wire using conductive silver paint. This attachment point was additionally sealed by UV-curable glue to insulate the contact point and mechanically reinforce the attachment (δ). Moreover, the entire chip was electrically insulated using red insulating varnish (δ). The varnish was carefully dip-coated onto the chip using a micromanipulator, leaving only the lever arm uncoated. This lever arm was insulated using a commercial transparent cathodic electropaint,[49, 61, 64–67] which was deposited under potentiostatic control (ε). Three coating cycles with intermediate heat annealing of the individual coating layers were performed to achieve a defect-free coating, especially at the edges of the lever arm. After completing these insulating steps, the sacrificial particle was removed mechanically by an etched

wire mounted to a motorized micromanipulator. The removal of the particle resulted in a defined hole in the insulation that uncovered the underlying gold coating of the cantilever, which acted in the following as the microelectrode of the EBP (ζ). Figure 6.1B shows an optical microscopy image illustrating the red insulation on the cantilever chip and the attached insulated wire. Figure 6.1C shows the insulated cantilever arm and the integrated electrode of the EBP by scanning electron microscopy (SEM).

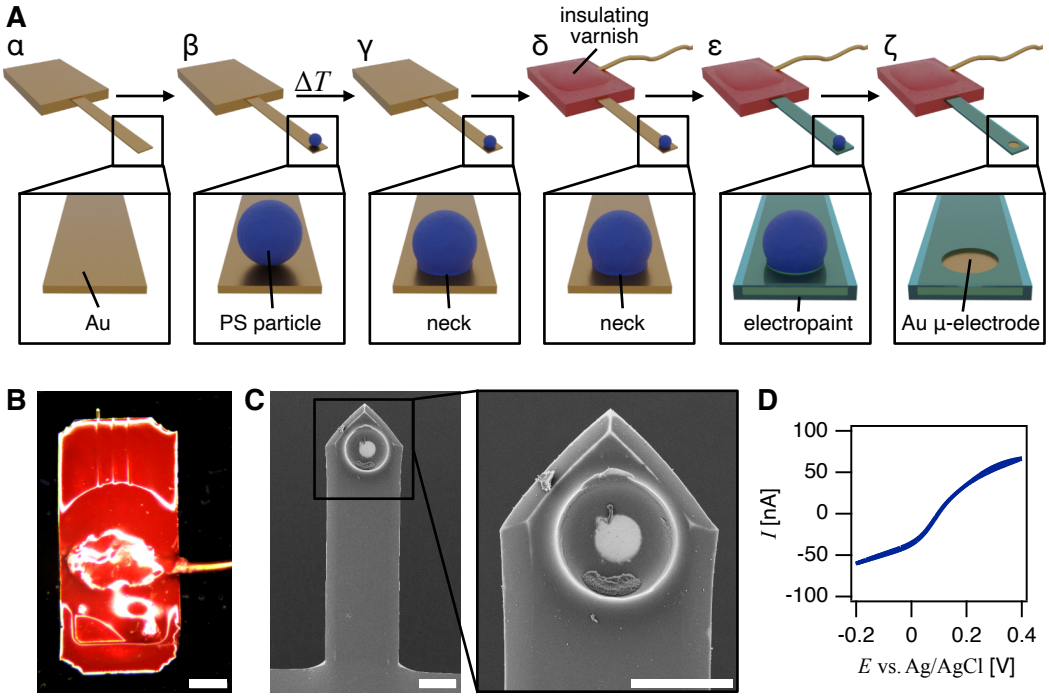

Figure 6.1. Fabrication and characterization of electrochemical balance probes. **A** Fabrication of electrochemical balance probes (EBPs), which were based on commercial tipless AFM cantilevers. (α) An Au-coated tipless cantilever formed the foundation for the EPs. (β) A polystyrene (PS) microsphere was placed on the free end of an AFM cantilever. (γ) Both were tempered at 200°C for 180 s to form an increased contact area. (δ) A polyimide-insulated Ag-wire was attached to the cantilever chip to provide electrical contact. The electrical contact and the carrier chip were insulated with a red insulating varnish. (ε) The cantilever arm was coated with a cathodic electropaint for insulation. This process has been repeated several times to achieve better insulation. (ζ) The sacrificial PS particle has been removed with a micromanipulator to expose the previously masked area on the Au-electrode. Thereby, a planar-circular microelectrode has been created at the free end of the insulated cantilever. **B** Overview of the insulated cantilever with the planar Au-electrode area at its free end, the connection cable, and the insulation painted over the carrier chip. The scalebar represents 500 µm. **C** SEM image of an insulated cantilever and a zoom-in on the microelectrode area of an EBP. Scale bars are 20 µm. **D** Cyclic voltammogram of the microelectrode on the EBP in an aqueous hexacyanoferrate solution (5 mM/5 mM $K_2/K_3[Fe(CN)_6]$ in 100 mM KNO_3) at 50 mV s^{-1}.

As we will demonstrate later, the multi-step insulation was essential to ensure that all faradaic currents originate only from the electrode area integrated into the fully insulated cantilever (cf. Figure 6.1C, Section 6.5.1 Figure 6.9). The flexibility and transparency of

the thin polymeric coating enabled photothermal excitation of the cantilever oscillation and facilitated the optical readout of the cantilever response while maintaining the required electrical insulation of the underlying gold coating of the cantilever. The coating did not show signs of wear or swelling, and also seems to be resistant to the IR laser illumination. In contrast, a thicker and opaque insulation layer could be applied to the cantilever chip, also providing mechanical stability to the attachment point of the wire.

6.3.2 Electrochemical Characterization of the Electrodes for the Picobalance

Cyclic voltammetry (CV) provides a direct approach for characterizing the performance of probes for electrochemical AFM.[60, 62, 63, 68, 69] Commonly, redox couples, such as ruthenium complexes or hexacyanoferrate, are used for CV of nm- or µm-sized electrodes on AFM cantilevers.[60, 68] Here, we characterized the electrode properties of the EBPs by CV with the redox couple 5 mM $K_2[Fe(CN)_6]$ and 5 mM $K_2[Fe(CN)_6]$ in 100 mM KNO_3 as supporting electrolyte.[49, 60, 70] The CVs with the EBP as a working electrode were acquired at 50 mV s^{-1} between −0.4 V and +0.2 V vs. Ag/AgCl in a three-electrode setup incorporated into a commercial AFM fluid cell.[49, 61]

Figure 6.1D shows a typical CV acquired with an EBP, which was mounted inside the same electrochemical cell that was also part of our picobalance setup (cf. Figure 6.2 and Figure 6.8). The shape of the acquired CV matched the one typically observed for microelectrodes or ultra-microelectrodes: No pronounced oxidation or reduction peaks and overlap of both scan directions.[1, 71] The limiting currents were in the order of 50 nA for this EBP, which is compatible with a microelectrode area of 533 µm^2, which corresponds to a circular diameter of ≈ 26 µm (cf. also SI Figure 6.12 for an SEM image of this EBP). The CV shown in Figure 6.1D was acquired with an EBP, which has been insulated by three repetition cycles of electropaint coating. For lever arms, which were less insulated, higher currents have been observed (cf. Section 6.5.2, Figure 6.9), indicating that faradic currents from the edges of the lever arm were involved.

6.3.3 Setup of the Electrochemical Picobalance

Figure 6.2 shows a schematic representation of the picobalance setup used in this study. A photograph of the setup is available in the Supporting Information (Section 6.5.1). The electrochemical cell was integrated into the AFM-based setup. The design of the electrochemical cell was analogous to those previously described.[49, 61] For the

picobalance experiments, the EBP acted as the working electrode (WE), the counter electrode (CE) was a coiled Pt-wire, and the reference electrode (RE) was a chlorinated silver wire (Ag/AgCl pseudo-RE). The mass-sensing part of the picobalance was based on a commercial AFM with additional photothermal excitation of the cantilever.[44, 46] Other groups have also used a similar setup to implement AFM-based picobalances.[39, 40, 44, 45, 58]

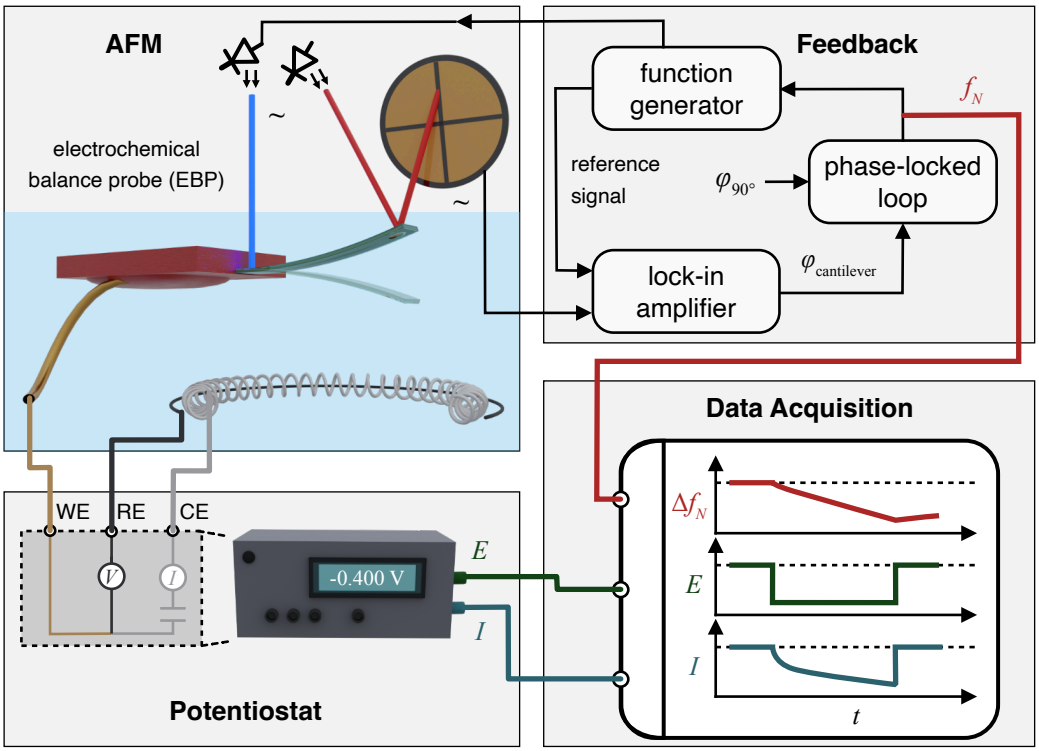

Figure 6.2. Schematic representation of the electrochemical picobalance setup. The central part of the setup was the custom-made electrochemical balance probe (EBP) based on a conductive AFM cantilever. The EBP was mounted in an AFM equipped with two separate lasers: an intensity-modulated laser, which drives the cantilever to oscillation close to its free end, and a readout laser reflected at the cantilever's free end to a position-sensitive photodiode. A function generator controlled the photothermal excitation. The lock-in amplifier analyzes the frequency and phase of the photodiode signal. A phase-locked loop (PLL) maintains a constant phase shift of 90° between the cantilever oscillation and the excitation by adjusting the excitation frequency. The EBP acted not only as a mass sensor but also as the working electrode controlled by a potentiostat. The coiled Pt wire (CE) and chlorinated Ag-wire were implemented into the fluid cell of the AFM to complete a three-electrode electrochemical cell. All data signals from the picobalance and the potentiostat were acquired with a common time stamp.

The general working principle of the picobalance is based on determining the frequency shift of an oscillating cantilever, which is driven near its resonance frequency f_N.[39] Here, the EBP was driven by an intensity-modulated laser diode that locally heats the cantilever close to its clamped end at the carrier chip. The resulting EBP oscillation was detected by a second laser, which is reflected on the free end of the EBP to a position-

sensitive photodiode according to the optical light-lever technique.[43] The frequency and phase of the readout signal were analyzed via a lock-in amplifier and correlated to the input signal modulating the excitation laser. A phase-locked loop (PLL) maintained a constant phase of 90° with respect to the excitation signal by continuously adjusting the excitation frequency. The corresponding frequency shift Δf_N was acquired and converted to a mass change as outlined below.

6.3.4 Theory of the Mass Sensing by the Picobalance

Commonly, the oscillation of an AFM-cantilever can be described in a first-order approximation as a driven underdamped oscillator.[72, 73] The oscillation is defined by the frequency f at which the oscillator is driven, the natural resonance frequency f_N, and the quality factor ($\widetilde{Q}_f > 1$). The oscillation amplitude A as a function of the resonator's frequency can be described according to [72, 73]

$$A = \frac{a f_N^2}{\sqrt{(f_N^2 - f^2)^2 + \frac{f_N f}{\widetilde{Q}_f}}} + a_1 f + a_2 \tag{6.1}$$

with a accounting for the amplitude of the excitation. The parameters a_1 and a_2 represent a description for a linear background due to the frequency dependent excitation efficiency and amplitude noise. The phase shift φ of a driven and damped harmonic oscillator is given by

$$\varphi = \arctan\left(\frac{\widetilde{Q}_f (f_N^2 - f^2)}{f_N f}\right) + b_1 f + b_2 \tag{6.2}$$

where b_1 accounts for phase lags of photothermal excitation and electronics, and b_2 is related to phase contributions of higher modes.[72, 73]

Generally, the resonance frequency f_N of a harmonic oscillator can be expressed by its effective mass m^* and its spring constant k:

$$f_N = \frac{1}{2\pi}\sqrt{\frac{k}{m^*}} \tag{6.3}$$

After attaching an additional mass M, e.g. colloidal particle, f_N is shifted to a lower frequency $f_N(M)$ as the effective mass changes to $m^* + M$:

$$f_N(M) = \frac{1}{2\pi}\sqrt{\frac{k}{m^* + M}} \tag{6.4}$$

Figure 6.3 summarizes the resulting changes in the amplitude $A(f)$ and the phase spectrum $\varphi(f)$ upon attachment of an additional mass, i.e., a tungsten microsphere with a diameter of 12.7 µm.

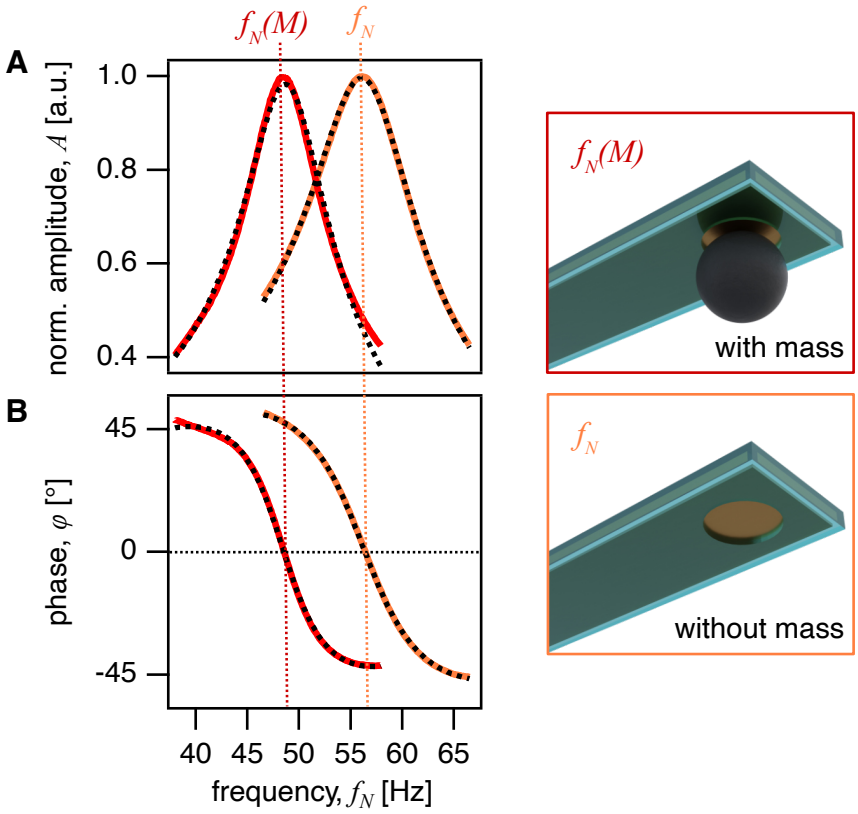

Figure 6.3. Mass sensing with an electrochemical balance probe. **A** Normalized amplitude A and **B** phase φ spectra of an EBP without and with a tungsten microsphere ($d = 12.7$ µm) as an external load. Amplitude and phase have been fitted to Eqs. 6.1 and 6.2 (dashed lines).

The attached mass M can in principle be directly calculated according to Eq. 6.5 based on the frequency shift $\Delta f_N = f_N - f_N(M)$:

$$M = \frac{k}{4\pi^2}\left[\frac{1}{(f_N - \Delta f_N)^2} - \frac{1}{f_N}\right] \tag{6.5}$$

However, Eq. 6.5 assumes that the mass is attached exactly at the free end of the cantilever, which is normally not the case.[39, 40, 45] The apparent mass depends on the position x_c of the mass M on the cantilever with a length L and the mode of oscillation (cf. Section 6.5.3). Here, only the first mode has been excited and was considered in the data evaluation. A correction factor based on the oscillation amplitude $\psi(x)$ is needed

to relate the apparent mass M to the actual mass m_{PB} (Supporting Information Section 6.5.3, Figure 6.11).

$$m_{\mathrm{PB}} = M \frac{1}{\psi(x)^2} \tag{6.6}$$

For a rectangular beam of the length L, the first oscillation mode can be described by

$$\psi(x) = \alpha \left[\sin(\xi x) - \sinh(\xi x) + \frac{(\sin(\xi L) + \sinh(\xi L))\,(\cosh(\xi x) - \cos(\xi x))}{\cosh(\xi L) + \cos(\xi L)} \right] \tag{6.7}$$

with a normalization constant α to fulfill condition $\psi(L)^2 = 1$. ξ is related to the cantilever length by

$$\cos(\xi L)\cosh(\xi L) + 1 = 0. \tag{6.8}$$

6.3.5 Added Mass as Static Calibration of Electrochemical Balance Probes

The added mass method, which is based on Eqs. 6.4 and 6.5, is widely used to calibrate spring constants of AFM cantilevers.[54] In this method, small, µm-sized, colloidal particles from high-density materials, such as gold or tungsten, are attached by capillary forces to the free end of an AFM-cantilever.[54, 74] The resulting frequency shift is related to the theoretical mass based on the top-view dimensions of the microsphere. However, it has been demonstrated that additional layers on the lever arm can impact the mechanical properties of cantilevers.[74, 75] The EBPs comprise a rather complex sandwich structure with a silicon core, enclosed by an adhesive Cr interlayer, the conductive gold coating, wrapped by the insulating electropaint layer. Consequently, we had to verify that mass sensing was possible for these non-standard probes using the added mass method. These experiments were performed in liquid, here 0.1 mM HCl and pH 4, in order to emulate the environmental conditions encountered during the electrochemical experiments. Moreover, the EBPs were driven photothermally, generating much clearer resonance peaks with higher amplitudes and quality factors than piezoelectric or thermal excitation.[42]

By evaluating the resonance frequency f_N, the experimental mass m_{PB} was calculated according to Eq. 6.5 and 6.6. This mass was compared to the theoretical mass m_{theo} (Eq. 6.9) as determined by the optical dimensions and the position of the respective particles on the cantilever.

$$m_{\mathrm{theo}} = \frac{4}{3}\pi \left(\frac{d}{2}\right)^3 \rho \tag{6.9}$$

We utilized tungsten microspheres of various sizes as externally attached masses M for these experiments. The theoretical mass m_{theo} was calculated from the volume V and the density ρ (Eq. 6.9). The volume was determined from the particle diameter d as measured by optical microscopy. Moreover, the position of the particles on the lever arm of the EBPs has been considered according to Eq. 6.6. The correction factor for an EBP depending on the location of the added mass is shown in Figure 6.11B in the SI. The position x_c was determined by allocating the particle's location via optical microscopy. A similar approach has been utilized previously for localizing cells in gravimetric studies by picobalance.[40, 44, 45, 76, 77]

Figure 6.4 summarizes the experimental results for weighing 10 individual tungsten microspheres of various sizes (6.8 µm $< d <$ 13.3 µm) in the picobalance with an EBP.

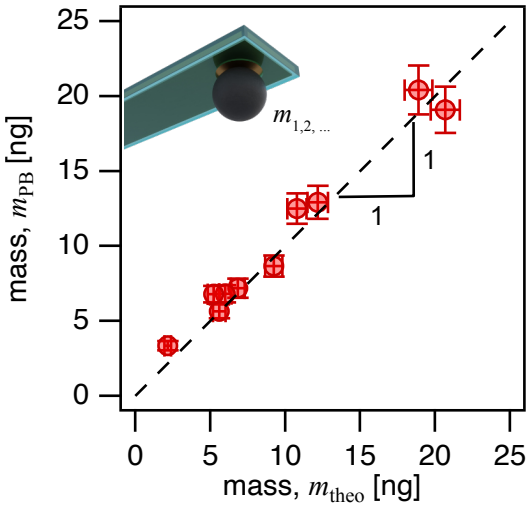

Figure 6.4. Added mass method for electrochemical balance probes. Comparison between the masses of tungsten microparticles of different sizes as determined by their top view dimensions (m_{theo}) and as determined by the resonance shift of an electrochemical balance probe (m_{PB}) as determined by the AFM-based picobalance. The dashed line represents a slope of 1, which means ideal correspondence between the two methods.

The respective theoretical masses m_{theo}, as determined by the radius and density, ranged thus between 2.1 ng and 20 ng. These masses m_{theo} have been compared to the ones determined by the picobalance m_{PB}. Ideally, one expects a ratio $\frac{m_{\text{PB}}}{m_{\text{theo}}} = 1$ as indicated by the dashed line in Figure 6.4. The error bars shown were determined by error propagation based on the uncertainty of the spring constant calibration for the cantilever with which m_{PB} has been determined and the inaccuracy of the diameter obtained by optical microscopy for the theoretical mass m_{theo}. The good agreement for all added masses, which scattered around the dashed line representing perfect agreement, demonstrated that despite their complex structure, the EBPs were capable of quantitative mass determination in the nanogram regime.

6.3.6 The Electrochemical Picobalance

The electrodeposition of copper on metal electrodes accounts for one of the most fundamental and best-studied processes in electrochemistry.[78] Here, we examined the deposition of Cu on the µm-sized Au-electrode (cf. Figure 6.1C and Figure 6.12) of an EBP in combination with the AFM-based picobalance (cf. Figure 6.2). The electron transfer and resulting Cu deposition have been followed simultaneously by the frequency shift $\Delta f_N(t)$ and the faradaic current $I(t)$. For comparison, we performed the experiment under analogous conditions on a macroscopic Au-electrode using the QCM-D technique. A reductive potential of $E_{\text{red}} = -0.4$ V vs. Ag/AgCl was applied to the Au-electrode for both setups.

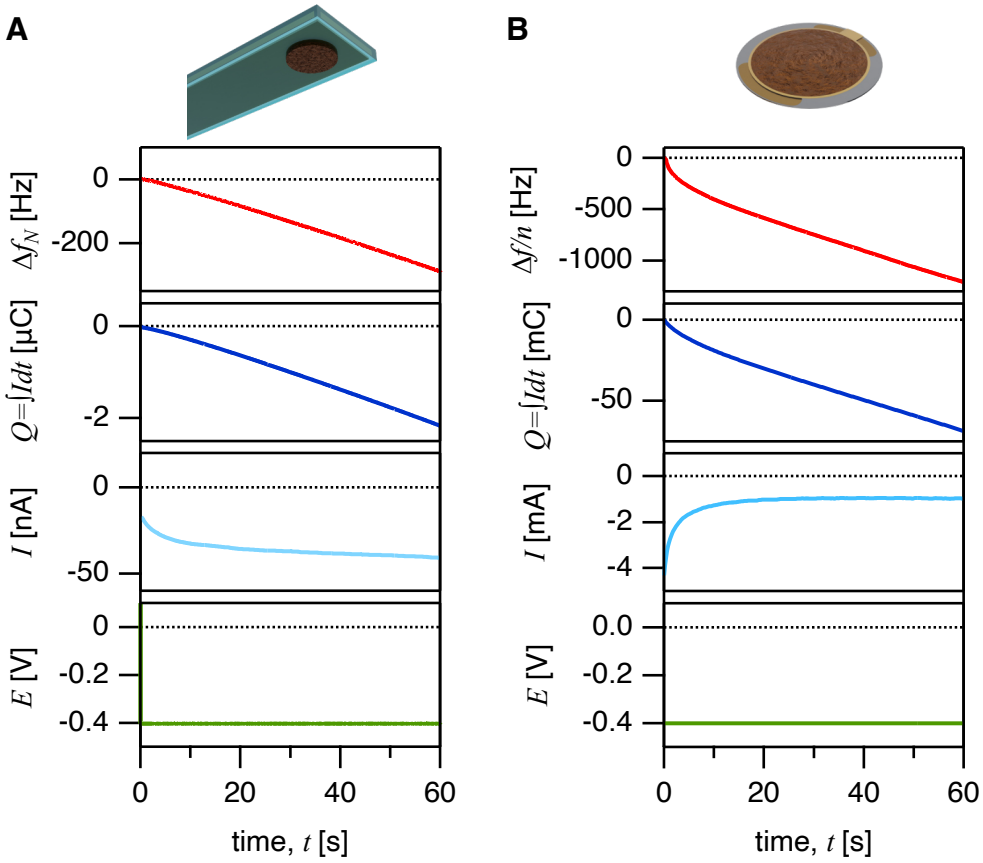

Figure 6.5. Cu electrodeposition on a electrochemical balance probe and a QCM sensor. **A** Frequency shift Δf_N, total charge $Q(t) = \int I(t)dt$, current I and potential E during electrochemical deposition of Cu on an EBP microelectrode in 3 mM $CuSO_4$ and 10 mM H_2SO_4 at -0.4 V for 60 s as detected by the electrochemical picobalance. **B** Frequency shift $\Delta f/n$, total charge $Q(t) = \int I(t)dt$, current I and potential E during electrochemical deposition of Cu on an Au-coated QCM sensor in 10 mM $CuSO_4$ and 10 mM H_2SO_4 at -0.4 V for 60 s. EQCM data is shown for the 3rd overtone. The onset of the potential was set to $t = 0$ for both types of sensors. Note the different axis scaling for the EBP microelectrode and the macroscopic QCM sensor due to the large differences in electrode size.

The deposition was carried out in 3 mM $CuSO_4$ (10 mM for the EQCM experiments) with 10 mM H_2SO_4 as a supporting electrolyte. These experimental conditions fall within the standard conditions reported in the literature for Cu deposition.[29, 31] The electrochemical reduction of Cu^{II} at the EBP microelectrode leads a deposition of solid Cu^0 on the electrode. According to Faraday's law of electrolysis, the faradaic mass m_{faraday} should equal the mass m_{PB} sensed by the picobalance (Eq. 6.6).

Figure 6.5A shows the frequency shift Δf_N, current I, charge Q, and potential E during the electrodeposition of Cu on an EBP as determined by the electrochemical picobalance when E_{red} was applied via the potentiostat. A negative frequency shift of up to −288 Hz after 60 s corresponded to a mass deposition on the microelectrode of the EBP. By contrast, no change in frequency could be detected when E_{red} was applied in pure supporting electrolyte only, i.e., without Cu in the measurement solution (cf. Section 6.5.4, Figure 6.13). Hence, the frequency shift can be assigned to the electrodeposition of copper and was not resulting from the electromechanical stress on the cantilever as it had been observed in some conditions for cantilevers with Au-coating.[79–81] After 5-10 s, the deposition current I was constantly ≈ 40 nA. The corresponding total charge $Q(t)$ was determined by integrating the current $I(t)$:

$$Q(t) = \int_0^t I(t)dt \tag{6.10}$$

We conducted an analogous electrodeposition of Cu on macroscopic Au-coated QCM sensors ($A = 1.13$ cm^2) in an EQCM (cf. Figure 6.5B). Again, a continuous negative frequency shift Δf was observed when a reductive potential of $E_{\text{red}} = -0.4$ V vs. Ag/AgCl was applied for 60 s to induce the copper deposition. The frequency shift is normalized to the overtone n, and data for the 3$^{\text{rd}}$ overtone are shown. The maximum shift was ≈ −1200 Hz after 60 s. In contrast to EBP, the currents were significantly higher, about 1 mA, due to the larger electrode area. However, a direct correlation between the frequency response Δf_N (or $\Delta f/n$) and transferred charge Q at the electrode became evident for both methods.

6.3.7 Correlation Between Electrochemical and Gravimetric Mass

Faraday's law of electrolysis states that the amount of an electrochemical reaction product is proportional to the charge Q transferred through the electrolyte/electrode interface.[1, 3] Hence, the mass of a reactant deposited by an electrochemical reaction is given by

$$m_{\text{faraday}} = -\frac{QM_W}{zF} \tag{6.11}$$

where z is the number of electrons transferred to form one mole of the reactive species with the molecular weight M_W, and F is the faraday constant.[1] Faraday used gravimetric determination of m_{faraday} in his original experiments. Faraday's law can be directly applied to the electrodeposition of Cu on the EBP microelectrode, and the faradaic mass m_{faraday} (Eq. 6.11) must equal the mass sensed by the picobalance m_{PB} (Eq. 6.6). This relation has also been used extensively to characterize EQCM sensors and determine their mass sensitivity.[30–32]

Here, we performed additional experiments by EQCM under identical conditions as a benchmark. The mass from EQCM data was evaluated by the Sauerbrey equation [19] which relates the frequency shift Δf_{EQCM} normalized to the overtone n to a mass per unit area $m_{E\text{EQCM}}/A$ via a sensitivity constant C of the quartz sensor.

$$\frac{m_{\text{EQCM}}}{A} = -\frac{\Delta f_{\text{EQCM}}}{n} C \text{ with : } C = \frac{2f_0}{A\sqrt{\rho\mu}} \tag{6.12}$$

The sensitivity constant $C = 17.7\ \text{ng}\,\text{cm}^{-2}\,\text{Hz}^{-1}$ is determined by the fundamental resonance frequency f_0, the area A of the electrode, the sensor's density ρ, and its shear modulus μ. Since the deposited Cu layer is thin and rigid, the Sauerbrey equation could be applied here without any corrections or viscoelastic modeling.[20]

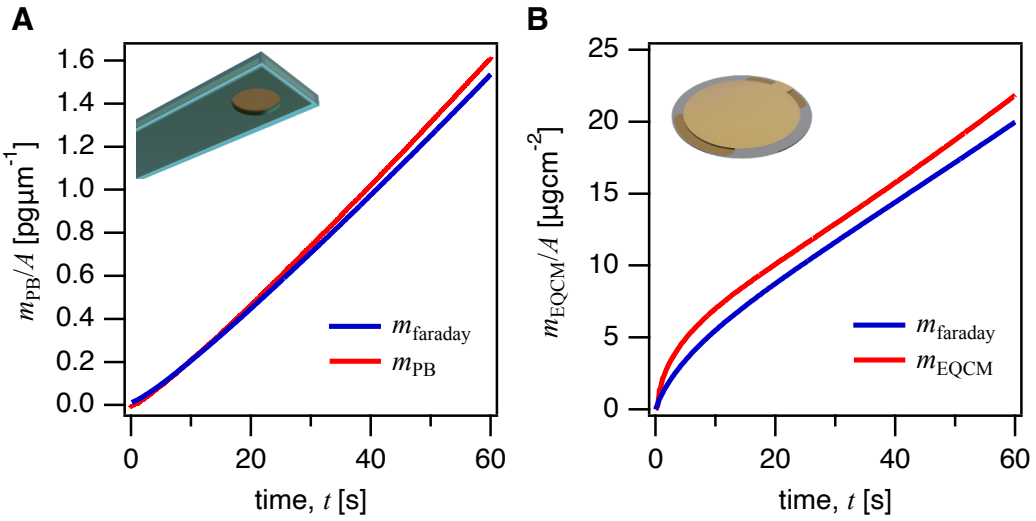

Figure 6.6. Deposited copper mass as determined by electrochemical picobalance, EQCM, and Faraday's Law. **A** Mass of Cu deposited electrochemically on the microelectrode of the EBP as determined from the frequency of shift in the picobalance (m_{PB}) and by integration of the current according to Faraday's law (m_{faraday}). **B** Mass of Cu deposited on an Au-coated quartz-crystal in an EQCM as determined from the Sauerbrey equation (m_{EQCM}) and Faraday's law (m_{faraday}). For both experiments, a potential of −0.4 V vs. Ag/AgCl was applied for 60 s. The faradaic m_{faraday} and gravimetric masses (m_{PB}, m_{EQCM}) have been normalized to the electrode areas (533 μm^2 vs. 1.13 cm^2).

Figure 6.6 summarizes the deposited mass versus time as determined gravimetrically by the electrochemical picobalance and the EQCM, respectively, and electrochemically by Faraday's law. To compare the results obtained by both techniques, the deposited masses have been normalized to the electrode areas of the respective sensors. The electrode area of the EBP was determined from SEM images after the deposition (cf. Figure 6.12). It should be noted that the areas of the two electrodes vary by several orders of magnitude (533 μm^2 versus 1.13 cm^2).

The normalized gravimetric masses agreed well with the masses determined according to Faraday's law of electrolysis for both techniques. Interestingly, the deviation between electrochemically determined mass and the gravimetric one is higher for EQCM. We attribute this to a higher surface area due to the electrode's roughness (Section 6.5.5, Figure 6.14). This type of effect has been reported previously for copper deposition on polycrystalline gold.[31, 32, 82] Moreover, roughness is generally known to impact QCM measurements in liquid.[83]

6.3.8 Mass Sensitivity of the Electrochemical Picobalance

The mass change determined by the two methods, i.e., gravimetrically and electrochemically, was in excellent agreement not only for the EQCM but in particular also for the AFM-based picobalance. Figures 6.5 and 6.6 corroborate that the picobalance can be utilized in an electrochemical mode. In the following, we will address the question of the detection limitations of the electrochemical picobalance. The combination of the picobalance with electrochemistry allows addressing the mass sensitivity and mass resolution of the picobalance technique in a new way: Electrodeposition allows for a defined mass deposition over time, in contrast to adding masses like the tungsten beads in Section 6.3.5 or small blocks of silicon.[39] Moreover, the deposited mass could be verified independently of optical or electron microscopy resolution by means of Faraday's law. In the following, we concentrate on the so-called mass-sensitivity.[40, 84, 85]

The resolution of the electrochemical channel of the picobalance depends strongly on the electrochemical performance of the EBPs (details in the SI, Sections 6.5.2, and 6.5.6). Accurate mass determination by Faraday's law requires optimal electrical insulation of the probes. Any defects in the insulation will lead to additional electrochemically active areas, which would lead to additional deposited masses outside the intended electrode area (cf. Figure 6.10). The chip could be coated with relatively thick layers of non-transparent insulating varnish. Moreover, mounting EBPs via paraffin provided additional mechanical stability and electrical insulation of the contact point between the chip and the wire. In consequence, we found that the quality of the electropaint insulation on the lever arm was crucial. Due to the small microelectrode area, even minor

defects on the lever arm disturbed the mass evaluation drastically. The electrochemical response of the EBPs varied with the number of layers of electropaint. This variation could also be traced in the CVs, where with an increasing number of layers, the overall current reduced significantly. Corresponding CVs are available in the Supporting Information (cf. Section 6.5.2, Figure 6.9). After three layers, the current density in the CVs did practically not change. Hence, we decided on 3 layers for all results presented in this study. For only one and two layers of electropaint, the coating showed imperfections, especially at the edges. Defects in the insulation became evident after electrodeposition and could be visualized by SEM examination of EBPs (cf. Section 6.5.2, Figure 6.10).

By contrast, the gravimetric mass resolution depended primarily on the choice of the cantilever (cf. Figure 6.14) and the accuracy with which the spring constant of the EBP could be determined according to equations 6.4 and 6.5, respectively. Due to the more complex structure of the EBPs, approaches that are based on geometrical dimensions and homogeneous material constants (e.g. [75]) will most likely not provide sufficiently accurate results. The thermal noise method [86] and added mass method [54] are more appropriate for the EBPs, as these methods are based directly on the resonator properties.

Combining the picobalance with electrochemistry allowed dynamic mass deposition on the picobalance for the first time. So far, the picobalance has been only tested by static loads, i.e., colloidal particles of defined mass (cf. Section 6.3.5) that have been attached to the cantilever.[39, 40] It should be kept in mind that the AFM-based picobalance was originally developed for following small mass changes in living cells. The linear increase of mass with time during Cu-deposition allowed for a dynamic approach for which the mass could be determined independently according to Faraday's law (cf. Figure 6.6).

For the picobalance, the absolute mass of Cu electrodeposited was 705 pg after 60 s with a resolution of 2.44 $\mathrm{pg\,Hz^{-1}}$, which demonstrated that mass changes < 1 pg can be readily detected by the picobalance (cf. Figure 6.16). The sensitivity has been extracted from the slope of a mass vs. frequency shift plot shown in Figure 6.7. For QCM and EQCM, the mass sensitivity is normally stated per unit area of the sensor. Hence, for the electrochemical picobalance, we found an 'area normalized' mass sensitivity of approximately 4.6 $\mathrm{fg\,\mu m^{-2}\,Hz^{-1}}$ (or 460 $\mathrm{ng\,cm^{-2}\,Hz^{-1}}$) following the QCM convention. By comparison, we determined a sensitivity of 17.5 $\mathrm{ng\,cm^{-2}\,Hz^{-1}}$ for the commercial QCM resonator, which is in good agreement with 17.7 $\mathrm{ng\,cm^{-2}\,Hz^{-1}}$ as stated by the manufacturer.[87] As the electrode of the EQCM is much larger than the one on the cantilever (533 μm^2 vs. 1.13 cm^2), we find that the mass sensitivity normalized to the electrode area is favorable for the EQCM. On the other hand, it should be kept in mind that on an absolute scale, the picobalance can detect significantly smaller absolute

mass change (cf. Figure 6.16C). The difference between the two techniques becomes especially evident for small frequency shifts (cf. insets in Figure 6.7).

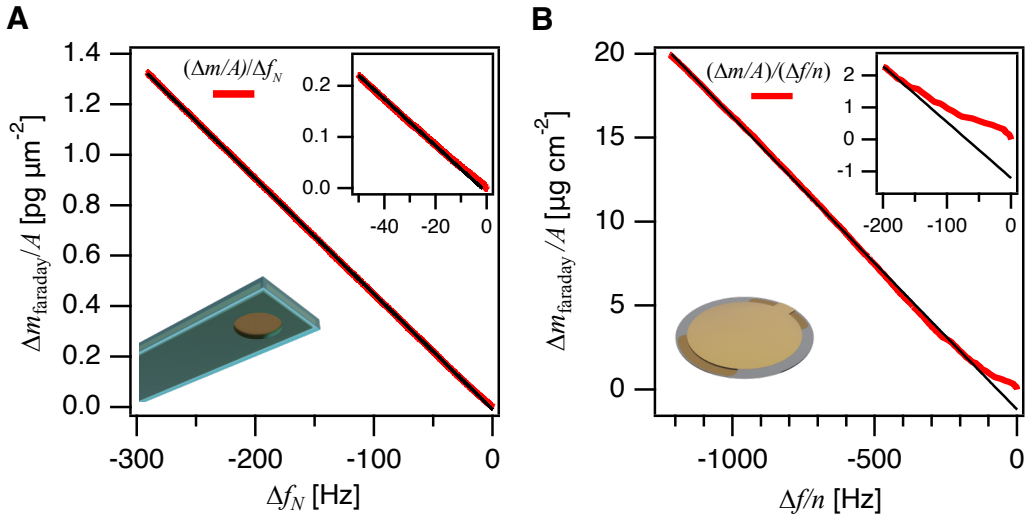

Figure 6.7. Mass sensitivity of the electrochemical picobalance and EQCM. **A** Mass sensitivity for the electrochemical picobalance extracted from the frequency change rate with the added Faraday mass $m_{faraday}$. **B** Mass sensitivity for the EQCM setup was determined in an analogous manner. The insets show the initial deposition at short deposition times and, thus, small frequency shifts.

6.4 Conclusions

In this feasibility study, we presented the combination of electrochemistry with an AFM-based picobalance (electrochemical picobalance), for the first time. The electrodeposition of Cu allowed for dynamic calibration of the picobalance as the deposited mass increased strictly linearly with time and could additionally be determined in an independent manner via the Faradaic current. While the mass sensitivity of the electrochemical picobalance is smaller than for the EQCM, it is able to determine mass changes for absolute masses several orders smaller than the EQCM. If one aims for the study of single-entity electrochemical effects, such as for cells, this absolute sensitivity will be advantageous and could be determined here for the first time by a combination of two independent techniques. In contrast, for homogeneous electroactive films, the EQCM might be the better choice, provided that these films do not require special hydrodynamic data treatment. With the experimental setup used here, we could confirm that mass changes of 1 pg could be resolved by the electrochemical picobalance. With some experimental improvements, e.g., the cantilever used (cf. Supporting Information, Section 6.5.6, Figure 6.15), and the digital resolution of AD converters, even higher mass resolutions seem feasible.

In the future, the combination of electrochemistry and the picobalance will provide alternative approaches to some electrochemical problems, especially in relation to soft matter. The hydrodynamic damping of extended polymeric films on QCM provides a number of challenges to determine the bound mass. In particular, probing the kinetics for electropolymerization and electrogelation is not straightforward for thicker films. In contrast to the EQCM, the electrochemical picobalance is not based on shear oscillations; hence, the hydrodynamic damping takes place by the vertical oscillation of the cantilever. Microcantilevers have been used in the past to successfully trace viscosity and mass density for bulk polymerizations in small volumes.[72] The electrochemical picobalance fosters direct electropolymerization on the mass sensor, i.e., the EBP microelectrode. Hence, this technique provides a complementary approach to studying the polymerization at interfaces.

So far, the picobalance has been primarily applied to monitor mass changes in living cells.[39, 40, 44–46] Addressing the mass changes of single cells upon external stimuli under various time scales represents an important tool for cell biology, and the here-presented setup can extend this approach to the cellular bioelectric state.[52, 88] The bioelectrochemical stimuli for the cell are supposed to have an influence on the cell metabolism.[51] With the implementation of the electrochemical picobalance, bioelectrical stimuli to cells and the resulting mass changes can be studied with unprecedented accuracy. The option of such studies should receive considerable interest.[52] It has also been shown that electrical stimulation can impact cell proliferation, signaling pathways, and immunomodulation.[89–91] So far, this relation has been studied primarily via volume changes and optical microscopy. However, the mass determination by the picobalance has the potential to provide a much higher mass and time resolution than previous approaches. It should be pointed out that these studies would not be limited to eukaryotic cells but could also be applied to, for example, bacteria.[92]

Acknowledgements

The authors gratefully acknowledge the help of Nina Volk, Sebastian Sittl, and the Keylab for Electron Microscopy of the Bavarian Polymer Institute with SEM imaging of the EBPs. Moreover, the authors thank LVH Coatings for the generous gift of the ClearClad electropaint. The authors thank Nanosurf AG (Liestal, Switzerland) and, in particular, Gotthold Fläschner (Nanosurf AG) for fruitful discussions on the picobalance during the initial stage of the project. Nadine Raßmann acknowledges financial support through a Kekulé stipend granted by the Fonds of the Chemical Industry.

6.5 Supporting Information

6.5.1 Instrumental Setup of the Electrochemical Picobalance

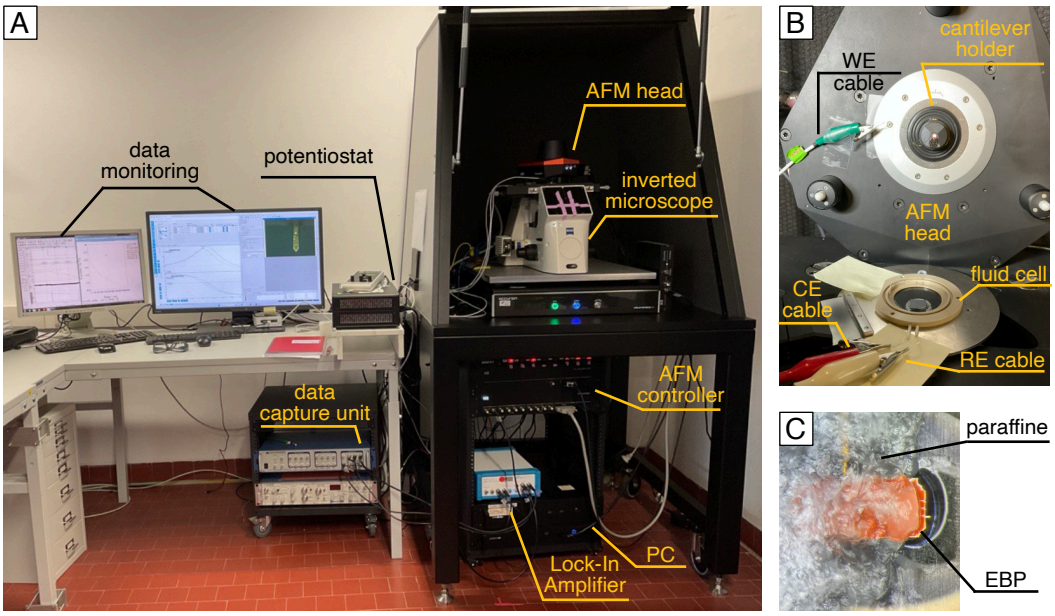

Figure 6.8. **A** Overview of the instrumental setup for the electrochemical picobalance. The electrochemical picobalance was based on a commercial Drive AFM mounted on an inverted optical microscope. The electrochemical balance probe (EBP), which was based on an Au-coated, tipless AFM cantilever, was mounted to the AFM inside a modified fluid cell. This cell comprised a three-electrode electrochemical cell controlled by a potentiostat with the EBP as the working electrode. The photothermal excitation and feedback were controlled externally using a lock-in amplifier in phase-locked-loop mode. A data acquisition unit captured the signals from the AFM, the lock-in amplifier (frequency, phase, amplitude), and the potentiostat (potential, current) with a common timestamp. **B** Image of the electrochemical cell mounted on the AFM for simultaneous mass tracking and electrochemistry at the EBP. **C** Image of an EBP mounted to a commercial cantilever holder using paraffine wax instead of the clamping mechanism to avoid damage to the EBP coating and unintended contacts of the metal clamp and the electrode setup.

6.5.2 Insulation of the Electrochemical Balance Probes

The insulation of the electrochemical balance probes (EBPs), especially of the lever arm, represented a crucial parameter for the electrochemical performance of the electrochemical picobalance. Small defects in the coating created large conductive areas outside the microelectrode area at the end of the lever arm. Therefore, we optimized the electrodeposition procedure for the electropaint to increase the insulating properties. Initially, only one deposition cycle (3 × 180 s at −3.0 V with intermediate dipping in MilliQ water) was used to insulate the lever arm of the EBP. However, the insulation performance, especially along the edges of the lever arm, could be enhanced by applying additional layers of the electropaint (each with 3 × 180 s at −3.0 V with intermediate dipping in MilliQ water) with intermediate annealing steps (20 min at 160°C). Figure 6.9 depicts CVs in 5 mM $K_2[Fe(CN)_6]$ and 5 mM $K_3[Fe(CN)_6]$ with 100 mM KNO_3 supporting electrolyte at 50 mV s^{-1} between −0.6 V and +0.6 V vs. Ag/AgCl of three different EBPs coated with 1-3 layers of electropaint. The current densities are normalized to the microelectrode area. Lower current densities indicate enhanced insulation.

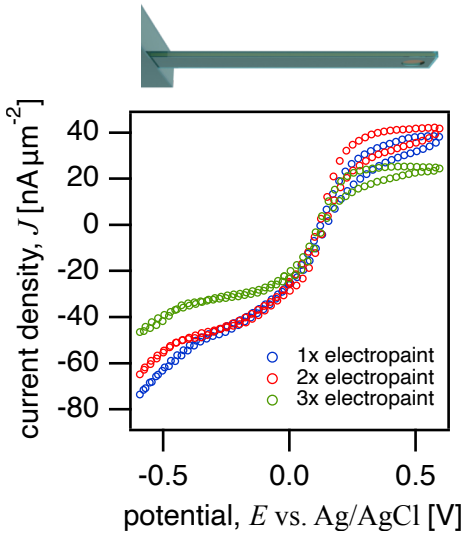

Figure 6.9. Cyclovoltammetry of EBPs with a different number of coating cycles of the insulating electropaint. CV of EBPs in 5mM $K_2[Fe(CN)_6]$ and 5mM $K_3[Fe(CN)_6]$ with 100mM KNO_3 supporting electrolyte at at 50 mV s^{-1} between −0.6 V and +0.6 V vs. Ag/AgCl. Three different EBPs with 1 (blue), 2 (red), and 3 (green) layers of insulating electropaint are compared. Current densities are displayed to account for the different sizes of the electrode area.

Insufficient insulation with the electropaint leads also to Cu deposition at the coating defects. These defects mainly occurred along the edges of the EBPs. Cu crystal growth at insulation defects can be demonstrated in SEM images (cf. Figure 6.10).

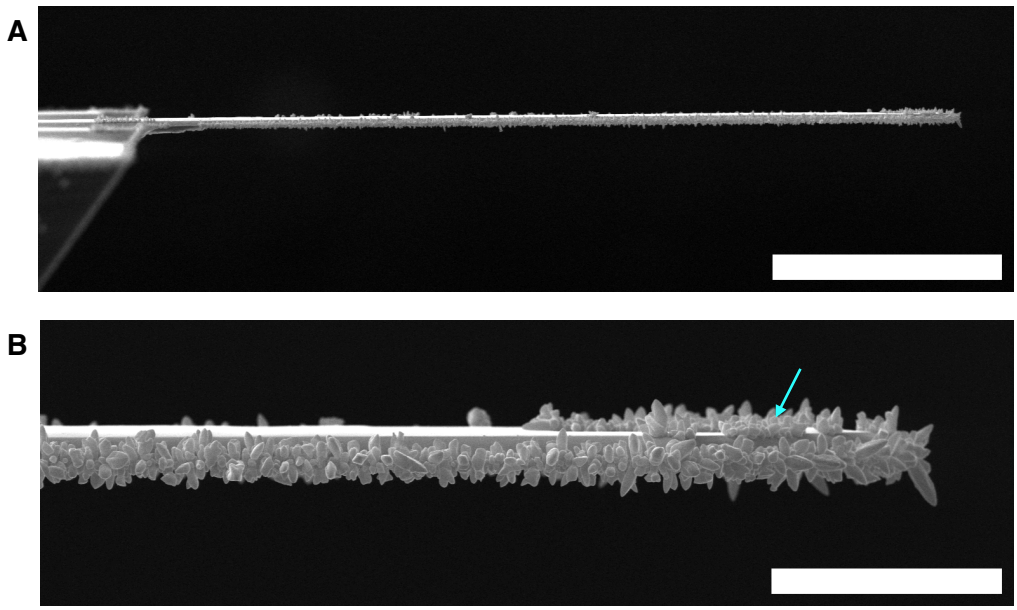

Figure 6.10. SEM images of insufficiently insulated EBPs. **A** Side view SEM image of an EBP with defective insulation of the cantilever after electrodeposition of Cu. Cu growth was observed along the bottom edge of the EBP. The scale bar represents 100 µm. **B** Zoom in on the free end of the EBP with the µm-sized electrode area indicated by a blue arrow. The scale bar represents 20 µm.

6.5.3 Mass Position on the Electrochemical Probe

For cantilever-based mass sensing, the external load is typically not placed precisely at the free end but at a position x_c along the cantilever arm with the length L.[76] The exact mass location must be accounted for by a correction factor, which depends on the cantilever's oscillation amplitude (Eq. 6.13).[39]

$$m_{PB} = M \frac{1}{\psi(x)^2} \tag{6.13}$$

For a rectangular beam of the length L, the first oscillation mode, which is excited photothermally, can be described by

$$\psi(x) = \alpha \left[\sin(\xi x) - \sinh(\xi x) + \frac{(\sin(\xi L) + \sinh(\xi L))(\cosh(\xi x) - \cos(\xi x))}{\cosh(\xi L) + \cos(\xi L)} \right] \tag{6.14}$$

with a normalization constant α to fulfill condition $\psi(L)^2 = 1$. ξ is related to the cantilever length by

$$\cos(\xi L)\cosh(\xi L) + 1 = 0. \tag{6.15}$$

Figure 6.11A illustrates the location of the mass on an EBP. The position is given by the center of mass of the microelectrode area. The corresponding correction factor $\frac{1}{\psi(x)^2}$ for an EBP (cf. Figure 6.12) with a length of $L = 142.9$ µm, dependent on the position of mass x_c, is displayed in Figure 6.11B.

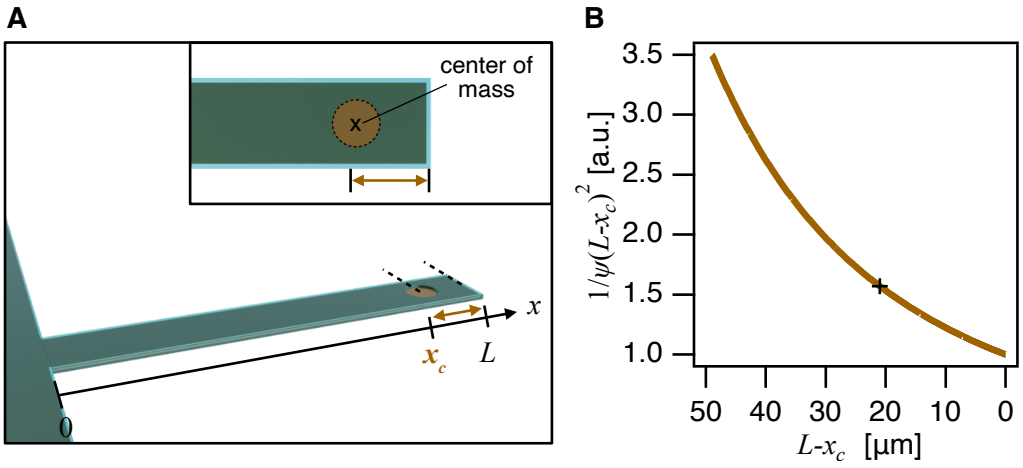

Figure 6.11. Center of mass on the electrochemical probes and correction factor for the mass position. **A** The position of the mass x_c on the EBP with a length L is defined by the center of mass of the integrated Au microelectrode on the EBP. The center of mass has been determined by SEM or optical microscopy. **B** The correction factor $\frac{1}{\psi(x)^2}$ was used to account for the mass position on the EBP. The symbol '+' marks the correction factor for the EBP shown in Figure S5 with a length of $L = 142.9$ µm and $L - x_c = 21.0$ µm.

The length L, the position x_c, and the electrode area A of the EBP used for the Cu deposition experiments (Figures 6.5-6.7) were determined from the SEM images shown in Figure 6.12.

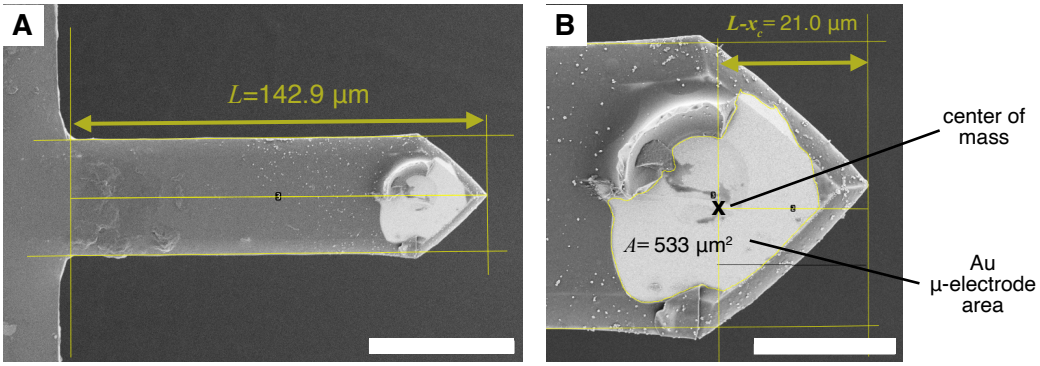

Figure 6.12. SEM images of an electrochemical balance probe with deposited copper. **A** SEM image of the EBP lever arm. The scale bar represents 50 µm. **B** Zoom in on the microelectrode area located at the free end of the EBP. The scalebar represents 20 µm. The electrode area was outlined in FiJi[57] (cf. yellow lines), and the position of the mass on the EBP was determined by the center of mass function in FiJi.

The overview image (cf. Figure 6.12A) of the entire lever arm shows the location of the electrode area close to its free end. Figure 6.12B shows the region of the microelectrode area in more detail. We determined the size of the microelectrode area to $A = 533\ \mu m^2$. Please note that the electropaint insulation was peeled off to some extent also around the contact area, when removing the sacrificial PS particle resulting in a non-circular electrode area. The center of mass was located 21.0 µm from the free end of the EBP. The resulting correction factor $\frac{1}{\psi(x)^2} = 1.57$ (marked with a + in Figure 6.11B) was used to convert the mass M (Eq. 6.5) to m_{PB} according to Eq. 6.6 and Eq. 6.13.

6.5.4 Control Experiments for Solutions Without Cu

We conducted a reference experiment in the pure supporting electrolyte (10 mM H_2SO_4) without adding Cu. Analogously to the Cu-deposition experiments (cf. Figure 6.5A), a reductive potential of $E_{red} = -0.4$ V was applied to the EBP for 60 s, and the frequency shift at the electrochemical picobalance was tracked (cf. Figure 6.13). The data in Figure 6.13 were acquired using the same EBP (SEM image cf. Figure 6.12), once with Cu and once without. No significant frequency shift was detected in pure supporting electrolyte (blue), while a shift of −293 Hz over 60 s occurred in the presence of Cu ions (red). Hence, the frequency shift in the $CuSO_4$ solution was caused by the electrodeposition of copper on the EBP. The applied potential alone did not affect the resonance frequency of the EBP.

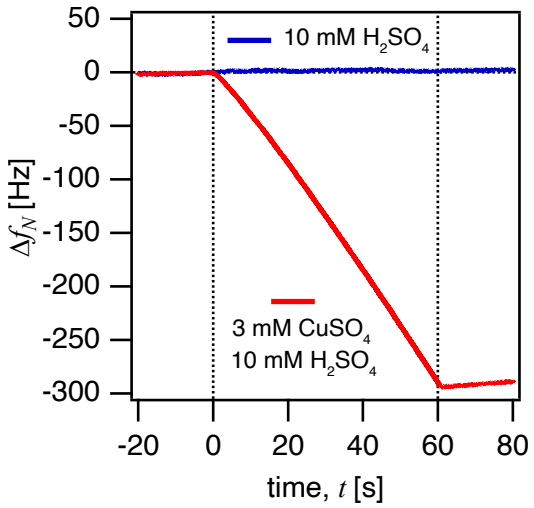

Figure 6.13. Control experiment in supporting electrolyte. Frequency response of an EBP in the electrochemical picobalance under a reductive potential $E_{red} = -0.4$ V ($t = 0 - 60$ s) in a pure 10 mM H_2SO_4 supporting electrolyte (blue) and with 3 mM $CuSO_4$ (red). No frequency shift is observed in the pure supporting electrolyte compared to a shift of −293 Hz in the presence of Cu^{2+}.

6.5.5 Roughness of Electrochemically Deposited Cu Films on QCM Sensors

Figure 6.14 shows the surface topography of a freshly cleaned QCM sensor (cf. Figure 6.14A) and a QCM sensor after Cu deposition at $E_{red} = -0.4$ V vs. Ag/AgCl for 300 s (cf. Figure 6.14B). The images were acquired in tapping mode under ambient conditions (Figure 6.14). The RMS roughness was evaluated on a 5 µm × 5 µm-sized scan area and increased from 1.8 nm after cleaning to 4.9 nm for the Cu deposit.

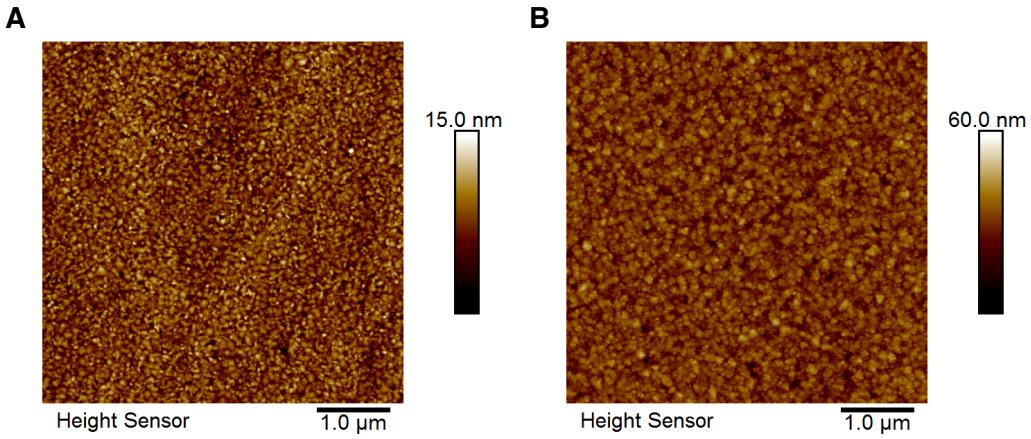

Figure 6.14. Roughness of QCM sensors before and after electrochemical Cu deposition. **A** AFM tapping mode image of a cleaned QCM sensor before Cu deposition with an RMS-roughness of 1.8 nm. **B** AFM image of a QCM sensor after reductive Cu deposition at −0.4 V vs. Ag/AgCl for 300 s in a 10 mM $CuSO_4$ solution containing 10 mM H_2SO_4 supporting electrolyte. The RMS roughness increased significantly to 4.9 nm.

6.5.6 Cantilevers as a Base for the Electrochemical Balance Probes and Mass Resolution

We considered two types of gold-coated tipless cantilevers to build EBPs: NSC35(C) with nominal resonance frequencies of 150 kHz in air and softer CSC37(B) with nominal resonance frequencies of 20 kHz in air. The resonance frequencies in liquid were in the range of 55-60 kHz and 5-7 kHz for the harder and softer ECBs, respectively (cf. Figure S8). We attached a known mass, i.e., a SiO_2 microsphere ($d = 24.5$ µm) with an approximate mass of ≈ 14 ng, to two prototypes of the EBPs based on NSC35 and CSC37 cantilevers. The respective phase and amplitude response to frequency sweeps with and without the external mass is depicted in Figure 6.15.

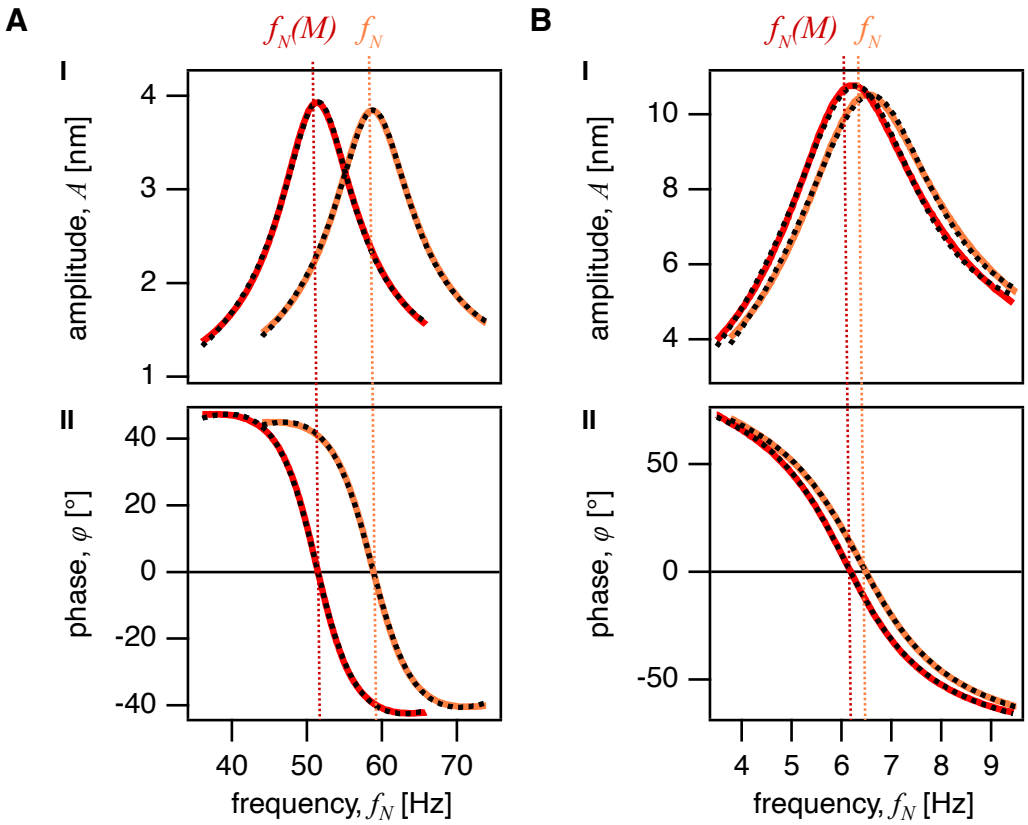

Figure 6.15. Cantilevers for building EBPs. Amplitude **I** and phase **II** response to frequency sweeps of **A** a NSC35-based EBP, and **B** a CSC37-based EBP without and with an external mass of ≈ 14 ng.

In general, the mass sensitivity of a microcantilever is defined as the frequency shift Δf_N induced by a specific change in mass ΔM (Eq. 6.16). Hence, the significantly larger

frequency shift of ≈ 7400 Hz compared to ≈ 310 Hz detected with the NSC-type EBP corresponds to a higher mass sensitivity than the CSC37-based EBP.

$$S = \frac{\Delta f_N}{\Delta M} \simeq \frac{2 f_N}{m^*} \tag{6.16}$$

These findings are in accordance with the approximation by the resonance frequency f_N and its effective mass m^*.[40, 85, 93] which implies that high-resonance cantilevers and small masses, corresponding to smaller cantilever top-view dimensions, are desirable.

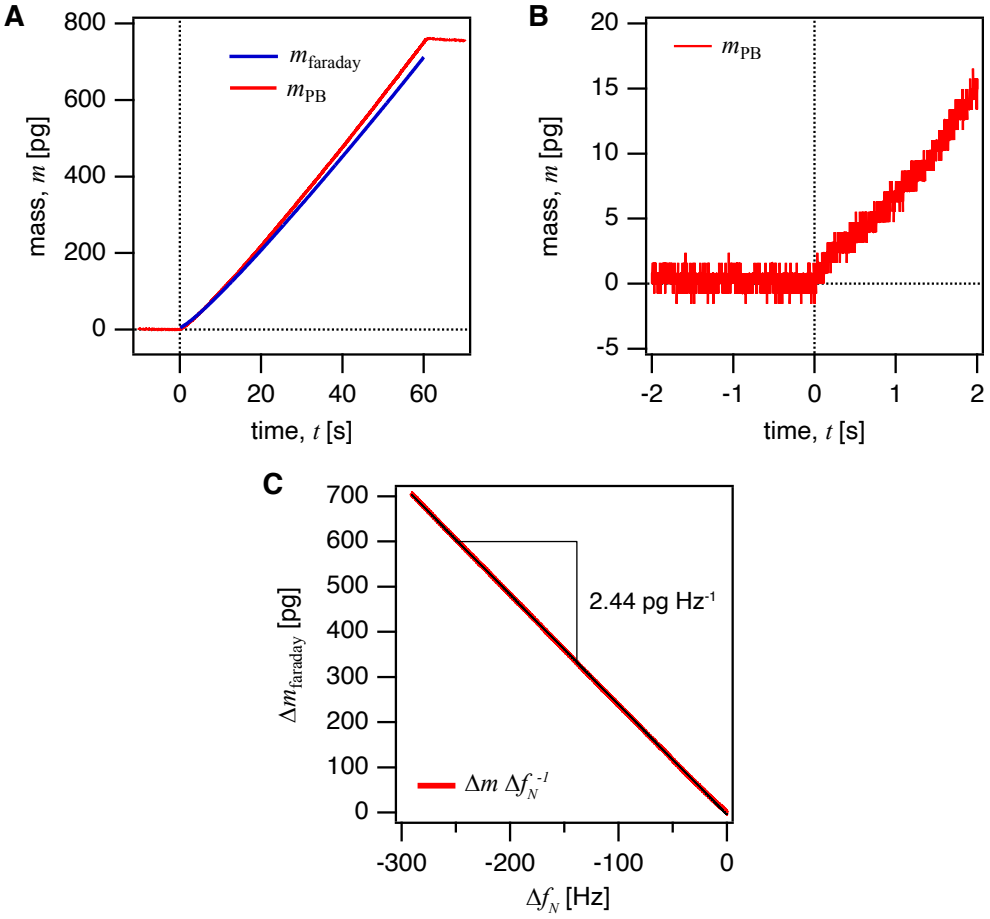

Figure 6.16. Experimental mass resolution of the EBPs in the electrochemical picobalance. **A** Absolute faradaic and picobalance masses during electrodeposition. Corresponding data normalized to the electrode area are shown in Figure 6.6A. **B** Before the start of the deposition, the noise was ≈ 1 pg for m_{PB}. However, the onset of deposition can be clearly identified. **C** The absolute mass sensitivity was determined as 2.4 pg Hz^{-1}.

The second parameter of interest is the lowest detectable mass, which is determined by the smallest detectable frequency shift $\delta(\Delta f_N)$

$$\delta(\Delta f_N) = \sqrt{\frac{f_N k_B T B}{\pi k_c \widetilde{Q}_f A^2}} \tag{6.17}$$

with the quality factor $\widetilde{Q}_f$, the amplitude A, the resonance frequency f_N, the temperature T, the Boltzmann constant k_B, spring constant k_c and the measurement bandwidth B.[39, 40]

The experimental mass resolution and detection limit of the electrochemical picobalance as determined by Cu-deposition on an EBP, is summarized in Figure 6.16.

References

(1) Bard, A. J.; Faulkner, L. R.; White, H. S., *Electrochemical Methods: Fundamentals and Applications*; John Wiley & Sons: Hoboken, 2022.

(2) Eliaz, N.; Gileadi, E., *Physical Electrochemistry: Fundamentals, Techniques, and Applications*; John Wiley & Sons: 2019.

(3) Faraday, M. *Phil. Trans. R. Soc.* **1834**, *124*, 77–122.

(4) Hillman, A. R. *J. Sol. State Electrochem.* **2011**, *15*(7-8), 1647–1660.

(5) Broch, L.; Johann, L.; Stein, N.; Zimmer, A.; Beck, R. *Rev. Sci. Instrum.* **2007**, *78*(6), 064101.

(6) Biermann, M.; Leppin, C.; Langhoff, A., et al. *Analyst* **2024**, *149*(7), 2138–2146.

(7) Cuenca, A.; Agrisuelas, J.; García-Jareño, J. J.; Vicente, F. *Electrochim. Acta* **2017**, *235*, 374–383.

(8) Nisiewicz, M.; Gajda, A.; Kowalczyk, A., et al. *Anal. Chim. Acta* **2022**, *1191*, 339290.

(9) Vanoppen, V.; Johannsmann, D.; Hou, X., et al. *Adv. Sens. Res.* **2024**, *3*(9), 2400025.

(10) Lemaire, P.; Dargon, T.; Alves Dalla Corte, D., et al. *Anal. Chem.* **2020**, *92*(20), 13803–13812.

(11) Nomura, A.; Ito, K.; Yu, D. Y.; Kubo, Y. *J. Power Sources* **2024**, *592*, 233924.

(12) Pastor, E.; Lian, Z.; Xia, L., et al. *Nat. Rev. Chem.* **2024**, *8*(3), 159–178.

(13) Cuesta, A. *Curr. Opin. Electrochem.* **2022**, *35*, 101041.

(14) Neubauer, D.; Scharpf, J.; Pasquarelli, A.; Mizaikoff, B.; Kranz, C. *Analyst* **2013**, *138*(22), 6746–6752.

(15) Baggio, B.; Grunder, Y. *Annu. Rev. Anal. Chem.* **2021**, *14*(1), 87–107.

(16) Wang, W.; Yan, H.; Gu, Y.; Yan, J.; Mao, B. *Annu. Rev. Anal. Chem.* **2024**, *17*(1), 103–126.

(17) Shi, X.; Qing, W.; Marhaba, T.; Zhang, W. *Electrochim. Acta* **2020**, *332*, 135472.

(18) Levi, M. D.; Daikhin, L.; Aurbach, D.; Presser, V. *Electrochem. Commun.* **2016**, *67*, 16–21.

(19) Sauerbrey, G. *Z. Phys.* **1959**, *155*(2), 206–222.

(20) Johannsmann, D., *The Quartz Crystal Microbalance in Soft Matter Research*; Springer International Publishing: Cham, 2015.

(21) Rubin, B.; Topper, J.; Farnell, C.; Yalin, A. *Rev. Sci. Instrum.* **2009**, *80*(10), 103506.

(22) Oberg, P.; Lingensjo, J. *Rev Sci. Instrum.* **1959**, *30*(11), 1053–1053.

(23) Kanazawa, K. K.; Gordon, J. G. *Anal. Chem.* **1985**, *57*(8), 1770–1771.

(24) Reviakine, I.; Johannsmann, D.; Richter, R. *Anal. Chem.* **2011**, *83*(23), 8838–8848.

(25) Alanazi, N.; Almutairi, M.; Alodhayb, A. *Sens. Imaging* **2023**, *24*(1), 10.

(26) Buttry, D. A.; Ward, M. D. *Chem. Rev.* **1992**, *92*(6), 1355–1379.

(27) Shpigel, N.; Levi, M.; Sigalov, S.; Daikhin, L.; Aurbach, D. *Acc. Chem. Res.* **2018**, *51*(1), 69–79.

(28) Ji, Y.; Yin, Z.-W.; Yang, Z., et al. *Chem. Soc. Rev.* **2021**, *50*(19), 10743–10763.

(29) Leppin, C.; Langhoff, A.; Höfft, O.; Johannsmann, D. *Electroanalysis* **2021**, *33*(12), 2529–2538.

(30) Gabrielli, C.; Keddam, M.; Torresi, R. *J. Electrochem. Soc.* **1991**, *138*(9), 2657–2660.

(31) Hu, J.; Xue, S.; Schneider, O., et al. *Electroch. Commun.* **2020**, *119*, 106826.

(32) Friedt, J.-M.; Choi, K. H.; Frederix, F.; Campitelli, A. *J. Electrochem. Soc.* **2003**, *150*(10), H229.

(33) Edvardsson, M.; Svedhem, S.; Wang, G., et al. *Anal. Chem.* **2009**, *81*(1), 349–361.

(34) Easley, A. D.; Ma, T.; Eneh, C. I., et al. *J. Pol. Sci.* **2022**, *60*(7), 1090–1107.

(35) Antonio, J. L.; Martins, V. L.; Córdoba de Torresi, S. I.; Torresi, R. M. *Electrochim. Acta* **2019**, *324*, 134887.

(36) Zhao, M.; Tang, X.; Zhang, H.; Gu, C.; Ma, Y. *Electrochem. Commun.* **2021**, *123*, 106913.

(37) Liu, Y.; Zhang, B.; Gray, K. M., et al. *Soft Matter* **2013**, *9*(9), 2703–2710.

(38) Sadman, K.; Wang, Q.; Chen, S.; Delgado, D.; Shull, K. *Langmuir* **2017**, *33*(8), 1834–1844.

(39) Martínez-Martín, D.; Fläschner, G.; Gaub, B., et al. *Nature* **2017**, *550*(7677), 500–505.

(40) Incaviglia, I.; Herzog, S.; Fläschner, G., et al. *Nano Lett.* **2023**, *23*(2), 588–596.

(41) Ramos, D.; Tamayo, J.; Mertens, J.; Calleja, M. *J. Appl. Phys.* **2006**, *99*(12), 124904.

(42) Ge, L. K.; Tuniz, A.; de Sterke, C. M., et al. *Adv. Sens. Res.* **2024**, *3*(8), 2300136.

(43) Meyer, G.; Amer, N. M. *Appl. Phys. Lett.* **1988**, *53*(12), 1045–1047.

(44) Cuny, A.; Tanuj Sapra, K.; Martinez-Martin, D., et al. *Nat. Commun.* **2022**, *13*(1), 3483.

(45) Herzog, S.; Fläschner, G.; Incaviglia, I., et al. *Nat. Commun.* **2024**, *15*(1), 1751.

(46) Colombo, F.; Villiou, M.; Taheri, F., et al. *Adv. NanoBiomed Res.* **2023**, *3*(7), 2200156.

(47) Zhu, J.; Tong, Y.; Wang, Z., et al. *Small Methods* **2024**, *in press*, e2401640.

(48) Yu, W.; Zhu, J.; Xu, Y., et al. *ACS Photonics* **2024**, *11*(6), 2316–2323.

(49) Karg, A.; Rößler, T.; Mark, A., et al. *Langmuir* **2021**, *37*(46), 13537–13547.

(50) Knittel, P.; Zhang, H.; Kranz, C.; Wallace, G.; Higgins, M. *Nanoscale* **2016**, *8*(8), 4475–4481.

(51) Schofield, Z.; Meloni, G.; Tran, P., et al. *J. R. Soc. Interface* **2020**, *17*(166), 20200013.

(52) Zhang, G.; Levin, M. *Mol. Biol. Cell* **2025**, *36*(2), pe2.

(53) Johannsmann, D.; Reviakine, I. *Nat. Rev. Methods Primers* **2024**, *4*(1).

(54) Cleveland, J. P.; Manne, S.; Bocek, D.; Hansma, P. K. *Rev. Sci. Instrum.* **1993**, *64*(2), 403–405.

(55) Rumble, J. R., *CRC Handbook of Chemistry and Physics*, 2024.

(56) Adams, J.; Frederix, P.; Bippes, C. *Rev. Sci. Instrum.* **2021**, *92*(12), 129503.

(57) Schindelin, J.; Arganda-Carreras, I.; Frise, E., et al. *Nat. Methods* **2012**, *9*(7), 676–682.

(58) Cuny, A. P.; Martínez-Martín, D.; Fläschner, G. *SoftwareX* **2019**, *10*, 100303.

(59) Caniglia, G.; Horn, S.; Kranz, C. *Faraday Discuss.* **2025**, *257*(0), 224–239.

(60) Kranz, C.; Friedbacher, G.; Mizaikoff, B., et al. *Anal. Chem.* **2001**, *73*(11), 2491–2500.

(61) Karg, A.; Kuznetsov, V.; Helfricht, N.; Lippitz, M.; Papastavrou, G. *Sci. Rep.* **2023**, *13*(1), 7885.

(62) Daboss, S.; Knittel, P.; Nebel, C.; Kranz, C. *Small* **2019**, *15*(48), e1902099.

(63) Daboss, S.; Lin, J.; Godejohann, M.; Kranz, C. *Anal. Chem.* **2020**, *92*(12), 8404–8413.

(64) Lindsay, A. E.; O'Hare, D. *Electrochim. Acta* **2006**, *51*(28), 6572–6579.

(65) Sripirom, J.; Kuhn, S.; Jung, U.; Magnussen, O.; Schulte, A. *Anal. Chem.* **2013**, *85*(2), 837–842.

(66) Thorgaard, S.; Bühlmann, P. *Anal. Chem.* **2007**, *79*(23), 9224–9228.

(67) Hussein, E.; Rice, B.; White, R. *Langmuir* **2024**, *40*(13), 7234–7241.

(68) Dobson, P.; Weaver, J.; Holder, M.; Unwin, P.; Macpherson, J. *Anal. Chem.* **2005**, *77*(2), 424–434.

(69) Nellist, M.; Chen, Y.; Mark, A., et al. *Nanotechnology* **2017**, *28*(9), 095711.

(70) Shin, H.; Hesketh, P.; Mizaikoff, B.; Kranz, C. *Anal. Chem.* **2007**, *79*(13), 4769–4777.

(71) *Nanoelectrochemistry*; Mirkin, M. V., Amemiya, S., Eds.; CRC Press: Boca Raton, 2015.

(72) Bircher, B. A.; Duempelmann, L.; Renggli, K., et al. *Anal. Chem.* **2013**, *85*(18), 8676–8683.

(73) Braun, T.; Barwich, V.; Ghatkesar, M., et al. *Phys. Rev. E* **2005**, *72*(3 Pt 1), 031907.

(74) Hazel, J. L.; Tsukruk, V. V. *Thin Solid Films* **1999**, *339*(1-2), 249–257.

(75) Sader, J. E.; Larson, I.; Mulvaney, P.; White, L. R. *Rev. Sci. Instrum.* **1995**, *66*(7), 3789–3798.

(76) Martinez-Garcia, F.; Fischer, T.; Hayn, A., et al. *Gels* **2022**, *8*(9), 535.

(77) Fläschner, G.; Roman, C.; Strohmeyer, N.; Martinez-Martin, D.; Müller, D. *Nat. Commun.* **2021**, *12*(1), 2922.

(78) Gamburg, Y. D.; Zangari, G., *Theory and Practice of Metal Electrodeposition*; Springer New York: New York, NY, 2011.

(79) Kramer, D.; Viswanath, R. N.; Weissmüller, J. *Nano Lett.* **2004**, *4*(5), 793–796.

(80) Tian, F.; Pei, J.; Hedden, D.; Brown, G.; Thundat, T. *Ultramicroscopy* **2004**, *100*(3-4), 217–223.

(81) Raiteri, R.; Butt, H.-J. *J. Phys. Chem.* **1995**, *99*(43), 15728–15732.

(82) Gileadi, E.; Tsionsky, V. *J. Electrochem. Soc.* **2000**, *147*(2), 567–574.

(83) Daikhin, L.; Gileadi, E.; Katz, G., et al. *Anal. Chem.* **2002**, *74*(3), 554–561.

(84) Te Riet, J.; Katan, A. J.; Rankl, C., et al. *Ultramicroscopy* **2011**, *111*(12), 1659–1669.

(85) Ghatkesar, M. K.; Barwich, V.; Braun, T., et al. *Nanotechnology* **2007**, *18*(44), 445502.

(86) Hutter, J. L.; Bechhoefer, J. *Rev. Sci. Instrum.* **1993**, *64*(7), 1868–1873.

(87) Edvardsson, M. B. S. *Application Note: The Sauerbrey Equation - A brief explanation of what it is and how it is derived* **2025**.

(88) McCaig, C.; Song, B.; Rajnicek, A. *J. Cell. Sci.* **2009**, *122*(Pt 23), 4267–4276.

(89) Chen, C.; Bai, X.; Ding, Y.; Lee, I. *Biomater. Res.* **2019**, *23*(1), 25.

(90) Wang, Y.; Rouabhia, M.; Lavertu, D.; Zhang, Z. *J. Tissue Eng. Regen. Med.* **2017**, *11*(4), 1110–1121.

(91) Barman, R. S.; Jhunjhunwala, S. *ACS Omega* **2024**, *9*(1), 52–66.

(92) Czerwińska-Główka, D.; Krukiewicz, K. *Bioelectrochemistry* **2020**, *131*, 107401.

(93) Shen, Z.; Shih, W. Y.; Shih, W.-H. *Rev. Sci. Instrum.* **2006**, *77*(6), 065101.

7

Determining the Elastic Modulus of Microgel Particles by Nanoindentation

Nadine Raßmann[#], Steffen Trippmacher[#], Agnes Specht, Katinka Theis, Tamino Rößler, Sebastian Wohlrab, Richard Kellnberger, Sahar Salehi, Hendrik Bargel, Nicolas Helfricht, Krystina Albrecht, Thomas Scheibel, Jürgen Groll, Stephan Gekle and Georg Papastavrou*

[#] These authors contributed equally.

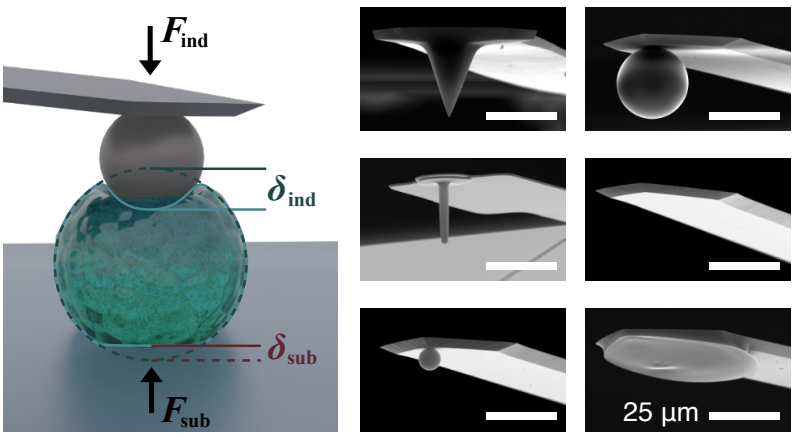

Reprinted with permission from:

„Determining the Elastic Modulus of Microgel Particles by Nanoindentation “

ACS Applied Nano Materials, **2025**, *8*(11), 5383-5398.

Abstract

The mechanical properties of materials and cells are key factors for many processes in biofabrication. Nanoindentation using atomic force microscopy represents an important technique to quantify the Young's elastic modulus in a locally resolved manner or for single microgel particles and cells, respectively. Here, we address the question of the best-suited indenter geometry and continuum model for contact mechanics to describe the nanoindentation of microgels. Two different microgel model systems have been synthesized using microfluidics with a very narrow size distribution of the particles: poly(acrylamide) and ene-functionalized polyoxazoline/thiol-functionalized hyaluronic acid. The respective microgel particles have been characterized by up to six different types of indenter geometries, including spherical, parallel plate, and cone. Moreover, the influence of experimental parameters, such as indentation depth and velocity, on the resulting Young's modulus has been studied. Compared to the Hertz model, the simplified double contact model (SDC model) provided a better description of the indentation process and a narrower distribution of Young's moduli with respect to the different indenter geometries. By numerical simulation of the indentation process, we demonstrated that the remaining variation of the Young's moduli is attributed to adhesion. The adhesive force between a particle and the substrate led to a prestress, which is similar to that of particle deformation by the substrate as accounted for by the SDC model. This effect varied in strength with the indenter geometries and can contribute significantly to the experimentally observed variation of Young's moduli for different indenter geometries. Importantly, these results can also be extended to the indentation of single living cells.

7.1 Introduction

The mechanical properties of cells, sometimes also referred to as mechanical phenotype, provide direct access to the physiological state of a cell.[1, 2] For example, the elastic modulus of the underlying substrate or surrounding matrix plays an important role in the development and regeneration of stemcells.[3, 4] Some diseases, such as cancer, sickle cell anemia, and malaria, to name only a few, result in significant changes in cell mechanics. Hence, cell mechanics and pathogenesis of human disease are often related, and the former can be used for diagnostic purposes.[5–8] Thus, the mechanical properties of cells have been studied extensively.[5, 7, 9–12] However, cell elasticity can vary over time and locally on the cell, as e.g., the cytoskeleton and the cell nucleus show deviating elastic moduli. Microgel particles are a widely used model system that allows mimicking cells in biomaterials research being more constant and homogeneous in terms of its elastic properties.[13–16] Therefore, the microgel particles allow to verify characterization

methods for applications with cells.[17] The size and elasticity of microgels can be easily tuned to match the properties of cells during synthesis, e.g., by varying the crosslinking density.[16–19] Micromechanical properties are key characteristics of microgels, and the Young's modulus is a typical measure of choice to characterize the elasticity of soft matter such as cells and microgels.[16, 20] Nanoindentation based on atomic force microscopy (AFM),[1, 14, 15, 21, 22] besides deformation in a flow channel,[2, 23–25] and micropipette aspiration,[11, 26] are the most widely used techniques to study Young's moduli of cells and microgels. While microfluidic based methods deform the entire particle,[2, 23] capillary aspiration [11, 26] and AFM nanoindentation [17, 21, 22] cause more local deformations.[1, 15, 19] In a typical AFM nanoindentation experiment, a cantilever equipped with a sharp tip or spherical colloidal particle is indented into the sample.[17, 21, 27–29] The resulting force vs. indentation data can be fitted to various mechanical contact models that allow extracting elastic properties.[20] For a long time, Hertzian contact mechanics represented the quasi-standard for data analysis.[5, 10, 30] The Hertz model assumes that the cell or microgel can be approximated as an infinite elastic half-sphere. Moreover, no adhesion between the indenter and sample is supposed to be acting.[20, 31] However, small samples, such as cells and microgel particles, have to be placed on a planar substrate in order to perform nanoindentation experiments on them. It is known that, the underlying substrate can lead to a significant overestimation of the Young's modulus for thin films,[32, 33] especially in the case when the indentation depth is larger than 10 % of the film thickness.[34, 35] To account for this effect, models to compensate for the contribution of the substrate have been introduced.[35] Recently, it has been demonstrated that also for small spherical soft samples, like microgels or cells, the presence of a hard substrate can lead to significant deviations from the classical Hertz model.[11, 36] As a first approximation, thin-film models have been applied to describe deep indentations on small microgel particles.[21, 37] However, there is some evidence that soft spherical objects are also deformed at their interface with the substrate while being indented from the top.[11, 17, 36, 38] This effect cannot be described adequately by thin-film models. Approximating cells and microgels as elastic hemispheres and neglecting the bottom deformation can significantly underestimate the Young's modulus, depending on the microgel and indenter characteristics.[38]

First, Dokukin et al. introduced a double contact model to describe loosely attached cells on nondeformable surfaces, thereby accounting for the additional cell deformation by the substrate during the indentation measurement.[36] This approach has been refined by Glaubitz et al., presenting a more general form for spherical samples, including the effects of predeformation, and discussing the theory of a variety of size ratios between particle, indenter, and substrate radii.[38] Later, Daza et al. adapted the model for conical indenters and reported a significant decrease in the deviation of Young's moduli as determined by AFM-based indentation experiments compared to micropipette

aspiration.[11] While these "double contact models" were introduced nearly a decade ago, they have been applied only sparsely so far.[11, 17, 36, 38–40] One reason could be that a systematic comparison for highly defined systems, such as microgel particles, has not been reported yet, and research concentrated primarily on more complex biological systems, such as cells. Such a systematic comparison needs to include different indenter geometries as those will affect the Young's moduli derived by the double-contact model differently.[38]

The best-suited indenter geometry for soft samples, such as cells and microgels, has been discussed extensively in the past.[29, 41–44] While micrometer-sized colloidal probes provide a well-defined geometry, they cannot account for laterally resolved variations in elasticity commonly observed in cells. On the other hand, nanometer-sized sharp tips might fall on a length scale where continuum models cannot always be inherently assumed for hydrogels. In recent years, purposely constructed AFM cantilevers hybridizing both aspects are increasingly used.[43, 45] Several studies observed significant deviations between elastic moduli when comparing indentation using sharp tips and spherical indenters.[10, 17, 27–30, 40, 42–44] This finding requires attention as the Young's modulus of microgels, or cells, is an intrinsic material property and should, therefore, be independent of the indenter geometry provided that a suitable continuum model has been applied to describe the mechanical response. Therefore, elastic continuum models to describe AFM-based indentation experiments must also account for the indenter geometry. Here, we studied the validity of the simplified double contact model (SDC model) and the effect of different indenter geometries for two highly defined microgels as model systems: microgels based on polyacrylamide (PAAm),[17] as well as enefunctionalized polyoxazoline (POx) together with a thiolfunctionalized hyaluronic acid (POx-HASH).[46, 47] Both microgel systems were synthesized using microfluidics, resulting in a narrow distribution of diameters of $\approx 25-30$ µm and Young's moduli in a cell-relevant range (< 10 kPa). By utilizing two different hydrogel systems originating from very different synthetic routes, we can exclude that the described mechanical properties are hydrogel specific. PAAm is a fully synthetic polymer that has been used in the past as a model for nanoindentation experiments and thus allows for a classification of the here-performed experiments.[17] In contrast, POx-HASH is a hybrid of ene-functionalized polyoxazoline and thiol-functionalized hyaluronic acid. It has been only recently introduced, primarily for biofabrication purposes.[46, 47] This hybrid polymer system combines the stiffer POx with the more elastic HASH to obtain elastic moduli in a cell-similar range. We compared up to six different indenter geometries in the AFM-based nanoindentation experiments. Our experimental results clearly favor the double-contact model. The remaining discrepancies between the different indenter geometries could be explained based on theoretical simulations considering the prestress due to the adhesive contact between the microgel particle and the substrate. Besides the

indenter geometry, we demonstrate the importance of choosing adequate measurement parameters, such as the proper alignment of the indenter to the microgel apex, the indentation velocity, and the loading force.

7.2 Experimental Methods

Materials

All aqueous solutions were prepared with Milli-Q water (IQ 7000, resistivity: 18 MΩ cm^{-1}, Merck KGaA, Darmstadt, Germany). Ammonia 25% (VWR International S. A. S, Rosny-sous-Bois, France), Krytox 157 FSH (H. Costenoble GmbH & Co. KG, Eschborn, Germany), methanol (Fisher Scientific, Loughborough, UK), ethanol (p.A. VWR Chemicals, Darmstadt, Germany), HFE 7100 (IOLITEC GmbH, Germany), Sylgard 184 elastomer kit (Mavom GmbH, Steinfurt, Germany), 2-propanol (VWR International S. A. S, France), acrylamide (AAm, ≥ 99%, Sigma-Aldrich, St. Louis, MO, USA), N,N'-methylenbis(acrylamide) (BIS, 99%, Sigma- Aldrich, USA), N-(3-aminopropyl)methacrylamide hydrochloride (APMA, 98%, Sigma-Aldrich, USA), ammonium persulfate (APS, 98%, Sigma-Aldrich, USA), N,N,N',N'-tetramethylethylenediamine (TEMED, ≥ 99%, Sigma-Aldrich, USA), 1H,1H,2H,2H-perfluoro-1-octanol (97%, Sigma-Aldrich, USA), phosphate buffered saline (1×PBS, pH 7.4, Sigma-Aldrich, USA), fluorescein 5-isothiocyanate (5-FITC, ≥ 90%, Cayman Chemical Company, Ann Arbor, MI, USA), SU-8 2015, SU-8 2050 photoresist and SU-8 developer (micro resist technology GmbH, Berlin, Germany), Hellmanex III (Hellma GmbH & Co. KG, Müllheim, Germany), isopropyl alcohol (p.a. VWR Chemicals, Darmstadt, Germany), hydrogen peroxide (30 w/v %, Fisher Scientific, Schwerte, Germany), lithium-phenyl-2,4,6-trimethylbenzoylphosphinate (LAP, TCI Chemicals, Eschborn, Germany), Span 80 (Sigma-Aldrich, Darmstadt, Germany), 3-aminopropyldimethylethoxysilane (APDMES, 97%, abcr, Karlsruhe, Germany) and mineral oil (Sigma-Aldrich, Darmstadt, Germany) were used as received.

Surfactant Synthesis

The surfactant was synthesized with minor modifications as described by Girardo et al.[17] Briefly, 10 g Krytox 157 FSH were dissolved in 60 mL methanol and 30 mL HFE 7100. Subsequently, 25 mL 0.1 M ammonia was added slowly over a dropping funnel. After overnight reaction, solvents were removed at the rotary evaporator, and the obtained oil was further dried under reduced pressure and at 80°C overnight. The viscous oil was stored at room temperature in an amber glass vial.

Microfluidic-Assisted Syxnthesis of PAAm-Particles

The synthesis of PAAm-particles follows a modified procedure based on Girardo et al.[17] First, the monomer solution of AAm and BIS with a total monomer content of 18.6% (w/v) and a BIS/AAm-ratio of 3.25% (w/w) was prepared. The solution was purged with argon for 30 min. Meanwhile, pure water was also purged with argon for 30 min. Afterward, APS was dissolved in purged water (16 $g\,L^{-1}$). For FITC-labeling of PAAm, a modified procedure of Hu et al. has been followed.[48] In difference to the preparation of bare PAAm particles, 5 mol % of AAm were replaced by APMA. The oil phase consisted of 1.5% (w/w) surfactant (synthesized) and 0.4% (v/v) TEMED in HFE7500. No purging with argon has been done. A microfluidic device was used for particle synthesis. Details on the device fabrication are available in the Supporting Information. The device was connected to two reservoirs via PEEK-tubing (1/32″ OD× 1/32″ ID, BGB Analytik Vertrieb GmbH, Lörrach, Germany). Two 2 mL vials acted as reservoirs. One vial was filled with 1 mL of oil phase; the other vial was filled with 300 µL monomer solution and 300 µL APS solution. The two aqueous solutions were mixed gently to minimize the dissolution of oxygen. The reservoirs were set under pressure by Flow EZ pressure controllers (Fluigent, Le Kremlin-Bicêtre, France) with additional Flow Unit S flow sensors (Fluigent, Le Kremlin-Bicêtre, France) enabling droplet formation under flow control. The flow rates during droplet formation were 300 $\mu L\,h^{-1}$ for the aqueous phase and 750 $\mu L\,h^{-1}$ for the oil phase. The droplets were collected in another vial containing 500 µL oil phase. Twenty minutes after mixing the aqueous phase, the procedure was stopped. The resulting emulsion was shaken overnight at 20°C (800 rpm). Afterward, the emulsion rested for the clear oil phase to settle. The clear oil was removed, and 500 µL emulsion breaker (20% (v/v) PFO in HFE7500) were added. The mixture was vortexed for 10 s and then centrifuged at 5000g for 1 min. The oil phase was removed, and 500 µL *n*-hexane were added. The mixture was vortexed for 10 s and then centrifuged (5000g, 1 min). *n*-hexane was removed, and 100 µL of phosphate-buffered saline (PBS) were added. In the case of the particles modified by APMA, 300 µL of PBS were added. The particle suspension was stored at 4°C. The stock suspension was diluted by adding PBS. of oil phase; the other vial was filled with 300 µL monomer solution and 300 µL APS solution. The two aqueous solutions were mixed gently to minimize the dissolution of oxygen. The reservoirs were set under pressure by Flow EZ pressure controllers (Fluigent, Le Kremlin-Bicêtre, France) with additional Flow Unit S flow sensors (Fluigent, Le Kremlin-Bicêtre, France) enabling droplet formation under flow control. The flow rates during droplet formation were 300 $\mu L\,h^{-1}$ for the aqueous phase and 750 $\mu L\,h^{-1}$ for the oil phase. The droplets were collected in another vial containing 500 µL oil phase. Twenty minutes after mixing the aqueous phase, the procedure was stopped. The resulting emulsion was shaken overnight at 20°C (800 rpm). Afterward, the emulsion rested for the clear oil phase to settle. The clear oil was

removed, and 500 µL emulsion breaker (20% (v/v) PFO in HFE7500) were added. The mixture was vortexed for 10 s and then centrifuged at 5000g for 1 min. The oil phase was removed, and 500 µL *n*-hexane were added. The mixture was vortexed for 10 s and then centrifuged (5000g, 1 min). *n*-hexane was removed, and 100 µL of phosphate-buffered saline (PBS) were added. In the case of the particles modified by APMA, 300 µL of PBS were added. The particle suspension was stored at 4°C. The stock suspension was diluted by adding PBS.

FITC-Labelling of PAAM Microgel Particels

The particles modified with APMA (150 µL stock suspension) were added to 2 mL of a 0.1 mg mL^{-1} FITC solution in PBS. The suspension was shaken overnight at 20°C (800 rpm). Then, the particles were centrifuged off (8000g, 2 min). The residue was resuspended in 1.5 mL PBS. The process of centrifugation and resuspension was repeated six times. After the final centrifugation, the particles were resuspended in 500 µL PBS and stored at 4°C.

Microfluidic-Assisted Synthesis of POx-HASH Micorgel Particles

For the synthesis, an ene-functionalized polyoxazoline(POx) and a HASH were used, which were synthesized as described previously.[46, 47] The pregel solution was obtained by dissolving POx and HASH, each with a concentration of 3.75% (w/v) in PBS buffer, pH 7.4, to obtain a total polymer content of 7.5% (w/v). Lithiumphenyl-2,4,6-trimethylbenzoylphosphinate was added to the aqueous solution in a concentration of 1% (w/v) as a photoinitiator for photocross-linking. Before use, the polymer solution was filtered through a 17 mm syringe filter (cellulose membrane with a pore diameter of 0.2 µm). The oil phase consisted of mineral oil and 2.5% (w/v) Span 80. The mixed precursor solutions were transferred to glass syringes (SYR1 mm 1001 TLL for the aqueous phase, 2 × SYR 5 mL 1005 TLL for the oil phase, Hamilton) that were installed into displacement-based syringe pumps (neMESYS, Cetoni GmbH, Korbussen, Germany). Using Luer-Lock connections, the syringes were connected to PE tubings (I.D. 0.28 mm, O.D. 0.64 mm, Scientific Commodities Inc., Lake Havasu City, USA) via precision tips (TIP 30GA 0.006×0.25, Nordson EFD, West Lake, USA). The PE tubes were connected to the inlet chambers of the microfluidic device (oil phases to the two outer inlets, polymer phase to the middle inlet. Details on the device fabrication are stated in the Supporting Information). The flow was adjusted using the QmixElements software (Cetoni GmbH, Korbussen, Germany) to control the syringe pumps. Flow rates were 460 µL h^{-1} (each, 920 µL h^{-1} in total) for the oil phase and 48 µL h^{-1} for the aqueous

phase. A high-framerate video camera (Phantom v1610, Vision Research Inc., Charlottetown, Canada) attached to a light microscope (Axio Vert.A1 FL, Zeiss, Oberkochen, Germany) was used to observe droplet production. After droplet formation on the chip, the droplets were exposed to a 405 nm power LED (Silver-LED-405, Fiber Coupled UV, Prizmatix, Holon, Israel) for photo-cross-linking via a thiol-ene click reaction in flow in a PE tubing connected to the outlet chamber of the microfluidic device for 5 s. The resulting microgel suspension in oil was collected in a 10 mL glass vial. The produced microgel beads in oil were washed two times via centrifugation (11500g, 2.5 min) in *n*-hexane and three times via centrifugation (11500g, 2.5 min) in 1× PBS. The final aqueous bead solution was stored at 4°C.

Surface Functionalization and Cleaning

PAAm microgel particles were immobilized on freshly cleaned glass discs, while POx-HASH microgel particles were immobilized on APDMES-modified glass discs, respectively. Briefly, circular glass discs (diameter: 35 mm, Irlbacher Blickpunt Glas, Schönsee, Germany) were cleaned by a modified three-step RCA cleaning procedure. The glass discs were sonicated in 2% (v/v) Hellmanex III (Hellma GmbH & Co. KG, Müllheim, Germany) in Milli-Q grade water at 40°C for 20 min and were rinsed extensively with Milli-Q water. Next, the glass discs were sonicated in a 3:1 (v/v) mixture of isopropyl alcohol and Milli-Q water. Afterward, the glass was thoroughly washed with Milli-Q water. In a third step, the glass discs were exposed to a 5:1:1 (v/v/v) mixture of Milli-Q water, ammonia, and hydrogen peroxide at 80°C for 20 min. Finally, the glass discs were rinsed extensively with Milli-Q water and dried under a nitrogen stream. Directly before surface modification, the discs were rinsed again with Milli-Q water, ethanol (EtOH), and Milli-Q water and dried under a nitrogen stream. The surface was activated by exposure to air plasma (Zepto, Diener Electronics, Ebhausen, Germany) for 20 min. If needed, the glass discs were coated with APDMES via vapor deposition at reduced pressure in a desiccator overnight. APDMES-modified slides were rinsed with Milli-Q water, EtOH, and Milli-Q water and dried under a stream of nitrogen. The success of the surface functionalization was verified by measuring the static water contact angle ($> 60°$).

AFM-Cantilever Calibration and Preparation of Colloidal Probes

Six different types of indenter geometries were realized based on three kinds of AFM cantilevers: tipless (HQ:CSC37B/tipless/CrAu, MikroMasch, Sofia, Bulgaria), sharp tip (CSCS12E, MikroMasch, Sofia, Bulgaria), and rounded-tip (SAA-SPH-1UM, Bruker Nano Surfaces, Wissembourg, France), with nominal resonance frequencies of 20, 12, and

40 kHz, and nominal spring constants of 0.3, 0.04 and 0.25 N m^{-1}, respectively. Please notice that the CSCS12E cantilevers are not produced anymore and were from an old stock in our laboratory. Sharp-tip and rounded-tip cantilevers were used as conical or spherical indenters without further modification. Spherical indenters with larger diameters, so-called colloidal probes, were fabricated by attaching two types of silica microspheres, small (d_{nom} = 6.80 µm, Bangs Laboratories, Fishers, USA) and large (d_{nom} = 24.77 µm, microParticles GmbH, Berlin, Germany), to the free end of the tipless cantilevers (HQ:CSC37B/tipless/Cr-Au, MikroMasch, Sofia, Bulgaria). First, a small droplet of UV curable glue (NOA 63, Norland Adhesives, Norland Products, Jamesburg, USA) was placed on the free end using etched tungsten wires employing a micromanipulator (DC-3 KS, Märzhäuser, Ebhausen, Germany) under the control of a fixed-stage microscope (Examiner D.1, Zeiss, Oberkochen, Germany). Subsequently, the respective microsphere was manipulated onto the glue droplet, and the glue was cured by exposure to UV light. Tipless cantilevers without modification were used as planar indenters. Furthermore, wedged cantilevers, which compensate for the 10° tilt angle of the MFP-3D cantilever holder, were fabricated using a modified procedure based on Stewart et al.[49] (details are available in the Supporting Information, Section 7.6). The spring constants of all cantilevers (HQ:CSC37B/tipless/CrAu, CSCS12E, MikroMasch, Sofia, Bulgaria) besides the precalibrated rounded-tip probes (SAA-SPH-1UM, Bruker, Nano Surfaces, Wissembourg, France) were calibrated according to the thermal noise method [50] in air before conducting the first measurements. Colloidal probes were calibrated in all cases before attaching the particle to the cantilever. The determined spring constant seems not to depend on order, i.e., attachment of particle or spring constant calibration, for the thermal noise method.[50] Spring constants ranged between 0.21 − 0.40 N m^{-1} and 0.02 − 0.08 N m^{-1} for the tipless and sharp tip cantilevers, respectively. Cantilevers were cleaned by repeatedly dipping into several solvents (Milli-Q water, ethanol, isopropanol, ethanol, Milli-Q water) and exposure to air plasma (Zepto, Diener electronic, Ebhausen, Germany) for 120 s prior to usage. Subsequently, we functionalized the cantilevers by immersion into a 1 g L^{-1} solution of poly(L-lysine)-*graft*-poly(ethylene glycol) (PLL-*g*-PEG) (SuSoS Surface Technologies, Dübendorf, Switzerland) in Milli-Q water for > 30 min to minimize adhesion to the microgel beads. Excess PLL-*g*-PEG was rinsed off by dipping into Milli-Q water.

Nanonindentation Experiments

AFM-based nanoindentation measurements were conducted on a MFP-3D AFM (Asylum Research, Oxford Instruments, Santa Barbara, USA) mounted on top of an inverted optical microscope (Axio Observer Z.1, Zeiss, Oberkochen, Germany) equipped with a 20× objective and a brightfield cube. A commercial fluid cell (Asylum Research, Oxford

Instruments, Santa Barbara, USA) with an exchangeable glass disc bottom allowed for optical control during all experiments. Glass discs were modified with APDMES by vapor deposition to immobilize POx-HASH microgels. For PAAm, glass discs were used after plasma activation (air plasma, 20 min) without further modification. The glass discs were mounted to the fluid cell, and 30 µL of the microgel suspension was placed into the cell. A few droplets of phosphate-buffered saline (PBS) were added to ensure complete wetting of the glass disc. The microgel beads were left to sediment for 15 min before exchanging the buffer in the cell three times and filling the fluid cell to its total volume of ≈ 2.5 mL PBS. Proper center-center alignment was ensured by acquiring an array of force-distance curves on an 8 × 8 grid of 4 µm × 4 µm. A height map was calculated in the AR software (AR v.16.33.234, Asylum Research, Oxford Instruments, Santa Barbara, USA) by evaluating the z-sensor position when the preset trigger point was reached. The internal nudger function of the AFM was used to position the cantilever over the apex of the microgel bead. In contrast to all other indenter geometries, the coarse optical alignment of the tipless and wedged cantilevers was sufficient due to the absence of any indenter curvature. Indentation measurements at the apex of a microgel bead were conducted by ramping the respective cantilever at a ramping velocity of 0.5 µm s^{-1} to the microgel bead until a predefined deflection was reached. The trigger deflection was chosen so that the indentation depth accounted for 5% of the microgel radius. Typical loading forces ranged between ≈ 1 − 15 nN, dependent on the indenter geometry. For some experiment series, either the indentation depth (1 − 10 % equivalent to ≈ 150 nm − 1.5 µm) or the ramping velocity (≈ 100 nm s^{-1} − 15 µm s^{-1}) was varied to study their influence on the determined Young's moduli systematically. The other parameter remained constant at the standard conditions of 5% indentation depth or 0.5 µm s^{-1}, respectively. For an in-depth study of the centering, 16 × 16 force vs. distance curves were acquired on an 8 µm × 8 µm sized grid across the center of the microgel bead. The indentation depth was kept at the typical value of 5%, while the ramping velocity of 2 µm s^{-1} was chosen to minimize instrument drift during the force curve acquisition. Before acquiring a set of force curves for a specific indenter/particle combination, we performed a number of force curves to determine an adequate setpoint (slightly higher than required). However, the final indentation depth was set during the data evaluation as the upper limit of the elasticity fit (maximum indentation depth). This approach was feasible as we did not observe any changes neither in the curves nor in the evaluated Young's moduli during multiple subsequent indentation cycles for both microgels. It has been verified that the data was consistent regardless whether starting from low or high indentation depths during the load depth-dependent studies. The inverse optical lever sensitivity (InvOLS) was calibrated for every microgel particle and data set by ramping the cantilever against the substrate next to the microgel on the bare glass surface and evaluating the constant compliance region of the resulting force vs. distance curve. Due

to the nondeformability of the hard glass disc, a linear deflection response with z-piezo movement is achieved.

AFM Data Analysis

AFM raw data was converted to force vs. distance curves by home-written procedures in IGOR Pro (v.8.04, Wavemetrics, Portland, OR, US), which were verified to the results obtained by the commercial software provided by the manufacturer of the instrument (AR v.16.33.234, Asylum Research, Oxford Instruments). The contact point was determined by iterative fitting of the contact model. The elastic properties were determined according to the simplified double contact model (Eqs. 7.11-7.14, Figure 7.1B)[11, 36, 38] and compared to the results obtained using the Hertz model (Eqs. 7.7-7.10, Figure 7.1A).[31] If not stated otherwise, the indentation fit range of the force was chosen to result in an indentation depth of 5% of the particle radius, typically $\approx 700-750$ nm. The Poisson's ratio was fixed at 0.5 for both particle types, which falls in the range commonly used for hydrogels.[17, 51] In the case of PAAm, a value close to 0.5 for the Poisson's ratio has been reported also by other techniques.[52]

AFM Images of Cantilevers

Scanning electron microscopy (SEM) images of AFM cantilevers were acquired at a SEM (Quanta FEG 250, FEI, Hilsboro, USA) after sputter-coating with a 1.0 nm thin layer of platinum. The acceleration voltage was set to 30 kV for the cantilever geometries and 15 kV for close-up images of the cone angle. The working distance was set to 10 mm to acquire SEM images using the ET detector.

Total Internal Reflection Fluorescence Microscopy

FITC-labeled PAAm-*co*-PAPMA particles were immobilized on a WillCodish glass bottom dish (GWST-3522, WillCo Wells B.V., Amsterdam, Netherlands). The glass bottom dish was cleaned with ethanol and dried in a stream of nitrogen. Subsequently, the dish was placed in a plasma cleaner (Zepto, Diener Electronics, Ebhausen, Germany) for 20 min to activate the glass surface. Afterward, 20 µL of the particle suspension was placed on the activated glass surface. 150 µL of PBS were added to prevent drying. After 5 min, the dish was filled with PBS. The contact area of the immobilized particles was imaged using a Leica DMi8 Infinity TIRF microscope (Leica, Wetzlar, Germany) equipped with a DFC9000GT-VSC13730 camera, using an oil immersion objective (HC PL APO 100×/1.47 Oil, Leica Microsystems GmbH, Wetzlar, Germany). The refractive index of the immersion oil was 1.518. A 488 nm laser was used to excite the FITC-labeled

particles. After automatic TIRF angle calibration, images of the immobilized particles were taken with a penetration depth setting of the evanescent wave of 70 nm. The azimuth was adapted manually for every image to optimize the TIRF illumination.

Simulations

We simulate the elastic deformation of hydrogel particles via a finite element approach. For this we used an in-house code based on previous studies [24] The radius of the microgel particle was fixed to 14.5 µm and the Young's modulus to 1 kPa. The Poisson's ratio has been set to 0.48 for numerical reasons. For the force calculation via a finite element approach, the particle was split into 108,810 small tetrahedrons of approximately equal size by the Gmsh algorithm.[53] Assuming the tetrahedrons are small enough, the macroscopic stress resulting from the particle's deformation can be modeled as an individual stress tensor $\underline{\sigma}$ (underline denotes a tensor) for each tetrahedron, which is constant across the tetrahedron's volume. This stress can now be calculated from the well-defined deformation of its tetrahedron. For the implementation, we use the Neo-Hookean model strain energy U[24]

$$U = \frac{\mu}{2}(I-3) + \frac{\kappa}{2}(J-1)^2 \tag{7.1}$$

where $I = \mathrm{Tr}(F^T F)$ and $J = \det(F)$ are derived from the gradient deformation tensor F.[54] The moduli μ and κ are related to the elastic modulus E and the Poisson's ratio ν via

$$\mu = \frac{E}{2(1+\nu)} \tag{7.2}$$

$$\kappa = \frac{E}{3(1+2\nu)} \tag{7.3}$$

The Poisson's ratio is set to 0.48 for all simulations as higher values make the problem numerically stiff and lead to numerical instability and long simulation times. For an elastic stress tensor $\underline{\sigma}$, the force F acting on each surface triangle of the tetrahedron can be written as

$$\vec{F} = A\underline{\sigma}\hat{n} \tag{7.4}$$

with A being the area of the triangle and $\hat{n}$ being its normal vector, with the hat indicating that it is a normalized vector of length 1. A third of this force is distributed to each vertex in the triangle. Knowing the force of every vertex in the particle, its trajectory can be calculated using damped classical dynamics. The force was recalculated every time-step. For the point movement in our damped classical dynamics algorithm, we used a Velocity-Verlet algorithm [55] with an additional dampening parameter ξ for

stability. It should be noted that these dampened dynamics do not intend to model the physical trajectory that the vertices take but do lead to the correct steady state of minimal energy, which is sufficient for modeling our experiments. Indenters were modeled using exponential potentials of appropriate shape. Since such potentials are not infinitely steep, they may lead to the simulations slightly overestimating the deformation. The force from the indenter acting on each vertex in the particle was calculated from the potential and added to the force caused by the elastic deformation. For adhesive substrates, a LennardJones potential was used to model adhesion instead of the exponential potential at the substrate location.

$$V(r) = 4\epsilon\left[\left(\frac{\sigma}{r}\right)^{12} - \left(\frac{\sigma}{r}\right)^{6}\right] \tag{7.5}$$

Here, σ is chosen so that the minimum of the potential is $1/5$ of the particle radius from the wall. Adhesion strength is modeled by the size of the prefactor ϵ. Because adhesion is a surface effect, a numeric surface integral of the force density on the surface triangles of the particle is performed and distributed to the points instead of evaluating the force at each point of the particle as done for the indenter. From the adhesion strength and the particle parameters, a dimensionless number Λ arises that can be used to quantify the adhesive strength independent of the specific particle parameters. Λ is the control parameter for our simulations and can be calculated as follows

$$\Lambda = \frac{\epsilon}{ER_{\text{part}}} \tag{7.6}$$

with the Young's modulus E and the microgel radius E_{part}. Appropriate values of Λ were determined by matching the adhesion radius, i.e., the radius of the contact area between the surface and the adhered particle, in experiments with the adhesion radius in simulations (cf. Figures 7.8 and 7.9A).

7.3 Theory

7.3.1 Contact Mechanics of the Indentation in Soft Microgels on a Planar Substrate.

The simplest continuum model for contact mechanics to describe the contact between two elastic bodies (here, the indenter and the microgel particle) dates back to the work of Heinrich Hertz in 1882.[31] He assumed both bodies were an infinite, homogeneous continuum and showed no interaction beyond elastic deformation like friction or adhesion. Additionally, the deformation is considered sufficiently small compared to the radii of the interacting bodies to fulfill a linear stress-strain relation. Then, the deformation δ and the force F are related by the reduced radius R_{12}, the reduced Young's modulus E_{12}, and the Poisson's ratio of the indenter and particle ν_1 and ν_1, respectively.

$$\delta = \left[\frac{3}{4}\frac{F}{E_{12}\sqrt{R_{12}}}\right]^{\frac{2}{3}} \Leftrightarrow F = \frac{4}{3}\sqrt{R_{12}}E_{12}\delta^{\frac{3}{2}} \tag{7.7}$$

$$\text{with}: \frac{1}{R_{12}} = \frac{1}{R_1} + \frac{1}{R_2} \text{ and } \frac{1}{E_{12}} = \frac{1-\nu_1^2}{E_1} + \frac{1-\nu_2^2}{E_2} \tag{7.8}$$

Considering that the indenter material is infinitely rigid compared to the sample ($E_1 \gg E_2$), the contribution of the indenter elasticity is negligible. Hence, the relation is simplified to

$$\delta = \left[\frac{3}{4}\frac{F(1-\nu_2^2)}{E_2\sqrt{R_{12}}}\right]^{\frac{2}{3}} \Leftrightarrow F = \frac{4}{3}\sqrt{R_{12}}\frac{E_2}{1-\nu_2^2}\delta^{\frac{3}{2}} \tag{7.9}$$

for a spherical indenter indenting a spherical microgel particle (Figure 7.1A-I). In the case of a planar surface deforming an elastic half-sphere (Figure 7.1A-II), the reduced radius R_{12} equals the sample radius R_2.

A similar relation between force and deformation can be stated for a rigid conical indenter (Figure 7.1A-III).[56]

$$\delta = \left[\frac{\pi}{2}\frac{F(1-\nu_2^2)}{E_2\tan\theta}\right]^{\frac{1}{2}} \Leftrightarrow F = \frac{2}{\pi}\frac{E_2}{1-\nu_2^2}\tan\theta\,\delta^2 \tag{7.10}$$

In this case, the cone half-angle θ of the indenter defines the interaction geometry. Figure 7.1A sketches the indentation described by the Hertz model for the three types of indenters mentioned above.

Spherical microgel particles are typically immobilized on a substrate for nanoindentation. Consequently, the assumption of an elastic half-sphere becomes insufficient. When the indenter exerts a force F_{ind} onto an elastic sphere, a counterforce F_{sub} acts from the substrate to the bottom half of the microgel (cf. Figure 7.1B). Hence, a double contact model should be used to describe the contact elastic interaction.[11, 36, 38]

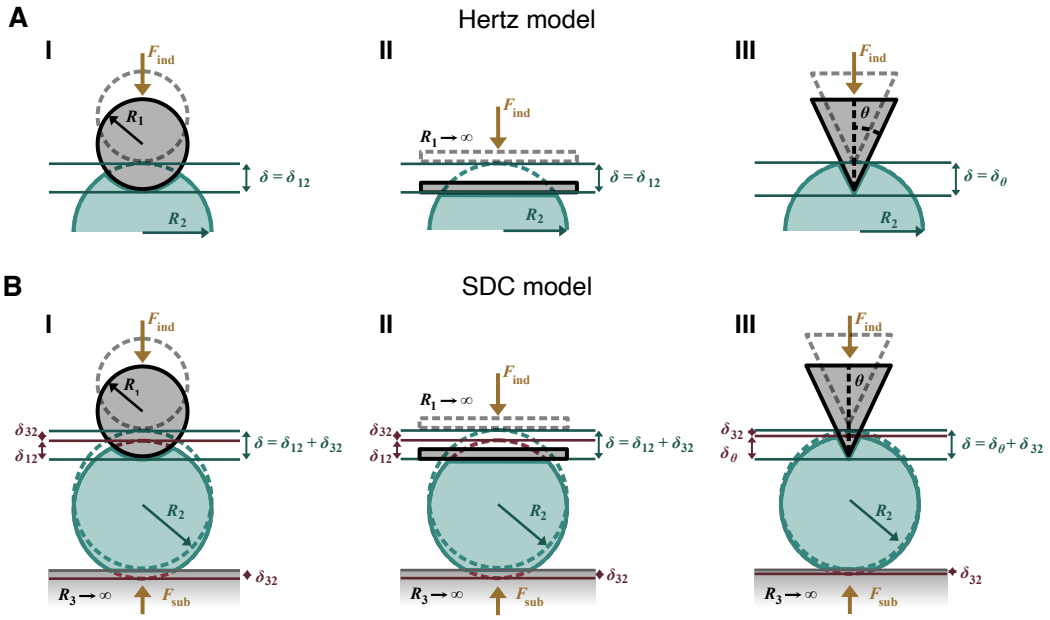

Figure 7.1. Schematic of the contact models describing the nanoindentation of microgel particles using three different indenter geometries: **I** sphere, **II** plane, and **III** cone. **A** The simple Hertz model describes the indentation of the indenter into the soft hydrogel particle. The deformation generated by the force applied to the indenter is limited to the indenter–sample contact. **B** The SDC model accounts for the deformation at the tip-sample interface and the force exerted on the microgel by the substrate when the tip indents the sample.

The simplified double contact model (SDC model) assumes that both deformations – at the indenter microgel contact δ_{12} for the sphere or δ_θ for the cone, and δ_{32} at the contact of the microgel with substrate – are independent and forces only act within the respective half-sphere. Hence, the total deformation δ is given by the sum of both half spheres (Eqs. 7.11-7.14). Accordingly, the deformation force relation for a sphere indenting a microgel on a planar substrate is expressed by:

$$\delta = \delta_{12} + \delta_{32} = \left[\frac{3}{4}\frac{F(1-\nu_2^2)}{E_2\sqrt{R_{12}}}\right]^{\frac{2}{3}} + \left[\frac{3}{4}\frac{F(1-\nu_2^2)}{E_2\sqrt{R_{32}}}\right]^{\frac{2}{3}} \tag{7.11}$$

$$\delta = \delta_{12} + \delta_{32} = \left[\frac{3}{4}\frac{F(1-\nu_2^2)}{E_2\sqrt{R_{12}}}\right]^{\frac{2}{3}} \cdot \frac{1}{k} \Leftrightarrow F = \frac{4}{3}\sqrt{R_{12}}\frac{E_2}{1-\nu_2^2}\delta^{\frac{3}{2}}k^{\frac{3}{2}} \tag{7.12}$$

$$\text{with}: k = \frac{R_{32}^{\frac{1}{3}}}{R_{32}^{\frac{1}{3}} + R_{12}^{\frac{1}{3}}}$$

A correction factor k, which depends on the reduced radii of the microgel particle and the indenter R_{12}, and the microgel and the substrate R_{32} is introduced to account for the deviation from the single Hertzian contact in Eq. 7.9.[38] Hence, it becomes clear that the deviation of the simple Hertzian contact and the SDC model strongly depends on the dimension of the indenter and microgel particle. The deformation in both half spheres is equal for a planar indenter on a planar substrate $\delta_{12} = \delta_{32}$. Thus, the SDC model equation reduces to

$$\delta = \delta_{12} + \delta_{32} = 2\left[\frac{3}{4}\frac{F(1-\nu_2^2)}{E_2\sqrt{R_{12}}}\right]^{\frac{2}{3}} \Leftrightarrow F = \frac{4}{3}\sqrt{R_{12}}\frac{E_2}{1-\nu_2^2}\left(\frac{\delta}{2}\right)^{\frac{3}{2}} \tag{7.13}$$

as $k = 0.5$.[36, 57] The total deformation of a cone indenting into a microgel sphere on a planar substrate is given by the sum of the deformation caused by the cone in the upper particle half δ_θ and the bottom deformation of the particle δ_{32}:[11]

$$\delta = \delta_\theta + \delta_{32} = \left[\frac{\pi}{2}\frac{F(1-\nu_2^2)}{E_2\tan\theta}\right]^{\frac{1}{2}} + \left[\frac{3}{4}\frac{F(1-\nu_2^2)}{E_2\sqrt{R_{12}}}\right]^{\frac{2}{3}} \tag{7.14}$$

In the case of cells, the spherical shape is less well fulfilled.[58] Nevertheless, the assumption of spherical shape is often used due to a lack of alternatives.[59] The SDC model has been applied to cells and cell nuclei on solid substrates.[11, 40] However, the role of cell-substrate adhesion might also play an important role.

7.4 Results

7.4.1 Different Indenter Geometries

Cantilevers with sharp tips and colloidal probes are currently the most commonly used indenter geometries for AFM-based nanoindentation on microgel particles. Discrepancies between data acquired with those two indenter geometries have been reported previously for microgels.[17] Similarly, deviations for the derived Young's moduli in dependence on the indenter geometry have been observed for different cell lines.[11, 29, 42] Here, six different indenter geometries have been utilized to study the influence on the derived Young's moduli. Moreover, due to the large statistical variation of the elastic moduli commonly observed for microgels,[17] we always measured on the same microgel particle

immobilized on the substrate, however, with the different nanoindenter geometries as indicated (cf. Figure 7.2).

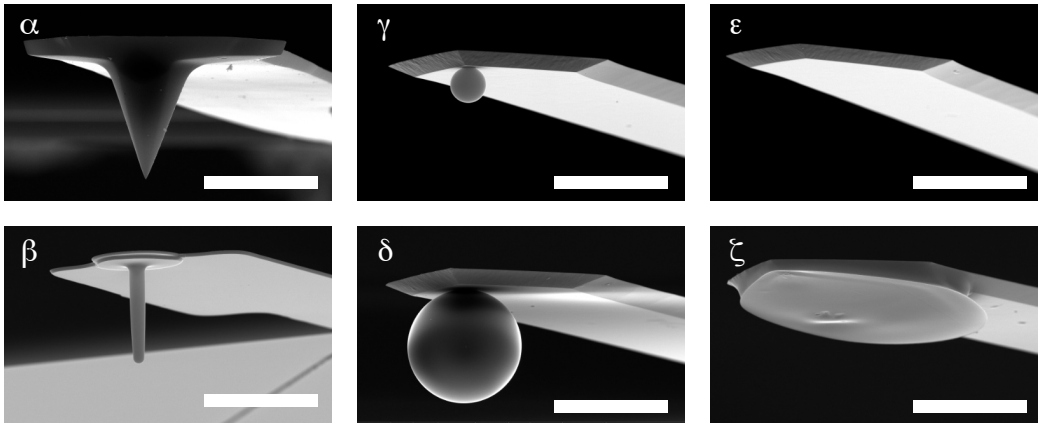

Figure 7.2. SEM images of six AFM cantilever-based nanoindenters: α sharp tip indenter (conical, $\theta = 25\,^{\circ}$, $R < 25$ nm); β a rounded tip (spherical, $R = 0.99$ µm), γ small (spherical, $R = 3.33$ µm) and δ large colloidal probes (spherical, $R = 10.45$ µm); ε tipless (planar, tilt angle 10°) and ζ wedged cantilevers (planar). Scale bars represent 25 µm.

Figure 7.2 shows scanning electron microscopy (SEM) images of the six indenter geometries ($\alpha - \zeta$) used in this study. The selection included (α) a 'classical' conical sharp tip and (β) a cantilever with a rounded tip with a radius of $R \approx 1$ µm. Conical tips (α) are characterized by their opening angle θ; however, they are not infinitely sharp but show typical tip radii of $R < 25$ nm. The rounded tip geometry (β) represents an intermediate between a conical tip and colloidal probes, which typically have radii in the order of several micrometers. Here, two different types of colloidal probes have been used: The first (γ) had radii about 3x smaller ($R \approx 3$ µm) than the latter (δ) with radii of $R \approx 10$ µm. It should be noticed that the radii of δ are approximately in the same order as the microgel particles to be indented. In addition, two types of tipless cantilevers have been used: (ε) a tipless cantilever that will indent under an angle of 10° and (ζ) a wedged cantilever that compensates for this angle and reduces it to about 0°.[49] In terms of the classical indenter terminology, (α) corresponds to a conical indenter, ($\beta - \delta$) to spherical indenters, and (ε, ζ) to a parallel plate. Only for PAAm, all indenter geometries have been used. In the case of POx-HASH, we did not use geometries β and ζ due to availability but not for scientific reasons.

7.4.2 Microgels and Nanoindentation

Two different types of microgel particles have been synthesized for this study by droplet microfluidics. The first microgel system (PAAm) was a fully synthetic cova-

lently crosslinked polyacrylamide, which is well-established in the literature, either for particles [16, 17] or for films [60]. The second microgel system (POx-HASH) has been recently introduced in the framework of inks for biofabrication and consisted of a synthetic ene-functionalized polyoxazoline (POx, a poly(ethyloxazoline-co-butenyloxazoline) with 10% butenyl-functionalization) and the biopolymer hyaluronic acid, which was thiol-functionalized (HASH).[46, 47] Both microgel particle systems have been synthesized via droplet microfluidics, resulting in diameters in the range of 25−30 µm. The diameter of each microgel particle was determined by optical microscopy during the AFM-based nanoindentation procedure (Figure 7.3A and B). We chose these two microgel systems fabricated by chemically different routes to verify that our findings from the nanoindentation experiments were independent of the specific microgel under investigation.

Even though droplet microfluidic fabrication facilitates the production of microgel particles with a narrow size distribution compared to other fabrication techniques,[17] the distribution of Young's moduli can still be broad.[16, 61] Therefore, we indented for a set of selected particles ($n = 5$), each particle with all six (PAAm) or four (POx-HASH) indenter types (cf. Figure 7.3C). This approach, as schematically outlined in Figure 7.3C, allowed us to address the influence of the indenter without having to determine the elastic moduli distribution for several hundreds of particles. It should be noticed that determining the Young's modulus of a statistically reliable number of particles with all six indenter types by nanoindentation would have been impossible timewise considering parameters like maximum indentation velocity and the requirement to center the indenter at the apex.

In a nanoindentation experiment, the probe, i.e., the indenter, is ramped towards the microgel particle while the resulting force response is acquired simultaneously. The indentation continues until a preset trigger value is reached and the motion is reversed.[58] The resulting force vs. distance profiles are then converted to force vs. indentation profiles. Exemplary force vs. indentation approach curves acquired at a constant ramping velocity of 0.5 µm s^{-1} and a maximal indentation depth of ≈ 5% of the particle radius are shown in Figures 3D and E for the different indenter geometries and the two studied microgel systems: PAAm and POx-HASH, respectively. The resulting loading forces to achieve the desired deformation varied from as low as 0.5 nN−1 nN for a conical indenter to 5 nN − 12 nN for the wedged cantilever. In general, the interaction forces increased with the size of the indenter (α to ζ) by up to an order of magnitude. It is important to notice that due to the fact that the indenter is mounted on a lever, the indentation velocity does not remain constant as the lever deflects. Hence, the ramping velocity refers to the velocity of the cantilever holder.

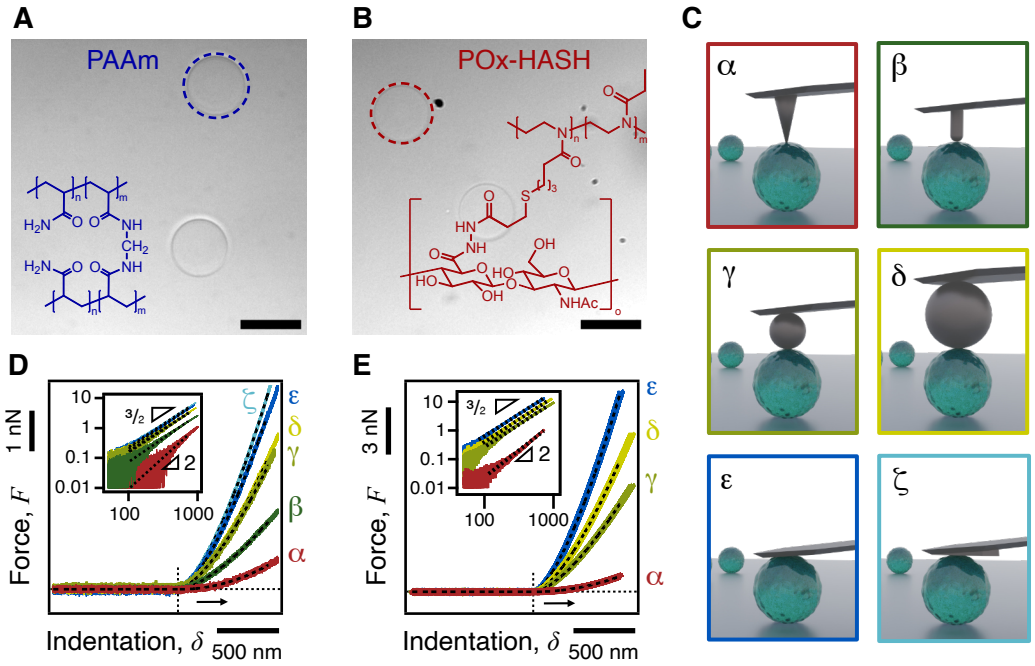

Figure 7.3. Brightfield optical microscopy images of **A** PAAm and **B** POx-HASH microgel particles produced via droplet microfluidics. The scale bars represent 30 µm. **C** Illustration of the experimental setup to indent the same particle with different indenter geometries $\alpha - \zeta$ by AFM: α sharp tip (conical) indenter; β a rounded tip ($R = 0.99$ µm), γ small ($R = 3.33$ µm) and δ large colloidal probes ($R = 10.45$ µm) (spherical); ε tipless and ζ wedged cantilevers (planar). **D**, **E** AFM force vs. indentation curves acquired on the same **D** PAAm or **E** POx-HASH microgel particle using several nanoindenter geometries ($\alpha - \zeta/\alpha$, $\gamma - \varepsilon$). Dashed lines show fits to the Hertz model to determine the Young's modulus. The insets in **D** and **E** depict a logarithmic representation of the force vs. indentation curves, which follow the expected power law coefficients of $F \propto \delta^2$ for a conical indenter (α); $F \propto \delta^{\frac{3}{2}}$ for spherical interaction ($\beta - \delta$) and planar compression ($\varepsilon - \zeta$).

The dashed lines in Figures 7.3D and E result from fitting the force vs. indentation profiles to the Hertz model and the different indenter geometries. Rearranging Eq. 7.9 and 7.10 shows that the force F should scale with the deformation δ by $F \propto \delta^{\frac{3}{2}}$ for spherical indenters, while for a conical indenter, one expects $F \propto \delta^2$. We extracted the corresponding power laws from the slopes in the logarithmic representation of the force vs. indentation curves shown in the insets of Figures 7.3D and E. The resulting power law coefficients have been compiled in Tables 7.1 and 7.2. The good correspondence between the theoretically expected values and the values obtained from the fits corroborates the validity of the assumed indenter geometries, also for the case of the conical indenter.

Table 7.1. Theoretical and fitted power law coefficients for the six indenter types ($\alpha - \zeta$) according to the Hertz model for a PAAm microgel particle.

indenter type		**sharp tip** α	**round tip** β	**small CP** γ	**large CP** δ	**tipless** ε	**wedge** ζ
geometry		cone	sphere	sphere	sphere	planar	planar
power law	theory	2.00	1.50	1.50	1.50	1.50	1.50
coefficient	fit	2.09	1.58	1.50	1.50	1.54	1.53

Table 7.2. Theoretical and fitted power law coefficients for the four indenter types (α, $\gamma - \varepsilon$) according to the Hertz model for a POx-HASH microgel particle.

indenter type		**sharp tip** α	**small CP** γ	**large CP** δ	**tipless** ε
geometry		cone	sphere	sphere	planar
power law	theory	2.00	1.50	1.50	1.50
coefficient	fit	1.80	1.56	1.56	1.54

The resulting Young's moduli for sets of five PAAm and five POx-HASH microgel particles were determined according to the indentation data acquired with the different indenters (cf. Figure 7.4). The particle indices indicate the five particles under investigation per microgel batch. Approximately 50 force vs. indentation curves acquired at the apex of the particle were evaluated for each data particle, and the error bars in Figure 7.4 represent one standard deviation of the mean. Here, we compared two contact models, namely the simple Hertz model [31] that is still widely used (cf. Figure 7.4A-I and 7.4B-I) and the simplified double contact model (SDC model, cf. Figure 7.4A-II and 7.4B-II) [11, 36, 38]. These Young's moduli based on the simple Hertz model and the SDC model have been contrasted in Figure 7.4. Please note that the fit quality and resulting power law dependencies are identical for indenter geometries $\alpha - \zeta$, and deviations are minimal for α (cf. Figure 7.10) for the Hertz and SDC model. Deviations in the Young's modulus arise from the different pre-factors for $\alpha - \zeta$ in Eq. 7.12, 7.14.

It is evident in Figure 7.4 that the Young's moduli determined in the framework of the Hertz model are significantly lower than for the SDC model, which was observed for both types of microgels. This difference has been expected as the indentation in the former case is completely attributed to the indentation of the probe. In contrast, in the latter case, the particle is also compressed at the contact with the planar substrate. This effect is also supposed to be more pronounced for large indenter probes, as observed here. The simple Hertz model significantly underestimates the Young's modulus of microgels at an

increasing percentage up to 64.5% compared to the SDC model when the radius of the indenter is increased to infinity.[38]

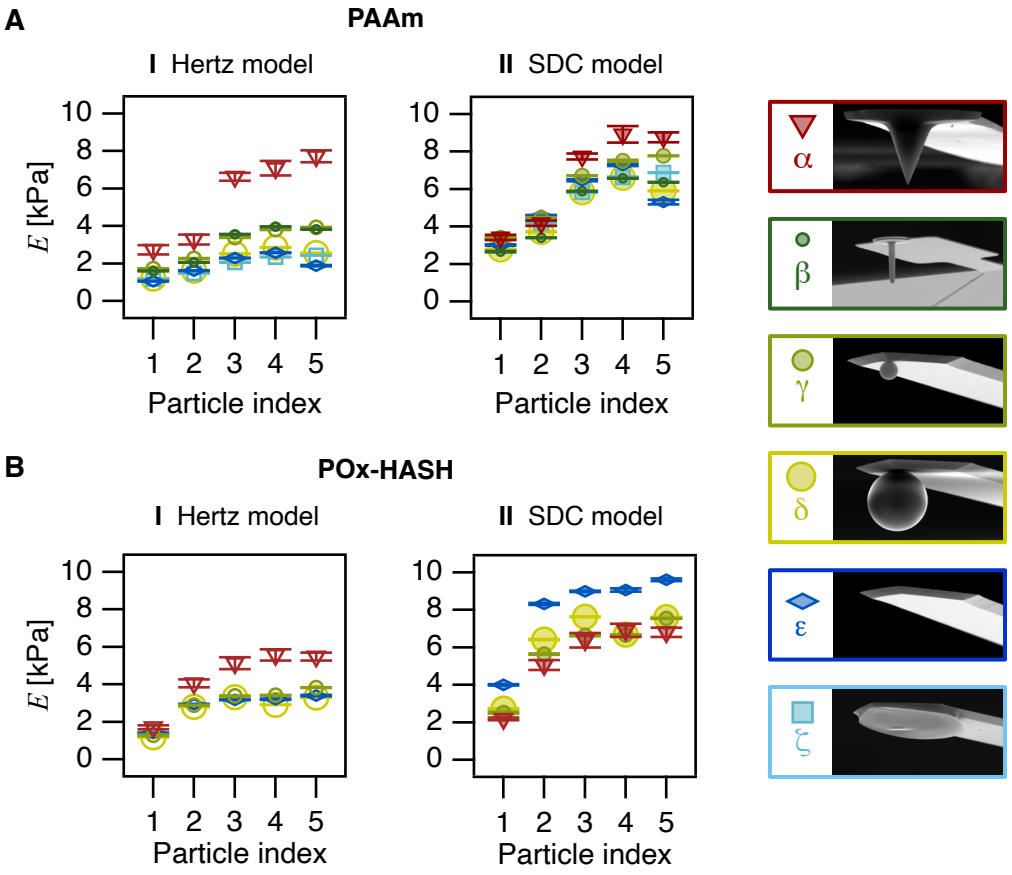

Figure 7.4. Young's modulus of **A** five PAAM and **B** five POx-HASH microgel particles, each characterized using α a sharp tip cantilever, β a rounded tip bio cantilever, γ a small and δ a large colloidal probe, as well as ε a tipless and ζ a wedged cantilever. **I** The Young's modulus was fitted according to the Hertz model [31], which considers only deformation at the contact of the microgel and the indenter (Figure 7.1A, Eq. 7.9-7.10). **II** The Young's modulus was fitted using the simplified double contact model (SDC model) [11, 36, 38], which takes the deformation of the microgel at the contact with the indenter and the contact with the substrate into account (Figure 7.1B, Eq. 7.12-7.14). The arbitrary particle index refers to individual particle from the respective microgel batch and has been arranged according to increasing Young's moduli using the small colloidal probe (γ).

Comparing the data of both models and the microgel type shows that the discrepancy in the calculated moduli for the various indenter types is significantly larger for the Hertz model. Nevertheless, some of the six indenter geometries still show different Young's moduli despite using the SDC model: The conical sharp tip indenter α and the tipless cantilever ε (POx-HASH microgel).

The conical sharp tip indenter plays a special role as it follows another power law and indents on a length scale substantially lower than the other indenters. Its cone half-angle θ is the geometric parameter relevant for the elasticity determination. Due to the nanometer dimensions of the apex, the cone angle and exact tip shape are subject to large errors, even after characterization using SEM (cf. Figure 7.11). We measured the half-angle of the sharp tip cantilever from SEM images over the relevant distance from its apex, which in our experiments is the maximum indentation depth of ≈ 700 nm. We determined this angle to be $\theta \approx 25°$ (cf. Figure 7.11A). The tip shape is rounded near the apex and significantly deviates from an ideal cone. Due to these uncertainties in the determination of the tip shape, the error for Young's moduli can be up to ±10%, as shown in the supporting information (cf. Figure 7.11B). However, these errors are caused only by the inaccuracy of the cone angle determination, while the impact of the rounded tip ($R \approx 25-30$ nm) at its very end has not been accounted for. Hence, the real error caused by the tip shape is expected to be even higher. While there have been approaches to account for alterations of the tip shape at its apex in the form of blunted cone or pyramid models[30, 62, 63], these approaches are not feasible for soft hydrogel networks. The associated length scales are similar to the local swollen polymeric network. Consequently, the conical indenter shape in general, along with its poor shape definition, is the most plausible cause for the large deviation of elastic moduli in Figure 7.4.

In the following, we will systematically exclude several other parameters that could potentially influence the observed deviation of the Young's moduli for the different indentation geometries, such as the influence of indentation depth and ramping velocity and the influence of fine alignment of the indenter on the apex. However, first, we determined how much the Young's moduli varied for respective batches of microgel particles prepared by microfluidics.

7.4.3 Distribution of Particle Size and Young's Moduli During Synthesis

In Figure 7.4, the sets of microgel particles were sorted according to their Young's modulus as determined using a small colloidal probe indenter (γ). However, the elastic moduli vary significantly between the different particles for both types of microgels. Hence, we sampled about 25 particles of each type by indentation using a small colloidal probe indenter (γ). Their Young's modulus was calculated using the SDC model to estimate the elastic modulus distribution for both microgel batches. Figure 7.5 depicts a scatter plot of Young's moduli E, the particle radius R, and the respective distributions of either parameter. All data sets have also been evaluated using the Hertz model, and

a plot contrasting the data obtained by the SDC model and Hertz model is available (Figure 7.12).

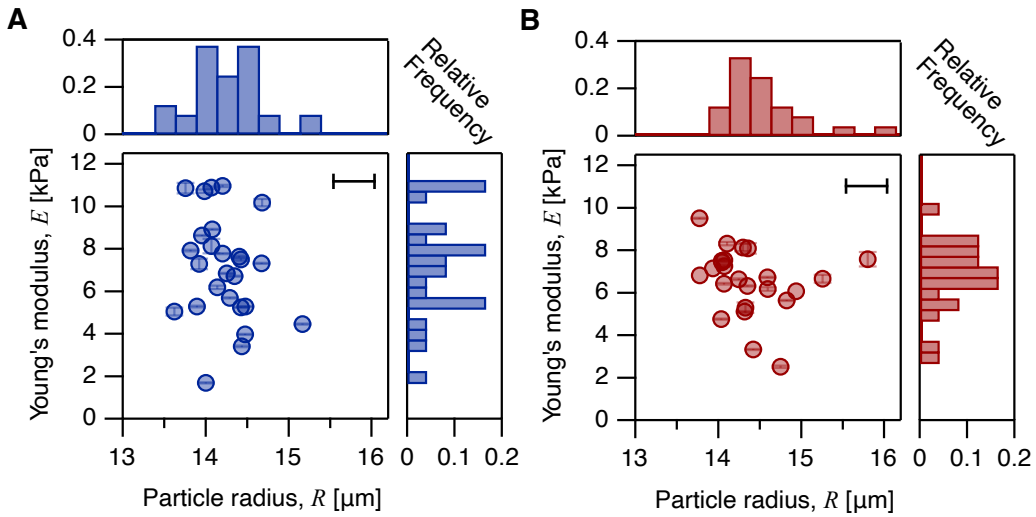

Figure 7.5. Scatter plot of Young's modulus E vs. particle radius R for **A** PAAm and **B** POx-HASH microgels as evaluated using the SDC model. Histograms depict the distribution of the respective moduli and radii. Error bars represent the standard deviation of the mean elasticity determined from 50 curves per particle. The accuracy of the particle radius determination from optical microscopy is estimated in the upper right corner of the plots.

Broad distributions of elasticity in the cell-relevant sub-10 kPa regime were observed for PAAm with 6.5 ± 1.6 kPa and 7.1 ± 2.5 kPa for POx-HASH, respectively. These results underline, on the one hand, why we chose to study the impact of the indenter geometry on individual particles and thereby exclude impacts of the elasticity distribution. On the other hand, the importance of studying a statistically significant number of microgel particles is evident.

7.4.4 Influence of Indentation Velocity and Depth

It is well known that both the indentation depth and the ramping velocity influence the derived Young's moduli of hydrogels, as demonstrated recently for ones made of PAAm.[60, 64] Therefore, we varied the ramping velocity in the range of 0.1 µm s^{-1} to maximally 15 µm s^{-1} while keeping the indentation depth constant at 5% of the particle radius (cf. Figure 7.6A). Moreover, we varied the indentation depth between 1% and 10% of the particle radius while keeping the ramping velocity constant at 0.5 µm s^{-1} (cf. Figure 7.6B). Both series of experiments have been carried out using small colloidal probes (γ, $R = 3.3$ µm) as indenters.

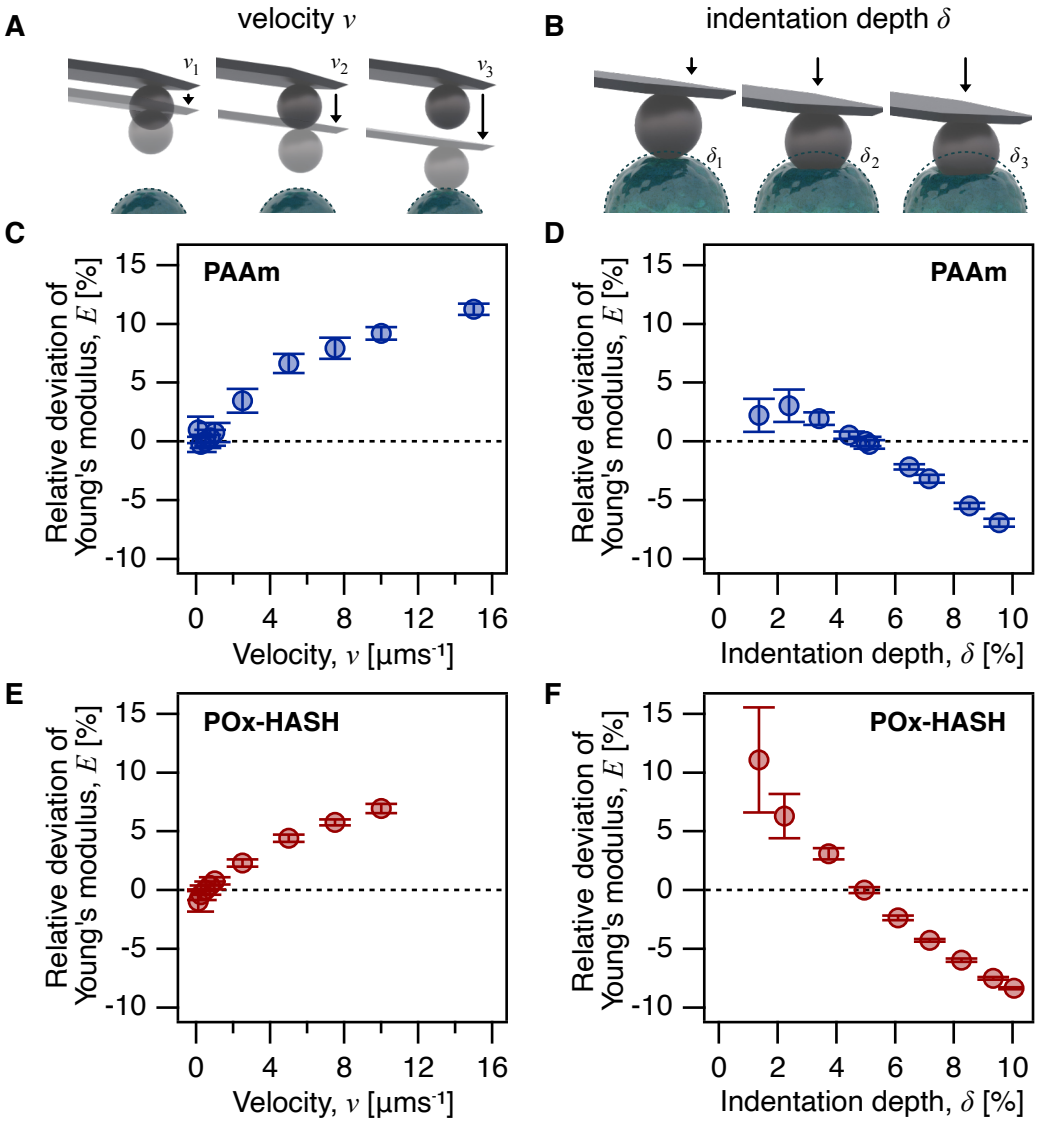

Figure 7.6. The influence of the ramping velocity v and the indentation depth δ on the resulting Young's modulus was studied. **A** and **B** Schematic illustration of the measurement parameters under investigation. The ramping velocity was varied between 0.1 µm s^{-1} and maximally 15 µm s^{-1}, and the indentation depth ranged from 1% to 10% with respect to the particle radius. Data was acquired with a small colloidal probe indenter (γ) and evaluated using the SDC model for **C**, **D** PAAm, and **E**, **F** POx-HASH microgel particles. The relative deviation of the Young's modulus is displayed with respect to the standard values used throughout this work: a ramping velocity of 0.5 µm s^{-1} and an indentation depth of 5% of the particle radius. Error bars describe ± one standard deviation of the mean from 15-50 curves.

The resulting data were evaluated using the SDC model and are summarized in Figure 7.6 as a relative deviation concerning the standard parameters we chose for our experiments, i.e., 0.5 µm s^{-1} and 5% indentation depth, respectively. Error bars represent ± one standard deviation from 25-50 curves, 15 curves for the lowest ramping velocity of

0.1 µm s^{-1} on one particle. Data for additional particles are shown in the Supporting Information (cf. Figure 7.13).

The apparent stiffening at high tip velocities was observed for PAAm as well as for POx-HASH (cf. Figure 7.6C and E) and is commonly reported for hydrogels.[60, 64] For both systems, the apparent stiffening is accompanied by a hysteresis between the approach and retract in the contact regime of the force curves. Representative force vs. indentation curves at various ramping velocities are presented in the supporting information (Figures 7.15 and 7.16). By contrast, at ramping velocities < 1 µm s^{-1}, there is no significant difference between the approach and retraction of the cantilever, which means that the material relaxation is faster than the indenter movement, and the force response of the microgel can be considered fully elastic (Figure 7.15A-E and Figure 7.16A-E). The data shown in Figures 7.4 and 7.5 were acquired at 0.5 µm s^{-1} and thus fall clearly in the elastic regimes of both microgels.

The indentation depth represents another critical parameter in nanoindentation experiments. As an approximation, the indentation depth should not exceed 10% of the thickness of thin films.[34] For the following experiments, we varied the indentation depth in the range of $\approx 1\% - 10\%$ of the particle radius. Exemplary force curves are presented with the respective fits to the SDC model in the supporting information (cf. Figure 7.17 and 7.18). For both microgels, the Young's moduli decreased with increasing indentation depth (cf. Figure 7.6D and F). This behavior is in stark contrast to thin films, where an increasing contribution of the substrate with increasing indentation depth is commonly reported.[32, 34] One possible explanation could be an internal material gradient due to crosslinking from the outside to the inside during the microfluidic fabrication.[29] For low indentation depths ($< 2\%$ of the particle radius), the data showed larger scattering, and it was not clear if the microgel interface with protruding polymer segments had been probed. Larger, spherical indenter geometries were supposed to average over surface roughness and heterogeneities. The higher consistency in curve quality and Young's modulus, obtained at a deeper indentation of 5%, provided a reasonable compromise. The effect of ramping velocity and indentation depth has been studied only for one indenter type, i.e., the small colloidal probe (cf. Figure 7.2, colloidal probe γ). Larger probes lead to other hydrodynamic limits in terms of ramping velocity, and the interaction would result in a more punch-like interaction geometry. How far the indenter scale affects the average Young's modulus remains an open question.[43]

7.4.5 Position of the Indenter on the Particle

Contact mechanics, either by the Hertzian or SDC model, are based on a contact of the indenter at the apex of the underlying particle. As AFM measures only the vertical force

component, any misalignment will lead to errors. It should be noticed that the coarse alignment is limited by the optical resolution of the experimental setup, which is in the order of $1-2$ µm. Coarse alignment was further complicated by the difference in height between the indenter and particle before starting the force vs. distance cycle. Hence, an AFM-based approach to align the center of the indenter to the apex of the microgel particle has been utilized throughout this work. We acquired an array of force curves, so-called force volume plots, around the optically identified region for the apex of the microgel. Evaluation of the height signal at the trigger point allowed the creation of a height map of the particle apex. Such a height map acquired on a PAAm microgel particle and the corresponding cross-sections along the fast and slow scan axis are depicted in Figures 7.7A-C.

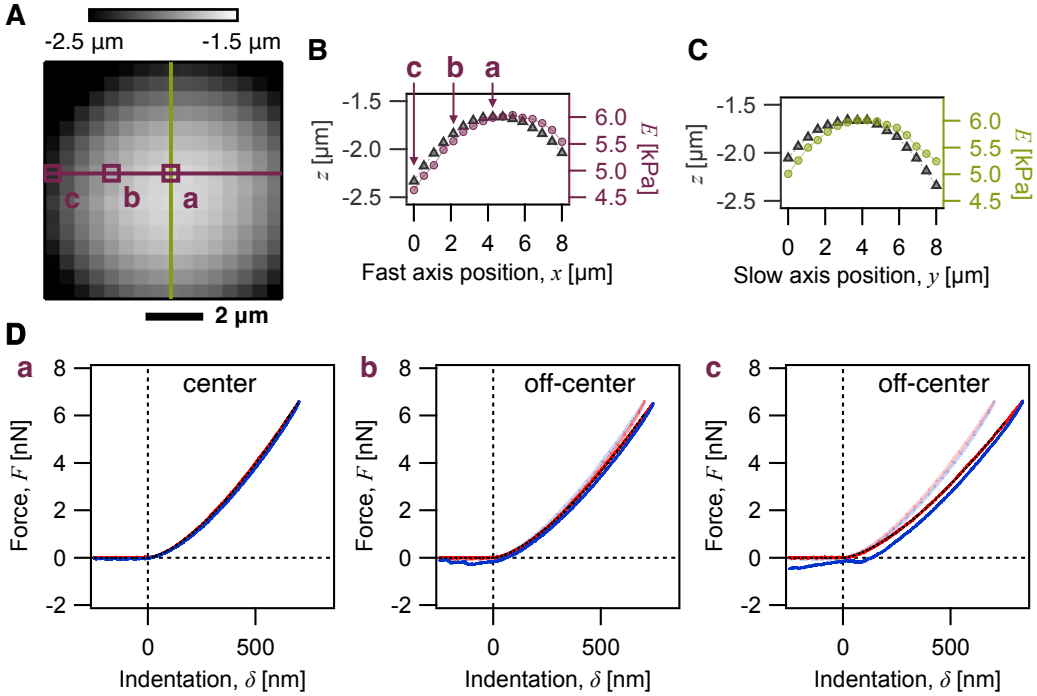

Figure 7.7. Alignment of the small spherical indenter (γ) to the center of the microgel bead apex. A force map consisting of 16 × 16 on an 8 µm × 8 µm area around the microgel apex has been acquired. **A** Height map shows the curvature around the microgel apex. Cross-sections (green and purple lines) of the respective height data and Young's modulus (SDC model) in the direction of **B**, the fast scan-axis (purple), and **C**, the slow scan-axis (green) of the AFM, show that the apparent elasticity decreases with distance from the apex of the microgel. **D** Force vs. indentation curves at the positions **a-c** as marked on the height map and the fast scan axis cross-section. The force curve acquired at the apex (**a**), appended to the plots of the off-center positions **b** and **c**, highlights the deviation.

The thereby achievable positional accuracy has been estimated to be $\lesssim 500$ nm. We fitted a sphere cap to the height map data (cf. Figure 7.19A, Eq. 7.16). The extracted microgel radius of $R = 15.1$ µm agreed reasonably with the radius $R = 14.7$ µm as

determined by optical microscopy (details in Section 7.6.5 and Figure 7.19A). It should be highlighted that the discrepancy between the two radii falls in the realistic resolution limit of the optical microscopy in our experimental setup, including the AFM. Moreover, the sphere cap fit was based on a relatively small number of force curves in a specific area covered by the force volume plots. Hence, the radius was associated with a certain uncertainty from the fitting procedure. Additional effects, such as steric contributions, e.g. protruding polymer segments, could come into play.

Young's moduli at each position on the height map have been determined by fitting the force vs. indentation curves to the SDC model (cf. Figures 7.7B, C). A full elasticity map depicting Young's moduli determined at each position on the grid is shown in the supporting information (cf. Figure 7.19B). A trend of apparent softening moving away from the center has been observed, which is also clearly visible in the cross-sections shown in Figures 7.7B and C. This effect can be rationalized in terms of the slope due to the particle's topography, which leads to a decomposition of the total indentation force.[65] In addition to the apparent softer moduli away from the apex, the quality of the force vs. indentation curves drastically decreases toward the outer parts of the microgel (cf. Figure 7.7D). Slip-off effects, visible in non-monotonous force curves, increased.

For all experiments conducted with indenters ($\alpha - \delta$), the particle's apex was located by a height map, and the indenter was positioned there using the point-and-shoot function of the control software. Optical alignment was sufficient for planar indenters (ε, ζ) due to the absence of an indenter curvature. Then, force-indentation curves for elasticity calculation were acquired at the apex of the microgel bead. This procedure was employed throughout this work to ensure precise alignment of the indenter and the microgel particle. We assume that the position accuracy was $\lesssim$ 500nm due to the acquisition of force-volume plots. On this length scale, the deviation of calculated Young's moduli is $< 5\%$ and would be, therefore, most likely not be sufficient to explain the differences observed for the different indenters on the very same particle.

7.4.6 Substrate-mediated Adhesion as Additional Stress During Indentation

The observed variation of the Young's modulus derived for the same particle by different indenter geometries contradicts the basic assumptions of the continuum models used to evaluate the data (cf. Figure 7.4). Hence, another mechanism that has not yet been accounted for must be in action. One possible mechanism would be adhesion between the microgel and the underlying substrate, leading to an additional deformation of the

soft particle in the contact area with the substrate.[66] The deformation of soft hydrogel particles on substrates is well known.[67] It should be noted that the deformation in the contact area is similar to the one encountered in the double contact model of indentation from the top. The importance of adhesion in the double contact model has already been pointed out before.[38]

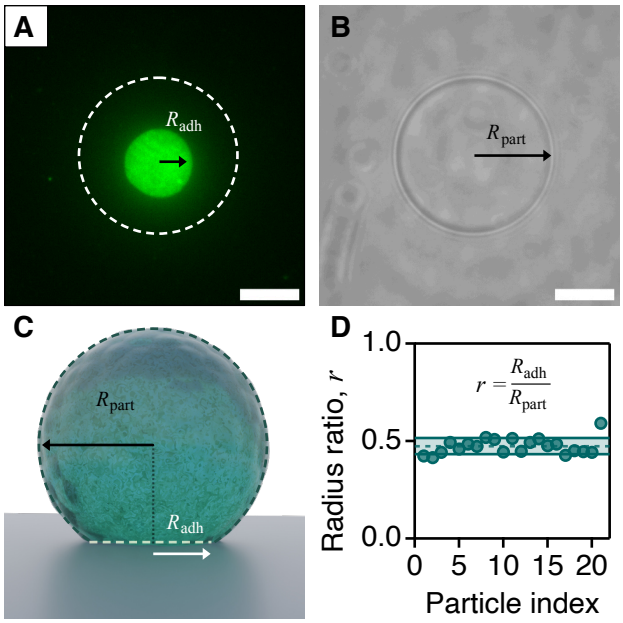

Figure 7.8. Determination of the contact radius of PAAm microgel particles. **A** Adhesion area and radius R_{adh}, as determined by total internal reflection fluorescence (TIRF) microscopy for the particle shown in **B**. Particle radius R_{part} as determined by brightfield microscopy for a fluorescence-labeled PAAm microgel particle. Scale bars represent 10 µm. **C** Schematic visualizing R_{part} and R_{adh}. **D** Distribution of the ratio R_{adh}/R_{part} for about 20 particles. The lines represent the average (dashed) and the standard deviation of the mean (solid), respectively.

To verify that adhesion is present and leads to a significant contact area, we used a technique that allowed us to visualize the contact area by optical microscopy. Total internal reflection fluorescence microscopy (TIRF) is an optical microscopy technique that allowed us to visualize the contact area upon fluorescence excitation in the direct vicinity of the substrate.[68] Consequently, the hydrogels had to be fluorescently labeled, which was done using the PAAm microgel system using FITC.

Figure 7.8A displays a TIRF image of a fluorescently labeled PAAm particle on a freshly cleaned glass substrate, which has also been used for the nanoindentation measurements. In TIRF imaging, an evanescent field excites fluorophores directly on the glass/solution interface, and the bright area in Figure 7.8A corresponds to the contact area, being circular with a radius R_{adh} to a high degree of approximation. Figure 7.8B shows the corresponding brightfield image, which has been used to determine the actual particle

radius R_{part}. Figure 7.8C illustrates the adhesive contact between a microgel particle and the glass substrate with the contact radius R_{adh} and the particle radius R_{part}. We used the ratio $r = R_{\text{adh}}/R_{\text{part}}$ to characterize the adhesive properties of the FITC-labeled PAAm microgels on the glass surface. Evaluating about 20 particles resulted in a value of $r = 0.47 \pm 0.04$. These data are summarized in Figure 7.8D. It should be noted that the fluorescently labeled PAAm is more positively charged than the pure PAAm, as determined by lipid adsorption experiments (data not shown). Hence, we see the value of $r = 0.47$ as the upper limit for the pre-deformation of the PAAm microgels characterized by nanoindentation due to adhesion.

7.4.7 Modeling Adhesion

We performed theoretical simulations to evaluate the effect of adhesion on the pre-deformation of microgel particles. In order to map the adhesive properties in the simulation, we used a simple model based on the dimensionless number Λ defined in equation 7.6 above:

$$\Lambda = \frac{\epsilon}{ER_{\text{part}}} \tag{7.15}$$

Λ is a dimensionless number modeling the ratio between adhesion forces and elastic particle forces. Here, ϵ is the Lennard-Jones potential constant, as defined in equation (7.5) above, which is responsible for adhesion to the substrate. According to our simulations based on the finite element method, the microgel particle deforms even without an external force, as depicted in Figure 7.9A. The adhesive contact area of radius R_{adh} increased as expected with Λ (cf. Figure 7.20). We fitted a power law to determine Λ corresponding to the experimental value $r = 0.47$ as determined by the TIRF data (details in the Supporting Information, Section 7.6.6, Figure 7.20), which resulted in $\Lambda \approx 0.015$. However, it should be highlighted that non-labeled PAAm microgels showed weaker adhesion, leading to smaller Λ values.

7.4.8 Indenter Geometry and Adhesion

After equilibrating the microgels on the adhesive substrates, the deformation using the respective six different indenter geometries ($\alpha - \zeta$) was simulated. An opening angle of 25° for the conical indenter (α), radii of 0.99 µm the rounded tip (β) and 3.3 µm, 10.5 µm for the colloidal probes (γ, δ); and a tilt angle of 10° for the tipless and 0° for the wedged cantilever have been utilized in agreement with the experimental conditions.

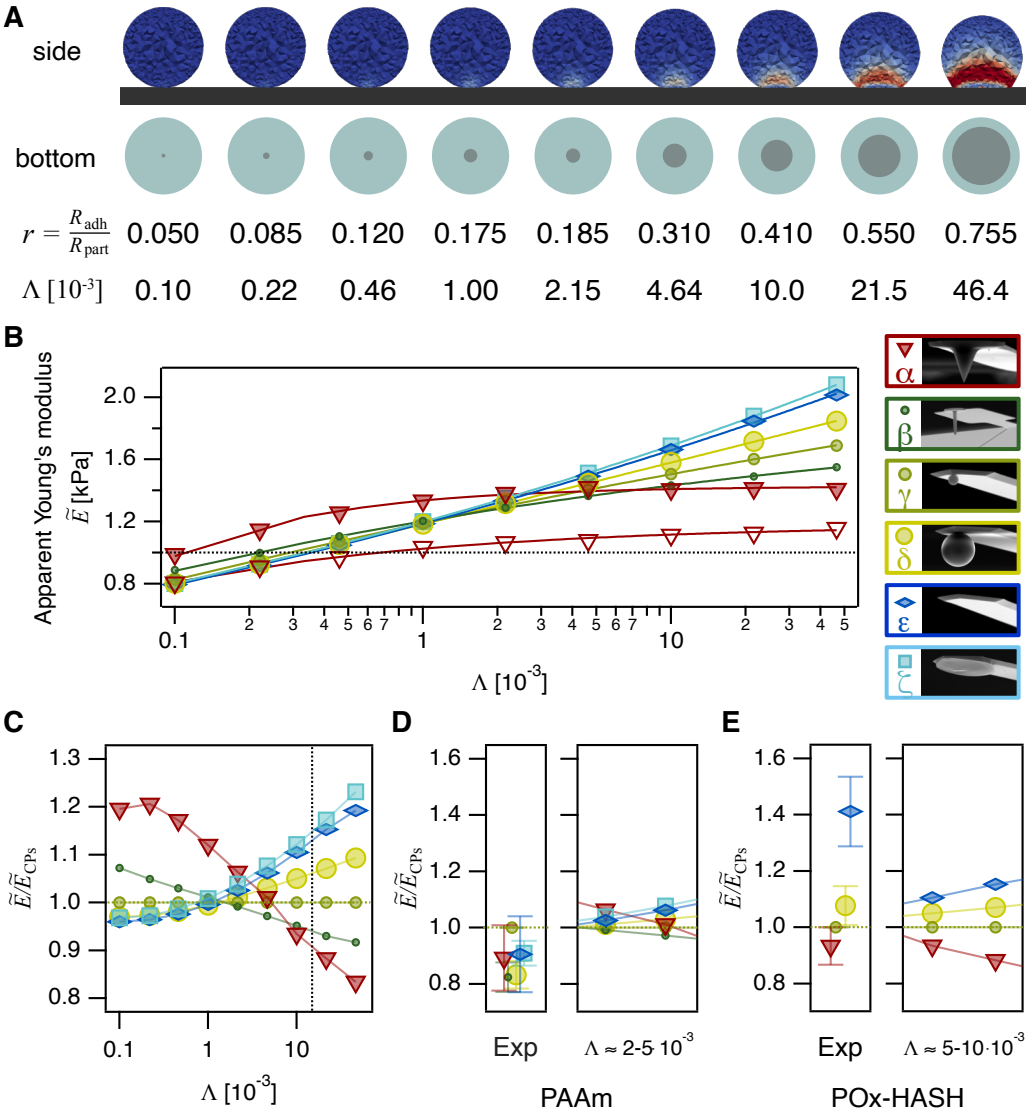

Figure 7.9. **A** Simulation of the pre-stress on the microgels due to the adhesive contact with the substrate (side view). The color scale indicates the stress within the microgel particle due to adhesion. The dimensionless parameter Λ is used to describe the adhesive strength. The resulting adhesive contact area (grey) with respect to the microgel size (blue) is illustrated in a bottom-view perspective. The ratio $r = R_{adh}/R_{part}$ characterizes the area of the adhesive contact. **B** The apparent Young's moduli $\tilde{E}$ as received from the simulation for a particle with a Young's modulus of 1 kPa for indenters $\alpha - \zeta$ depends on Λ. Closed symbols represent the SDC model, open triangles refer to the Hertz data for the conical indenter. **C** Normalization of the apparent Young's modulus from simulation to the small colloidal probe (γ). **D**, **E** Normalized experimental Young's moduli and approximate range of Λ to describe the data from the simulation for **D** PAAm and **E** POx-HASH microgels. Mean values ± one standard deviation of the mean from 5 particles (cf. Figure 7.4) for each indenter geometry are presented.

The force vs. deformation data from the numerical simulations have been fitted to the SDC model similarly to the experimental data. The resulting apparent Young's moduli $\tilde{E}$ from the fits to Eq. 7.12 and Eq. 7.14, respectively, are summarized in Figure 7.9B as

a function of Λ. In the case of the conical indenter (open symbols), the classical Hertz model is shown in addition to the SDC model. The simulated force vs. indentation curves and fits are available in Figures 7.21 and 7.22 in the supporting information. It is evident that depending on the geometry and type of the indenter, the apparent elastic modulus deviated from the Young's modulus, which was set to 1 kPa for the simulation. With stronger adhesion, i.e., higher values of Λ, the deviation between the different indenter geometries became more pronounced, especially for larger geometries, like the large colloidal probe δ and the planar indenters γ, ζ.

The non-linear dependence between apparent elastic moduli and adhesion for the different indenter geometries provides an explanation for the observed deviations in the experimental data for both types of microgels (cf. Figure 7.4). It should be pointed out that the Young's moduli reported in Figure 7.9B are only apparent elastic properties originating from fitting simulated data for particles with a homogeneous 'true' Young's modulus of 1 kPa. However, in the simulation, the elastic properties scale linearly and are, therefore, also valid for the higher elastic modulus of the experimentally studied particles and allow further semi-quantitative analysis: We normalized the apparent Young's moduli from the simulation $\tilde{E}$ to the small colloidal probe data $\tilde{E}_{\mathrm{CPs}}$, i.e., the simulations for geometry γ (cf. Figure 7.9C). Figures 7.9D and E show the same normalization for the experimental data, i.e., $\tilde{E}/\tilde{E}_{\mathrm{CPs}}$. The data reported in Figures 7.9D and E were averaged over all five particles of each type of microgel from Figure 7.4. The separate data for all individual particles are available in the supporting information (Figure 7.23). The normalized apparent Young's moduli $\tilde{E}/\tilde{E}_{\mathrm{CPs}}$ in Figure 7.9D for PAAm microgels are clustered, approximately corresponding to the simulation data for $\Lambda = 2-5\cdot10^{-3}$. By contrast, the data for POx-HASH in Figure 7.9E are more compatible with $\Lambda = 5-10\cdot10^{-3}$. While an accurate quantitative match between simulation and experimental values is not to be expected due to the qualitative nature of our adhesion model and the parameter Λ, there is a good qualitative match for the normalized Young's moduli with respect to the different indenter geometries if one considers the effect of adhesion and utilizes SDC model.

7.5 Conclusions

The simplified double contact model (SDC model) represents a more realistic description of the elastic properties of microgel particles than the classical Hertz model, which is still widely used to quantitatively report Young's moduli as determined by AFM-based nanoindentation. Our study on two different microgel model systems also demonstrates that adhesion plays an important role in the quantitative description by SDC model. Moreover, the pre-stress between particle and substrate due to adhesion provides an explanation for the variation in the elastic moduli as determined by different indenter geometries by means of the SDC model. The microgel particles studied here, prepared by microfluidics, are similar to cells in many aspects, albeit better defined in their physical properties. Nevertheless, our results should also be helpful for the characterization of cells. However, for cells, the incorporation of adhesion in the double contact model will be even more important. We are not aware of such models, and the numerical simulations presented here are not a fully adequate replacement. In the future, the SDC model might also become important to analyze experiments that probe the dynamic nanoindentation of hydrogels,[69, 70] especially for microgel particles.

The long-standing question of the best-suited indenter geometry, which has been discussed extensively in the literature, can be reduced in the framework of the SDC model to more practical aspects. We suggest the following approach: (i) Adhesion effects are less pronounced for small indenter dimensions, such as sharp conical tips, rounded tips, or small colloidal probes. However, the exact geometrical dimension will be less-well traceable for conical indenters, and the indentation depth will be limited for rounded tips. In this respect, small colloidal probes, which allow a sufficient indentation depth without violating the small indentation limitation of the Hertzian contact mechanics, should be the best compromise for practical purposes.

Based on the experimental findings, (ii) we encourage the use of force volume measurements to enhance the alignment precision compared to the optical alignment of the indenter and sample. Thereby, the underestimation of the Young's modulus by off-center data acquisition should be minimized. Moreover, (iii) measurement parameters like the indentation depth and velocity can impact the accuracy and comparability of the reported moduli. The herein-presented values can be helpful as starting points; however, they cannot entirely replace reassessment for the chosen combination of sample and indenter. Finally, (iv) accurately reporting all experimental parameters like indenter and sample radii, indentation depth, and velocity, calibration of instrument sensitivity, and spring constants improves the cross-study comparability of AFM-based elasticity measurements.

Acknowledgements

The authors thank Sebastian Sittl for help with the SEM images of the cantilevers and the Keylab Electron Microscopy of Bavarian Polymer Institute (BPI). Funding by the Deutsche Forschungsgemeinschaft (DFG, German Research Foundation) – Projekt Nummer 326998133-TRR225 (subprojects A08, B03 and B07) is gratefully acknowledged. N.R., S.T., A.S., and T.R. thank the Elite Network Bavaria (ENB) for support within the program 'Macromolecular Science'.

7.6 Supporting Information

7.6.1 Additional Experimental Methods

Fabrication of Wedged Cantilevers

Wedged cantilevers were fabricated after a modified procedure based on Stewart et al.[49] to compensate for the tilt angle (10°) of the cantilever holder. Briefly, a small amount of UV-curing adhesive (≈ 30 pL, NOA63, Norland Products Inc., Jamesburg, NJ, USA) was placed on the tip of the cantilever via micromanipulation using an etched tungsten wire under a dedicated optical microscope (Axio Examiner.D1, Zeiss, Oberkochen, Germany) with a micromanipulator (DC-3K, Märzhäuser, Wetzlar, Germany). The cantilever was mounted on a metal wedge that imitated the cantilever holder, and its mounting angle was 10°. The metal wedge itself was mounted to a metal 90°-angle piece fixed on a microscope glass slide. The glass slide was placed under the optical microscope (Axio Examiner D1, Zeiss, Germany), and the cantilever was focused. A counterpart showing no adhesion to the UV-curing adhesive is needed. For this purpose, a microscope glass slide was cleaned using the modified RCA procedure described in the experimental methods. Subsequently, the substrate was activated in a plasma cleaner (Zepto, Diener Electronics, Ebhausen, Germany) for 10 min. After the activation, the substrate was placed in a desiccator together with a petri dish containing 100 µL 1H,1H,2H,2H-Perfluorooctyldimethylchlorosilane (97%, abcr GmbH, Karlsruhe, Germany). The evacuated desiccator was placed in an oven overnight at 40°C. The silanized substrate was rinsed with ethanol (≥ 99.9%, Merck, Darmstadt, Germany), followed by Milli-Q water, and dried in a stream of nitrogen.

The silanized microscope glass slide was mounted to the micromanipulator (DC-3K, Märzhäuser, Germany), aligned, and driven in contact with the lever. The UV-curing glue formed a wedge between the glass slide and the cantilever. Care was taken that the cantilever remained unbent. The wedge was cured for 90 min through the glass slide with a UV lamp (80% power, Bluepoint-LED Eco, Dr. Hönle AG, Gräfelfing, Germany) equipped with an LED head (365 nm, Dr. Hönle AG, Gilching, Germany) and an Optic 3 lens (Dr. Hönle AG, Gilching, Germany).

Microfluidic Device Fabrication

PAAm particles were synthesized on single-layer PDMS chips. To fabricate the master mold, a 4-inch silicon wafer (CrysTec GmbH Kristalltechnologie, Berlin, Germany) was cleaned with 2-propanol and dried in a stream of nitrogen. SU-8 2015 photoresist was spin-coated onto the wafer at 1000 rpm for 30 s, leading to a layer thickness of 30 µm.

Subsequently, the wafer was soft-baked on a 95°C-hot plate for 4 min. The microfluidic device design was exposed onto the soft-baked wafer using a chrome photomask (JD photo data, Hitchin, UK) and a MJB4 mask aligner (SUSS MicroTec SE, Garching, Germany) for 12 s with a wavelength of 365 nm (lamp intensity: 18.6 mW cm^{-2}). After post-exposure-baking on a 95°C-hot plate for 5 min, the master structures were developed for 3 min in SU-8 developer under gentle agitation. The developed structures were cleaned with 2-propanol, dried in a stream of nitrogen, and hard-baked on a 150°C-hot plate for 15 min.

Sylgard184 elastomer base and curing agent were mixed in a ratio of 10:1 (w/w) and poured on the master mold. The master mold was placed in a desiccator under reduced pressure for 1 h to degas the elastomer mix. After curing at 150°C for 1 h, the PDMS was cut from the master, and holes were punched into the inlet and outlet chambers using a biopsy puncher (diameter 0.75 mm, Micro to Nano BV, Haarlem, Netherlands) for tubing connection. The punched PDMS was cleaned with 2-propanol in an ultrasonic bath for 15 min and dried at 90°C overnight.

Finally, the PDMS microchannels were sealed with microscope glass slides via air plasma activation (power: Hi, equilibration time: 30 s, plasma time: 30s, pressure: 380 mTorr, PDC-32G plasma cleaner, Harrick Plasma, Ithaca, NY, USA) and placed in an oven at 100°C overnight. Besides two inlet and one outlet chamber, the microfluidic device included two perpendicular channels (width: 40 µm) at the cross junction and an orifice (width: 10 µm) supporting the droplet formation.

POx-HASH microgels were synthesized on multi-layer PDMS chips. On those chips, the aqueous phase flowing through a central channel is 3D-focussed at the cross junction by the oil phase flowing in top and bottom channels. 2 To fabricate the master mold, a 4-inch silicon wafer (CrysTec GmbH Kristalltechnologie, Berlin, Germany) was cleaned with 2-propanol and dried in a stream of nitrogen. For the first layer, the SU-8 2050 photoresist was spin-coated onto the wafer with a spin speed of 2500 rpm for 30 s, leading to a layer thickness of 50 µm. Subsequently, the wafer was soft-baked on a 65°C-hot plate for 6 min and a 95°C-hot plate for 18 min. A digital photomask designed in AutoCAD (Autodesk, Inc., USA) was exposed onto the soft-baked wafer using a MicroWriter ML3 (Durham Magneto Optics Ltd., UK) equipped with a 385 nm light source assuming a resist sensitivity of 3000 MJ cm^{-2}. After post-exposure-baking on a 65°C-hot plate for 1 min and a 95°C-hot plate for 5 min, the wafer cooled to room temperature. For the second layer, the SU-8 2050 photoresist was spin-coated onto the first layer again with a spin speed of 2500 rpm for 30 s, leading to a layer thickness of 70 µm. Soft-baking, exposure, and post-exposure-baking were the same as for the first layer. The second layer was aligned on the top layer using the virtual mask alignment function of the MicroWriter. After post-exposure-baking, the master structures were developed for 12

min in SU-8 developer under gentle agitation. The developed structures were cleaned with 2-propanol and dried in a stream of nitrogen.

Sylgard184 elastomer base and curing agent were mixed in a ratio of 10:1 (w/w) and poured on the master mold. The master mold was placed in a desiccator under reduced pressure for 1 h to degas the elastomer mix. After curing at 150°C for 1 h, the PDMS chip halves were cut from the master, and holes were punched into the inlet and outlet chambers of the top halves using a biopsy puncher (diameter: 0.5 mm, Micro to Nano BV, Haarlem, Netherlands) for tubing connection. The chip halves were cleaned with 2-propanol in an ultrasonic bath for 15 min and dried at 90°C overnight.

Finally, the chip halves were bonded together via air plasma activation (power: Hi, equilibration time: 30 s, plasma time: 30 s, pressure: 380 mTorr, PDC-32G plasma cleaner, Harrick Plasma, Ithaca, NY, USA). After activation, 30 µL of Milli-Q water was pipetted onto the bottom half, and both chip halves were aligned under a microscope using special self-locking structures at the sides of each chip. The aligned chips were placed in an oven at 60°C overnight to finish the bonding process.

Besides two oil phase inlets, one aqueous phase inlet, and one outlet chamber, the microfluidic device included an orifice (width: 60 µL) at the cross junction supporting the droplet formation.

7.6.2 Impact of the Half-Angle on the Young's Modulus Determination Using the Conical Indenter

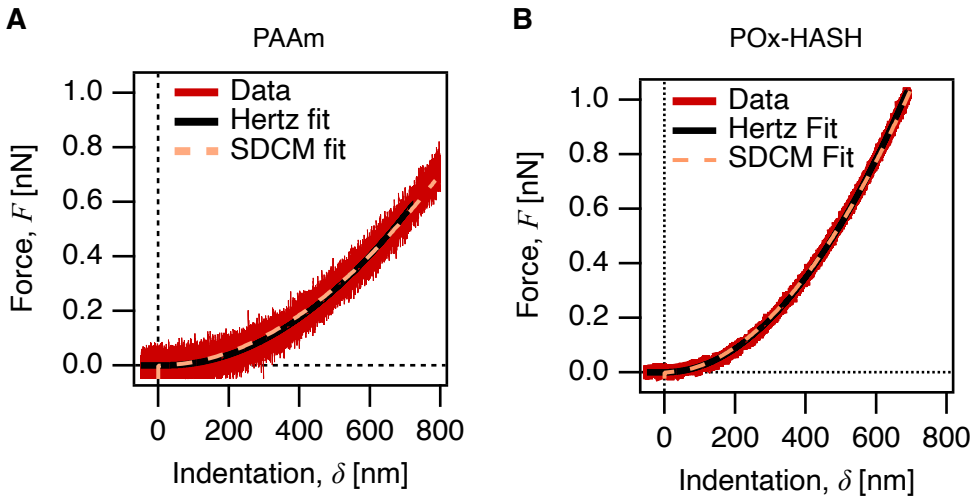

Figure 7.10. Representative force vs. indentation curve acquired with a conical indenter. **A** A PAAm and **B** a POx-HASH microgel particle. Data was fitted according to the SDC model (yellow dashed line) and Hertz model (solid black line) to determine the Young's modulus of the microgel.

In contrast to spherical indenters, which can easily be characterized by the radius R, the geometry of a conical indenter is defined by its half angle θ. Figure 7.11A depicts an SEM image of the sharp tip with a cone angle of $24.5° \pm 2.0°$ employed for the geometry comparison study. The angle was measured at the maximal indentation depth of ≈ 700 nm; however, it differed significantly closer to its apex.[62] The rounded apex (with $R \approx 25 - 30$ nm) also impacts the measurement of the tip angle at ≈ 700 nm, yielding a relatively large error of $\pm 2.0°$. The effect of the inaccuracy of the tip angle determination on the Young's modulus calculation is shown in Figure 7.11B.

The cone half angle input to the elasticity fit was varied between 5° and 45° and significantly impacted the apparent Young's modulus. The shaded area marks the inaccuracy of half-angle determination from the SEM image, and the dashed line marks a cone angle of 24.5°. The effect is more pronounced at smaller tip angles; hence, our tip choice is already in the moderate impact regime. Nevertheless, we observed a deviation of the moduli calculated from the sharp tip indenter data compared to the other indenter geometries on the same particle.

One reason is the finite tip radius, which is $25 - 30$ nm, rather than the infinitely sharp conical shape assumed by the contact model. The curvature of the indenter dominates

the interaction geometry at small indentations or closer to the apex. Hence, the half-angle gets larger, closer to the apex or with decreasing indentation depth, approaching a spherical or even punch-like interaction at very low indentation depths (< 50 nm). However, on these length scales, the surface roughness, i.e., the local structure of the swollen hydrogel network and protruding polymer segments, plays a role.[12]

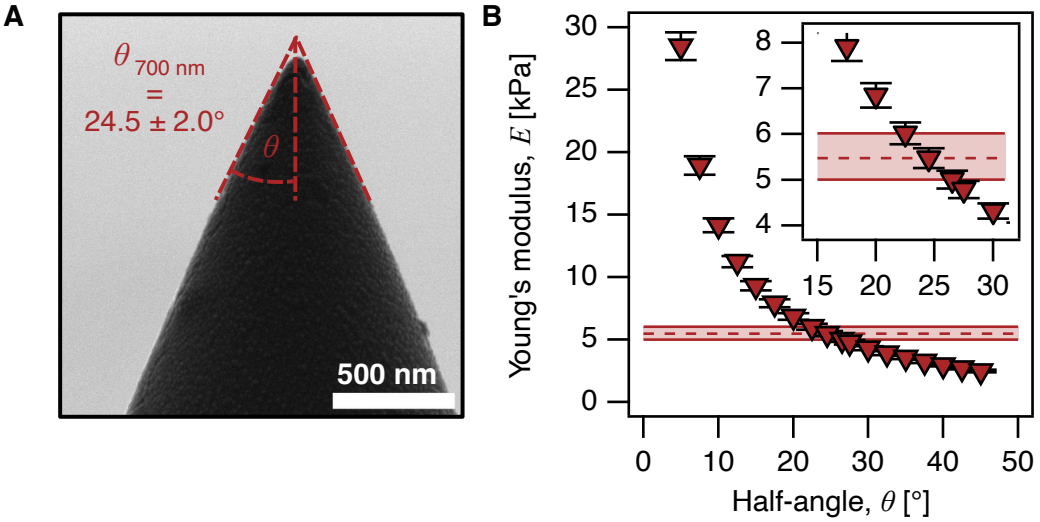

Figure 7.11. Influence of the cone half-angle on the Young's modulus calculation. **A** Close-up SEM image of the conical indenter, which was used to indent the POx-HASH microgel particle, illustrating the half-angle θ of 24.5±2.0° at a maximum indentation depth of 700 nm. **B** Apparent Young's modulus assuming half-angles between 5° and 45°. The inset enlarges the region of interest around the experimental half-angle θ. The shaded area marks the deviation of the Young's modulus with respect to errors from the half-angle determination.

7.6.3 Distribution of Young's Moduli Evaluated with SDC and Hertz Model

In addition to the Young's moduli (SDC model) for PAAm and POx-HASH presented in Figure 7.5, all data has been evaluated using the Hertz model. Hertz moduli have been appended in Figure 7.12.

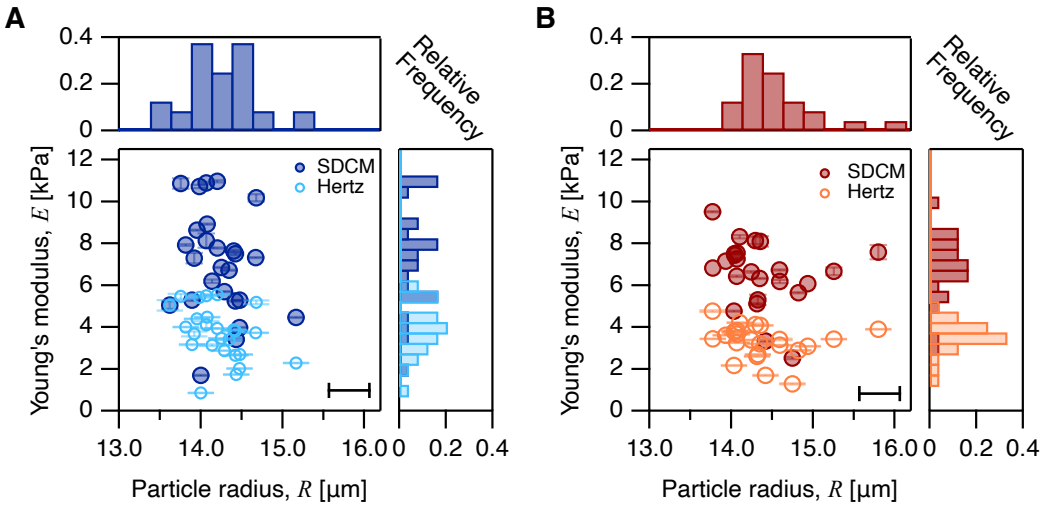

Figure 7.12. Scatter plot of Young's modulus E vs. particle radius R. **A** PAAm and **B** POx-HASH microgels as evaluated using the SDC model and the Hertz model. Data was acquired using a small colloidal probe indenter γ. Histograms depict the distribution of the respective moduli and radii. Error bars represent the standard deviation of the mean elasticity determined from 50 curves per particle. The accuracy of the particle radius determination from optical microscopy is estimated in the bottom right corner of the plots.

7.6.4 Details on the Influence of Ramping Velocity and Indentation Depth on the Young's moduli

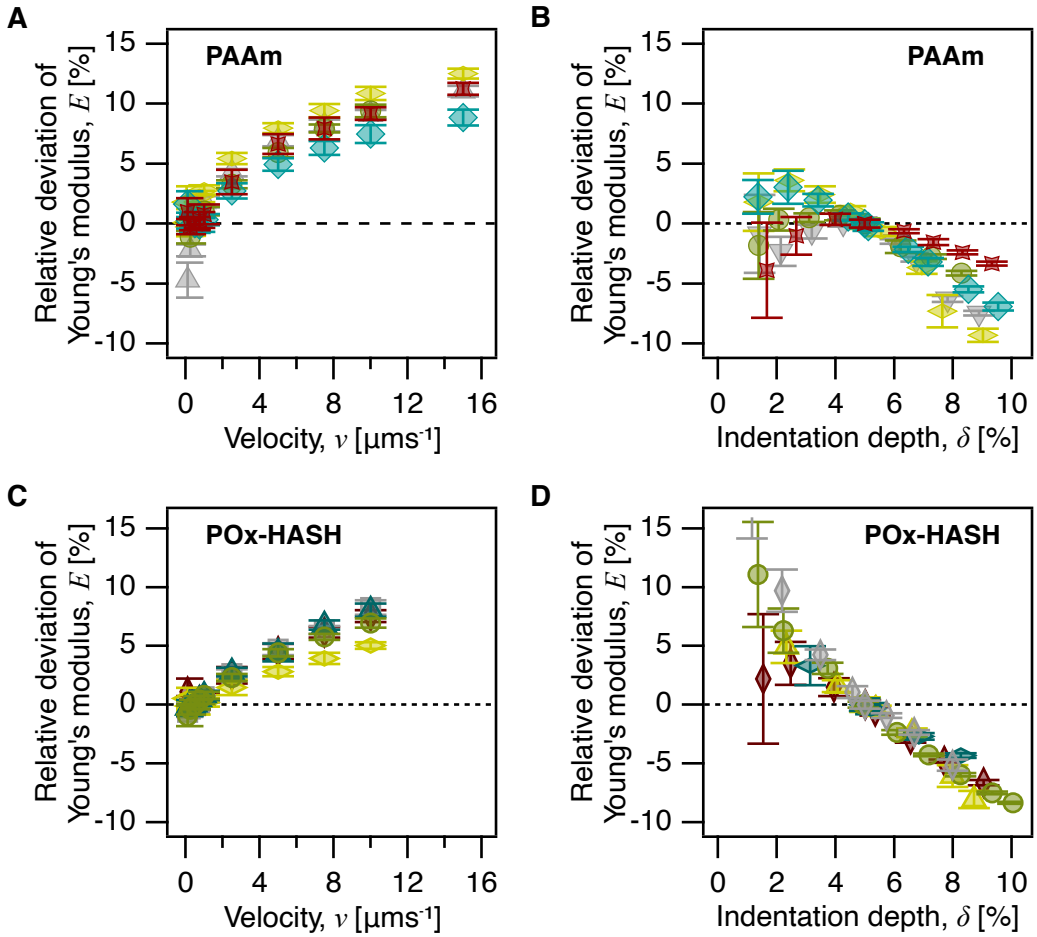

Figure 7.13. Relative deviation of the Young's modulus, depending on the measurement parameters. The relative deviation is consistent for a set of **A**, **B** five PAAm and **C**, **D** five POx-HASH microgel particles. **A**, **C** Ramping velocity v and **B**, **D** the indentation depth δ. Different symbols and colors indicate the different particles under investigation. Data was acquired with a small colloidal probe indenter γ and evaluated using the SDC model.

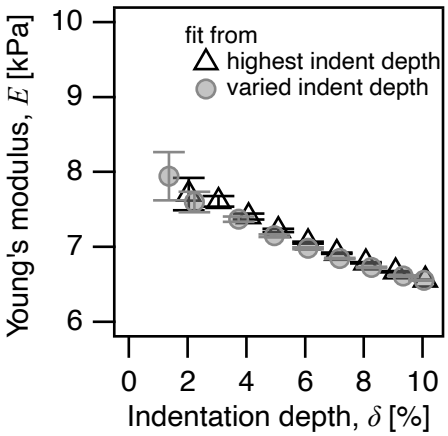

Figure 7.14. Comparison of two methods to determine the indentation depth-dependent behavior on POx-HASH microgel. Data sets with different indentation depths were evaluated (closed symbols). In contrast, the data set with the largest indentation was fit only partially (1.4 – 10%) and is displayed with open symbols.

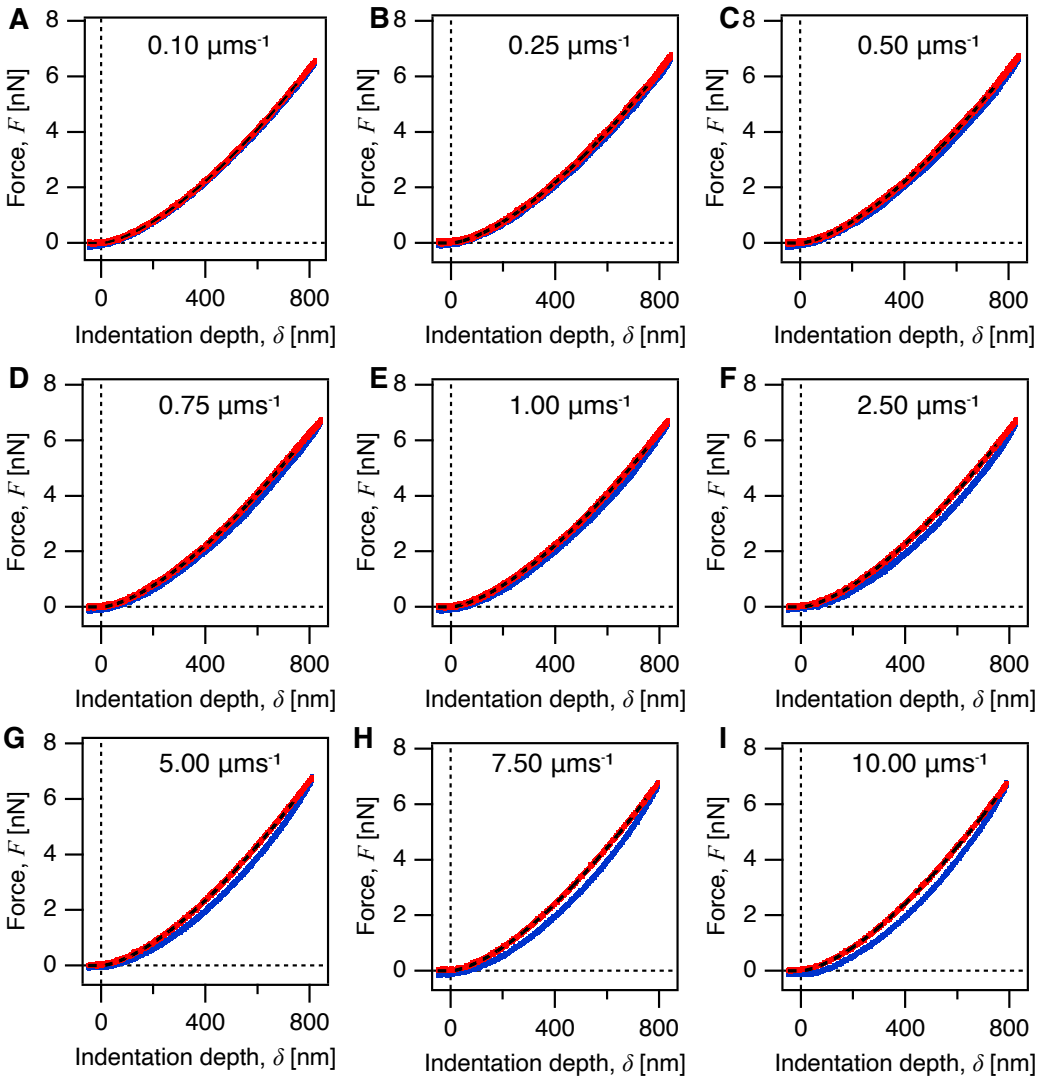

Figure 7.15. Representative force vs. indentation curves on PAAm microgel particles at varied ramping velocities v. Fits are shown in solid black lines. **A** 0.10 µm s^{-1}; **B** 0.25 µm s^{-1}; **C** 0.50 µm s^{-1}; **D** 0.75 µm s^{-1}; **E** 1.00 µm s^{-1}; **F** 2.50 µm s^{-1}; **G** 5.00 µm s^{-1}; **H** 7.50 µm s^{-1}; **I** 10.00 µm s^{-1}. Increasing hysteresis of approach and retract curves is visible with increasing velocity, especially at velocities above 1 µm s^{-1}.

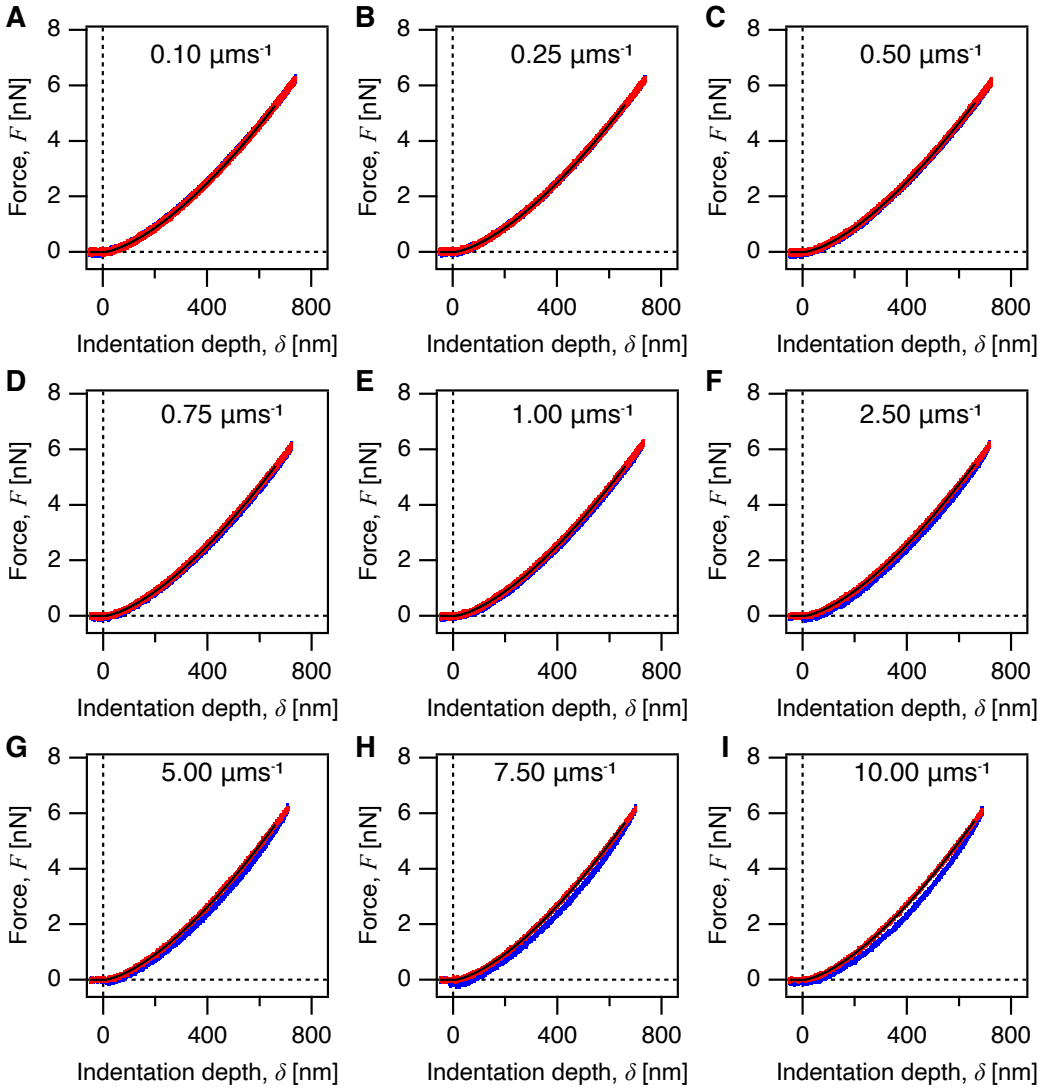

Figure 7.16. Representative force vs. indentation curves on POx-HASH microgel particles at varied ramping velocities v. Fits are shown in solid black lines. **A** 0.10 µm s^{-1}; **B** 0.25 µm s^{-1}; **C** 0.50 µm s^{-1}; **D** 0.75 µm s^{-1}; **E** 1.00 µm s^{-1}; **F** 2.50 µm s^{-1}; **G** 5.00 µm s^{-1}; **H** 7.50 µm s^{-1}; **I** 10.00 µm s^{-1}. Increasing hysteresis of approach and retract curves is visible with increasing velocity, especially at velocities above 1 µm s^{-1}.

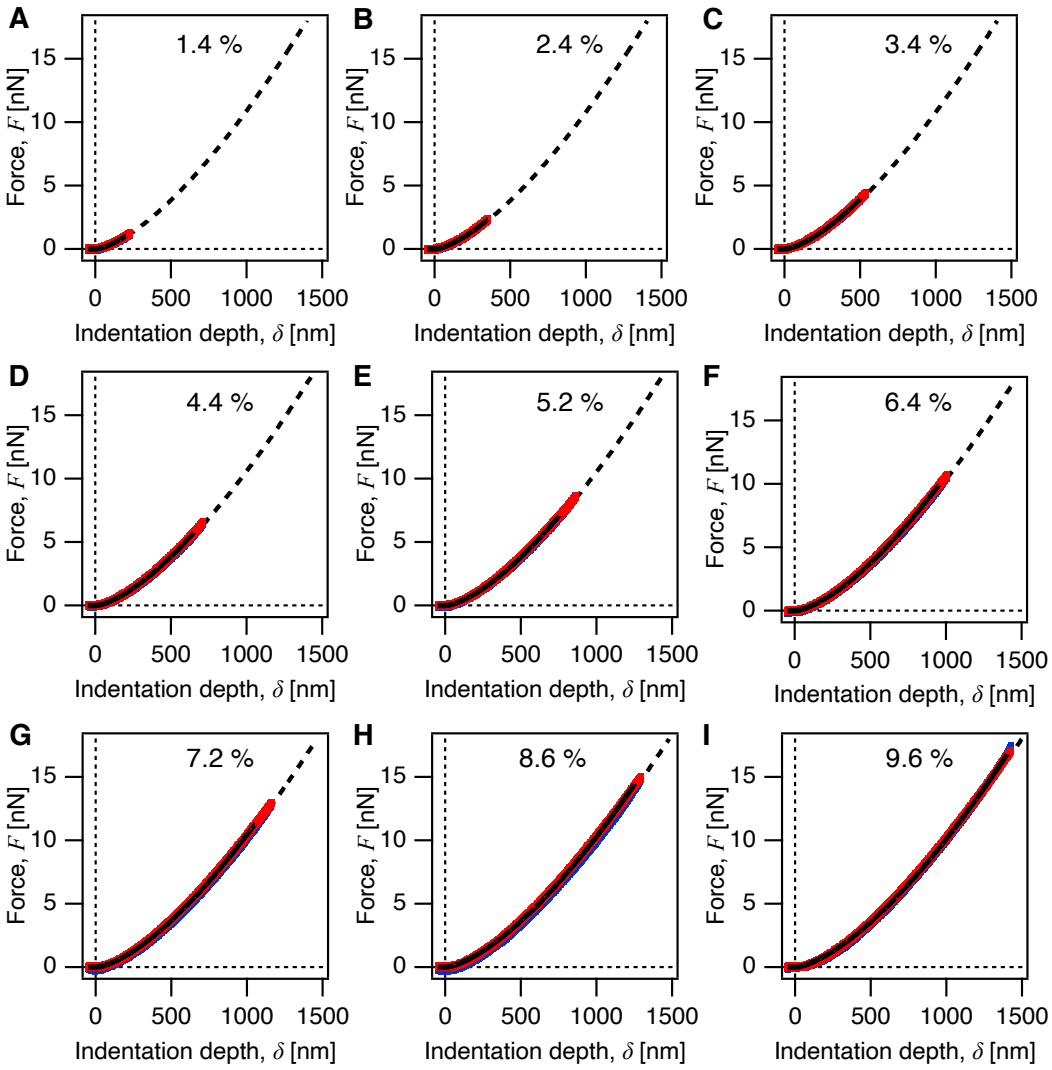

Figure 7.17. Representative force vs. indentation curves on PAAm microgels at varied indentation depths. Fits are shown in solid black lines. Dashed lines represent the theoretical extrapolation of the data provided by the contact model. **A** 1.4%; **B** 2.4%; **C** 3.4%; **D** 4.4%; **E** 5.2%; **F** 6.4%; **G** 7.2%; **H** 8.6%; **I** 9.6% indentation depth concerning the microgel radius.

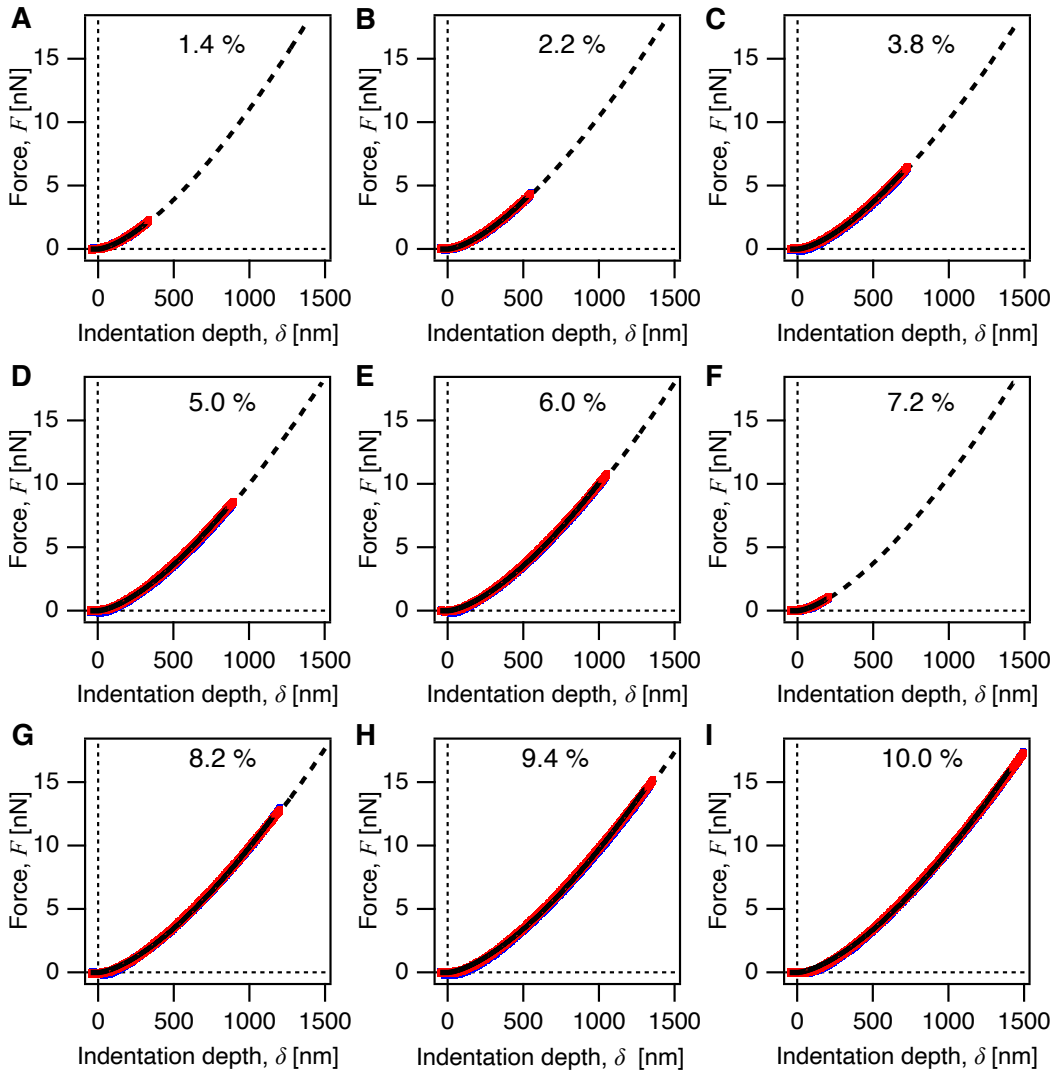

Figure 7.18. Representative force vs. indentation curves on POx-HASH microgels at varied indentation depths. Fits are shown in solid black lines. Dashed lines represent the theoretical extrapolation of the data provided by the contact model. **A** 1.4%; **B** 2.2%; **C** 3.8%; **D** 5.0%; **E** 6.0%; **F** 7.2%; **G** 8.2%; **H** 9.4%; **I** 10.0% indentation depth concerning the microgel radius.

7.6.5 Sphere Cap Fit to the Height Map and Young's Modulus Distribution at the apex of the microgel particle

A sphere cap function (Eq. 7.16) was fit to the height map presented in Figure 7.7A to estimate the particle diameter and validate a spherical geometry.

$$f(x,y) = \sqrt{r^2 - (x - x_0)^2 - (y - y_0)^2} + z_0 \tag{7.16}$$

The calculated particle radius is $R = 15.14 \pm 0.06$ µm, which is in good accordance with the radius of $R = 14.67$ µm as determined by optical microscopy. Figure 7.19A shows a three-dimensional overlay of the height map (grey surface area) and the sphere cap fit (red grid).

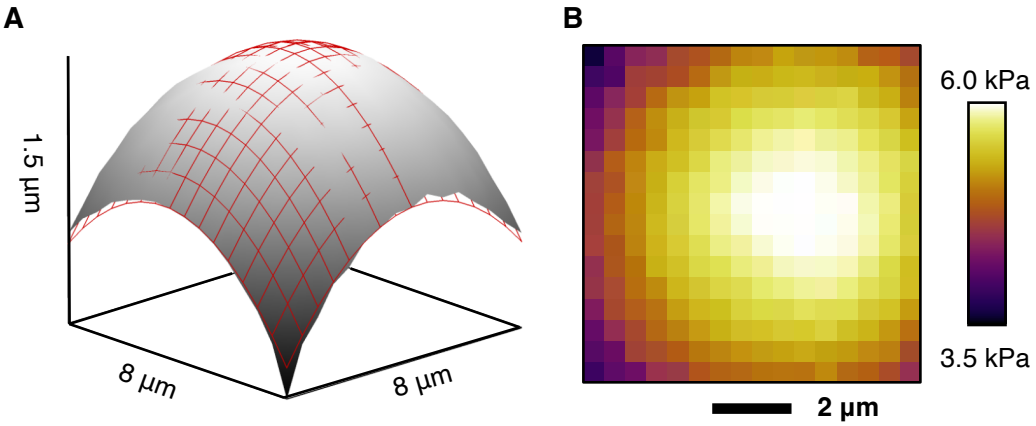

Figure 7.19. Sphere cap fit and elasticity distribution around the apex of a PAAm Microgel particle. **A** Three-dimensional representation of the height map shown in Figure 7.7A and sphere cap fit (red grid) show high agreement. **B** Elasticity Map showing the Young's moduli evaluated using the SDC model at every position on Height Map in **A** and Figure 7.7A.

7.6.6 Simulations of the Adhesive Contact and Resulting Deformations

The finite element simulations yield different deformations (Figure 7.20A) of the microgel particles at the contact with the substrate depending on the dimensionless parameter Λ, which we used to describe the adhesive particle-substrate interaction. Figure 7.20B plots the relation of Λ and the radius ratio r, which we fit using a power law function with the empirical parameters a and b,

$$r = \frac{R_{\text{adh}}}{R_{\text{part}} = a \cdot \Lambda^b} \tag{7.17}$$

resulting in $a = 2.525 \pm 0.073$; $b = 0.320 \pm 0.008$. Hence, the maximum Λ can be approximated

$$\Lambda = \left(\frac{r}{a}\right)^{\frac{1}{b}} \approx \left(\frac{0.47}{2.525}\right)^{\frac{1}{0.320}} \approx 0.015 \tag{7.18}$$

Inserting the maximal $r = 0.47$ as determined from TIRF data (cf. Figure 7.8), which we consider the upper limit, results in a maximal value of $\Lambda \approx 0.015$. Figure 7.20C depicts a zoom-in on the region of our interest.

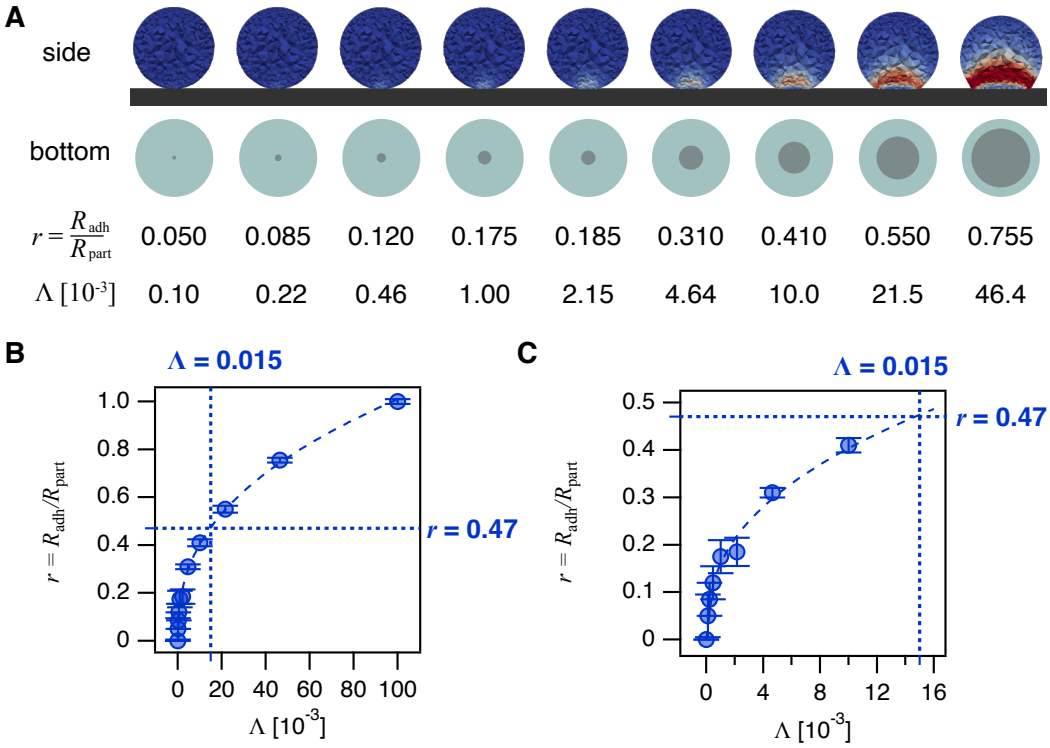

Figure 7.20. Simulation of the deformation of a microgel particle caused by adhesive interaction with the substrate. **A** Simulation of the stress on the microgels due to the adhesive contact with the substrate (side view). The dimensionless parameter Λ is used to describe the adhesive strength. The resulting adhesive contact area (grey) with respect to the microgel size (blue) is illustrated in a bottom-view perspective and characterized by the radius ratio r. **B** Plot of radius ratio r vs. Λ with power law fit. **C** Zoom-in of **B** on the region of interest ($\Lambda < 0.015$). Dashed lines indicate the here-defined upper limit values of $\Lambda \pm 0.015$ and $r = 0.47$.

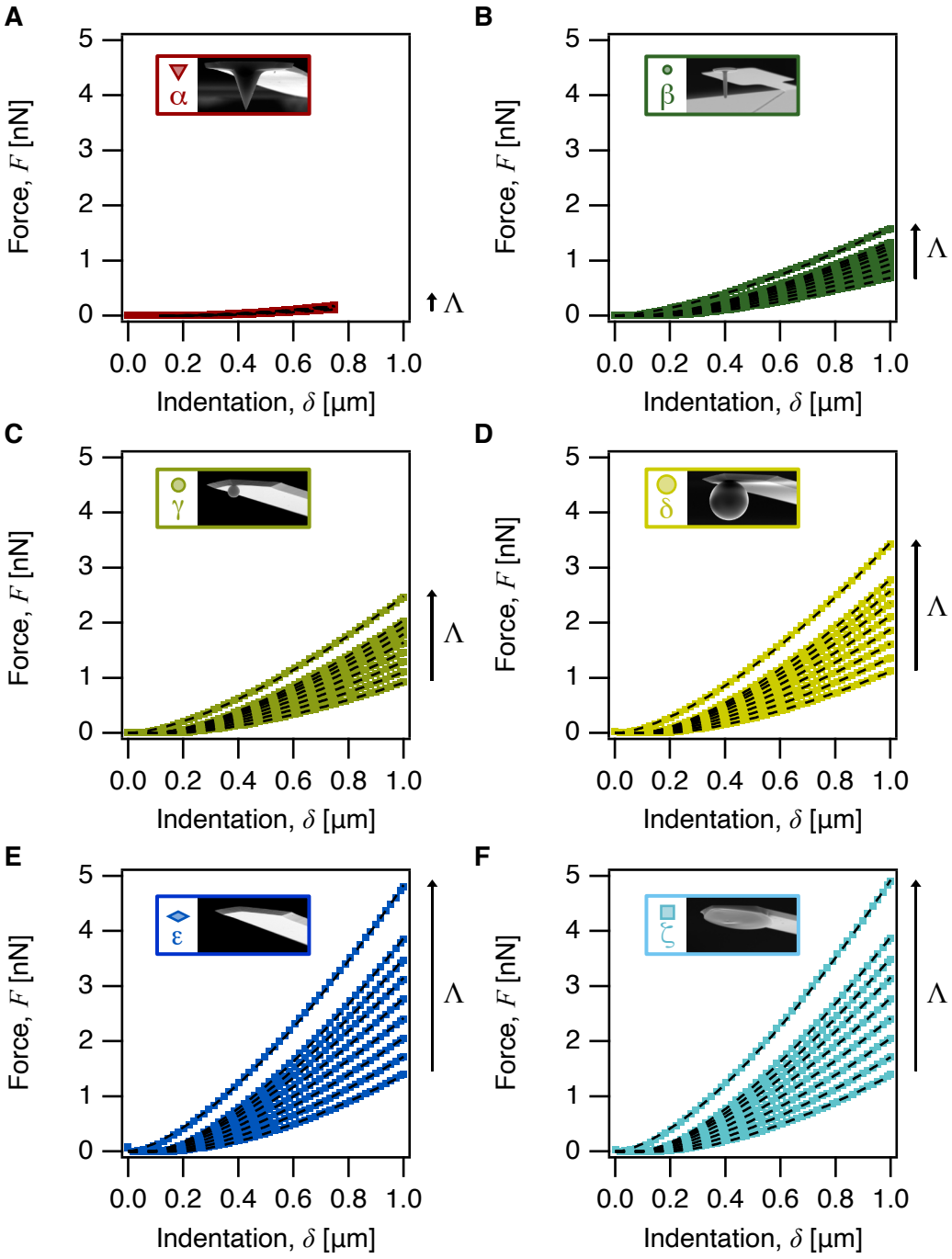

Figure 7.21. Force vs. indentation curves as determined from the numerical simulation with all six indenter types ($\alpha - \zeta$) depending on Λ. Data was fit to the SDC model (Eq. 7.11-7.14) to calculate the apparent moduli $\tilde{E}$. Fits are represented as dashed lines. **A-F** Indenter geometries $\alpha - \zeta$.

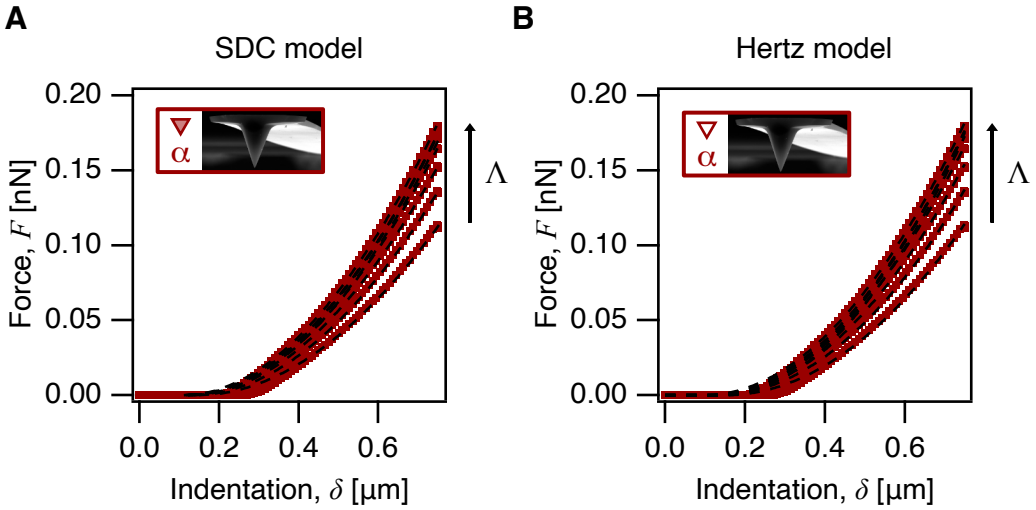

Figure 7.22. Force vs. indentation curves as determined from the numerical simulation with the conical indenter (α) depending on Λ. Data was fit to **A** the SDC model (Eq. 7.14) and the **B** Hertz model (eq. 7.10) to calculate apparent moduli $\tilde{E}$. Fits are represented as dashed lines.

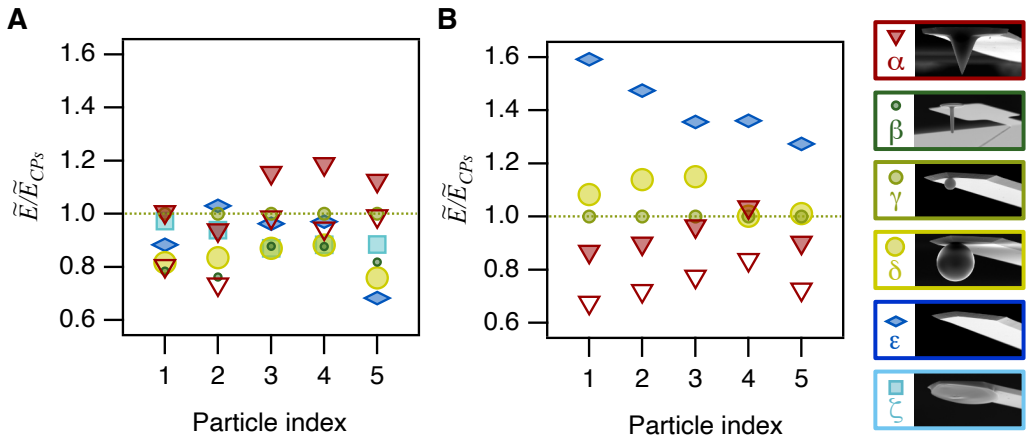

Figure 7.23. Apparent Young's moduli normalized to the data acquired with the small colloidal probe γ. Apparent Young's moduli of **A** five PAAm **B** five POx-HASH microgel particles as determined with different indenter geometries ($\alpha - \zeta$) normalized to the data acquired with the small colloidal probe (γ).

References

(1) Hao, Y.; Cheng, S.; Tanaka, Y., et al. *Biotechnol. Adv.* **2020**, *45*, 107648.

(2) Urbanska, M.; Muñoz, H.; Shaw Bagnall, J., et al. *Nat. Methods* **2020**, *17*(6), 587–593.

(3) Yi, B.; Xu, Q.; Liu, W. *Bioact. Mater.* **2022**, *15*, 82–102.

(4) Vining, K.; Mooney, D. *Nat. Rev. Mol. Cell. Biol.* **2017**, *18*(12), 728–742.

(5) Lekka, M.; Laidler, P.; Gil, D., et al. *Eur. Biophys. J.* **1999**, *28*(4), 312–316.

(6) Radman, B.; Alhameed, A.; Shu, G.; Yin, G.; Wang, M. *J. Mater. Chem. B* **2024**, *12*(22), 5299–5324.

(7) Zemla, J.; Danilkiewicz, J.; Orzechowska, B., et al. *Semin. Cell. Dev. Biol.* **2018**, *73*, 115–124.

(8) Costa, K. *Dis. Markers* **2003**, *19*(2-3), 139–154.

(9) Pérez-Domínguez, S.; Kulkarni, S.; Pabijan, J., et al. *Nanoscale* **2023**, *15*(40), 16371–16380.

(10) Fortier, H.; Variola, F.; Wang, C.; Zou, S. *Anal. Methods* **2016**, *8*(22), 4421–4431.

(11) Daza, R.; González-Bermúdez, B.; Cruces, J., et al. *J. Mech. Behav. Biomed. Mater* **2019**, *95*, 103–115.

(12) Ding, Y.; Xu, G.; Wang, G. *Sci. Rep.* **2017**, *7*, 45575.

(13) Raz, N.; Li, J. K.; Fiddes, L. K., et al. *Macromolecules* **2010**, *43*(17), 7277–7281.

(14) Kumachev, A.; Tumarkin, E.; Walker, G. C.; Kumacheva, E. *Soft Matter* **2013**, *9*(10), 2959.

(15) Kim, E.; Lee, H. *J. Pol. Sci.* **2022**, *60*(11), 1670–1699.

(16) Labriola, N.; Mathiowitz, E.; Darling, E. *Biomater. Sci.* **2016**, *5*(1), 41–45.

(17) Girardo, S.; Träber, N.; Wagner, K., et al. *J. Mater. Chem. B* **2018**, *6*(39), 6245–6261.

(18) Li, W.; Zhang, L.; Ge, X., et al. *Chem. Soc. Rev.* **2018**, *47*(15), 5646–5683.

(19) Heida, T.; Neubauer, J. W.; Seuss, M., et al. *Macromol. Chem. Phys.* **2017**, *218*(2).

(20) Oyen, M. L. *Int. Mater. Rev.* **2014**, *59*(1), 44–59.

(21) Backes, S.; Von Klitzing, R. *Polymers* **2018**, *10*(9), 978.

(22) Kilpatrick, J.; Revenko, I.; Rodriguez, B. *Adv. Healthc. Mater.* **2015**, *4*(16), 2456–2474.

(23) Mietke, A.; Otto, O.; Girardo, S., et al. *Biophys. J.* **2015**, *109*(10), 2023–2036.

(24) Müller, S.; Weigl, F.; Bezold, C., et al. *Biomech. Model Mechanobiol.* **2021**, *20*(2), 509–520.

(25) Huber, D.; Oskooei, A.; Casadevall I Solvas, X.; Andrew, d.; Kaigala, G. *Chem. Rev.* **2018**, *118*(4), 2042–2079.

(26) González-Bermúdez, B.; Guinea, G.; Plaza, G. *Biophys. J.* **2019**, *116*(4), 587–594.

(27) Harris, A.; Charras, G. *Nanotechnology* **2011**, *22*(34), 345102.

(28) Thomas-Chemin, O.; Séverac, C.; Trévisiol, E.; Dague, E. *Micron* **2023**, *174*, 103523.

(29) Zemla, J.; Bobrowska, J.; Kubiak, A., et al. *Eur. Biophys. J.* **2020**, *49*(6), 485–495.

(30) Rico, F.; Roca-Cusachs, P.; Gavara, N., et al. *Phys. Rev. E* **2005**, *72*(2 Pt 1), 021914.

(31) Hertz, H. *J. Reine Angew. Mathematik* **1882**, *1882*(92), 156–171.

(32) Miyake, K.; Satomi, N.; Sasaki, S. *Appl. Phys. Lett.* **2006**, *89*(3), 031925–031921.

(33) Akhremitchev, B. B.; Walker, G. C. *Langmuir* **1999**, *15*(17), 5630–5634.

(34) Domke, J.; Radmacher, M. *Langmuir* **1998**, *14*(12), 3320–3325.

(35) Dimitriadis, E.; Horkay, F.; Maresca, J.; Kachar, B.; Chadwick, R. *Biophys. J.* **2002**, *82*(5), 2798–2810.

(36) Dokukin, M.; Guz, N.; Sokolov, I. *Biophys. J.* **2013**, *104*(10), 2123–2131.

(37) Burmistrova, A.; Richter, M.; Eisele, M.; Üzüm, C.; von Klitzing, R. *Polymers* **2011**, *3*(4), 1575–1590.

(38) Glaubitz, M.; Medvedev, N.; Pussak, D., et al. *Soft Matter* **2014**, *10*(35), 6732–6741.

(39) Berry, J.; Biviano, M.; Dagastine, R. *Soft Matter* **2020**, *16*(22), 5314–5324.

(40) Chang, D.; Hirate, T.; Uehara, C., et al. *Microsc. Microanal.* **2021**, *27*(2), 392–399.

(41) Rosenhek-Goldian, I.; Cohen, S. R. *J. Vac. Sci. Technol. A* **2023**, *41*(6), 062801.

(42) Chiou, Y.; Lin, H.; Tang, M.; Lin, H.; Yeh, M. *PLoS One* **2013**, *8*(10), e77384.

(43) Kulkarni, S.; Pérez-Domínguez, S.; Radmacher, M. *J. Mol. Recognit.* **2023**, *36*(7), e3018.

(44) Managuli, V.; Roy, S. *Exp. Tech.* **2017**, *41*(6), 673–687.

(45) Stylianou, A.; Mpekris, F.; Voutouri, C., et al. *Acta Biomater.* **2022**, *154*, 324–334.

(46) Reineke, B.; Paulus, I.; Löffelsend, S., et al. *Biofabrication* **2024**, *16*(2), 025038.

(47) Brand, J.; Forster, L.; Böck, T., et al. *Macromol. Biosci.* **2022**, *22*(4), e2100274.

(48) Hu, X.; Tong, Z.; Lyon, L. *Colloid Polym. Sci.* **2010**, *289*(3), 333–339.

(49) Stewart, M. P.; Hodel, A. W.; Spielhofer, A., et al. *Methods* **2013**, *60*(2), 186–194.

(50) Hutter, J. L.; Bechhoefer, J. *Rev. Sci. Instrum.* **1993**, *64*(7), 1868–1873.

(51) Boudou, T.; Ohayon, J.; Picart, C.; Tracqui, P. *Biorheology* **2007**, *44*(2), 139–139.

(52) Takigawa, T.; Morino, Y.; Urayama, K.; Masuda, T. *Polym. Gels Networks* **1996**, *4*(1), 1–5.

(53) Geuzaine, C.; Remacle, J.-F. *Int. J. Num. Methods Eng.* **2009**, *79*(11), 1309–1331.

(54) Bower, A. F., *Applied Mechanics of Solids*; CRC Press: Boca Raton, 2009.

(55) Frenkel, D.; Smit, B., *Understanding Molecular Simulation*; Elsevier Academic Press: Cambridge, 2002.

(56) Sneddon, I. N. *Int. J. Eng. Sci.* **1965**, *3*(1), 47–57.

(57) Hidaka, K.; Nakamura, M.; Osuga, K.; Miyazaki, H.; Wada, S. *J. Mech. Behav. Biomed. Mater.* **2010**, *3*(7), 497–503.

(58) Krieg, M.; Fläschner, G.; Alsteens, D., et al. *Nat. Rev. Phys.* **2019**, *1*, 41–57.

(59) Lomakina, E.; Spillmann, C.; King, M.; Waugh, R. *Biophys. J.* **2004**, *87*(6), 4246–4258.

(60) Simic, R.; Mathis, C. H.; Spencer, N. D. *Polymer* **2018**, *137*, 276–282.

(61) Hidaka, K.; Moine, L.; Collin, G., et al. *J. Mech. Behav. Biomed. Mater.* **2011**, *4*(8), 2161–2167.

(62) Owen, D. *Microsc. Res. Tech.* **2023**, *86*(1), 84–96.

(63) Boccaccio, A.; Papi, M.; De Spirito, M.; Lamberti, L.; Pappalettere, C. *Appl. Phys. Lett.* **2013**, *102*(13).

(64) Huth, S.; Sindt, S.; Selhuber-Unkel, C. *PLoS One* **2019**, *14*(8), e0220281.

(65) Grafström, S.; Ackermann, J.; Hagen, T.; Neumann, R.; Probst, O. *J. Vac. Sci.Technol. B* **1994**, *12*(3), 1559–1564.

(66) Johnson, K. L.; Kendall, K.; D., R. A. *Proc. R. Soc. London A* **1971**, *324*(1558), 301–313.

(67) Wang, Y.; Rouabhia, M.; Lavertu, D.; Zhang, Z. *J. Tissue Eng. Regen. Med.* **2017**, *11*(4), 1110–1121.

(68) Fish, K. *Curr. Protoc.* **2022**, *2*(8), e517.

(69) Nalam, P.; Gosvami, N.; Caporizzo, M.; Composto, R.; Carpick, R. *Soft Matter* **2015**, *11*(41), 8165–8178.

(70) Wang, W.; Yan, H.; Gu, Y.; Yan, J.; Mao, B. *Annu. Rev. Anal. Chem.* **2024**, *17*(1), 103–126.

Appendix 8

8.1 Full Supplementary Information for Chapter 4

ADVANCED FUNCTIONAL MATERIALS

Supporting Information

for *Adv. Funct. Mater.*, DOI 10.1002/adfm.202402257

pH-Responsive Virus-Based Colloidal Crystals for Advanced Material Platforms

*Bettina Tran, Samuel Watts, Jules D. P. Valentin, Nadine Raßmann, Georg Papastavrou, Madeleine Ramstedt and Stefan Salentinig**

Supporting information

pH-responsive Virus-based Colloidal Crystals for Advanced Material Platforms

Bettina Tran[1], Samuel Watts[1], Jules Valentin[1], Nadine Raßmann[2], Georg Papastavrou[2], Madeleine Ramstedt[3], Stefan Salentinig[1]*

[1] Department of Chemistry, University of Fribourg, Chemin du Musée 9, 1700 Fribourg, Switzerland

[2] Physical Chemistry II, University of Bayreuth, 95447 Bayreuth, Germany

[3] Department of Chemistry, Umeå University, 90187 Umeå, Sweden

[*]Corresponding author: Stefan Salentinig, email: stefan.salentinig@unifr.ch, Tel: +41 26 300 8794

Content

Materials and Methods

Chemicals/ Materials

[2-(methacryloyloxy)ethyl] trimethylammonium chloride solution (METAC) (75wt % in H_2O, Sigma-Aldrich), copper (II) bromide (99% Sigma-Aldrich), Ethyl α-bromoisobutyrate 98% (EBiB 98%, Sigma-Aldrich), L-Ascorbic Acid (AscA, 99%, Sigma-Aldrich), 2,2′-Bipyridyl (BiPy, >99%, Sigma-Aldrich and methanol (MeOH, >99.8%, Fisher Chemicals) were used as is. Deuterated water (D 99.9%) was purchased from Cambridge Isotope Laboratories, Inc., USA. In all cases, ultra-pure water (resistivity > 18 MΩ cm) was used.

Qubevirus durum (Qbeta) (DSMZ 13768, DSMZ, Germany) was replicated in *Escherichia coli (E.coli)* strain W1485 (DSMZ 5695, DSMZ, Germany). Tryptone (Fluka Analytics, St. Louie MO, USA), yeast extract (Sigma life science, St. Louie MO, USA), NaCl (≥ 99.5% purity, SigmaAldrich Chemie GmbH, Steinheim, Germany), $CaCl_2$ (97% purity, Fluka Analytics, Buchs, Switzerland), Dextrose (Biotechnology grade, Amresco, Solon OH, USA), Streptomycin (Fluka Chemie GmbH, Buchs, Switzerland), Agar (Sigma-Aldrich, Spain), Mueller-Hinton Broth (MHB, Sigma-Aldrich,Spain), $NaH_2PO_4{\cdot}2H_2O$ (≥ 98.0% purity, SigmaAldrich Chemie GmbH, Steinheim, Germany), NaOH (≥ 99% purity, Carl Roth GmbH, Karlsruhe, Germany) and HCl (ACS reagent grade, Sigma-Aldrich, Buchs, Switzerland) were used with ultra-pure water (resistivity > 18 MΩ cm). Bovine serum albumin (BSA, Fraction V, > 99%, PAN Biotech, USA), was used without further purification.

Synthesis poly [2-(methacryloyloxy)ethyl] trimethylammonium chloride (pMETAC)

The synthesis of pMETAC has been adapted from Visnevskij et al. [1]: In an aliquot of 10 ml methanol, 5.33 g of METAC 75wt% (1.92×10^{-2} mol METAC), 43.1 mg $CuBr_2$ (1.93×10^{-4} mol), 301 mg BiPy (1.93×10^{-3} mol) and 0.28 ml EBiB (1.93×10^{-3} mol) were mixed in a Schlenk flask, while 1 ml of MeOH is used to dissolve 43.8 mg AscA (2.49×10^{-4} mol) in a separate flask. Both flasks were degassed by three freeze-thawing cycles with argon. The Schlenk flask with the polymerization solution was stirred at 25°C under argon while adding the ascorbic acid solution of 1ml/4min. The reaction was carried out for 18 hrs at 25°C. The reaction was stopped by stirring the solution under air.

The reaction mixture was poured into a 10-fold excess of cold acetone to precipitate the polymer. After the centrifugation at 1367 relative centrifugal force (rcf) for 10 minutes and decantation of the supernatant (Centrifuge Eppendorf 5804 R, Germany), the polymer was redissolved in methanol. The precipitation was repeated three times. The pellet was dried in an oven at 40°C until constant weight. Under these conditions, a short chain denoted as pMETAC1 was synthesized.

For the synthesis of a longer pMETAC, here denoted as pMETAC2, the amounts were adapted to 13.4 g METAC 75wt% (4.82×10^{-2} mol METAC), 10.8 mg $CuBr_2$ (4.82×10^{-5} mol), 75.3 mg BiPy (4.82×10^{-4} mol), 0.07ml EBiB (4.82×10^{-4} mol) and 43.8 mg Asc A (2.49×10^{-4} mol) in an aliquot of 25 ml MeOH.

Virus propagation and purification

Qbeta was replicated in *Escherichia coli (E. coli)* strain W1485 or ATCC 23631. The modified LB-broth was prepared by adding 10 g/l of tryptone, 1 g/l of select yeast extract, 8 g/l of NaCl, 0.3 g/l of $CaCl_2$, 1 g/l Dextrose and 2 mg/l Streptomycin in ultra-pure water.

E. coli was incubated in the prepared broth at T = 37°C at 80 rpm (ES-20, Biosan, Latvia). When the bacteria culture reached an optical density of 0.04 (Ultrospec 10, biochrom, USA), it was infected with Qbeta at a multiplicity of infection (MOI) of 0.1 to *E. coli*. At T = 37°C incubation of the infected *E. coli* without shaking took place for 4 – 5 h (NB205QMC, n-biotek, Korea). The virus dilution buffer (VDB) was prepared by adding 0.78 g/l $NaH_2PO_4 \cdot 2H_2O$ and 0.58 g NaCl in ultra-pure water. The pH of the buffer was adjusted to 7.0 using NaOH and HCl.

Bacterial debris was removed by centrifugation at 2600g for 20 min (Eppendorf 5810R, Eppendorf Germany). The phage-containing supernatant was filtered with 0.22 µm sterile filters (MillexGP, Millipore, Ireland) to remove any remaining bacterial debris. The flow-through was then concentrated from 7 l to approximately 5 ml with centrifugal filters (100 kDa Amicon Ultra-15 centrifugal filters, Millipore, Ireland). The Qbeta suspension was washed with at least 5 l of virus dilution buffer at pH 7.0 by multiple 13 − 15 ml washing steps in the centrifugal filters. The suspension was finally filtered through 0.1 µm sterile filters (MillexVV, Millipore, Ireland), in agreement with the virus purification method previously reported.[2] The final phage titer was determined by plaque assay using a soft agar layer method, as described elsewhere.[3] Briefly, bottom agar of LB-broth was prepared by adding 10 g/l agar in petri dishes. A soft overlay agar was prepared by adding 5 g/l agar to the LB-broth and mixing it with *E. coli*, which had been prepared overnight (T = 37°C) and inoculated in fresh media to reach its exponential growth. This soft agar culture was poured over the bottom agar and let dry. Serial dilution of phage suspensions was spotted on the soft agar layer and incubated overnight at 37°C.

Infectivity assay of Qbeta: Plaque forming unit (PFU) and concentration determination

For the infectivity assays of Qbeta and Qbeta/pMETAC1, the same protocol has been used, whereby the media concentration was adapted to 100% MHB (21 g/l MHB) and with 12 g/l agar for the bottom agar. *E. coli* (ATCC 23631) was inoculated overnight in 100% MHB, using an orbital shaker-incubator at 160 rpm. The next day a pre-culture of the *E. coli* is prepared by growing 1:10 of the overnight culture into fresh 100% MHB for 4 hrs at 37°C and 160 rpm. Soft agar of 0.21 g/l MHB with 5 g/l agar was mixed with the *E. coli* pre-culture to obtain 5 ml of 10^6 CFU/ml suspension. This soft agar culture was poured over an MHB agar plate and let dry. Qbeta and the Qbeta/pMETAC1 samples were gently homogenized by pipette mixing, serial diluted (by factors of 10 down to 10^{-12}) and spotted on bacteria lawn. Plaque forming units (PFU) were counted after overnight incubation at 37°C. The assays were performed in three technical repeats.

The resulting Qbeta concentration was approximately 10^{13} PFU/ml. We then employed PFU/ml values to estimate the mg/ml, factoring in the molecular weight reported in the structure of Qbeta and accounting for inactive particles not reflected in the PFU analysis. This resulted in an estimated concentration of 1 mg/ml.

When determining the infectivity of the aggregates, the Qbeta/pMETAC1 suprastructures have been equilibrated for 24 hrs before the assays. The viral infectivity after pellet formation, in the

centrifuge (Centrifuge IKA G-L, Germany) at 13'000 rcf for 3 min, decantation of the supernatant and redispersion in fresh VDB by gentle pipette-mixing, was compared to non-centrifuged aggregates. The centrifugal head was pre-cooled in the fridge for 1 hr before usage.

Estimation of Qbeta concentration from SAXS

A Qbeta batch with known PFU/ml, from the infectivity assay was measured in small-angle X-ray scattering (SAXS). 1 mg/ml Bovine serum albumin (BSA) in VDB, was measured under the same conditions as Qbeta. The forward scattering *I(0)* was determined by performing a linear fit in the Guinier regime, when the data is plotted as *ln(I(q))* vs q^2 (see Eq. S1), whereby q is the magnitude scattering vector and *Rg* the radius of gyration. From the forward scattering of BSA ($I(0)_{st}$) and Qbeta ($I(0)_m$), the molecular mass of BSA (MM_{st}), 66.43 kDa and the molecular mass of a complete Qbeta (MM_m), 3'968.88 kDa [4], the concentration of Qbeta (c_m) can be estimated with Eq. S2 [5], whereby the concentration of BSA (c_{st}) is known. Results indicated that different Qbeta batches containing ~10^{13} PFU/ml had concentrations around 2.6 mg/ml from SAXS. It is important to note that these estimates overstate the actual concentration, due to larger impurities observed in the TEM data and errors from extrapolating SAXS data to *I(0)*. Consequently, we maintained a conservative estimate of 1 mg/ml (see section above).

$$I = I(0)\, e^{-\frac{q^2 R_g^2}{3}} \tag{S1}$$

$$MM_m = \frac{I(0)_m}{c_m}\left(\frac{MM_{st}}{\frac{I(0)_{st}}{c_{st}}}\right) \tag{S2}$$

Gel permeation chromatography

Gel permeation chromatography (GPC) was performed with PSS NOVEMA Max columns (Perfect Separation Solutions PSS, Mainz, Germany). 0.5 M acetic acid and 0.5 M sodium acetate were used as eluent at a flow rate of 0.5 ml/min. The system was maintained at 25°C. The polymer concentration was between 2.8 – 3.5 g/l, and a volume of 100 µl was injected. From the obtained number-average molecular weight (Mn), the degree of polymerization can be calculated with Eq. S3.

^{1}H Nuclear magnetic resonance spectroscopy (^{1}H NMR)

^{1}H NMR was performed on a 400 MHz Bruker Avance III spectrometer (Bruker, Zürich, Switzerland) using deuterated water as a solvent. Chemical shifts, in ppm, were referenced to the deuterated solvent peak. The concentration of the prepared samples was 10 mg/ml.

Raman spectroscopy

Raman spectra of the monomer and polymers were measured with a confocal Raman microscope (WiTec Alpha 300 R with UHTS 300 spectrometer, Ulm, Germany). The laser wavelength was 785 nm, and a 20x magnification objective (Zeiss EC Epiplan-Neofluar HD Dic 20x, NA=0.5) was used. The spectroscopic grating was 300 g/mm. The measurement time was 30 x 1 second with a 40 - 50 mW laser power. The data were processed with the WITec data processing software (Control Five v5.2).

Polymer chain length estimation

The equilibrium geometry of the polymer with 6 repeating units (*RU*) was simulated with the density functional B3LYP (with basis sets of 6-31G*) in vacuum using the software Spartan '14 Version 1.1.8. (Wavefunction inc, Irvine, USA). The length of each *RU* was measured. The average length of one RU was calculated and used to estimate the length of the polymers with the known number-average molecular mass. From the number-average molecular mass, the molecular mass of the initiator, (M(EBIB) = 195.1 g/mol) was subtracted and divided by the molecular weight of the monomer (M(METAC) = 207.7 g/mol) (see Eq. S3) to calculate the degree of polymerization (DP_n). In the case of pMETAC1 DP_n is 11.8, and for pMETAC2 DP_n is 52.2. The polymer chain length was calculated by multiplying DP_n with the average *RU* length.

$$DP_n = \frac{Mn\ (pMETAC) - M(EBIB)}{M(METAC)} \tag{S3}$$

Model-independent SAXS data analysis: GIFT

The generalized indirect Fourier transformation (GIFT) method allows the simultaneous fitting of *P(q)* and *S(q)* by selecting a suitable *S(q)* model.[6-9] The resulting pair-distance distribution function *p(r)*, calculated from the *P(q)* contains direct information on the size and shape of the particles. [10-11]

$$P(q) = 4\pi \int_0^\infty p(r) \frac{\sin(qr)}{qr}\, dr \tag{S4}$$

Where

$$p(r) = r^2 \Delta\tilde{\rho}^2(r) \tag{S5}$$

with $\Delta\tilde{\rho}^2(r)$ being the convolution square of the spatially averaged excess electron density *Δρ(r)* In the case of spherical geometry, deconvolution of the *p(r)* gives the radial contrast profile in electron density *Δρ(r)* relative to the mean value of the solvent. This gives information about the internal structure of the scattering particles. [12-13]

Model dependent SAXS data analysis

The form factor for a spherical shell $P_s(q,R,\Delta R)$ is defined as follows: [14]

$$P_s(q,R,\Delta R) = \left[\frac{4}{3}\pi(R+\Delta R)^3 \Delta\eta_2 3\, \frac{\sin(q(R+\Delta R)) - q(R+\Delta R)\cos(q(R+\Delta R))}{(q(R+\Delta R))^3} - \frac{4}{3}\pi R^3(\Delta\eta_2 - \Delta\eta_1)3\, \frac{\sin(qR) - qR\cos(qR)}{(qR)^3}\right]^2 \quad (S6)$$

ΔR corresponds to the shell thickness, $\Delta\eta_1$ to the excess electron density difference of the matrix (VDB) and the core and $\Delta\eta_2$ to the scattering length density difference of the matrix and the shell.

To account for polydispersity, the normalized Gaussian distribution of the spherical particles is defined as follows, with R being the core-radius, R_0 the mean value, and s the standard deviation.

$$f_g(R) = \frac{N}{s\sqrt{2\pi}} \exp\left(-\frac{(R-R_0)^2}{2s^2}\right) \quad \text{(S7)}$$

The Gaussian chain has been modelled with the following equation: [15]

$$P_G(q) = I_0\, 2\frac{\left(\exp\left(-q^2R_g^2\right) + q^2R_g^2 - 1\right)}{(q^2R_g^2)^2} \quad \text{(S8)}$$

Whereby, R_g describes the radius of gyration of the chain.

For the assemblies, the scattering intensity is a combination of P_s with the Gaussian distribution f_g with the hexagonal structure factor S_{hex} accounting for the superstructure. The structure factor of a hexagonal lattice consists of the lattice factor $Z(q)$ and the Debye-Waller factor $G(q)$, containing the information of the observable Bragg reflection and the thermal fluctuation, respectively. [16-17] $G(q)$ dependence on the relative mean square displacement σ_a^2 of the particles from the ideal lattice point due to thermal effects and on the closest distance of two adjacent particles $\bar{a}$ (see Eq. S11). For the fitting, the thermal effects were omitted giving $G(q) = 1$.

For the model to represent the overall scattering curve, an additional power law decay had to be included to account for the contribution of aggregates with a scaling factor N. In case of Qbeta alone, S_{hex} was equal to 1, the power law was omitted. The scaling factor in the core-shell model was set to 1.

$$I_{assembly}(q) = \left(\int P_s(q,R)\, f_g(R)\, dR\right) S_{hex}(q) + P_G\left(q, R_g\right) + N\, q^{-\alpha} \quad \text{(S9)}$$

$$S_{hex}(q) = (Z_0(q) - 1)\, G(q) + 1 \quad \text{(S10)}$$

$$G(q) = \exp(-\sigma_a^2 \bar{a}^2 q^2) \quad \text{(S11)}$$

The scattering length density of Qbeta protein capsid was estimated with the known peptide sequence.[18-19] With the scattering length density of VDB, $\Delta\eta_2$ was calculated to be 4.1, due to sample concentration the value was scaled down for the fitting. (see Table S1)

Negative-stain transmission electron microscopy (TEM)

For negative-stain TEM, samples 300 mesh copper grids (EMS,USA) were covered with 0.7 wt% Formvar and carbon coated to 2 – 3 nm thickness using EM ACE200 (Leica Microsystems, Germany). The grids were glow discharged in PELCO easiGLow (Ted Pella, inc. USA).3.5 µl liquid samples were adsorbed to the cabron surface for 2 min, washed in two 50 µl H_2O drops and subsequently stained with 1.5% aqueous uranyl acetate (UA) solution (Electron Microscopy Science (EMS), USA), 10s in three 50 µl drops, blotted to filter paper in between each drop with subsequent washing and rinsing cycles in H_2O in between. Grids were analyzed with Talos L1200 TEM (FEI, Netherlands) at 2200x and 73000x magnification and images recorded with CETA CMOS detector using TIA software (FEI).

Preparation of Qbeta in different salt solutions for SAXS

For Qbeta/pMETAC1 with varying the NaCl concentration in VDB. The minimum NaCl concentration is at 10mM in the original VDB.

For the study of electrostatic interactions in absence of pMETAC1, Qbeta in VDB was mixed with NaCl or $MgCl_2$ with the equivalent amount of charge as estimated from pMETAC1. It was assumed that each repeating unit (RU) of the polymer holds one quarternary ammonium. From the number-average molecular mass, the molecular mass of the initiator, (M(EBIB) = 195.1 g/mol) is subtracted and divided by the molecular weight of the monomer (M(METAC) = 207.7 g/mol) (see Eq.S3). The total number of charges on one polymer chain (Q_{chain}) corresponds to the degree of polymerisation (DP_n), in case of pMETAC1 Q_{chain} is 11.8 and for pMETAC2 Q_{chain} is 52.2. To calculate the total number of charge in the solution (Q_{total}), the total number of chains in the solution (N_{chain}) is derived from the number of mols (n) with Eq. S12, S13 and S14. Therefore, 1 mol of pMETAC1 contains $11.8 \times 6.02214076 \times 10^{23}$ positive charges.

$$n = \frac{m(pMETAC)}{Mn(pMETAC)} \tag{S12}$$

$$N_{chain} = n * N_A \tag{S13}$$

$$Q_{total} = Q_{chain} * N_{chain} \tag{S14}$$

To achieve comparable charge interaction of Qbeta with NaCl or $MgCl_2$ as with pMETAC1, Eq. S15 relates *Qtotal* to the total number of cations (N_{cation}), depending on the valency of the cation. From this, the molar concentration (c) needed is calculated with Eq. S16 and S17, with V being the volume of the required solution.

$$N_{cation} = \frac{Q_{total}}{valency} \tag{S15}$$

$$n_{cation} = \frac{N_{cation}}{N_A} \tag{S16}$$

$$c = \frac{n_{cation}}{V} \tag{S17}$$

For the SAXS experiments, 50 mg/ml pMETAC1 is mixed in a 1:1 volume ratio with Qbeta. The equivalent concentration for NaCl, followed by this calculation, is 0.223 M and 0.112 M for $MgCl_2$.

Dynamic light scattering (DLS)

The DLS autocorrelation functions were fitted with Eq. S18 to determine the average decay constant (Γ) and the second cumulant (μ_2) with the fit parameter β and variable τ for time.[20] The scattering vector magnitude q was determined (with λ = 532 nm, n the refractive index, and θ being the scattering angle) to calculate the diffusion coefficient D (see Eq. 1 and Eq. S19)

$$g^2(\tau) - 1 = \beta \exp(-2\Gamma\tau)\left(1 + \frac{\mu_2}{2!}\tau^2\right)^2 \tag{S18}$$

$$D = {}^{\Gamma}/_{q^2} \tag{S19}$$

From the diffusion coefficient and with the Stokes-Einstein equation (Eq. S20) the apparent hydrodynamic radius (R_H) can be determined, where k_B is the Boltzmann constant, T the

absolute temperature, η the viscosity of the solvent (for water: η(25°C) = 0.89 mPas). The polydispersity index (PDI) was calculated from Eq. S20.

$$R_H = \frac{k_B T}{6\pi\eta D} \quad \text{(S20)}$$

$$PDI = {}^{\mu_2}/_{\Gamma^2} \quad \text{(S21)}$$

Time-dependent DLS data were evaluated by fitting with the diffusion-limited cluster aggregation (DLCA) model given in Eq. S22.[21] t is the time, A, B, and C are fitting parameters.

$$R_H(t) = A * t^B + C \quad \text{(S22)}$$

Parameter A indicates the aggregation rate, while parameter B is the inverse of the fractal dimension D_f. C corresponds to the starting size of the aggregates at time zero. From the fractal dimension, the scaling prefactor k_f can be determined, and thus an estimate of the number of particles in the cluster (i), at the end of the measurement where t = t_f, can be estimated. Rp corresponds to the size of the individual particle, in this case, the radius of Qbeta.[22-23] Generally, Rp and C should be the same if the whole aggregation from a single particle to assembly is observable.

$$i = k_f \left(\frac{R_H(t_f)}{R_p}\right)^{D_f} \quad \text{(S23)}$$

$$k_f = 4.46 D_f^{-2.08} \quad \text{(S24)}$$

Additional Results and Discussion

Structure of Qbeta in suspension and pH-triggered aggregation

The scattering curves of Qbeta at different pH values between 5.0 and 9.0 are shown in Figure S3A. The SAXS curves have characteristic minima and maxima of spherical particles. At the Guinier region of $q < 0.2$ for systems at pH ≥ 5.0 showing a slope close to 0, indicating particles within the size-range accessible with the SAXS set-up. Contrary, the SAXS curve for the sample at pH 3.0, shows an upturn, which may arise from the aggregation of the virus particles to aggregates larger than the resolution limit of the SAXS setup (125.6 nm).

In the range $0.1 < q < 0.4$ nm^{-1}, the shape of the second maxima and first minima show differences when compared to that of pH 5.0, 7.0, 9.0, indicating a change in the scattering contribution with pair distances between 31 nm and 7.85 nm which correspond to the larger dimensions of the Qbeta particle.

To gain further insight into the particle structure, the *I(q)* curves at pH 7.0 and 9.0 were analyzed with the indirect Fourier transformation method. For the analysis of the aggregated sample at pH 3.0, the generalized indirect Fourier transformation method using a hard sphere and a fractal aggregate structure factor was used. The pair distribution functions (*p(r)*) obtained are presented in Figure S3B. At pH 7.0, the *p(r)* is characteristic of a spherical particle with a diameter of 27.0 nm from *p(r)* = 0. At pH 9.0, the maximum particle dimension shifts to about 28.5 nm. Moreover, the shape of the *p(r)* function has a maximum that is shifted to larger *r* values, 16.5 nm versus 14.7 nm at pH 7.0. In addition to this, a slight shoulder can be observed around separation distances of about 5 nm.

Supporting Figures

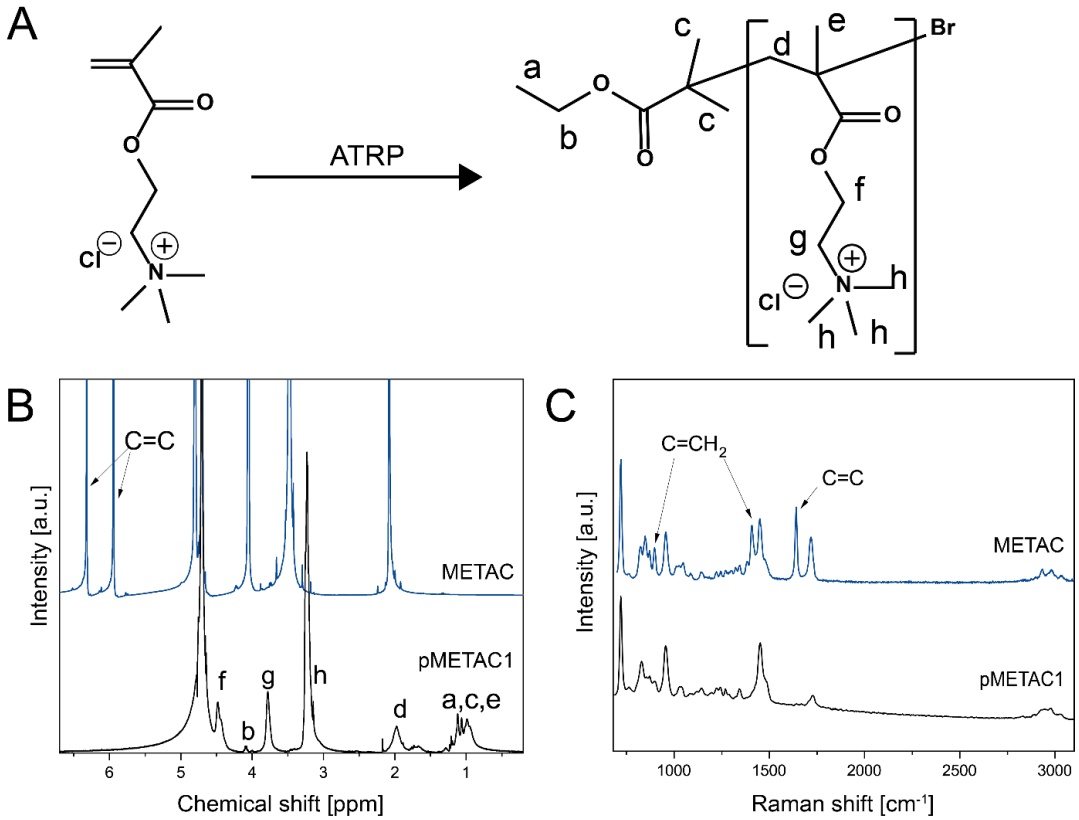

Figure S1: Structural formula of pMETAC1, a-h are labels for H-atoms in the polymer, in (A) and the corresponding ^{1}H NMR peaks in (B) compared to the monomer METAC. (C) shows the Raman spectrum of METAC and pMETAC1.

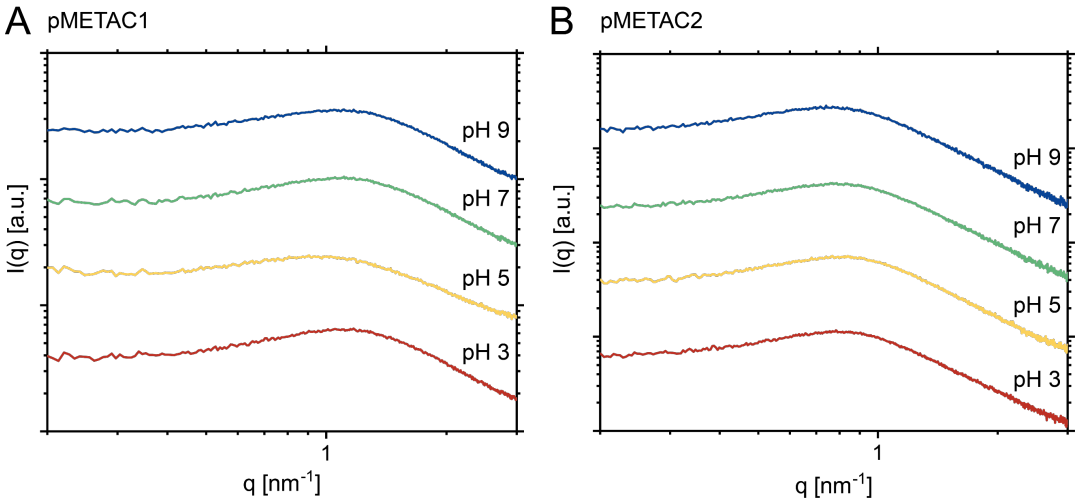

Figure S2: SAXS data of 50 mg/ml pMETAC1 and 50 mg/ml pMETAC2 at different pH values.

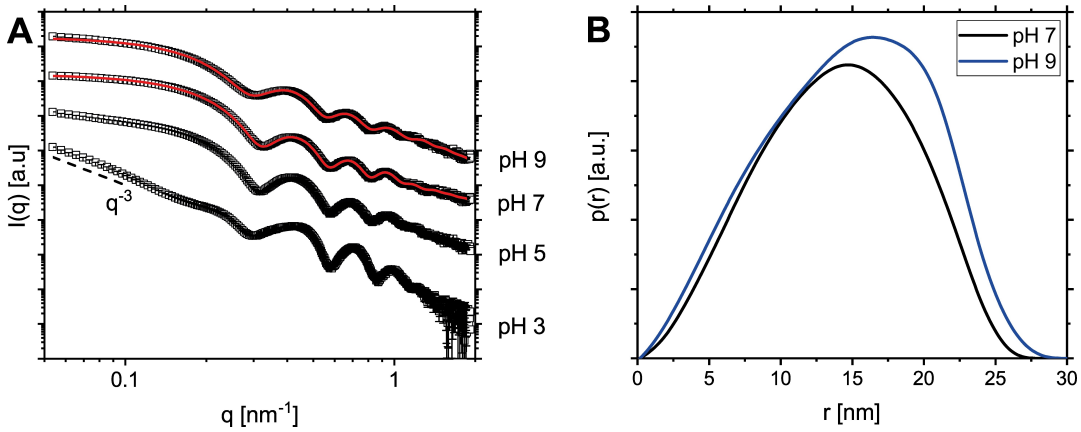

Figure S3: Nanostructure of Qbeta. (A) Experimental SAXS scattering curves black squares of Qbeta at different pH values with the corresponding fits calculated with the IFT method (red curve). (B) Corresponding pair distance distribution functions *p(r)* calculated from experimental SAXS scattering curves of Qbeta at different pH values.

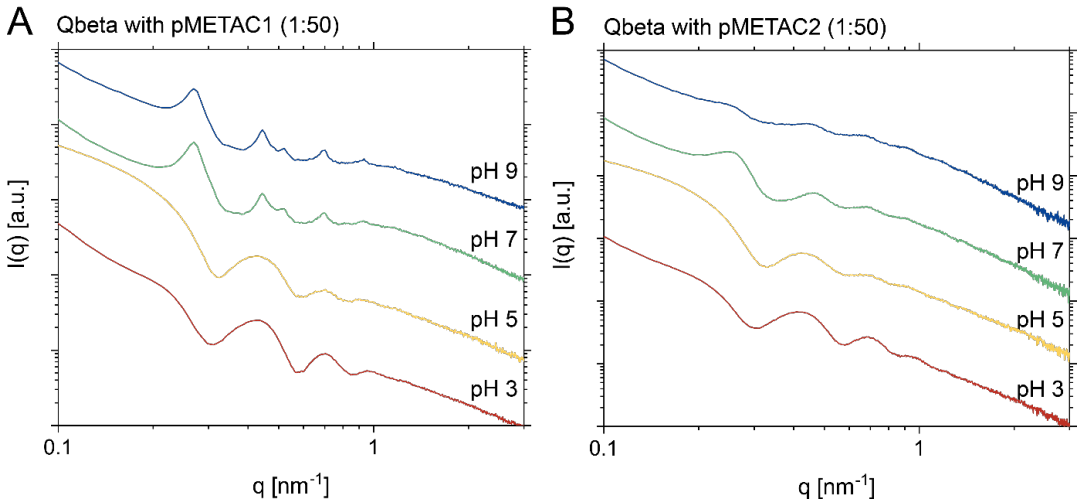

Figure S4: (A) SAXS data of 1 mg/ml Qbeta with 50 mg/ml pMETAC1 at different pH values and (B) with 50 mg/ml pMETAC2, respectively

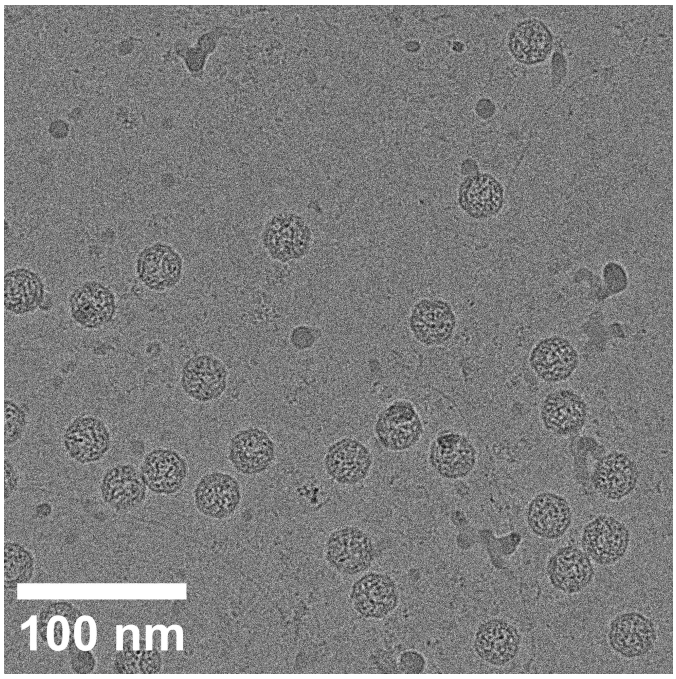

Figure S5: Representative cryo-TEM image of a Qbeta suspension, corresponding to the image in Figure 1.

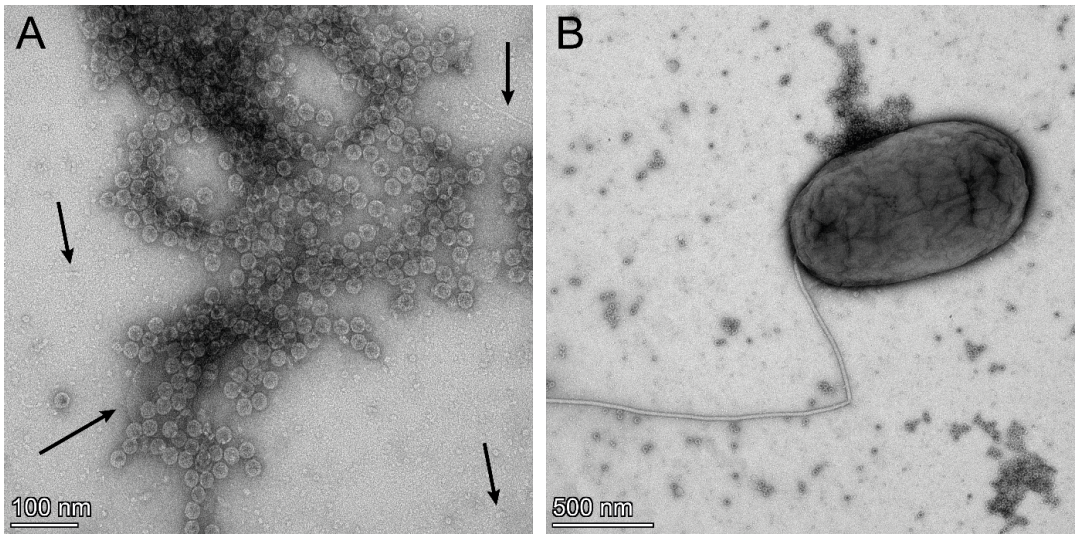

Figure S6: TEM images of UA stained Qbeta, (A) Arrows show potential bacteria debris. (B) whole dead bacteria with flagella were also found in some of the samples. The bacteria appear distorted as the membrane barrier function is destroyed by the phages that proliferate inside the cell and are imaged leaving the cell.

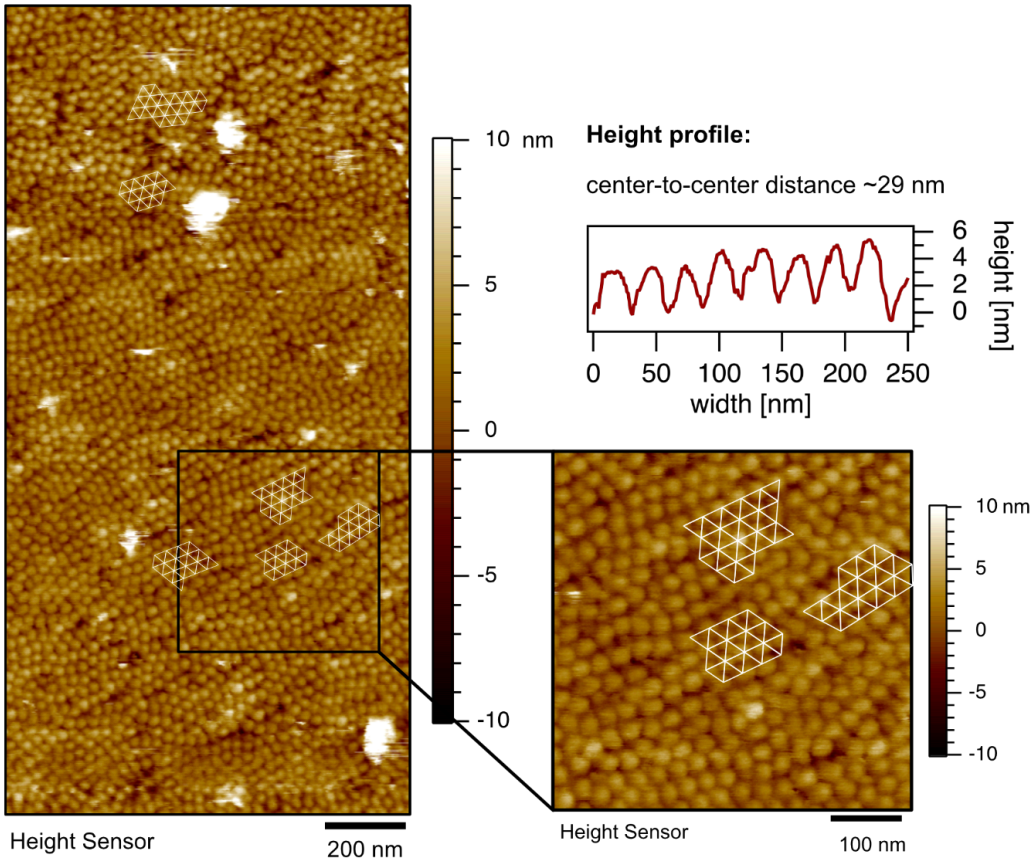

Figure S7: AFM image of Qbeta/pMETAC1 assembly acquired in VDB. Hexagonal arrangements were marked with a white pattern. The enlarged height profile indicates a center-to-center distance of ~29 nm for the Qbeta in this structure.

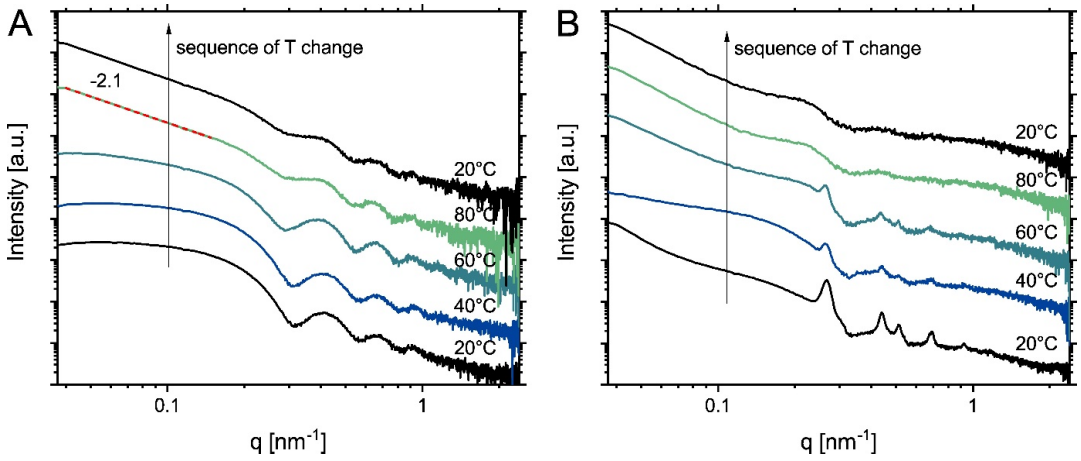

Figure S8: SAXS data of Qbeta (A) and Qbeta/pMETAC1 1:50 (B) showing temperature triggered structural modifications. The temperature was increased from 20°C to 80°C, before cooling back to 20°C. The samples were equilibrated for 5 mins at each temperature before measurement.

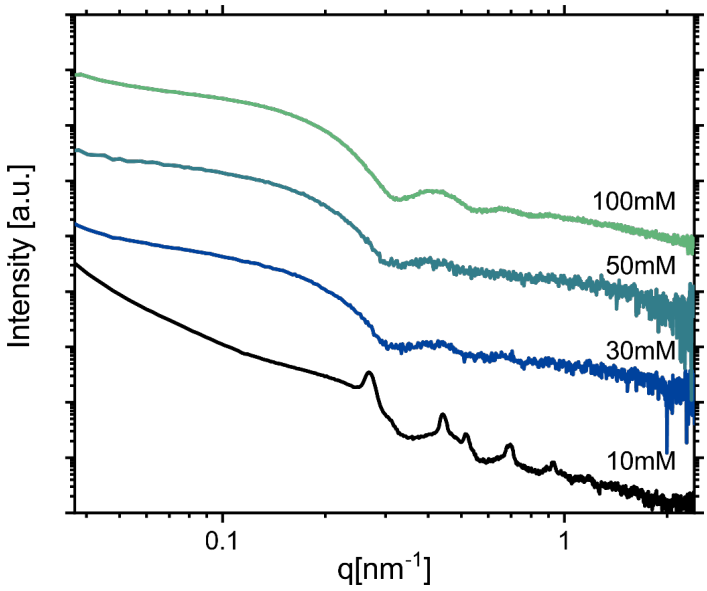

Figure S9: SAXS data of Qbeta/pMETAC1 1:50 with increasing concentration of NaCl. At 30 mM and 50 mM NaCl, small sediments have formed that could not be measured in our setup.

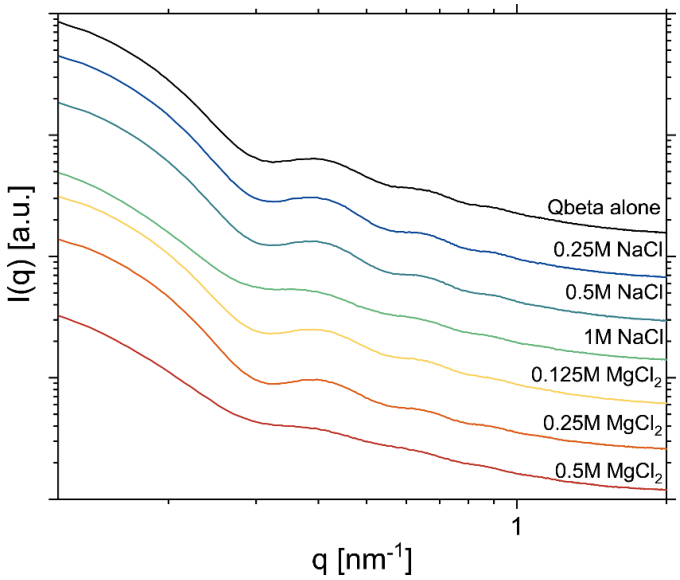

Figure S10: SAXS data of Qbeta at different salt concentrations (ionic strengths) using monovalent (NaCl) and di-valent ($MgCl_2$) ions. Despite not having performed any background correction of the scattering curve, no major change can be seen from the initial scattering pattern of Qbeta in the absence of any pMETAC.

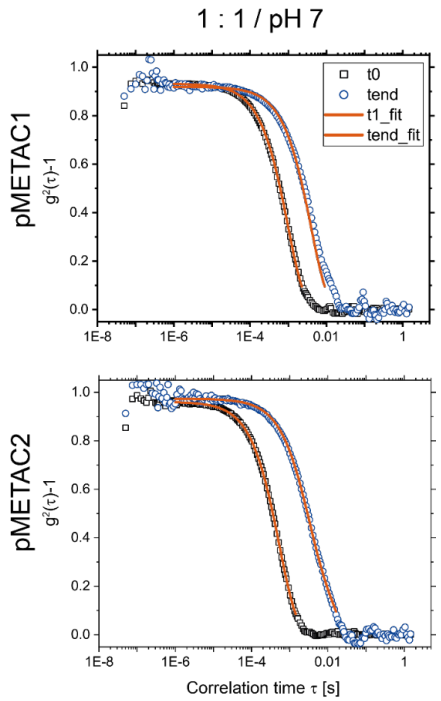

Figure S11: Correlation curves from the DLS measurements of Qbeta-pMETAC1 and Qbeta-pMETAC2 in 1:1 ratio at pH 7.0 and measured at 90° from the first and last data point of the time series in Figure 4.

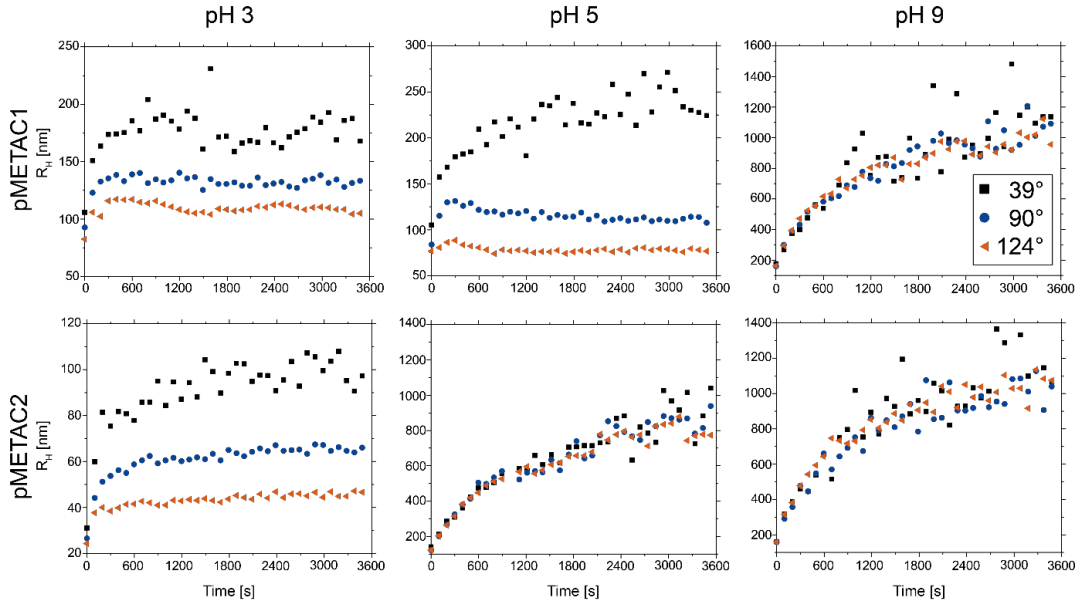

Figure S12: Time-dependent DLS curves of Qbeta-pMETAC1 and Qbeta-pMETAC2 at 1:1 ratio and different pH values, measured at three different angles. The corresponding correlation curves to the first and last time point of each dataset can be found in Figure S13.

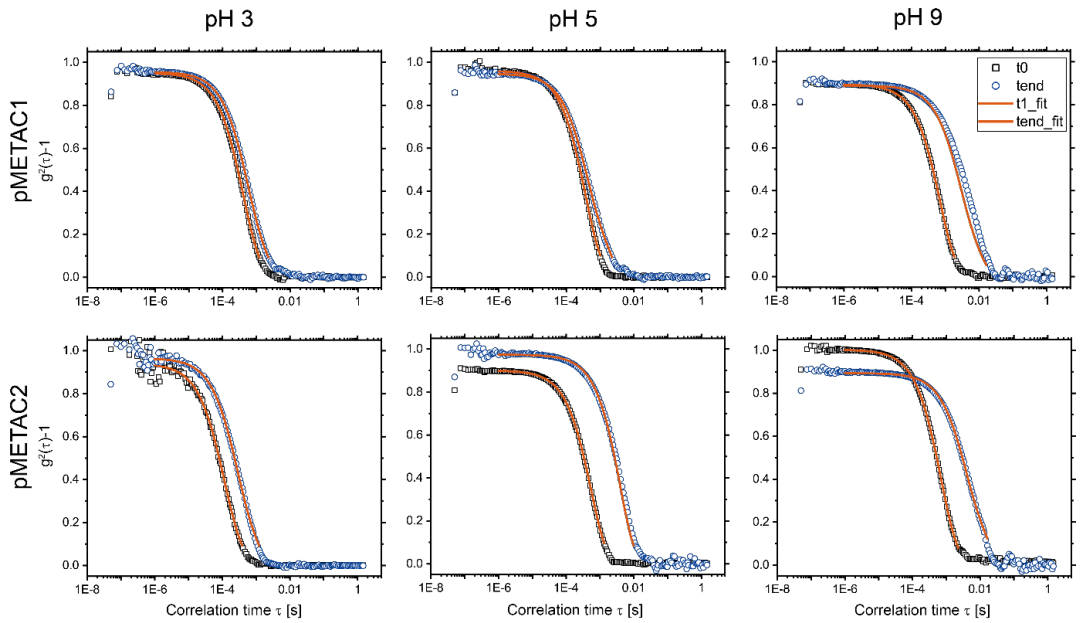

Figure S13: DLS-correlation curves for Qbeta-pMETAC1 and Qbeta-pMETAC2 at different pH and measured at 90° from the first and last data point of the time series in Figure S12.

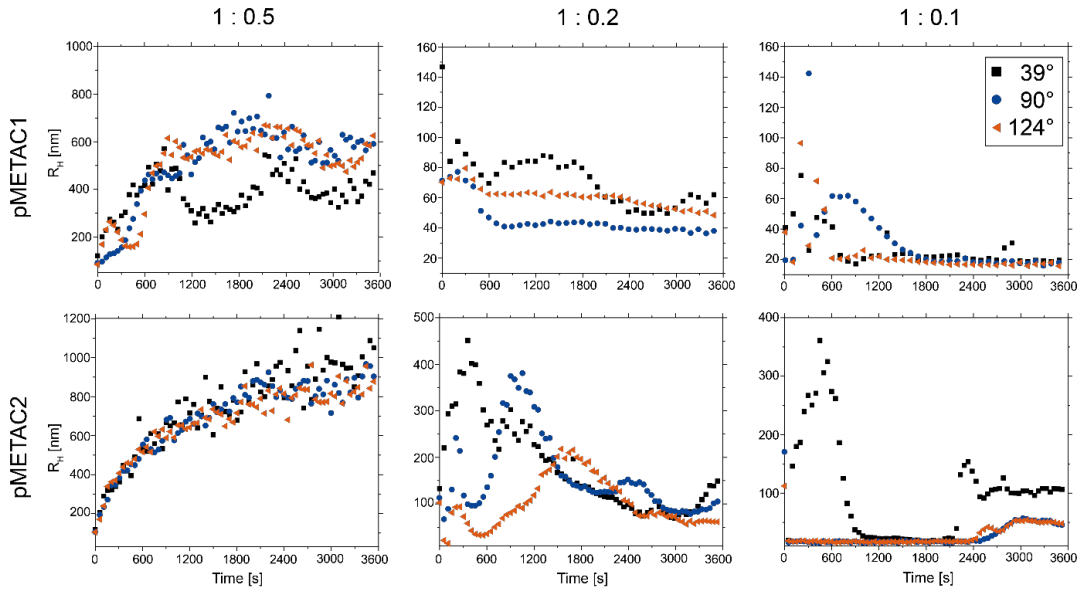

Figure S14: Time-dependent DLS curves of Qbeta-pMETAC1 and Qbeta-pMETAC2 at different Qbeta/pMETAC ratios and measured at three different angles showing the change in R_H over one hour. The corresponding correlation curves to the first and last time point of each dataset can be found in Figure S15.

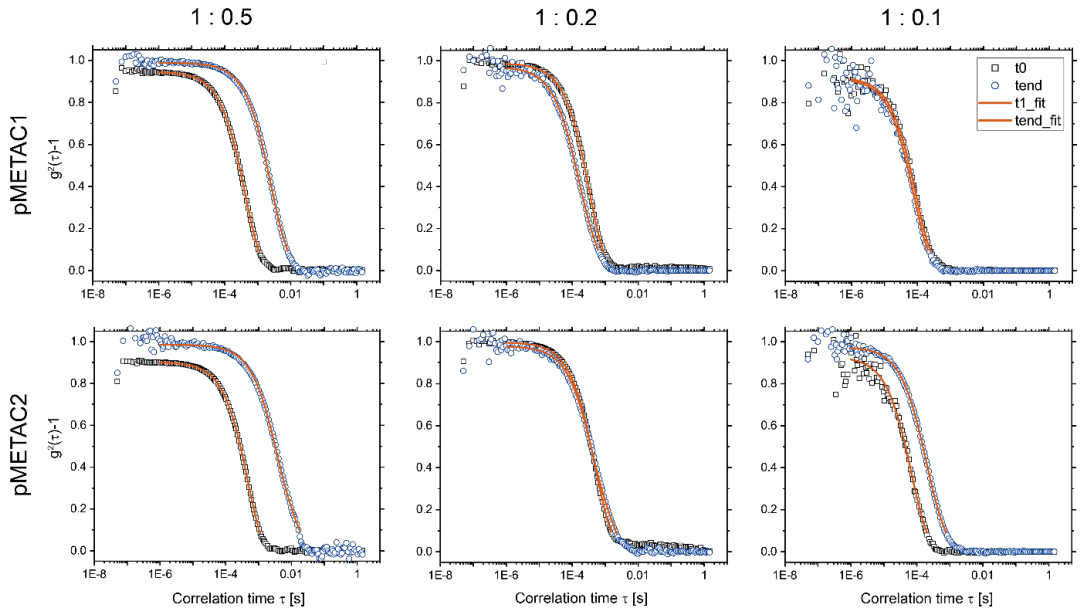

Figure S15: DLS correlation curves for the Qbeta-pMETAC1 and Qbeta-pMETAC2 at different ratios at 90° from the first and last data point of the aggregation study in Figure S14.

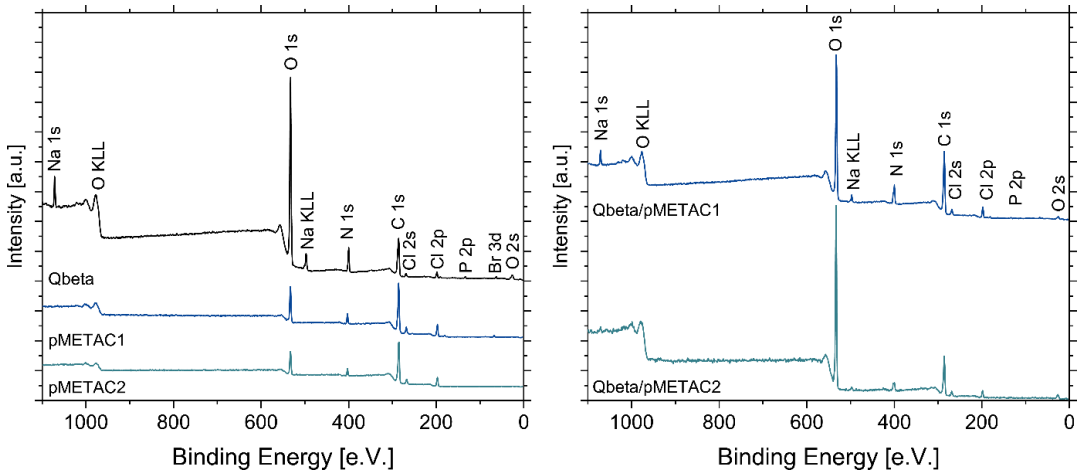

Figure S16: XPS survey spectra of Qbeta, pMETAC1, pMETAC2 and the assemblies at a ratio of 1:50 at pH 7.0.

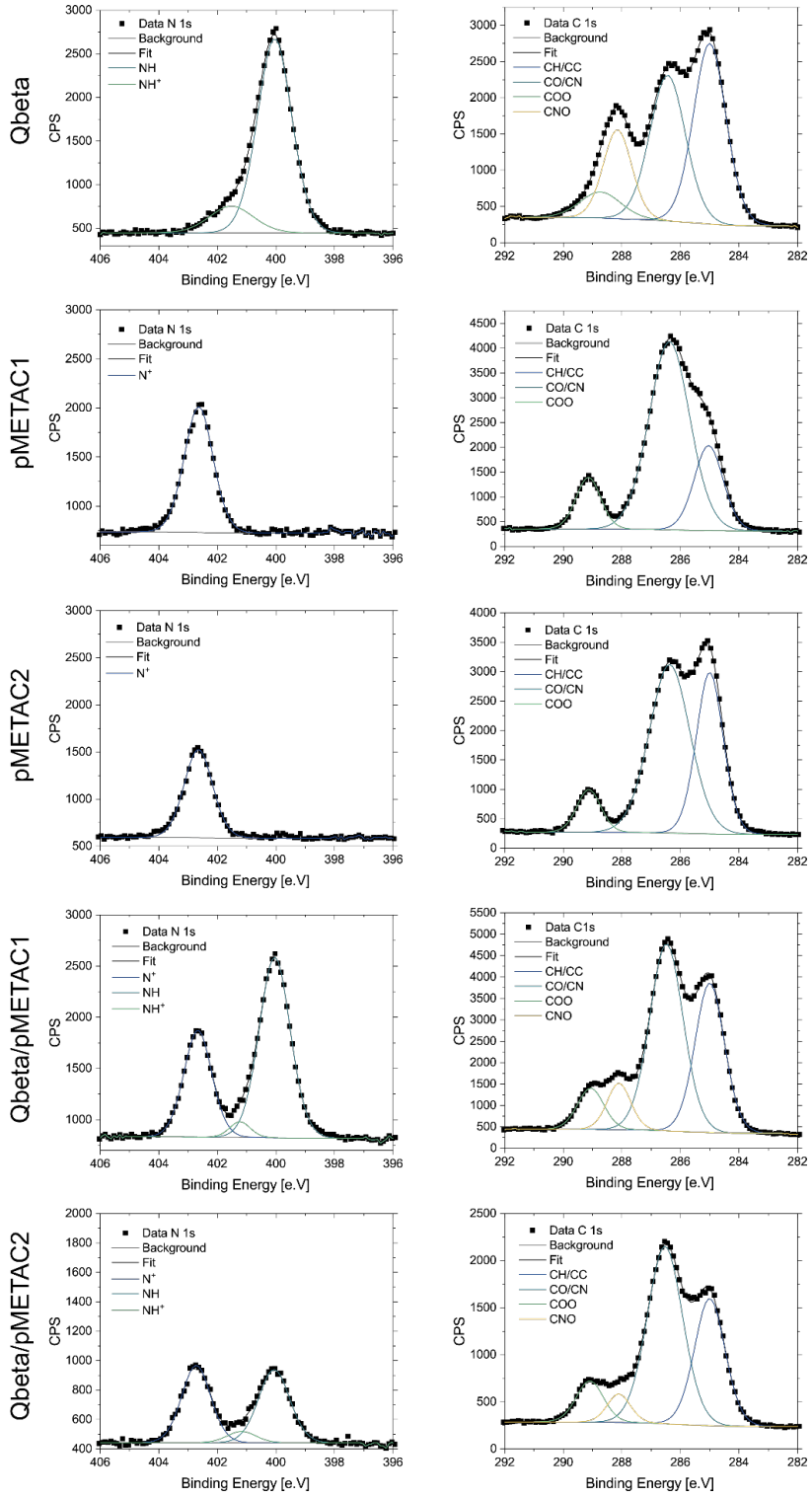

Figure S17: N 1s (left column) and C 1s XPS spectra (right column) of Qbeta, the individual polymers and Qbeta/pMETAC (1:50) assemblies at pH 7.0 with the fits.

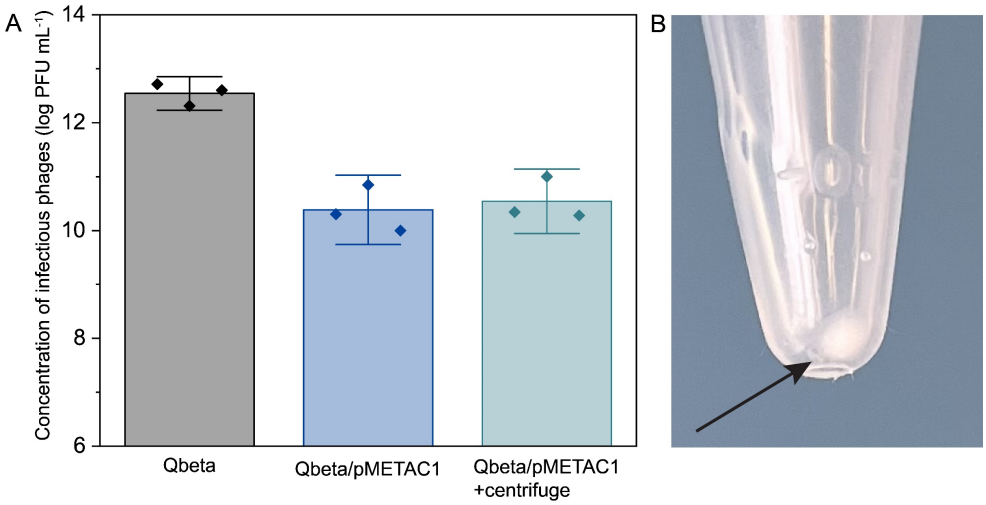

Figure S18: (A) Infectivity of Qbeta before pMETAC addition, the Qbeta/pMETAC1 1:50 suprastructures, and the Qbeta/pMETAC1 1:50 suprastructures after separation from the liquid phase as macroscopic aggregate, using centrifugation, and resuspension in fresh VDB on *E. coli* at pH 7.0. The phage suspensions were serial-diluted and spotted on an *E. coli* bacterial lawn on agar to quantify the plaque-forming units (PFU). The results represent the mean ± standard deviations of three readouts. (B) Representative picture of the macroscopic Qbeta/pMETAC1 1:50 suprastructure after centrifugation. The arrow points to the pellet inside the Eppendorf tube.

Table S1: fitting parameter used to fit the SAXS data of Qbeta and the assembly Qbeta-pMETAC1 with the described model. The scale factor for core-shell was fixed to 1, and scaling due to concentration was adjusted by scaling the scattering length density of the shell. High standard deviations were observed for $\Delta\eta 1$, likely from a mixture of RNA-loaded and empty Qbeta particles.[24]

Fitting parameter for SAXS scattering of Qbeta		
	Variable	Parameter/ Fitted result
$f_g(R)$ of core-shell particle	N (Scaling factor)	1
	s	1.11 ± 0.01
$P_s(q,R)$	$\Delta\eta 1$	0.002 ± 0.002
	$\Delta\eta 2$	0.0041
	Radius of core R	10.1 ± 1.2 nm
	Thickness of shell ΔR	2.7 ± 0.1 nm
$P_G(q)$	R_g	0.9 ± 0.1 nm
	I_0	0.3 ± 0.06
Fitting parameter for SAXS scattering of Assembly (Qbeta and pMETAC1)		
$F_g(R)$ of core-shell particle	N (Scaling factor)	1
	s	2.06 ± 0.06
$P_s(q,R)$	$\Delta\eta 1$	0.002 ± 0.04
	$\Delta\eta 2$	0.0041
	Radius of core R	16.2 ± 0.2 nm
	Thickness of shell ΔR	1.6 ± 0.5 nm
$S_{hex}(q)$	Lattice constant a	of 27.8 ± 0.1 nm
	Thermal Lattice displacement σ_a	0
	Peak width δ	0.038 ± 0.027
	cL (scaling factor of Z_0)	1
	Max(hkl)	6
$P_G(q)$	R_g	1.1 ±0.2 nm
	I_0	1.83 ± 0.03
	N (scaling factor)	0.03 ± 0.34
	Alpha	3 ± 0.2

Table S2: Aggregation kinetics of Qbeta with pMETAC: Fitting parameters (*A*, *B*, *C*) from DLCA model, whereby C was kept constant. The resulting fractal dimension (D_f), scaling factor (K_f) and estimate of the number of particles in aggregate (*i*) after 1 hour, were calculated according Eq. S22, S23 and S24.

Sample	***A***	***B***	***C***	D_f	K_f	R_H	***i***	$I/V*10^{-7}$
						[nm]		[particles /nm^3]
Qbeta: pMETAC1 (1:1), pH7	16.5 ± 5.8	0.48 ± 0.05	180	2.1	0.95	991	1793	4.4
Qbeta: pMETAC1 (1:1), pH9	29.3 ± 6.4	0.43 ± 0.03	160	2.3	0.77	1098	4144	7.5
Qbeta: pMETAC2 (1:1), pH7	19.7± 8.7	0.47 ± 0.06	110	2.1	0.93	935	1719	5
Qbeta: pMETAC2 (1:1), pH9	29.8± 14	0.38± 0.05	150	2.3	0.8	1121	3931	6.7
Qbeta: pMETAC2 (1:0.5), pH7	40.8 ± 14.7	0.38± 0.05	63	2.6	0.6	986	7147	17.8

Table S3: XPS data for pMETAC, Qbeta and its composites. pMETAC spectras were acquired at room temperature, while the rest was acquired with cryo-XPS in VDB buffer.

Sample	**C 1s** Binding Energy (eV) / Concentration(at%)								**N 1s** Binding energy (eV) / Concentration(at%)					
	CH/CC		CO/CN		CNO		COO		NH		NH+		N+	
pMETAC 1	285.0	15.8	286.4	49.0	-	-	289.1	8.1	-	-	-	-	402.6	6.6
pMETAC 2	285.0	27.5	286.4	43.2	-	-	289.1	6.4	-	-	-	-	402.7	5.6
Qbeta	285.0	14.8	286.5	13.0	288.2	6.3	288.7	2.7	400.1	7.9	401.5	1.4	-	-
Qbeta + pMETAC 1	285.0	18.3	286.5	26.1	288.1	4.6	289.1	4.5	400.0	5.6	401.2	0.3	402.7	2.9
Qbeta + pMETAC 2	285.0	9.4	286.5	15.3	288.1	1.6	289.1	2.7	400.1	2.0	401.2	0.3	402.7	2.0

References

[1] C. Visnevskij, R. Makuska, *Macromolecules* **2013**, 46, 4764.

[2] A. Armanious, M. Aeppli, R. Jacak, D. Refardt, T. Sigstam, T. Kohn, M. Sander, *Environmental Science & Technology* **2016**, 50, 732.

[3] A. M. Kropinski, A. Mazzocco, T. E. Waddell, E. Lingohr, R. P. Johnson, in *Bacteriophages: Methods and Protocols, Volume 1: Isolation, Characterization, and Interactions*, DOI: 10.1007/978-1-60327-164-6_7 (Eds: M. R. J. Clokie, A. M. Kropinski), Humana Press, Totowa, NJ **2009**, p. 69.

[4] J.-Y. Chang, K. V. Gorzelnik, J. Thongchol, J. Zhang, *Viruses* **2022**, 14, 225.

[5] E. Mylonas, D. I. Svergun, *Journal of Applied Crystallography* **2007**, 40, s245.

[6] J. Brunner-Popela, O. Glatter, *Journal of Applied Crystallography* **1997**, 30, 431.

[7] J. Brunner-Popela, R. Mittelbach, R. Strey, K. V. Schubert, E. W. Kaler, O. Glatter, *The Journal of Chemical Physics* **1999**, 110, 10623.

[8] B. Weyerich, J. Brunner-Popela, O. Glatter, *Journal of Applied Crystallography* **1999**, 32, 197.

[9] G. Fritz, A. Bergmann, O. Glatter, *The Journal of Chemical Physics* **2000**, 113, 9733.

[10] O. Glatter, *Journal of Applied Crystallography* **1977**, 10, 415.

[11] O. Glatter, *Journal of Applied Crystallography* **1980**, 13, 577.

[12] O. Glatter, *Journal of Applied Crystallography* **1981**, 14, 101.

[13] O. Glatter, B. Hainisch, *Journal of Applied Crystallography* **1984**, 17, 435.

[14] J. S. Pedersen, *Advances in Colloid and Interface Science* **1997**, 70, 171.

[15] P. Debye, *The Journal of Physical and Colloid Chemistry* **1947**, 51, 18.

[16] S. Förster, S. Fischer, K. Zielske, C. Schellbach, M. Sztucki, P. Lindner, J. Perlich, *Advances in Colloid and Interface Science* **2011**, 163, 53.

[17] S. Förster, A. Timmann, M. Konrad, C. Schellbach, A. Meyer, S. S. Funari, P. Mulvaney, R. Knott, *The Journal of Physical Chemistry B* **2005**, 109, 1347.

[18] H. Berman, K. Henrick, H. Nakamura, *Nature Structural & Molecular Biology* **2003**, 10, 980.

[19] R. Golmohammadi, K. Fridborg, M. Bundule, K. Valegård, L. Liljas, *Structure* **1996**, 4, 543.

[20] A. G. Mailer, P. S. Clegg, P. N. Pusey, *Journal of Physics: Condensed Matter* **2015**, 27, 145102.

[21] J. Sabín, G. Prieto, J. M. Ruso, P. Messina, F. Sarmiento, *Physical Review E* **2007**, 76, 011408.

[22] H. Wu, M. Lattuada, M. Morbidelli, *Advances in Colloid and Interface Science* **2013**, 195-196, 41.

[23] L. Ehrl, M. Soos, M. Lattuada, *The Journal of Physical Chemistry B* **2009**, 113, 10587.

[24] U. Bachrach, A. Friedmann, *Applied Microbiology* **1971**, 22, 706.

Eidesstattliche Versicherungen und Erklärungen

§ 8 Satz 2 Nr. 3 PromO Fakultät für Biologie, Chemie und Geowissenschaften

Hiermit versichere ich eidesstattlich, dass ich die Arbeit selbstständig verfasst und keine anderen als die von mir angegebenen Quellen und Hilfsmittel benutzt habe (vgl. Art. 97 Abs. 1 Satz 8 BayHIG).

§ 8 Satz 2 Nr. 3 PromO Fakultät für Biologie, Chemie und Geowissenschaften

Hiermit erkläre ich, dass ich die Dissertation nicht bereits zur Erlangung eines akademischen Grades eingereicht habe und dass ich nicht bereits diese oder eine gleichartige Doktorprüfung endgültig nicht bestanden habe.

§ 8 Satz 2 Nr. 4 PromO Fakultät für Biologie, Chemie und Geowissenschaften

Hiermit erkläre ich, dass ich Hilfe von gewerblichen Promotionsberatern bzw. –vermittlern oder ähnlichen Dienstleistern weder bisher in Anspruch genommen habe noch künftig in Anspruch nehmen werde.

§ 8 Satz 2 Nr. 7 PromO Fakultät für Biologie, Chemie und Geowissenschaften

Hiermit erkläre ich mein Einverständnis, dass die elektronische Fassung der Dissertation unter Wahrung meiner Urheberrechte und des Datenschutzes einer gesonderten Überprüfung unterzogen werden kann.

§ 8 Satz 2 Nr. 8 PromO Fakultät für Biologie, Chemie und Geowissenschaften

Hiermit erkläre ich mein Einverständnis, dass bei Verdacht wissenschaftlichen Fehlverhaltens Ermittlungen durch universitätsinterne Organe der wissenschaftlichen Selbstkontrolle stattfinden können.

Bayreuth, 17.04.2026

Colophon

This thesis was typeset with Overleaf. I used the Clean Thesis style developed by Ricardo Langner. The design of the Clean Thesis style is inspired by user guide documents from Apple Inc. You can download the Clean Thesis style at `http://cleanthesis.der-ric.de/`. Grammarly was used for checking spelling and grammar. The figures displayed in this thesis were created using IgorPro 8.0, Affinity Designer 2.6, and Blender 3.6.

Nadine Raßmann

Developing Atomic Force Microscopy Methods
for Soft Matter Characterization

Dissertation, 2025.

University of Bayreuth
Faculty for Biology, Chemistry and Earth Sciences
Department of Physical Chemistry II: Interfaces and Nanoanalytics
Universitätsstraße 30
95447 Bayreuth